Shedding X-rays on molecules through the lenses of relativistic electronic structure theory

Wilken Aldair Misael

To cite this version:

Wilken Aldair Misael. Shedding X-rays on molecules through the lenses of relativistic electronic structure theory. Theoretical and/or physical chemistry. Université de Lille, 2023. English. NNT : 2023ULILR043 . tel-04609458

HAL Id: tel-04609458

https://theses.hal.science/tel-04609458

Submitted on 12 Jun 2024

Université de Lille

Doctoral School **ED 104 - Sciences de la Matière, du Rayonnement et de l'Environnement**
University Department **Laboratoire PhLAM**

Thesis defended by **Wilken Aldair Misael**

Defended on **October 6, 2023**

In order to become Doctor from Université de Lille

Academic Field **Physics**
Speciality **Theoretical chemical physics**

Shedding X-rays on Molecules through the Lenses of Relativistic Electronic Structure Theory

Thesis supervised by André Severo Pereira Gomes

Committee members

Referees	Dominique Guillaumont	Directrice de recherche au CEA Marcoule	
	Erik Donovan Hedegård	Assistant professor/HDR à University of Southern Denmark	
Examiners	Valérie Vallet	Directrice de recherche au CNRS/Université de Lille	
	Julien Toulouse	Maître de conférences à la Sorbonne Université	
	Philippe Sainctavit	Directeur de recherche au CNRS/Sorbonne Université	Committee President
Supervisor	André Severo Pereira Gomes	Chargé de recherche au CNRS/Université de Lille	

COLOPHON

Doctoral dissertation entitled “Shedding X-rays on Molecules through the Lenses of Relativistic Electronic Structure Theory ”, written by Wilken ALDAIR MISAEL, completed on December 12, 2023, typeset with the document preparation system LaTeX and the yathesis class dedicated to theses prepared in France.

Université de Lille

Doctoral School **ED 104 - Sciences de la Matière, du Rayonnement et de l’Environnement**
University Department **Laboratoire PhLAM**

Thesis defended by **Wilken Aldair Misael**

Defended on **October 6, 2023**

In order to become Doctor from Université de Lille

Academic Field **Physics**
Speciality **Theoretical chemical physics**

Shedding X-rays on Molecules through the Lenses of Relativistic Electronic Structure Theory

Thesis supervised by André Severo Pereira Gomes

Committee members

Referees	Dominique Guillaumont	Directrice de recherche au CEA Marcoule	
	Erik Donovan Hedegård	Assistant professor/HDR à University of Southern Denmark	
Examiners	Valérie Vallet	Directrice de recherche au CNRS/Université de Lille	
	Julien Toulouse	Maître de conférences à la Sorbonne Université	
	Philippe Sainctavit	Directeur de recherche au CNRS/Sorbonne Université	Committee President
Supervisor	André Severo Pereira Gomes	Chargé de recherche au CNRS/Université de Lille	

Université de Lille

École doctorale **ED 104 - Sciences de la Matière, du Rayonnement et de l'Environnement**
Unité de recherche **Laboratoire PhLAM**

Thèse présentée par **Wilken Aldair Misael**
Soutenue le **6 octobre 2023**

En vue de l'obtention du grade de docteur de l'Université de Lille

Discipline **Physique**
Spécialité **Physico-Chimie Théorique**

L'interaction des rayons X avec des molécules à travers le prisme de la théorie de la structure électronique relativiste

Thèse dirigée par André Severo Pereira Gomes

Composition du jury

Rapporteurs	Dominique Guillaumont	Directrice de recherche au CEA Marcoule	
	Erik Donovan Hedegård	Assistant professor/HDR à University of Southern Denmark	
Examinateurs	Valérie Vallet	Directrice de recherche au CNRS/Université de Lille	
	Julien Toulouse	Maître de conférences à la Sorbonne Université	
	Philippe Sainctavit	Directeur de recherche au CNRS/Sorbonne Université	président du jury
Directeur de thèse	André Severo Pereira Gomes	Chargé de recherche au CNRS/Université de Lille	

This thesis has been prepared at

Laboratoire PhLAM
Laboratoire PhLAM
CNRS UMR 8523
Université de Lille
Bâtiment P5
59655 Villeneuve d'Ascq
France

☎ (33)(0)3 20 43 44 84
✉ `cristian.focsa@univ-lille.fr`
Web Site `http://phlam.univ-lille.fr`

To those who made the great music, books, and movies that followed me during these years and that literally crossed the sea with me.

To all my patient and kind teachers, as well as those who always believed in me, even when it was (really) hard for me to see that (somehow) I was doing the right thing.

And most importantly, to me. ***Deu tudo certo.***

Acknowledgments

Initially, I express my gratitude to the Netherlands. I've had a big time, like in the ***silver*** *screen.*

With that in mind, although I am known for extensive acknowledgments, I will strive for brevity and apologize beforehand for any unintentional omissions. Additionally, certain acknowledgments are omitted for evident reasons.

I would like to express my sincere gratitude to Valérie Vallet, the director of the *Physico-Chimie Moléculaire Théorique* (PCMT) research group, for her patience and support throughout my thesis development. To my thesis supervisor, André Gomes, for trusting me and allowing me to pursue my dream of studying abroad. Nadiya Zhutova, for all of our conversations about The Netherlands (and France sometimes), fashion, good food, good life... we've dreamed a lot. Furthermore, I also want to express my appreciation to my friend Jessica Martinez. Our sincere exchanges, along with the shared moments over *real food* and caipirinhas during the last year of my thesis, were incredibly meaningful, thank you for being part of my story.

Furthermore, I am deeply grateful to the *Centre National de la Recherche Scientifique* (CNRS) for providing the necessary funding and resources for this thesis. I'd like to extend my gratitude to the staff of the *European Synchrotron Radiation Facility* (ESRF) for their exceptional competence in conducting experiments within one of the most remarkable installations in human history. I also have to acknowledge Patrick Norman, Trond Saue, and Kenneth Ruud for being exceptional scientists whom I never imagined having the privilege of meeting and learning from. I will cherish every lesson I learned from them in the *Molecular Response Properties Summer School 2021*. And especially, *the devil is in the details*, as Trond likes to say.

I am fortunate to have three long-term friends, Elaneide, Nathália, and Laura, who have always been there for me despite the distance. Thank you for your unwavering support and belief in me, and for the countless times we shared laughter, even in moments when we probably shouldn't have. Furthermore, I must also acknowledge my dear friend Nayanna Passos for all the times we helped each other since our time as undergraduates, for our discussions about

anything, and for teaching me about *integrity* and *perseverance*. Thank you for accepting me as your friend and for always reminding me how important it is to have *faith*.

I would also like to acknowledge Maria Luiza Rocco, who introduced me to spectroscopy and was once my supervisor when I was sure about giving up on science. Now, she is a close friend who has always motivated and inspired me. Despite her inability to convince me of the wonders of Berlin, I am grateful for her willingness and patience to help, our endless audio messages, and our friendship.

Another person who tried to convince me about Berlin is Tati Sarkis, for whom I'm so grateful for our unexpected friendship. One could say it is destiny. Thank you for being there for me and providing me with advice, such as how fleece clothes are great in winter (which was useful *throughout the year* in the north of France). Thank you for helping me achieve this, I will always be grateful for everything; we still have many *kebabs* around the world to share.

I would like to thank my aunt Edriane (*Binha*) for her company during my walks and discoveries across Europe (especially on the *Citadelle*, my shelter) and for being a constant presence in my life, despite the distance. Thank you for being with me in the greatest and hardest moments. You brought more lightness to my life than you could know.

Furthermore, I would like to acknowledge my mother, Helena Fátima da Silva, who passed away in the final stage of this thesis. For being the strong woman she was and always helping all of us, even when our resources were running low, for the food that I will always miss, for playing with toy cars with me, sometimes just listening and for being the excellent dressmaker she was. I hope she was proud of me for fulfilling her dream of studying. It was really hard. I will always regret that you weren't there to give me a thumbs up at the door when all of this was happening. I love you, mother. Thank you.

And finally, I need to acknowledge myself. Please don't mistake this for egocentricity, dear reader. However, as someone who was raised in poverty and darkness, who was subjected to an educational system light years from what is considered prestigious, who couldn't even fathom studying Darwinism and the Big Bang theory, much less going to university, I'm extremely proud of having accomplished something this meaningful in my life. I hope one day I can encourage others to overcome their struggles, even though they don't need to study electronic structure theory.

Despite hearing much about my perceived lack of patience and focus, merely an example of gaslighting, I have successfully pursued the study of quantum chemistry, which I chose to delve into during my first semester in college exactly ten years ago. Time has passed, I have crossed the ocean, and over the years, I have acquired (what I believe to be) valuable knowledge about atoms, molecules, and light, mostly through self-guided learning. Along the way, I have encountered both the best and the worst inside and outside academia. Yet, I have remained resilient and determined, and I have also experienced a lot of fun moving through the different spectra of human life.

As I've reached this point, I've occasionally questioned whether I might have taken a negative turn along the way – perhaps I've become something monstrous. Yet, what remains consistent is that I am still a sensitive human being with countless flaws. Considering all that I've experienced in my 28 years, who could craft such acknowledgments and truly understand them? That remains a matter for a sensitive yet determined individual.

If I didn't require the privileges that many have enjoyed their entire lives to reach this juncture, what more can I do now with this experience? Achieving all this without being at my best, what lies ahead?

Whatever that will be, having conquered those challenges, I genuinely believe I can achieve anything I set my mind to, including peace of mind.

Must've been forces, that took me on them wild courses
Who knows how many poses that I've been in
I worried 'bout rain and I worried bout lightning
But I watched them off to the light of the morning
Marking the slope, slung low in the highlands
The days have no numbers

00000 Million, Bon Iver

SHEDDING X-RAYS ON MOLECULES THROUGH THE LENSES OF RELATIVISTIC ELECTRONIC STRUCTURE THEORY

Abstract

This thesis aims to investigate the electronic structure of actinides by means of *ab initio* relativistic quantum chemistry methods, with a specific emphasis on the spectroscopic observables of the uranyl moiety (UO_2^{2+}). Considering the pivotal role of this unit in the solid-state and solution chemistry of uranium, one of the most abundant and stable actinides on earth, as well as recent advancements in synchrotron radiation facilities, our investigation relies on evaluating the interaction of x-ray photons with the uranyl unit in varying degrees of complexity, ranging from molecules to crystalline solids.
First, we showcase how the resonant-convergent formulation of response theory can be employed to investigate the X-ray absorption fine structure (XAFS) of actinides. 4-component damped-response time-dependent density functional theory (4c-DR-TD-DFT) simulations for the uranyl tetrachloride dianion ($UO_2Cl_4^{2-}$) were found to be consistent with previous data for angle-resolved near edge x-ray absorption spectroscopy (NEXAFS) at the oxygen K-edge and high energy resolution fluorescence detected (HERFD) at the uranium M_4- and L_3-edges of the dicesium uranyl tetrachloride crystal ($Cs_2UO_2Cl_4$), a prototype system for actinide electronic structure investigations. We then will present the results of collaborative work with the Rossendorf Beamline at the European Synchrotron Radiation Facility (ESRF). 2-component TD-DFT simulations within the Tamm-Dancoff approximation (2c-TDA) and HERFD measurements of linear and bent uranyl systems highlight the role of charge transfer states in determining the spectral features at the uranium M_4-edge. The role of orbital correlation and relaxation in the core-ionization energies of heavy elements was investigated using the recently developed core-valence-separation equation-of-motion coupled-cluster method (CVS-EOM-CC). We also evaluated the performance of various 4- and 2-component Hamiltonians for calculating these properties. The results of this investigation demonstrate qualitative agreement with previously reported X-ray photoemission spectroscopy (XPS) data for $Cs_2UO_2Cl_4$ in the soft x-ray range (0.1 – 1 keV) and highlight the importance of computing two-electron interaction beyond the zeroth order truncation, i.e., the Coulomb term, when working at the tender (1 keV – 5 keV) and hard x-ray (5 keV – 200 keV) ranges. We also evaluated the performance of quantum-chemical embedding methods to account for environmental effects. Specifically, we employed the frozen density embedding (FDE) method, which allowed us to gain valuable insights into how the equatorial ligands of the uranyl ion influence its spectroscopic properties. Notably, this method successfully addressed the role of such interactions in binding energies in the soft x-ray range and in the peak splittings observed in the emission spectra at the U M_4-edge. The latter is particularly significant as it has been instrumental in addressing a long-standing problem in actinide science: the role of 5*f* orbitals in actinyl bonding.
In summary, this thesis presents fundamental research work that aims to push the boundaries of *ab initio* quantum chemical methods when addressing spectroscopic observables towards the bottom of the periodic table, and the findings of this work capture how these approaches can provide further insights into state-of-the-art experiments.

Keywords: x-ray spectroscopy, electronic structure theory, actinides

---

Laboratoire PhLAM
Laboratoire PhLAM – CNRS UMR 8523 – Université de Lille – Bâtiment P5 –
59655 Villeneuve d'Ascq – France

L'INTERACTION DES RAYONS X AVEC DES MOLÉCULES À TRAVERS LE PRISME DE LA THÉORIE DE LA STRUCTURE ÉLECTRONIQUE RELATIVISTE

Résumé

Cette thèse vise à étudier la structure électronique des actinides au moyen de méthodes de chimie quantique relativiste *ab initio*, avec une emphase particulière sur les observables spectroscopiques de l'unité uranyle (UO_2^{2+}). Considérant le rôle central de cette unité en chimie des solides et en milieux aqueux et organique, ainsi que les avancées récentes dans les installations de rayonnement synchrotron, notre étude repose sur l'évaluation de l'interaction des photons de rayons X avec l'unité uranyle dans des degrés de complexité variés, allant des molécules aux solides cristallins.

Tout d'abord, nous mettons en avant comment la formulation résonante-convergente de la théorie de la réponse peut être utilisée pour étudier la structure fine d'absorption des rayons-X (XAFS) des actinides. Les simulations de la théorie de la fonctionnelle de la densité dépendante du temps avec réponse amortie en 4 composantes (4c-DR-TD-DFT) pour le dianion tétrachlorure de diuranyl ($UO_2Cl_4^{2-}$) se sont avérées cohérentes avec les données antérieures de méthodes spectroscopiques avec résolution angulaire, à savoir celles d'absorption des rayons X près du seuil (NEXAFS) au seuil K de l'oxygène et de détection de fluorescence à haute résolution énergétique (HERFD) aux seuils M_4 et L_3 de l'uranium du cristal de tétrachlorure de diuranyl de dicesium ($Cs_2UO_2Cl_4$), un système prototype pour les études de structure électronique des actinides. En plus, nous présenterons les résultats d'un travail collaboratif avec la ligne de lumière Rossendorf de l'Installation Européenne de Rayonnement Synchrotron (ESRF). Les simulations TD-DFT dans l'approximation de Tamm-Dancoff à 2 composantes (2c-TDA) et HERFD des différents complexes d'uranyle mettent en évidence le rôle des états de transfert de charge dans la détermination des caractéristiques spectrales au niveau du seuil M_4 de l'uranium. Le rôle de la corrélation et de la relaxation des orbitales dans les énergies d'ionisation de cœur des éléments lourds a été étudié en utilisant la méthode des équations de mouvement de cluster couplé avec la séparation cœur-valence (CVS-EOM-CC) récemment développée. Nous avons également évalué les performances de différents Hamiltoniens à 4- et 2- composantes pour le calcul de ces propriétés. Les résultats de cette étude soulignent l'importance du calcul des intégrales à deux électrons au-delà de la troncature d'ordre zéro, c'est-à-dire du terme de Coulomb, lorsqu'on travaille dans les gammes de rayons X tendres (1 – 5 keV) et durs (5 – 200 keV). Par ailleurs, nous avons également évalué les performances des méthodes de chimie quantique pour tenir compte des effets environnementaux. Plus précisément, nous avons utilisé la méthode d'intégration de densité figée (FDE) qui nous a permis d'acquérir des connaissances précieuses sur la manière dont les ligands équatoriaux de l'ion uranyle influencent ses propriétés spectroscopiques. Notamment, cette méthode a réussi à aborder le rôle des interactions électrostatiques dans les énergies de liaison dans la gamme des rayons X mous et dans les dédoublements de pics observés dans les spectres d'émission au niveau du seuil M_4 de l'uranium. Ce dernier est particulièrement significatif car il contribue de manière déterminante à aborder un problème de longue date dans la science des actinides : le rôle des orbitales 5*f* dans la liaison actinyle.

En résumé, cette thèse présente un travail de recherche fondamentale qui vise à repousser les limites des méthodes quantiques *ab initio* dans l'étude des observables spectroscopiques pour les éléments situés en bas du tableau périodique. Les résultats de cette étude illustrent comment ces approches peuvent apporter de nouvelles compréhensions sur les expériences de pointe.

Mots clés : spectroscopie des rayons x, théorie de la structure électronique, actinides

Contents

Introduction

> *"Perhaps we can even put an end to the dispute over whether light is a body."*
>
> — Isaac Newton in *"A letter to the Royal Society presenting a new theory of light and colours"*, 1672.

The response of an assembly of atoms to an external electromagnetic field can provide invaluable insights into the fundamental building blocks of our universe, ranging from subatomic particles to celestial bodies far away from our eyes.

X-rays have played a central role in fundamental and applied sciences since their discovery by Röntgen in 1895. These encompass a broad range of the electromagnetic spectrum and are commonly classified into three primary energy windows: soft X-rays (0.1 – 1 keV), tender X-rays (2 – 4 keV), and hard X-rays (5 – 200 keV) [1]. Furthermore, the field of X-ray spectroscopy has greatly benefited from recent technological innovations, resulting in highly advanced synchrotron radiation facilities and X-ray free-electron laser (XFEL) facilities. In this thesis, our focus is on performing simulations to reproduce experiments using synchrotron radiation.

In synchrotron radiation facilities, the radiation originates from electrons moving at relativistic velocities. The underlying physical phenomenon is known as *magnetobremsstrahlung radiation* [1]. This phenomenon occurs when insertion devices, such as bending magnets, deflect high-energy electrons in a storage ring, as illustrated in Figure 1.

Synchrotron radiation possesses several prominent features, including a broad energy spectrum, high brightness, wide energy range, tunable wavelength,

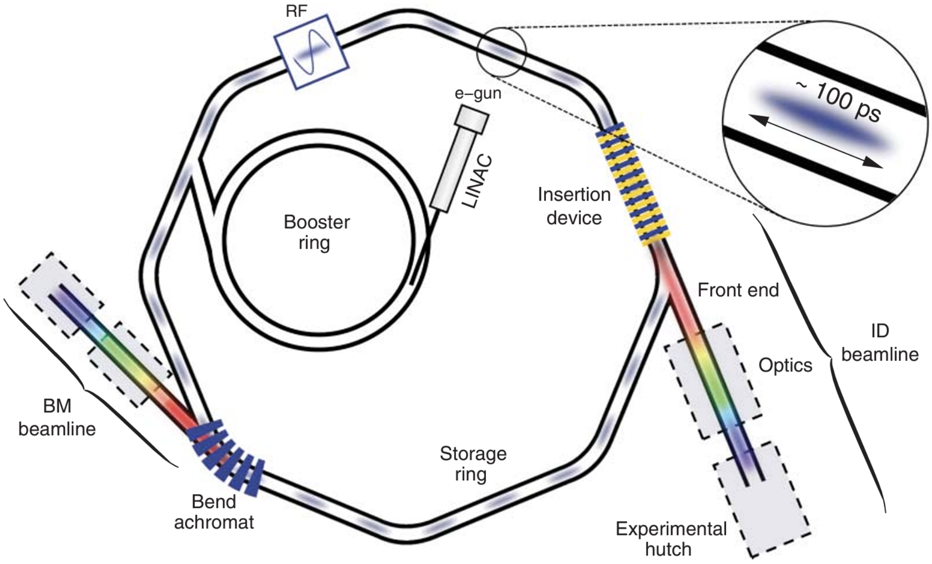

Figure 1: Schematic representation of a synchrotron light source. An electron gun generates electrons (depicted in blue) and undergoes acceleration in a linear accelerator (LINAC) before being injected into a storage ring. The trajectory of the electrons within the storage ring is altered by bending magnets, leading to the emission of synchrotron radiation. This emitted radiation is collected at the connected end-stations. – Adapted from Willmott [1]. Figure used with permission from John Wiley & Sons, Ltd.

and polarization [1–4]. For example, the extremely brilliant source storage ring of the European Synchrotron Radiation Facility (ESRF-EBS) operates at an electron beam energy of 6.04 GeV, and experiments are typically performed at photon energies between 5 and 60 keV.

In summary, these state-of-the-art installations have opened up new frontiers in various scientific domains, including chemistry. The experiments conducted in these facilities have yielded valuable insights into various aspects of the electronic structure of atoms and molecules. For instance, angle-resolved X-ray photoemission spectroscopy (ARPES) experiments have provided insights into the band structure and surface properties of materials [5, 6], while X-ray absorption spectroscopy (XAS) has been used to investigate the oxidation states of transition metals [7–10] and actinides [11–18], among other applications. Furthermore, a recent study has successfully investigated the spectroscopic properties of a single iron atom through XAS experiments [19].

However, these novel experiments require theoretical calculations to aid in their interpretation and analysis, shedding light on the most fundamental aspects of the matter. In fact, a considerable fraction of state-of-art studies with experimental techniques such as high energy resolution fluorescence detection-XAS [20, 21], ultrafast X-ray transient absorption spectroscopy [22] and those with X-rays produced by high-harmonic generation [23–25] have been supported by theoretical simulations.

The following thesis aims to contribute to this field of research by exploring the theoretical modeling of core excited states, taking into account the unique characteristics of both the system's ground and excited states using relativistic quantum chemistry methods.

Fundamentals of X-ray spectroscopies

The energy levels of core electrons, i.e., those located in inner shells, fall precisely within the X-ray range. Unlike valence electrons, core electrons do not actively participate in chemical bonding but remain localized around their respective atomic nuclei. Moreover, specific inner shells of an element possess distinct characteristic energies that differentiate them from other shells within the same element and from core levels of different elements. These factors emphasize the element-specific and orbital-selective character of X-ray spectroscopies.

X-ray spectroscopies not only reflect the characteristics of the investigated element but also provide valuable insights into the immediate environment surrounding specific atoms. This is characterized, for instance, by the peak shifts observed in photoemission experiments. X-ray photoelectron spectroscopy (XPS), which is based on the photoelectric effect [26, 27] and established by Siegbahn [28], is widely acknowledged as one of the most powerful tools for probing local coordination environments or oxidation states across the entire periodic table. Additionally, photoelectron spectroscopies enable the observation of many-electron effects, such as satellite peaks [1, 4, 29, 30].

When an incident X-ray photon has a frequency below or near the core ionization threshold, a core electron absorbs this photon and is promoted to an unoccupied state, resulting in the formation of a core hole, i.e.:

$$M + \hbar\omega' \rightarrow M^* \tag{1}$$

where M denotes the system in its ground state and M^* corresponds to the system in its electronically excited state with a core hole. This process is named *photoabsorption*.

Conversely, when the energy of the incoming X-ray photon surpasses the core ionization threshold, the core electron is detached from the atom, i.e:

$$M + \hbar\omega \rightarrow M^* + e^- \tag{2}$$

The ejected electron is referred to as a photoelectron, and the process is known as *photoionization*.

The processes of photoabsorption and photoionization are depicted in Figure 2. The former is studied in X-ray absorption spectroscopy (XAS), while the latter is explored in X-ray photoelectron spectroscopy (XPS), which will be briefly described below.

X-ray absorption spectroscopy

In an XAS experiment, the quantity under measurement is the absorption coefficient, μ, which can be expressed in the linear regime as [1]:

$$\mu = -\frac{\ln(I/I_0)}{\rho_m} \tag{3}$$

where I is the transmitted X-ray intensity, I_0 is the incident X-ray intensity, and ρ_m is the mass density of the material.

On the left side of Figure 3, beryllium, silicon, and lead atoms are presented as examples to illustrate the behavior of the X-ray absorption coefficient. It is evident that for these atoms, the coefficient exhibits a pronounced and rapid increase at different energy ranges, indicating the presence of absorption edges. These absorption edges, located near the ionization threshold, signify the excitation of electrons from specific energy levels rather than the transmission of X-rays through the sample.

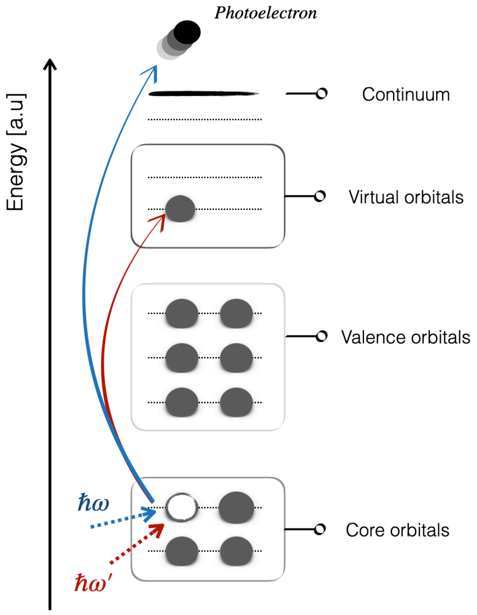

Figure 2: Schematic representation of the absorption process (depicted in red) and ionization process (depicted in blue) for core-level electrons. In the absorption process, an atom absorbs an X-ray photon with energy below the ionization threshold ($\hbar\omega'$), resulting in the excitation of a core electron to a virtual orbital. Conversely, when the photon energy exceeds that of the ionization threshold ($\hbar\omega$), a photoelectron is emitted from the system.

Another useful quantity is the photoabsorption cross-section, σ, whose relation with μ is given by:

$$\sigma = \frac{\mu}{\rho_m} \tag{4}$$

σ is defined as the number of electrons excited per unit of time divided by the number of incident photons per unit of time divided by the number of incident photons per unit of time and per unit of area [3]:

$$\sigma = \frac{P_{if}}{F_{ph}} \tag{5}$$

where F_{ph} is the photon flux and P_{if} is the probability of the transition from an initial state $|\psi_i\rangle$ to a final state $|\psi_f\rangle$ per unit of time. From time-dependent perturbation theory, one can obtain the following expression to σ [31]:

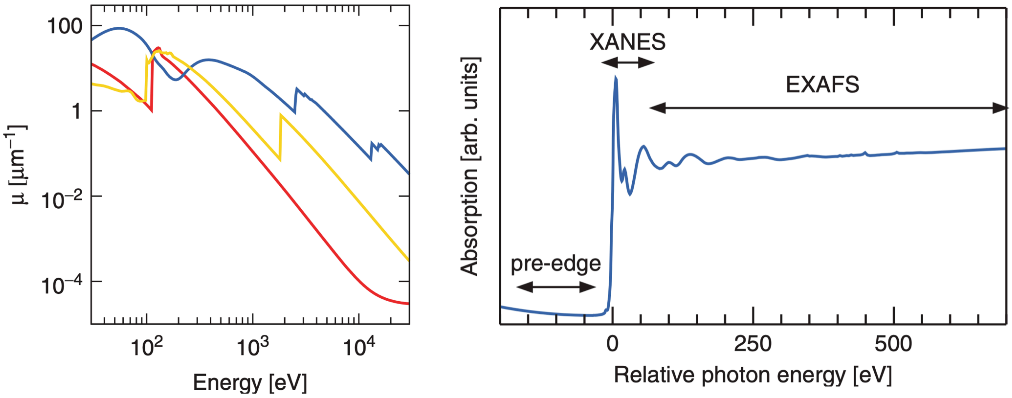

Figure 3: The X-ray absorption coefficient (μ) for beryllium (red curve), silicon (yellow), and lead (blue) as a function of the photon energy. Right: Regions of the X-ray absorption fine structure (XAFS). At lower energies, pre-edge features appear, followed by the absorption edge, constituting the Near Edge X-ray Absorption Fine Structure (NEXAFS) region. At higher energies, oscillations characterize the Extended X-ray Absorption Fine Structure (EXAFS) region – Taken from Willmott [1]. Figure used with permission from John Wiley & Sons, Ltd.

$$\sigma(\omega) = \frac{4\pi\omega}{3c} \sum_{|\psi_f\rangle} \left| \left\langle \psi_f | \hat{T} | \psi_i \right\rangle \right|^2 \delta(\omega_f - \omega_i - \omega) \tag{6}$$

where $\hat{T}$ represents an interaction operator, such as the dipole moment operator ($\hat{\mu}$). $\left\langle \psi_f | \hat{T} | \psi_i \right\rangle$ is the transition matrix element. The term $\delta(\omega_f - \omega_i - \hbar\omega)$ corresponds to the Dirac delta, which ensures that the transition occurs only if $\omega = \omega_f - \omega_i$.

The X-ray absorption fine structure (XAFS) is a spectral region that encompasses the X-ray absorption process [1, 3]. Within this region, a further division reveals two distinct regions, as illustrated on the right side of Figure 3. The first region, often referred to as the X-ray absorption near edge structure (XANES) region or near edge X-ray absorption fine structure (NEXAFS), encompasses both the pre-edge features and the absorption edge. Within this region, one can observe spectral features resulting from the excitation of a core electron to an unoccupied energy level. Additionally, Rydberg and shape resonances, as well as self-absorption features, can be present at high energies [1, 3].

The second region, known as the Extended X-ray Absorption Fine Structure (EXAFS) region, is situated approximately 20–30 eV above the ionization threshold. Within this region, the core electron under investigation is in an unbound state, i.e., in the continuum. The observed features in the EXAFS spectra come from the interaction between the photoelectrons and their surrounding environment, leading to constructive or destructive interference patterns. These manifest as oscillations in the absorption cross-section and are commonly employed to obtain structural parameters.

X-ray photoelectron spectroscopy

X-ray photoelectron spectroscopy (XPS) is a technique based on the photoelectron effect, experimentally observed by Hertz in 1887 [26] and theoretically described by Einstein in 1905 [32]. In this technique, an energy analyzer is used to evaluate the kinetic energies and angular distributions of the emitted photoelectrons of a sample.

The kinetic energy of a photoelectron, represented as E_k, can be determined by subtracting the binding energy of the electron (E_b) from the energy of the incident X-ray photon ($\hbar\omega$).

$$E_k = \hbar\omega - E_b \tag{7}$$

In addition, the intensity of the photoelectron signal in XPS is directly proportional to the photoelectron matrix element, which can be approximately expressed as [33]:

$$D_k = \left\langle \phi_k \psi^{N-1} | \hat{T} | \psi^N \right\rangle \tag{8}$$

where ψ^N and ψ^{N-1} correspond to the many-body wavefunctions of the initial and final (ionized) states, respectively, while ϕ_k represents the wavefunction of the ejected electron.

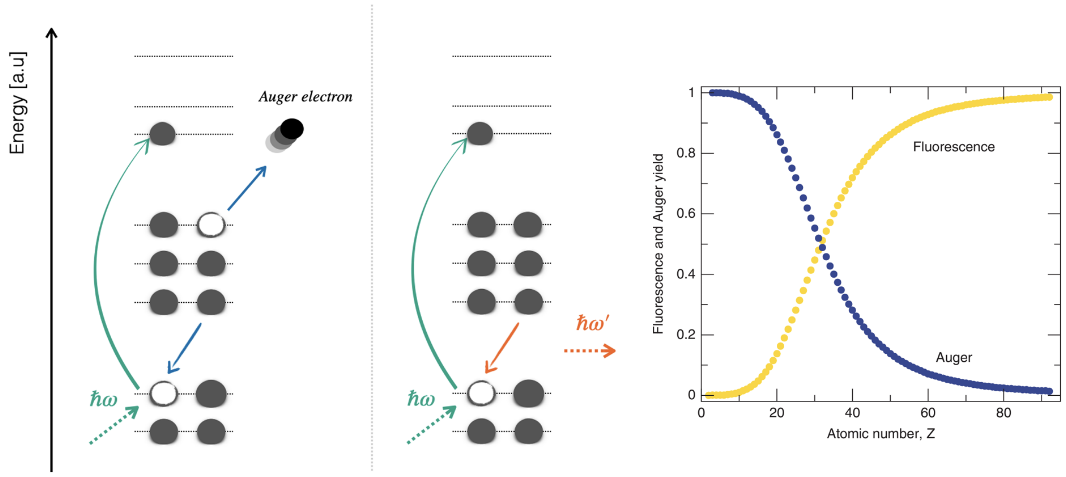

(a) Non-radiative decay (b) Radiative decay (c) Fluorescence and Auger yields

Figure 4: Schematic representation of the (a) non-radiative and (b) radiative decay channels following the absorption of an X-ray photon. (c) Fluorescence yields for K-radiation of the elements and Auger yield for K-shell vacancies, plotted as a function of atomic number, Z – Adapted from Willmott [1]. Figure used with permission from John Wiley & Sons, Ltd.

Excited state dynamics

After the X-ray absorption process, the system enters a highly excited state with a core hole. The decay of the core hole occurs through different channels, as illustrated in Figure 4. In the first case (Figure 4a), relaxation takes place through a non-radiative Coulomb interelectron interaction known as the Auger-Meitner effect [34–36]. This process involves the emission of a secondary electron, called the Auger electron when an electron from an upper shell fills the core hole. In photoionization processes, Auger decay, specifically the normal Auger decay process, is the dominant mechanism, resulting in the formation of two holes in the system [36]. Furthermore, the characteristics of this decay channel can be observed as satellite peaks in XPS spectra [29].

Returning to the relaxation dynamics, Figure 4b illustrates a scenario in which relaxation occurs via electromagnetic interaction, i.e. fluorescence emission, following the decay of an electron from an upper shell [34]. When a core hole can decay via both radiative and non-radiative channels, these channels compete with each other. Furthermore, the decay rate (d/dt) for the total number of core holes (N) can be expressed as follows [35]:

$$\frac{dN(\chi,t)}{dt} = -N(\chi,t)(k_{\mathrm{FY}}(\chi) + k_{\mathrm{AY}}(\chi)) \tag{9}$$

where k_{FY} and k_{AY} are the decay constants for the radiative and non-radiative channels of a given core hole state χ, respectively. These constants reflect the extent to which these channels can occur. This aspect highlights another benefit of element-specificity and orbital-selectivity in X-ray spectroscopies. The probability of a particular decay occurring depends on the atomic number of the studied chemical element and the excited orbital. This allows for the selection of the detection mode in experiments that exploit a specific core hole decay.

Figure 4c depicts the Auger and fluorescence yields for 1s (K-edge) vacancy as a function of atomic number, A. For elements with low atomic numbers (Z), the Auger yield is higher, indicating a predominance of the non-radiative process. Techniques such as total electron yield (TEY) and partial electron yield (PEY) are commonly employed to study the XAS of these elements at their absorption edges. Conversely, for elements with higher atomic numbers, the radiative process is dominant. This necessitates the use of detection modes such as total fluorescence yield (TFY) and partial fluorescence yield (PFY) in such spectroscopies [1, 3].

Furthermore, in systems where radiative decay dominates, further investigation of the X-ray emission process can be conducted using X-ray scattering techniques, such as non-resonant inelastic X-ray scattering (NIXS) and resonant inelastic X-ray scattering (RIXS) techniques. These scattering processes can be described by the Kramers-Heisenberg dispersion formula [37, 38]. In the specific scenario of resonant X-ray scattering, the differential cross-section is given by the proportionality [34, 39]:

$$\frac{d^2\sigma^{RXS}(\omega,\omega')}{d\omega'} \propto \frac{\omega'}{\omega}\sum_{|\psi_f\rangle}\left|\sum_{|\psi_n\rangle}\frac{\langle\psi_f|\hat{T}|\psi_n\rangle\langle\psi_n|\hat{T}|\psi_i\rangle}{\omega-\omega_{0n}+i\frac{\Gamma_n}{2}}\right|^2 \delta(\omega-\omega'-\omega_{fn},\frac{\Gamma_f}{2}) \tag{10}$$

where $\sum_{|\psi_f\rangle}$ and $\sum_{|\psi_n\rangle}$ denotes the sum over all the final and intermediate states, respectively. ω_{kl} is the transition energy between states $|\psi_k\rangle$ and $|\psi_l\rangle$. Γ_n is the full width at half maximum (FWHM) of the core-excited state $|\psi_n\rangle$. The term $\delta(\omega - \omega' - \omega_{fn}, \frac{\Gamma_n}{2})$ is the delta function of Γ_n, which accounts for the conservation of energy during the photon-in photon-out process. Additionally, the lifetime broadening of the intermediate and final states is represented by the terms Γ_n and Γ_f, respectively.

RIXS measurements have been shown to be instrumental in overcoming the limitations of TFY detection, which is considerably affected by saturation and self-absorption effects. These effects lead to strongly distorted spectral intensities that do not accurately represent the 'true XAS spectra', as highlighted by some authors [9, 35]. Specifically, the information obtained from a RIXS spectrum can assist in conducting XANES experiments in the High Energy Resolution Fluorescence Detected mode (HERFD) [40], achieving unprecedented spectral resolution. Further details about this fluorescence detection technique will be discussed in the subsequent sections.

It is important to note that regardless of whether the incoming X-ray photon has energy near or above the ionization threshold, the system continues its relaxation dynamics by ionizing upper shells to fill the core hole formed in each subsequent process until it reaches a more stable state. These complex excited-state dynamics give rise to phenomena such as Resonant Auger (Participant and Spectator processes) and Auger cascades, which have the potential to cause the breaking of chemical bonds [41–43].

Exploring the excited states of uranyl-containing compounds

The majority of this thesis focuses on investigating the interaction between X-rays and compounds containing the actinide element uranium, particularly those that include the uranyl moiety (UO_2^{2+}). Various spectroscopic techniques are available to gain insights into the low-energy excited states of these compounds. Laser-based techniques, such as Time-resolved Laser-induced Fluorescence Spectroscopy (TRLFS) and Laser-induced fluorescence (LIF), have been extensively employed to investigate systems containing the UO_2^{2+} unit, as highlighted in the works of Collins et al. [44] and Natrajan [45]. Along with Transient Absorption Spectroscopy measurements, these techniques have been shown to provide valuable information on actinide coordination chemistry, as reviewed by Natrajan [45]. Considering their potential risks to human health, these spectroscopic techniques have also demonstrated their relevance in understanding the biogeochemistry of actinides, as discussed by Collins et al. [44]. Additionally, authors like Oher et al. [46–48] have reported investigations in which such measurements were further complemented by theoretical investigations.

In terms of photoelectron spectroscopy, previous studies have reported investigations of the $UO_2Cl_4^{2-}$ dianion [49] and the $Cs_2UO_2Cl_4$ crystal [50] using valence-band XPS. This technique has also been applied to other actinide-containing systems such as the uranyl dioxide (UO_2) [51] and trihydrides (AnH_3, An=U, Pu, Am) [52], as well as thorium penta-hydride (ThH_5). These investigations cover both solid-state and gas-phase systems, with the latter generated through methods like surface ionization or heating of solid samples.

Despite advancements in laser-based techniques and valence-level XPS, as exemplified by the work Haubitz et al. [53], the presence of vibrational progressions in absorption and photoelectron spectra leads to broad, unresolved features. Therefore, understanding the spectroscopic features of the low-lying excited states in these systems by means of valence-level spectroscopic techniques can be quite challenging.

The introduction of this thesis effectively highlights the advantages of X-ray spectroscopies, specifically their element-specificity, and orbital-selectivity. These spectroscopic techniques have emerged as the forefront tools for studying actinides in current research. Similar to the rest of the periodic table, it can also be affirmed that advancements in *f*-block element spectroscopy are closely intertwined with the enhancements in synchrotron light source facilities and associated beamlines in recent years. Additionally, as mentioned earlier, theoretical methods have been playing a crucial role in further elucidating these investigations forward at the bottom of the periodic table.

In summary, the progress made in synchrotron radiation facilities and XFELs, along with significant advancements in theoretical methods over the past decade, have facilitated the exploration of actinide electronic structure through the probing of their core excitations. With this foundation established, the following sections of this thesis present our contribution to this field. We aim to explore the excited states of uranyl-containing systems with varying degrees of complexity, employing various *ab-initio* relativistic quantum chemistry calculations.

This thesis is organized as follows:

The first part of the thesis is dedicated to discussing the theoretical aspects of this work,

- In Chapter 1 we delve into the many-body problem in quantum chemistry. We briefly review the approaches in theoretical chemistry that have been used throughout the thesis, including Density Functional (DFT) and Equation-of-Motion Coupled Cluster (EOM-CC) theories. The inclusion of environmental effects by means of quantum embedding approaches is discussed within the framework of Frozen Density Embedding theory (FDE).
- Chapter 2 introduces the relativistic theory of the electron and some of the approximations used in this work.
- In Chapter 3 we present the framework used in this work for the investigation of excited states, which is response theory. First, we introduce resonant-divergent and convergent (also known as damped-response) formulations for the first-order polarization propagator. We finish this chapter by presenting how the first-order properties can be obtained within time-dependent density functional theory (TD-DFT).

In the second part, we present the main research projects developed in this thesis:

- Chapter 4 presents the first manuscript of this thesis, in which core-excited states of the uranyl ion and uranyl tetrachloride dianion were studied by means of damped-response time-dependent density functional theory

(DR-TD-DFT) simulations. The effect of the equatorial ligands in the core-excited states of the uranyl ion was also evaluated by means of the inclusion of a frozen density embedding potential in calculations.

- Chapter 5 presents an investigation of the core-absorption spectra of different linear and bent uranyl complexes using different approximations employing TD-DFT simulations. We compare this data with High Energy Resolution Fluorescence Detected (HERFD) measurements carried out by Dr. Kristina Kvashnina's group at the Rossendorf Beamline (ROBL) in the European Synchrotron Radiation Facility (ESRF) in Grenoble.
- In Chapter 6, we investigate the core-ionized states of the uranyl ion and uranyl tetrachloride dianion using EOM-CC. The FDE approach was also employed in this work.

Finally, we present our conclusions and outline some future research directions in the last chapter of this thesis.

Bibliography of the current chapter

(1) Willmott, P., *An introduction to synchrotron radiation: techniques and applications*; John Wiley & Sons: 2019.

(2) Wiedemann, H.; Wiedemann, H., *Synchrotron radiation*; Springer: 2003.

(3) Stöhr, J., *NEXAFS spectroscopy*; Springer Science & Business Media: 2013; Vol. 25.

(4) Shin, S. New era of synchrotron radiation: fourth-generation storage ring. *AAPPS Bulletin* **2021**, *31*, 21.

(5) Lv, B.; Qian, T.; Ding, H. Angle-resolved photoemission spectroscopy and its application to topological materials. *Nature Reviews Physics* **2019**, *1*, 609–626.

(6) Kalha, C.; Fernando, N. K.; Bhatt, P.; Johansson, F. O.; Lindblad, A.; Rensmo, H.; Medina, L. Z.; Lindblad, R.; Siol, S.; Jeurgens, L. P., et al. Hard x-ray photoelectron spectroscopy: a snapshot of the state-of-the-art in 2020. *Journal of Physics: Condensed Matter* **2021**, *33*, 233001.

(7) De Groot, F.; Kotani, A., *Core level spectroscopy of solids*; CRC press: 2008.

(8) Miedema, P. S.; De Groot, F. M. The iron L edges: Fe 2p X-ray absorption and electron energy loss spectroscopy. *Journal of Electron Spectroscopy and Related Phenomena* **2013**, *187*, 32–48.

(9) Bauer, M. HERFD-XAS and valence-to-core-XES: new tools to push the limits in research with hard X-rays? *Physical Chemistry Chemical Physics* **2014**, *16*, 13827–13837.

(10) Kubin, M.; Guo, M.; Kroll, T.; Löchel, H.; Källman, E.; Baker, M. L.; Mitzner, R.; Gul, S.; Kern, J.; Föhlisch, A., et al. Probing the oxidation state of transition metal complexes: a case study on how charge and spin densities determine Mn L-edge X-ray absorption energies. *Chemical science* **2018**, *9*, 6813–6829.

(11) Ilton, E. S.; Bagus, P. S. XPS determination of uranium oxidation states. *Surface and Interface Analysis* **2011**, *43*, 1549–1560.

(12) Kvashnina, K.; Butorin, S. M.; Martin, P.; Glatzel, P. Chemical state of complex uranium oxides. *Physical review letters* **2013**, *111*, 253002.

(13) Kvashnina, K. O.; De Groot, F. M. Invisible structures in the X-ray absorption spectra of actinides. *Journal of Electron Spectroscopy and Related Phenomena* **2014**, *194*, 88–93.

(14) Shi, W.-Q.; Yuan, L.-Y.; Wang, C.-Z.; Wang, L.; Mei, L.; Xiao, C.-L.; Zhang, L.; Li, Z.-J.; Zhao, Y.-L.; Chai, Z.-F. Exploring actinide materials through synchrotron radiation techniques. *Advanced Materials* **2014**, *26*, 7807–7848.

(15) Tobin, J.; Yu, S.-W.; Booth, C.; Tyliszczak, T.; Shuh, D.; Van Der Laan, G.; Sokaras, D.; Nordlund, D.; Weng, T.-C.; Bagus, P. Oxidation and crystal field effects in uranium. *Physical Review B* **2015**, *92*, 035111.

(16) Epifano, E.; Naji, M.; Manara, D.; Scheinost, A.; Hennig, C.; Lechelle, J.; Konings, R.; Guéneau, C.; Prieur, D.; Vitova, T., et al. Extreme multivalence states in mixed actinide oxides. *Communications Chemistry* **2019**, *2*, 59.

(17) Pan, Z.; Bártová, B.; LaGrange, T.; Butorin, S. M.; Hyatt, N. C.; Stennett, M. C.; Kvashnina, K. O.; Bernier-Latmani, R. Nanoscale mechanism of UO2 formation through uranium reduction by magnetite. *Nature communications* **2020**, *11*, 4001.

(18) Amidani, L.; Retegan, M.; Volkova, A.; Popa, K.; Martin, P. M.; Kvashnina, K. O. Probing the local coordination of hexavalent uranium and the splitting of 5f orbitals induced by chemical bonding. *Inorganic Chemistry* **2021**, *60*, 16286–16293.

(19) Ajayi, T. M.; Shirato, N.; Rojas, T.; Wieghold, S.; Cheng, X.; Latt, K. Z.; Trainer, D. J.; Dandu, N. K.; Li, Y.; Premarathna, S., et al. Characterization of just one atom using synchrotron X-rays. *Nature* **2023**, *618*, 69–73.

(20) Vitova, T.; Kvashnina, K.; Nocton, G.; Sukharina, G.; Denecke, M.; Butorin, S.; Mazzanti, M.; Caciuffo, R.; Soldatov, A.; Behrends, T., et al. High energy resolution x-ray absorption spectroscopy study of uranium in varying valence states. *Physical Review B* **2010**, *82*, 235118.

(21) Vitova, T.; Pidchenko, I.; Fellhauer, D.; Bagus, P. S.; Joly, Y.; Pruessmann, T.; Bahl, S.; Gonzalez-Robles, E.; Rothe, J.; Altmaier, M., et al. The role of the 5 f valence orbitals of early actinides in chemical bonding. *Nature communications* **2017**, *8*, 16053.

(22) Haugen, E. A.; Hait, D.; Scutelnic, V.; Xue, T.; Head-Gordon, M.; Leone, S. R. Ultrafast X-ray Spectroscopy of Intersystem Crossing in Hexafluoroacetylacetone: Chromophore Photophysics and Spectral Changes in the Face of Electron-Withdrawing Groups. *The Journal of Physical Chemistry A* **2023**.

(23) Epshtein, M.; Scutelnic, V.; Yang, Z.; Xue, T.; Vidal, M. L.; Krylov, A. I.; Coriani, S.; Leone, S. R. Table-top X-ray spectroscopy of benzene radical cation. *The Journal of Physical Chemistry A* **2020**, *124*, 9524–9531.

(24) Vidal, M. L.; Epshtein, M.; Scutelnic, V.; Yang, Z.; Xue, T.; Leone, S. R.; Krylov, A. I.; Coriani, S. Interplay of open-shell spin-coupling and Jahn–Teller distortion in benzene radical cation probed by x-ray spectroscopy. *The Journal of Physical Chemistry A* **2020**, *124*, 9532–9541.

(25) Epshtein, M.; Tenorio, B. N. C.; Vidal, M. L.; Scutelnic, V.; Yang, Z.; Xue, T.; Krylov, A. I.; Coriani, S.; Leone, S. R. Signatures of the Bromine Atom and Open-Shell Spin Coupling in the X-ray Spectrum of the Bromobenzene Cation. *Journal of the American Chemical Society* **2023**, *145*, 3554–3560.

(26) Hertz, H. Ueber einen Einfluss des ultravioletten Lichtes auf die electrische Entladung. *Annalen der Physik* **1887**, *267*, 983–1000.

(27) Einstein, A. Indeed, it seems to me that the observations regarding" blackbody radiation," photoluminescence, production of cathode rays by ultraviolet. *Annalen der Physik* **1905**, *17*, 132–148.

(28) Siegbahn, K. ESCA: atomic, molecular and solid state structure studies by means of electron spectroscopy. *Nova Acta Regiae Societatis Scientiarum Upsaliensis* **1967**.

(29) De Groot, F. Multiplet effects in X-ray spectroscopy. *Coordination Chemistry Reviews* **2005**, *249*, 31–63.

(30) Zimmermann, P.; Peredkov, S.; Abdala, P. M.; DeBeer, S.; Tromp, M.; Müller, C.; van Bokhoven, J. A. Modern X-ray spectroscopy: XAS and XES in the laboratory. *Coordination Chemistry Reviews* **2020**, *423*, 213466.

(31) Norman, P.; Ruud, K.; Saue, T., *Principles and practices of molecular properties: Theory, modeling, and simulations*; John Wiley & Sons: 2018.

(32) Einstein, A. Über einen die Erzeugung und Verwandlung des Lichtes betreffenden heuristischen Gesichtspunkt, 1905.

(33) Krylov, A. I. From orbitals to observables and back. *The Journal of Chemical Physics* **2020**, *153*, 080901.

(34) Gel'mukhanov, F.; Ågren, H. Resonant X-ray Raman scattering. *Physics Reports* **1999**, *312*, 87–330.

(35) Kurian, R.; Kunnus, K.; Wernet, P.; Butorin, S. M.; Glatzel, P.; de Groot, F. M. Intrinsic deviations in fluorescence yield detected x-ray absorption spectroscopy: the case of the transition metal L2, 3 edges. *Journal of Physics: Condensed Matter* **2012**, *24*, 452201.

(36) Borges, B.; Roman, L.; Rocco, M. Femtosecond and attosecond electron transfer dynamics of semiconductors probed by the core-hole clock spectroscopy. *Topics in Catalysis* **2019**, *62*, 1004–1010.

(37) Kramers, H. A.; Heisenberg, W. Über die streuung von strahlung durch atome. *Zeitschrift für Physik* **1925**, *31*, 681–708.

(38) Dirac, P. A. M. The quantum theory of the emission and absorption of radiation. *Proceedings of the Royal Society of London. Series A, Containing Papers of a Mathematical and Physical Character* **1927**, *114*, 243–265.

(39) Gel'mukhanov, F.; Odelius, M.; Polyutov, S. P.; Foehlisch, A.; Kimberg, V. Dynamics of resonant x-ray and Auger scattering. *Reviews of Modern Physics* **2021**, *93*, 035001.

(40) Kvashnina, K. O.; Butorin, S. M. High-energy resolution X-ray spectroscopy at actinide M 4, 5 and ligand K edges: what we know, what we want to know, and what we can know. *Chemical Communications* **2022**, *58*, 327–342.

(41) Knotek, M.; Feibelman, P. J. Stability of ionically bonded surfaces in ionizing environments. *Surface Science* **1979**, *90*, 78–90.

(42) Cazaux, J. Correlations between ionization radiation damage and charging effects in transmission electron microscopy. *Ultramicroscopy* **1995**, *60*, 411–425.

(43) Travnikova, O.; Marchenko, T.; Goldsztejn, G.; Jänkälä, K.; Sisourat, N.; Carniato, S.; Guillemin, R.; Journel, L.; Céolin, D.; Püttner, R., et al. Hard-x-ray-induced multistep ultrafast dissociation. *Physical Review Letters* **2016**, *116*, 213001.

(44) Collins, R. N.; Saito, T.; Aoyagi, N.; Payne, T. E.; Kimura, T.; Waite, T. D. Applications of time-resolved laser fluorescence spectroscopy to the environmental biogeochemistry of actinides. *Journal of environmental quality* **2011**, *40*, 731–741.

(45) Natrajan, L. S. Developments in the photophysics and photochemistry of actinide ions and their coordination compounds. *Coordination Chemistry Reviews* **2012**, *256*, 1583–1603.

(46) Oher, H.; Réal, F.; Vercouter, T.; Vallet, V. Investigation of the Luminescence of [UO2X4] 2–(X= Cl, Br) Complexes in the Organic Phase Using Time-Resolved Laser-Induced Fluorescence Spectroscopy and Quantum Chemical Simulations. *Inorganic Chemistry* **2020**, *59*, 5896–5906.

(47) Oher, H.; Ferru, G.; Couston, L.; Berthon, L.; Guillaumont, D.; Réal, F.; Vercouter, T.; Vallet, V. Influence of the First Coordination of Uranyl on Its Luminescence Properties: A Study of Uranyl Binitrate with N, N-Dialkyl Amide DEHiBA and Water. *Inorganic Chemistry* **2021**, *61*, 890–901.

(48) Oher, H.; Vercouter, T.; Réal, F.; Shang, C.; Reiller, P. E.; Vallet, V. Influence of Alkaline Earth Metal Ions on Structures and Luminescent Properties of Na m M n UO2 (CO3) 3 (4–m–2 n)–(M= Mg, Ca; m, n= 0–2): Time-Resolved Fluorescence Spectroscopy and Ab Initio Studies. *Inorganic Chemistry* **2020**, *59*, 15036–15049.

(49) Dau, P. D.; Su, J.; Liu, H.-T.; Huang, D.-L.; Li, J.; Wang, L.-S. Photoelectron spectroscopy and the electronic structure of the uranyl tetrachloride dianion: UO2Cl42-. *The Journal of Chemical Physics* **2012**, *137*, 064315.

(50) Teterin, Y. A.; Maslakov, K. I.; Ryzhkov, M. V.; Teterin, A. Y.; Ivanov, K. E.; Kalmykov, S. N.; Petrov, V. G.; Suglobov, D. N. Valence XPS structure and chemical bond in Cs2UO2Cl4. *Nuclear Technology and Radiation Protection* **2016**, *31*, 37–50.

(51) Maslakov, K. I.; Teterin, Y. A.; Ryzhkov, M. V.; Popel, A. J.; Teterin, A. Y.; Ivanov, K. E.; Kalmykov, S. N.; Petrov, V. G.; Farnan, I. The nature of the chemical bond in UO2. *International journal of quantum chemistry* **2019**, *119*, e26040.

(52) Evans, W. J.; Hanusa, T. P., *The Heaviest Metals: Science and Technology of the Actinides and Beyond*; John Wiley & Sons: 2019.

(53) Haubitz, T.; Drobot, B.; Tsushima, S.; Steudtner, R.; Stumpf, T.; Kumke, M. U. Quenching mechanism of Uranyl (VI) by chloride and bromide in aqueous and non-aqueous solutions. *The Journal of Physical Chemistry A* **2021**, *125*, 4380–4389.

Part I

Atoms, Molecules & Fields

Chapter 1

Electronic Structure Theory

"I... a universe of atoms, an atom in the universe."

— Richard Feynman

This chapter provides a comprehensive overview of quantum mechanics – the leading theory (to date) for analyzing and predicting the behavior of matter – and its applications in solving chemical problems.

Section 1.1 introduces the fundamental principles of quantum mechanics, followed by a detailed discussion of the building blocks of quantum chemistry. The Schrödinger equation cannot be solved analytically for systems with more than one electron in atoms and molecules. Despite significant advances in computational and theoretical chemistry over the last decades, investigating the trustworthiness of approximations and improving the description of the electron-electron interaction in the many-body electronic Hamiltonian still represents a considerable portion of research efforts. In Section 1.2, we introduce the Hartree-Fock theory, which provides a mean-field approximation to the electronic structure problem. Section 1.3 briefly introduces the limitations of this approximation. Then we delve into an overview of the *ab-initio* methods used in this thesis.

Coupled-Cluster theory (CC), discussed in Section 1.4, is known for its accuracy and is often used as the reference for other computational methods. Density

Functional Theory (DFT), presented in Section 1.5, is considered the workhorse of quantum chemistry due to its broad applicability and ability to handle large systems. Approximations that do not significantly impact the overall quality of the simulations are usually employed, given limited computational and time resources. Section 1.6 presents a particular approach for describing environmental effects in calculations using the Frozen Density Embedding method (FDE). Finally, we finish this chapter by extending the discussion on DFT by introducing its density functional approximations (DFAs) in Section 1.7.

Atomic units (a.u.) are used throughout the text unless stated otherwise.

1.1 Foundations

The state of a quantum mechanical system (e.g., an electron) at any given time is represented by its state vector, which is denoted by $|\Psi(t)\rangle$. This mathematical object belongs to a Hilbert space of square-integrable functions (L^2), and its wave function, denoted by $\Psi(\mathbf{r};t)$, can be obtained by projecting its state vector onto a given vector basis [54–56]. The Copenhagen interpretation, the most accepted interpretation of quantum mechanics, holds that the wave function provides a complete description of the system [57–60].

The probability density for finding the system in a particular state is given by the squared modulus of the wave function, $|\Psi(\mathbf{r};t)|^2$. This rule is referred to as the Born rule [61], one of the fundamental postulates of quantum mechanics [62–65].

Within a non-relativistic framework, a quantum mechanical system has its dynamics described by the time-dependent Schrödinger equation,

$$i\hbar\frac{\partial}{\partial t}\Psi(\mathbf{r};t) = \hat{H}\Psi(\mathbf{r};t) \tag{1.1}$$

where $\hbar$ denotes the reduced Planck constant, and $\hat{H}$ is the Hamiltonian operator. This operator describes the motion and interactions of a system under study.

Alternatively, we could investigate the stationary states of a system by solving the time-independent version of the Schrödinger equation,

$$E_n|\Psi_n\rangle = \hat{H}|\Psi_n\rangle \tag{1.2}$$

where E_n and $|\Psi_n\rangle$ denote the eigenvalues and eigenfunctions of the Hamiltonian operator, respectively. Thus, by diagonalizing the matrix representation of $\hat{H}$, the energy eigenspectrum of the Hamiltonian should, in principle, be obtained. Therefore obtaining a set of eigenvectors $\{|\Psi_n\rangle\}$ (wave functions) and their associated eigenenergies $\{E_n\}$. We will drop the subscript n to simplify notation throughout the following discussion.

For atoms and molecules in the absence of external fields, $\hat{H}$ reads:

$$\hat{H} = \hat{T}_e + \hat{T}_n + \hat{V}_{ee} + \hat{V}_{nn} + \hat{V}_{en} \tag{1.3}$$

where the electronic and nuclear kinetic energy terms are denoted by T_e and T_n. The following terms correspond to electrostatic (Coulomb) interactions from electronic (V_{ee}) and nuclear (V_{nn}) sources and the electron-nuclei attraction term (V_{en}).

For a system with N-electrons and M-protons, we can expand Equation 1.3 to yield:

$$\hat{H} = -\frac{1}{2}\sum_{i}^{N}\nabla_i^2 - \frac{1}{2}\sum_{A}^{M}\frac{1}{M_A}\nabla_A^2 + \sum_{i<j}^{N}\frac{1}{r_{ij}} + \sum_{A<B}^{M}\frac{Z_A Z_B}{r_{AB}} - \sum_{i,A}^{M,N}\frac{Z_A}{r_{iA}} \tag{1.4}$$

However, using this Hamiltonian operator to describe the behavior of electrons confined in atoms yields analytical solutions only for hydrogen-like systems, typically expressed as a product of radial and angular functions [66, 67]. To solve this problem for many-electron systems, we must seek approximate solutions [66, 67], which we will explore in the following sections of this chapter. But before that, it's significant to mention one of the pillars of quantum chemistry: the Born-Oppenheimer approximation.

Born-Oppenheimer approximation

The Born-Oppenheimer approximation [61] relies on the significant difference in mass between electrons and nuclei in molecules. It assumes that electronic motion is much faster than nuclear motion and treats the nuclei as classical particles. Or in the words of Yarkony [68], *the nuclei move on a single potential energy surface created by the faster-moving electrons.*

Within this approximation, the total wave function of a molecule reads in terms of its electronic and nuclear components,

$$\Psi(\mathbf{r};\mathbf{R}) = \Psi_e(\mathbf{r};\mathbf{R})\Psi_n(\mathbf{R}) \tag{1.5}$$

where $\mathbf{r}$ and $\mathbf{R}$ denote electronic and nuclear coordinates, respectively. $\Psi_e(\mathbf{r};\mathbf{R})$ and $\Psi_n(\mathbf{R})$ are the electronic and nuclear wave functions, respectively.

This way, the electronic Schrödinger equation for each fixed nuclear configuration is solved, and the resulting electronic wave function and electronic energy depend on the coordinates of the nuclei only parametrically. To achieve this separation, T_n is set to zero, and V_{nn} is considered constant. The resulting eigenvalue problem to be solved is:

$$E_e|\Psi_e\rangle = \hat{H}_e|\Psi_e\rangle \tag{1.6}$$

where the electronic Hamiltonian is given by:

$$\hat{H}_e = \hat{T}_e + \hat{V}_{ee} + \hat{V}_{en} \tag{1.7}$$

For the remainder of this text, unless otherwise stated, we will focus solely on electronic wave functions and thus drop the subscripts e and n in the equations that follow.

While this thesis does not explore non-adiabatic effects in chemical systems, it is significant to acknowledge that the Born-Oppenheimer approximation may break down when different electronic states of a system have similar energies, resulting in the formation of conical intersections [68–73]. At these points, the electronic and nuclear degrees of freedom become strongly coupled, requiring further exploration of molecular dynamics to account for non-adiabatic effects in spectroscopic observables [69, 74, 75]. In the X-ray domain, such *non-adiabatic dynamics* play an important role when investigating ultrafast processes [76–78].

1.2 Hartree-Fock theory

Since the early development of quantum chemistry, two frameworks are commonly used to build molecules using wave functions. The first, known as *valence bond theory*, is based on the early works of Heitler and London [79], Pauling [80], and Slater [81]. This theory describes molecules as being built from the wave functions of individual atoms and is often considered a more suitable framework for studying the nature of chemical bonding [82–84]. However, most modern electronic structure methods rely on a different formulation.

In studies such as the thesis here developed, Hund [85] and Mulliken [86] *molecular orbital theory* is used to build molecules. This theory assigns each electron to a single-particle wave function called an *orbital*, therefore providing a simple way to understand spectroscopic processes such as excitation and ionization, as further suggested by Roothaan [87] and Hall [88].

Based on the seminal work by Hartree [89], the independent particle model expresses the total wave function of a many-body system as the product of individual wave functions. For a two-electron system, this reads:

$$\Psi(\mathbf{r}_1, \mathbf{r}_2) = \psi(\mathbf{r}_1)\psi(\mathbf{r}_2) \tag{1.8}$$

However, such a wave function has some issues. Firstly, it does not contain the electronic degree of freedom known as spin (s_i), which was observed by Gerlach and Stern [90] in one of the most important experiments of the last century. Additionally, this expression lacks the proper treatment of electron indistinguishability. Electrons, being fermions, respect the Pauli exclusion principle [91] and thus obey Fermi-Dirac statistics [92, 93], which require the total wave function to be antisymmetric concerning the pairwise exchange of electrons, i.e.,

$$\Psi(\mathbf{r}_1, \mathbf{r}_2) = -\Psi(\mathbf{r}_2, \mathbf{r}_1) \tag{1.9}$$

To address these limitations, Fock [94, 95] and Slater [96, 97] proposed a way to account for the electronic spin and ensure the antisymmetry of the electronic wave function by introducing spin-orbitals into theory and expressing the total wave function as a Slater determinant.

A spin-orbital account for spatial and spin degrees of freedom by factoring the wave function into spatial and spin contributions,

$$\psi_i(\mathbf{r}_i, s) = \varphi_i^{\alpha}(\mathbf{r}_i)\alpha(s) \quad \text{or} \quad \varphi_i^{\beta}(\mathbf{r}_i)\beta(s) \tag{1.10}$$

where $\alpha(s)$ and $\beta(s)$ respectively denote eigenfunctions for spin up and down states. $\varphi_i^{\alpha}(\mathbf{r}_i)$ and $\varphi_i^{\alpha}(\mathbf{r}_i)$ are spatial orbitals.

As previously mentioned, it is also necessary to account for Fermi-Dirac statistics. For a system with a total of N electrons that occupy orthonormal spin-orbitals $\left\{\psi_i, \psi_j, ..\right\}$, the antisymmetry of the N-electron wave function is ensured by writing the total wave function as a Slater determinant,

$$\Psi(\mathbf{r}_1, s_1; \mathbf{r}_2, s_2; ...) = \frac{1}{\sqrt{N!}} \begin{vmatrix} \psi_i(\mathbf{r}_1, s_1) & \psi_i(\mathbf{r}_2, s_2) & \cdots & \psi_i(\mathbf{r}_N, s_N) \\ \psi_j(\mathbf{r}_1, s_1) & \psi_j(\mathbf{r}_2, s_2) & \cdots & \psi_j(\mathbf{r}_N, s_N) \\ \vdots & \vdots & \ddots & \vdots \end{vmatrix} \tag{1.11}$$

where $\frac{1}{\sqrt{N!}}$ is a normalisation factor.

A simplified way to express this mathematical object would be to focus solely its diagonal:

$$\Psi(\mathbf{x}_1, \mathbf{x}_2, \cdots, \mathbf{x}_N) = |\psi_1(\mathbf{x}_1), \psi_2(\mathbf{x}_2) \cdots \psi_k(\mathbf{x}_n)\rangle \tag{1.12}$$

In the above equation, spatial and spin coordinates are written together as $\mathbf{x}_i = \mathbf{r}_i, s_i$. Throughout the rest of the text, this notation will be used when spatial and spin coordinates are not explicitly discussed.

Hartree-Fock equations

The variation principle is one of the central tenets invoked in quantum mechanics [66, 98], dictating that the "best" wave function will yield the lowest possible expectation value of the energy. Using the electronic Hamiltonian defined in Equation 1.7, this translates to:

$$E_0 \leq \langle \Psi | \hat{H}_e | \Psi \rangle = \langle \Psi | \hat{T}_e | \Psi \rangle + \langle \Psi | \hat{V}_{ee} | \Psi \rangle + \langle \Psi | \hat{V}_{ne} | \Psi \rangle \tag{1.13}$$

To determine the ground state wave function and its corresponding energy within Hartree-Fock theory, one commonly uses an iterative solution of the set of HF equations:

$$\hat{f}\psi_i(\mathbf{x}) = \epsilon_i \psi_i(\mathbf{x}) \tag{1.14}$$

This is an integro-differential equation, with ϵ_i denoting the orbital energy and $\hat{f}$ denoting the one-electron Fock operator:

$$\hat{f} = \hat{h}(i) + v^{HF}(i) = -\frac{1}{2}\sum_{i}^{N} \nabla_i^2 - \sum_{A}^{N} \frac{Z_A}{\mathbf{r}_{iA}} + v^{HF}(i) \tag{1.15}$$

Here, $v^{HF}(i)$ represents the average electronic repulsion between an electron i and all other remaining electrons in the system, indicating that the HF theory treats inter-electron repulsion in a *mean-field* fashion.

Equation 1.14 is solved for each of the i-th electrons in the system, and therefore at each iteration, the mean-field potential (v^{HF}) has to be updated. This results in the *self-consistent field method* (SCF), which uses an ideally well-behaved trial wave function to obtain a set of orthonormal spin-orbitals $\{\psi_i\}$ (also called canonical orbitals) and their associated orbital energies $\{\epsilon_i\}$. Since the spin orbitals must satisfy the orthogonality condition, Lagrange's method of undetermined multipliers is used to obtain a stationary solution for a given threshold when $\delta E_0 = 0$. This results in the following ground-state HF energy:

$$E_0 = \sum_{i}^{N} h_{ii} + \frac{1}{2}\sum_{ij}^{N} (J_{ij} - K_{ij}) \tag{1.16}$$

where J_{ij} and K_{ij} are the so-called one- and two-electron integrals. The one-electron integral contains the electronic kinetic energy and the electron-nuclei interaction, and it reads as

$$h_{ii} = \int \psi_i^*(\mathbf{x}_i)\left(-\frac{1}{2m}\nabla_i^2 - \sum_A^M \frac{Z_A}{r_{iA}}\right)\psi_i(\mathbf{x}_i)d\mathbf{x}_i \tag{1.17}$$

Two-electron integrals are usually divided into two terms and expressed in terms of two-electron coordinates, labeled as $\mathbf{x}_1$ and $\mathbf{x}_2$ from now on. The first contribution is that from the classical repulsion between two electrons, known as the Coulomb integral,

$$J_{ij} = \int\int \psi_i^*(\mathbf{x}_1)\psi_j^*(\mathbf{x}_2)\left(\frac{1}{\mathbf{r}_{12}}\right)\psi_j(\mathbf{x}_2)\psi_i(\mathbf{x}_1)d\mathbf{x}_2 d\mathbf{x}_1 \tag{1.18}$$

This contribution gives the average electrostatic repulsion between electrons in orbitals ψ_i and ψ_j and therefore is not an instantaneous description of the electron-electron interaction.

The following term in Equation 1.16, K_{ij}, is a purely quantum mechanical contribution from Fermi-Dirac statistics. It lowers the J_{ij} contribution and is known as the exchange term. It is given by

$$K_{ij} = \int\int \psi_i^*(\mathbf{x}_1)\psi_j^*(\mathbf{x}_2)\left(\frac{1}{\mathbf{r}_{12}}\right)\psi_i(\mathbf{x}_2)\psi_j(\mathbf{x}_1)d\mathbf{x}_2 d\mathbf{x}_1 \tag{1.19}$$

It is important to note that the contribution of these two-electron integrals in Equation 1.16 is written in a way that produces an exact cancellation for the terms of self-repulsion (J_{ii}) and self-exchange (K_{ii}). This feature avoids the computation of these terms, making it a positive aspect of HF theory. We shall return to this aspect when discussing one of the sources of errors in density functional theory.

Basis Sets

Although it is possible to solve the HF equations numerically, such a method is more practical for atomic calculations, given their spherical symmetry. Hall [88] and Roothaan [87] proposed an efficient method to tackle this problem in molecules in the early 1950s. In his paper, Roothaan generalized the linear combination of atomic orbitals (LCAO) method to represent all electrons in a molecular system.

In this method, the spatial part of the molecular orbitals $\{\varphi_i\}$ in a system is expressed as an expansion in terms of a known set of basis functions, denoted by $\left\{\chi_\mu(\mathbf{r})|\mu = 1, 2, 3.., K\right\}$:

$$\varphi_i(\mathbf{r}) = \sum_{\mu=1}^{K} c_{i\mu}\chi_\mu(\mathbf{r}) \tag{1.20}$$

This method produces $2K$ spin orbitals for a given set of basis functions, with N being the number of occupied orbitals and $2K - N$ being the number of virtual orbitals. Using this expansion in Equation 1.16 is possible to move from an integro-differential problem to an eigenvalue equation for a hermitian matrix known as Roothan-Hall equations,

$$F_{\mu\nu}C_{\nu i} = S_{\mu\nu}C_{\nu i}\epsilon_i \tag{1.21}$$

where $F_{\mu\nu}$ is the Fock matrix and $S_{\mu\nu}$ is the overlap matrix among basis functions, defined as

$$F_{\mu\nu} = \int \varphi^*_\mu(\mathbf{x}_i)\hat{f}_i\varphi_\nu(\mathbf{x}_i)d\mathbf{x}_i \tag{1.22}$$

$$S_{\mu\nu} = \int \varphi^*_\mu(\mathbf{x}_i)\varphi_\nu(\mathbf{x}_i)d\mathbf{x}_i \tag{1.23}$$

This reduces the problem of obtaining the matrix of expansion coefficients $C_{\nu i}$ through matrix diagonalization.

As anticipated, a wave function is a mathematical object that belongs to the Hilbert space of L^2 functions. Since this space is infinite-dimensional, it is common practice to truncate Equation 1.20, which means that such an expansion is not exact. However, a larger expansion generally yields a more flexible basis set. In this work we employed Slater-type (STOs) [99] and Gaussian-type orbitals (GTOs) [100, 101], two of the most commonly used basis sets in quantum chemistry. STOs reads as:

$$\chi_{\zeta,n,l,m}(\mathbf{r}, \theta, \phi) = NY_{l,m}(\theta, \phi)r^{n-1}e^{-\zeta r} \tag{1.24}$$

GTOs, on the other hand, are defined as

$$\chi_{\zeta,n,l,m}(\mathbf{r},\theta,\phi) = N Y_{l,m}(\theta,\phi) r^{3n-2-l} e^{-\zeta r^2} \tag{1.25}$$

In both equations, the four defining parameters are the quantum numbers (n, l, m) and ζ, which is an exponent that defines the extent of the orbital. Both equations also include a normalization constant N and a real-valued spherical harmonic $Y_{l,m}$ in their respective formulations.

As is apparent, the difference between Slater- and Gaussian-type functions is the exponential dependence on r. Specifically, in STOs, the exponential has a linear dependence in r, while in GTOs exhibits a quadratic dependence, leading to distinct behavior in the vicinity of atomic nuclei and a more gradual decline at greater distances from the atomic nuclei.

1.3 Electronic correlation

Post-HF methods in quantum chemistry aim to recover one particular contribution missing in HF theory, the so-called *correlation energy*. In the following, we briefly introduce the role of electronic correlation in quantum chemistry. For more detailed information, please refer to the references provided throughout the text.

Consider a two-electron system described by a single Slater determinant as defined in Equation 1.11. The probability density for this system reads:

$$\begin{aligned} p(\mathbf{r}_1,\mathbf{r}_2) &= \int |\Psi(\mathbf{r}_1,s_1;\mathbf{r}_2,s_2)|^2 ds_1 ds_2 \\ &= |\varphi_{1s}(\mathbf{r}_1)\varphi_{1s}(\mathbf{r}_2)|^2 = |\varphi_{1s}(\mathbf{r}_1)|^2 |\varphi_{1s}(\mathbf{r}_2)|^2 \end{aligned} \tag{1.26}$$

As can be seen, these two electrons (of different spin) are not spatially dependent on each other, and their movements are said to be uncorrelated.

Following Löwdin [102], within a non-relativistic framework and for a given basis set, electronic correlation is the difference between the exact energy and the energy obtained by solving the HF equations,

$$E^{correlation} = E^{exact} - E^{HF} \tag{1.27}$$

This lack of electronic correlation is unphysical and leads to an *overestimation* of the electron-electron repulsion energy and an *overlocalization* of electron density. Therefore, these impact chemical properties, including underestimating ionization and bond dissociation energies [67].

Electronic correlation is usually divided into two counterparts. *Static* (or non-dynamical) correlation [103] is present in systems that cannot be described by a single Slater determinant, as they present, for instance, near-degeneracies of the Hartree-Fock occupied and virtual orbitals. These have a multi-reference character, i.e., systems with partially occupied degenerate orbitals.

In this work, we have investigated the contribution of dynamical correlation in ionization energies, whose configuration interaction (CI) and coupled-cluster (CC) methods can recover. These methods apply an excitation operator to a single Slater determinant, and the total wave function is a combination of the reference and its excited determinants.

1.4 Equation-of-Motion Coupled Cluster

Coupled-cluster (CC) is a wave-function theory that has become an area of interest in quantum chemistry due to its ability to predict thermodynamic and spectroscopic quantities with high accuracy [104–108]. EOM-CC is a framework that employs the coupled-cluster formalism to explore phenomena beyond the ground state, including electronically excited, ionized, or attached states, making it suitable for a broad range of problems [109–114].

Before we continue, we would like to make two points. Firstly, we will be using some convenient notations throughout this section. In particular, we will use the indexes i, j, and k for occupied orbitals and a, b, and c for virtual ones. Secondly, for a singly excited wave function, we will use the notation $|_{i}^{a}\rangle$. The same stands for a doubly excited wave function, denoted by $|_{ij}^{ab}\rangle$.

This chapter does not aim to provide an exhaustive overview of CC methods. The references cited throughout the text provide further details on this topic.

Coupled-Cluster theory

The early works of Coester [115], Čıžek and Paldus [104, 116–118] form the basis of CC theory, whose premise is to obtain a wave function from the following exponential ansätze:

$$|\Psi_{CC}\rangle = e^{\hat{T}}|\Phi_0\rangle \tag{1.28}$$

In this expression, $|\Phi_0\rangle$ represents a reference wave function, typically a Slater determinant obtained from the self-consistent field method described in Section 1.2. The so-called cluster operator, denoted by $\hat{T}$, is applied to this reference (given by Equation 1.11) to generate a wave function consisting of a combination of excited Slater determinants with different numbers of excitations and their associated amplitudes. For a system with N electrons, this operator generates N-tuple excited determinants:

$$\hat{T} = \hat{T}_1 + \hat{T}_2 + \cdots + \hat{T}_N \tag{1.29}$$

Here, $\hat{T}_1$ is a single excitation operator that generates all possible singly excited determinants when applied to $|\Phi_0\rangle$:

$$\hat{T}_1|\Phi_0\rangle = \sum_i \sum_a |_i^a\rangle t_i^a \tag{1.30}$$

In this equation, t_i^a denotes a cluster amplitude associated with a singly excited determinant. In the same fashion, when $\hat{T}_2$ acts on a reference and generates all doubly excited determinants multiplied by their amplitude:

$$\hat{T}_2|\Phi_0\rangle = \sum_{i<j} \sum_{a<b} |_{ij}^{ab}\rangle t_{ij}^{ab} \tag{1.31}$$

and so on.

Furthermore, we can evaluate the exponential operator $e^{\hat{T}}$ as a series expansion that reads:

$$e^{\hat{T}} = 1 + \hat{T} + \frac{1}{2}\hat{T}^2 + ... = \sum_{i=0}^{N} \frac{1}{i!}\hat{T}^i \tag{1.32}$$

Truncating at triple excitations and assembling terms with the same excitation level, we obtain:

$$e^{\hat{T}} = 1 + \hat{T}_1 + \left\{\hat{T}_2 + \frac{1}{2}\hat{T}_1^2\right\} + \left\{\hat{T}_3 + \frac{1}{6}\hat{T}_1^3 + \hat{T}_2\hat{T}_1\right\} + \cdots \tag{1.33}$$

$\hat{T}_1$ and $\hat{T}_2$ are known as *connected cluster excitation operators* because they generate a product of a single or double-excited wave function and their associated amplitudes when acting on a reference wave function. A different scenario is obtained for terms like $\hat{T}_1^2$, i.e.:

$$\frac{1}{2}\hat{T}_1^2|\Phi_0\rangle = \frac{1}{2}\sum_{ai}\sum_{bj}|{}^{ab}_{ij}\rangle(t_i^a t_j^b - t_i^b t_j^a) \tag{1.34}$$

Although the same doubly excited determinant appears in this expression, it is multiplied by products of single excitation amplitudes. And thus, operators like $\hat{T}_1^2$ are called *disconnected excitation operators*.

Finally, including such cluster operators into Ψ_{CC} one obtains:

$$|\Psi_{CC}\rangle = |\Phi_0\rangle + \sum_{ia}|{}^{a}_{i}\rangle t_i^a + \sum_{i<j}\sum_{a<b}|{}^{ab}_{ij}\rangle(t_{ij}^{ab} + t_i^a t_j^b - t_i^b t_j^a) + \cdots \tag{1.35}$$

Configuration interaction (CI) methods [119] yields a simular expression:

$$|\Psi_{CI}\rangle = |\Phi_0\rangle + \sum_{ia}|{}^{a}_{i}\rangle C_i^a + \sum_{i<j}\sum_{a<b}|{}^{ab}_{ij}\rangle C_{ij}^{ab} + \cdots \tag{1.36}$$

where C_i^a and C_{ij}^{ab} denote the first and second-order expansion coefficients of the CI wave function. It is important to note that although they have a similar form, the disconnected excitation operators in CC theory turn CC methods size-extensive and thus a better approach than those derived from CI.

In conclusion, including all possible excitations in a CC calculation would lead to an exact result for a given basis, as one would obtain by including all possible excitations into a CI calculation (i.e. full CI). But this is not practical, and thus the excitation operator is truncated. In this work the excitation operator was truncated to singles and doubles excitations (CCSD).

Coupled Cluster energy

The coupled cluster Schrödinger equation is given by

$$\hat{H}|\Psi_{CC}\rangle = E_{CC}|\Psi_{CC}\rangle \tag{1.37}$$

where $\hat{H}$ is the Hamiltonian, $|\Psi_{CC}\rangle$ is the coupled-cluster wave function, and E_{CC} is the corresponding energy.

In a similar fashion to Møller and Plesset perturbation theory [120], the coupled cluster energy expression is obtained by solving different-order equations and projecting higher-order solutions onto the zeroth-order wavefunction. For further detailed discussion on the topic, we recommend referring to the textbook by Helgaker et al. [66].

We can introduce a similarity-transformed Hamiltonian ($\hat{\hat{H}}$) on the left-hand side of this expression by multiplying both sides by $e^{-\hat{T}}$,

$$e^{-\hat{T}}\hat{H}|\Psi_{CC}\rangle = e^{-\hat{T}}\hat{H}e^{\hat{T}}|\Phi_0\rangle = \hat{\hat{H}}|\Phi_0\rangle \tag{1.38}$$

$$e^{-\hat{T}}E_{CC}|\Psi_{CC}\rangle = E_{CC}e^{-\hat{T}}e^{\hat{T}}|\Phi_0\rangle = E_{CC}|\Phi_0\rangle \tag{1.39}$$

yielding

$$\hat{\hat{H}}|\Phi_0\rangle = E_{CC}|\Phi_0\rangle \tag{1.40}$$

Since we are using a Hartree-Fock reference, the Kronecker delta, $\langle\Phi_\mu|\Phi_\nu\rangle = \delta_{\mu\nu}$ holds. Therefore, the main equations in CC theory are obtained by means of projection techniques. Projecting the Schrödinger equation onto $\langle\Phi_0|$ yields the coupled cluster energy expression:

$$\langle\Phi_0|\hat{\hat{H}}|\Phi_0\rangle = E_{CC}\langle\Phi_0|\Phi_0\rangle = E_{CC} \tag{1.41}$$

Next, projecting onto the set of μ-excited determinants results in the amplitudes equation:

$$\langle \Phi_\mu | \hat{\bar{H}} | \Phi_0 \rangle = \langle \Phi_\mu | E_{CC} | \Phi_0 \rangle = E_{CC} \langle \Phi_\mu | \Phi_0 \rangle = 0 \tag{1.42}$$

Since these are coupled amplitudes, an iterative solution to the CC equations must be employed, similar to the Hartree-Fock equations. The expressions for the CCSD energy and amplitudes are complex and lengthy. Interested readers should refer to the previous references for a broader discussion.

EOM-CC formalism

The CC formalism presented in the previous section provides a powerful framework for calculating the electronic structure of atoms and molecules but is constrained to the system's ground state. And thus, this formulation of CC theory must be extended to explore beyond the ground state. In the following, we present one possible extension of the CC theory to compute excited states, namely the equation-of-motion coupled-cluster theory. Our derivation is similar to that presented by Krylov [113] and Bartlett [114].

We can apply a linear transformation to map two eigenvectors within the same Hilbert space. Using the coupled-cluster wave function, we may obtain an excited state $|\Psi_f\rangle$ by doing

$$|\Psi_f\rangle = \hat{R} |\Psi_{CC}\rangle = \hat{R} e^{\hat{T}} |\Phi_0\rangle \tag{1.43}$$

where $\hat{R}$ is a linear operator.

In a similar fashion to what we have previously done for $|\Psi_{CC}\rangle$ we can write the Schrodinger equation for $|\Psi_f\rangle$ as

$$\hat{H} \hat{R} e^{\hat{T}} |\Phi_0\rangle = E_f \hat{R} e^{\hat{T}} |\Phi_0\rangle \tag{1.44}$$

where E_f is the eigenenergy of $|\Psi_f\rangle$.

Applying the exponential operator to both sides of this equation and using the fact that the operators $\hat{R}$ and $\hat{T}$ commute [66], we can write:

$$e^{-\hat{T}} \hat{H} \hat{R} e^{\hat{T}} |\Phi_0\rangle = e^{-\hat{T}} e^{\hat{T}} E_f \hat{R} |\Phi_0\rangle = E_f \hat{R} |\Phi_0\rangle \tag{1.45}$$

where we have defined the similarity transformed Hamiltonian ($\hat{\bar{H}}$).

Furthermore, we can apply the linear operator $\hat{R}$ to the coupled cluster energy (Equation 1.40) to yield

$$\hat{R}\hat{\bar{H}}|\Phi_0\rangle = E_i \hat{R}|\Phi_0\rangle \tag{1.46}$$

where $E_i = E_{CC}$.

By subtracting Equations 1.45 and 1.46, we obtain the following equation:

$$\left(\hat{\bar{H}}\hat{R} - \hat{R}\hat{\bar{H}}\right)|\Phi_0\rangle = \omega_{fi}\hat{R}|\Phi_0\rangle \tag{1.47}$$

where $\omega_{fi} = E_f - E_i$.

Introducing the normal-ordered Hamiltonian, $\hat{\bar{H}}_N = \hat{\bar{H}} - \langle\Phi_0|\hat{\bar{H}}|\Phi_0\rangle$, and after some algebraic techniques, for a given set of excited determinants $\{\Phi_i\}$ one may obtain the following matrix eigenvalue problem,

$$\sum_{\nu}\langle\Phi_\mu|\hat{\bar{H}}_N|\Phi_\nu\rangle\langle\Phi_\mu|\hat{R}|\Phi_\nu\rangle = \omega_{fi}\sum_{\nu}\langle\Phi_\mu|\hat{R}|\Phi_\nu\rangle \tag{1.48}$$

$$\hat{\bar{H}}R = \omega_{fi}R \tag{1.49}$$

Therefore, the EOM-CC problem is a simple diagonalization of $\bar{H}$ that can be done in an iterative way by employing the Davidson diagonalization scheme [121]. Furthermore, the form of the $\hat{R}$ operator depends on the problem tackled, and its general form is:

$$\hat{R} = \hat{R}_0 + \hat{R}_1 + \hat{R}_2 + \cdots \hat{R}_n \quad ; \quad \hat{R}_n = \sum_{\mu} r_\mu^{(n)}\Omega_\mu^{(n)} \tag{1.50}$$

for one-electron ionizations we have,

$$\hat{R}^{IP} = \sum_i r_i \hat{a}_i + \sum_{i<j}\sum_a r_{ij}^a \left\{\hat{a}_a^\dagger \hat{a}_i \hat{a}_j\right\} + \cdots \tag{1.51}$$

where we have introduced second-quantization operators of creation $\{\hat{a}_a^\dagger\}$ and annihilation $\{\hat{a}_i, \hat{a}_j\}$. The application of this operator in a CCSD reference will generate a combination of ionized determinants.

Core-Valence Separated EOM-CC

In Section 6, we apply the theoretical framework presented in this section to obtain the values of ω_{fi} (given by Equation 1.48) corresponding to the ionization energies of heavy elements. However, since our investigation focused on *core ionized states*, we had to introduce an approximation called the Core-Valence Separation (CVS) in our EOM-CCSD simulations (CVS-EOM-CCSD).

Based on the early work of Cederbaum et al. [122] and introduced within coupled-cluster theory by Coriani and Koch [123], the CVS approximation is a strategy to address convergence and numerical stability issues that arise when dealing with core-excited states. Such an approximation reflects the need to converge several valence-level excited states before reaching the core-excited states and the significant number of roots needed to span the core-excited states.

Another challenge when determining core-excited states is the pseudo-continuum states from diffuse orbitals that can be occupied by any electron, even though they should be physically already ionized [124–128]. Thus, the CVS technique addresses these issues and achieves faster convergence by applying a projector P^{CVS} to the iterative space. This operator removes trial/solution vectors that contain rotations involving occupied orbitals with lower energies than those within the specified energy window. The desired excited states are obtained by doing

$$P^{CVS}\left(\hat{\bar{H}}P^{CVS}|R_\mu\rangle\right) = \omega_{fi}P^{CVS}|R_\mu\rangle \tag{1.52}$$

where R_μ denotes the manifold of eigenvectors of the excited states of interest.

The articles cited earlier provide more details on the implementation of the CVS approximation for CC-based methods. Furthermore, we will not delve into the projection scheme utilized in DFT-based simulations, as the Restricted-Excitation-Window (REW) approximation shares a similar philosophy with the CVS method described in this section [129–131].

To finish this section, we shall mention that CC-based methods provide excellent results for ground and excited states of atoms and molecules and are thus extensively used in benchmarks for other theory levels. For example, the CCSD(T) level is considered by many to be the *gold standard* in computational chemistry [132, 133]. However, the performance of such CC-based methods suffers from its considerable computational scaling, e.g. at the CCSD level, the asymptotic computational scale is in the order of $\mathcal{O}(N^6)$, where $N^6 = (occupied)^2(virtual)^4$, thus making its applications considerably limited to small and few-electron systems [134]. This way, we recognize that the efforts presented in this thesis to investigate the core-ionized states of uranyl-based compounds (Section 6) showcases the progress of such CC-based methods in the last decade.

1.5 Density Functional Theory

Part of this thesis focuses on simulating core-excited spectra of systems containing heavy elements. However, the computational scaling of CC methods, discussed in Section 1.4, limits their applicability even for systems with low atomic number elements. Therefore, this work aims to extend the applicability of density functional theory (DFT) to investigate the core-excited states of actinides. In the following, we present an introduction to the DFT formalism for describing the ground state of atoms and molecules, similar to the discussion presented by Engel and Dreizler [135], Toulouse [136], and Sholl and Steckel [137]. In Section 3, we will also briefly introduce its time-dependent formalism (TD-DFT).

While our aim in the following sections is to cover the foundational concepts underlying DFT to obtain information about the ground state of a many-body system, it is worth noting that DFT involves approximations that preclude an exhaustive overview of the topic in this chapter. For more detailed information, we refer the reader to the references cited throughout the following sections, as well as to broader discussions on this topic in works by Pribram-Jones et al. [138], Mardirossian and Head-Gordon [139], and Teale et al. [140].

General theory

Unlike the previously discussed approaches to solving the many-body problem, DFT maps the electronic density, $\rho[(\mathbf{r})]$, to the ground state energy E_0, rather than obtaining a wave function spanning the entire Hilbert space. For an N-electron system, the electronic density, which is related to the one-body density matrix, is defined as: reads as:

$$\rho(\mathbf{r}) = N \int \int |\Psi(\mathbf{r}_1 s_1, \mathbf{r}_2 s_2, \cdots, \mathbf{r}_N s_N)|^2 \, ds_1 \cdots ds_N d\mathbf{r}_2 \cdots d\mathbf{r}_N \tag{1.53}$$

This leads to a substantial decrease in computational complexity, from the $3N$ spatial coordinates of an N-electron wave function to only three coordinates of the one-electron density, turning its applications to quantum chemistry and solid-state physics more feasible than wave-function-based methods.

The early development of DFT was in the late 1920s, shortly after Schrödinger proposed his equation, when Thomas [141], Fermi [141] and Dirac [142] proposed a model for treating the fictitious homogeneous gas of interacting electrons, also known as the uniform electron gas (UEG) or *jellium*. In their method, the total electronic energy of a N-electron system reads as a functional of the electronic density, which reads as

$$E[\rho] = T_e[\rho] + E_H[\rho] + E_{xc}[\rho] + E_{ne}[\rho] + V_{nn} \tag{1.54}$$

Each term in the equation above represents a different contribution to the energy, such as kinetic energy ($T_e[\rho]$), electron-nucleus attraction ($E_{ne}[\rho]$), and nuclei repulsion (V_{nn}). The electron-electron repulsion terms ($V_{ee}[\rho]$) reads as classical electrostatic repulsion for a charge distribution ($E_H[\rho]$) and exchange-correlation ($E_{xc}[\rho]$). It is worth noting that, in contrast to the Hartree-Fock energy (Equation 1.14), this model replaces the exchange term K_{ij} with the $E_{xc}[\rho]$ term. We will further return to the electron-electron repulsion term in this text.

The goal of DFT is then to find a functional that can accurately map the electron density to the ground state energy of a system, i.e., $\rho \to E_0$. This is a challenging task, particularly for correlated systems, such as electrons confined in atoms, where the electronic density is not uniform. In fact, for a long time, only $E_x[\rho]$ in the exchange-correlation contribution for the UEG was known to have an exact expression, leaving strongly correlated systems hopeless to be treated.

The development of DFT was significantly advanced in the early 1960s when Hohenberg and Kohn [143] introduced the mathematical formalism for an exact variation principle for mapping the electron density to the ground state energy. Subsequently, Kohn and Sham [144] further expanded the possibilities of DFT by proposing a set of equations, which established the theory as we know it today.

Hohenberg-Kohn theorems

For the sake of brevity, from this point forward in the text, we will drop spin coordinates unless explicitly stated otherwise, and therefore wave functions will be expressed only with their spatial coordinates (e.g. $\psi(r)$).

Hohenberg and Kohn theorems [143], developed in 1964, were proposed for a system of N interacting electrons subjected to a local external potential $v_{ext}(\mathbf{r})$, such as the stationary electrostatic potential generated by the nuclei within the Born-Oppenheimer approximation.

By solving the Schrödinger equation, it is possible to determine the system's ground-state wave function ($\Psi_0(\mathbf{r}) = \Psi$), further used to map $v_{ext}(\mathbf{r})$ to Ψ. By rewriting the Schrödinger equation in terms of the ground-state electronic density ($\rho_0(\mathbf{r}) = \rho(\mathbf{r})$), such a mapping can be applied to this quantity, yielding $v_{ext}(\mathbf{r}) \rightarrow \rho(\mathbf{r})$.

The first of Hohenberg and Kohn theorems demonstrate the invertibility of this mapping. Therefore, the ground-state density uniquely determines the external local potential up to an arbitrary additive real-valued constant, $\rho(\mathbf{r}) \rightarrow v_{ext}(\mathbf{r}) + \text{const}$. Once $v_{ext}(\mathbf{r})$ is determined, the system Hamiltonian it is as well, and thus this constitutes an alternative to solving the many-body problem. Hohenberg and Kohn, which we will simply refer to as HK, also recognized that the ground-state wave function for such a potential is a functional of the electronic density, leading to the definition of the so-called *universal density functional*

$$F[\rho] = \langle \Psi[\rho] | \hat{T}_e + \hat{V}_{ee} | \Psi[\rho] \rangle \tag{1.55}$$

which, when added to the external potential under consideration, generates the total electronic energy functional (which we will henceforth refer to as the density functional),

$$E[\rho] = F[\rho] + \int v_{ext}\ \rho(\mathbf{r})\ d\mathbf{r} \tag{1.56}$$

Furthermore, in the second of their theorems, HK showed that for a given set of v-representable densities, the density functional reaches its minimum value for the exact ground state,

$$E_0[\rho] = \min_{\rho\ \in\ v} \left\{ \langle \Psi[\rho] | \hat{T}_e + \hat{V}_{ee} | \Psi[\rho] \rangle + \int v_{ext}\ \rho(\mathbf{r})\ d\mathbf{r} \right\} \tag{1.57}$$

and therefore $E[\rho]$ satisfies the variation principle in a similar way as previously discussed for HF theory.

Despite the exact variation principle established by Hohenberg and Kohn, the exact exchange-correlation functional is still unknown. Therefore, approximate functionals to compute $F[\rho]$ are employed, often resulting in compromised accuracy for density and ground-state energy values.

It is worth noting, however, that the work of HK was initially limited to the existence of a local potential associated with $\rho(\mathbf{r})$ (and the corresponding set of v-representable densities), as well as nondegenerate ground states. Nonetheless, Levy [145, 146] and Lieb [147] later extended this work by suggesting a *constrained search formulation*, in which $E[\rho]$ also shows to satisfy a variational property.

To conclude this section, while Hohenberg and Kohn derived their theorems, they did not provide a formalism for obtaining densities. However, within a year of their work, Kohn and Sham proposed an alternative to address this issue, as will be introduced in the following section.

Kohn-Sham theory

The work of Kohn and Sham (hereafter referred to as KS) is the landmark of the current formulation of DFT. Their method involves decomposing $F[\rho]$ as

$$F[\rho(\mathbf{r})] = T_s[\rho(\mathbf{r})] + E_{Hxc}[\rho(\mathbf{r})] \tag{1.58}$$

where $E_{Hxc}[\rho]$ is the Hartree-exchange-correlation functional (which will be discussed later in this text), and $T_s[\rho]$ is the non-interacting kinetic energy functional given by

$$T_s[\rho] = \langle \Psi(\mathbf{r}) | \hat{T}_e | \Psi(\mathbf{r}) \rangle = \langle \Psi[\rho] | \hat{T}_e | \Psi[\rho] \rangle \tag{1.59}$$

where we have utilized the previously mentioned fact that $\rho(\mathbf{r})$ can be reconstructed from any arbitrary external potential $v(\mathbf{r})$ (and vice versa) and that a v-representable density $\rho(\mathbf{r})$ can be used to construct a wave function $\Psi(\mathbf{r})$. Hence, the wave function can be considered a functional of the density, $\Psi[\rho]$.

KS proposed a reformulation of the variational property of the universal density functional in terms of single-determinant wave functions. In the KS method, the kinetic energy of an interacting system comes from a single-determinant wave function, $T_S = \langle \Psi^{KS} | \hat{T} | \Psi^{KS} \rangle$. The remaining contributions (comprised in E_{Hxc}) to be calculated are approximated as a functional of the density. Therefore, in the exact case, i.e., the Equation 1.58 is known, minimization yields the exact ground-state energy (E_0) and KS wave function (Ψ^{KS}).

Before proceeding, we shortly mention that Seidl et al. [148] showed that is possible to formulate $F[\rho]$ in other ways than the one proposed by Kohn and Sham, achieving the same variational property and a similar set of KS equations, therefore constituting the *generalized Kohn-Sham method* (GKS).

According to the KS method, the total electronic energy for a system of N non-interacting electrons with electronic density $\rho(\mathbf{r})$ and kinetic energy T_S, subjected to some local external one-body potential $v_{ext}(\mathbf{r})$, can be expressed as a functional of $\rho(\mathbf{r})$. By using the previously discussed decomposition of $F[\rho]$ (Equation 1.58) yields,

$$E[\rho] = T_S[\rho] + v_{ext}[\rho] + E_H[\rho] + E_{xc}[\rho] \tag{1.60}$$

where the classical electrostatic repulsion energy functional, also known as the Hartree energy functional ($E_H[\rho]$) reads:

$$E_H[\rho] = \frac{1}{2} \int \int \frac{\rho(\mathbf{r}_1)\rho(\mathbf{r}_2)}{|\mathbf{r}_1 - \mathbf{r}_2|} d\mathbf{r}_1 d\mathbf{r}_2 \tag{1.61}$$

Assuming a unique Kohn-Sham wavefunction (Ψ^{KS}), the E_{xc} term in Equation 1.60 can be further decomposed into:

$$E_{xc}[\rho] = E_x[\rho] + E_c[\rho] + T[\rho] - T_s[\rho] \tag{1.62}$$

At the far right, a correction term ($T[\rho] - T_s[\rho]$) is introduced to account for the difference in kinetic energy between the interacting system ($T[\rho]$) and the corresponding non-interacting reference system ($T_s[\rho]$).

Alternatively, the total energy functional can be expressed in terms of the set of spin orbitals of the system $\left\{\psi_i^{KS}(\mathbf{r}) = \psi_i(\mathbf{r})\right\}$,

$$E[\rho] = \sum_{i=1}^{N} \int \psi_i^*(\mathbf{r}) \left(-\frac{1}{2}\nabla^2 + v_{ext}(\mathbf{r})\right) \psi_i(\mathbf{r})\, d\mathbf{r} \, + E_{Hxc}[\rho] \tag{1.63}$$

By taking the sum of the squared magnitudes of the orbitals, the electronic density reads:

$$\rho(\mathbf{r}) = \sum_i \left|\psi_i(\mathbf{r})\right|^2 \tag{1.64}$$

The method of Lagrange multipliers can be evoked in a similar fashion as done in Hartree-Fock theory (Equation 1.16) to optimize the total energy functional by setting $\delta E[\rho] = 0$. The assumption of v-representability and differentiability of $E_{Jxc}[\rho]$ leads to a resulting set of equations known as the KS equations:

$$\left(-\frac{1}{2}\nabla_i^2 + v_{ext}(\mathbf{r}) + v_{Hxc}(\mathbf{r})\right) \psi_i(\mathbf{r}) = \epsilon_i \psi_i(\mathbf{r}) \tag{1.65}$$

where, the Hartree-exchange-correlation potential v_{Hxc} is defined as:

$$v_{Hxc} = v_H + v_{xc} = \frac{\delta E_H[\rho]}{\delta \rho} + \frac{\delta E_{xc}[\rho]}{\delta \rho} \tag{1.66}$$

Combining the terms inside the bracket in Equation 1.65 to define the Kohn-Sham (KS) Hamiltonian ($\hat{h}_{KS}$) results in an elegant and compact eigenvalue equation:

$$\hat{h}_{KS}\psi_i(\mathbf{r}) = \epsilon_i \psi_i(\mathbf{r}) \tag{1.67}$$

Similar to the discussion on the Hartree-Fock equation, the Kohn-Sham equation is a set of coupled equations whose self-consistent solution yields a set of optimal KS orbitals $\{\psi_i\}$ and their corresponding KS orbital energies $\{\epsilon_i\}$.

Basis sets

As previously demonstrated for the HF case, it is possible to rewrite the KS equations by writing the KS orbitals as an expansion of known basis functions $\{\chi_\nu(\mathbf{r})\}$. Assuming orthonormal wave functions, Equation 1.67 can be projected into the complex conjugate of $\psi_i^{KS}(\mathbf{r})$ to yield:

$$\sum_{\nu=1} F_{\mu\nu} c_{\nu i} = \epsilon_i \sum_{\nu=1}^{M} S_{\mu\nu} c_{\nu i} \tag{1.68}$$

where $S_{\mu\nu}$ is the previously defined overlap matrix, and the one-electron KS Fock matrix reads as

$$F_{\mu\nu} = h_{\mu\nu} + J_{\mu\nu} + V_{xc,\mu\nu} \tag{1.69}$$

where $h_{\mu\nu}$ denotes a one electron contribution that reads as

$$h_{\mu\nu} = \int \varphi_\mu^*(\mathbf{r}) \left(-\frac{1}{2}\nabla^2 + v_{ext}(\mathbf{r}) \right) \varphi_\nu(\mathbf{r}) d\mathbf{r} \tag{1.70}$$

The two electron $J_{\mu\nu}$ contribution is given by

$$J_{\mu\nu} = \int \varphi_\mu^*(\mathbf{r}) v_H \varphi_\nu(\mathbf{r}) d\mathbf{r} \tag{1.71}$$

The exchange-correlation contribution reads as

$$V_{xc,\mu\nu} = \int \varphi_\mu^*(\mathbf{r}) v_{xc}(\mathbf{r}) \varphi_\nu(\mathbf{r}) d\mathbf{r} \tag{1.72}$$

and as can be seen, this will depend on the chosen form of E_{xc}, discussed in Section 1.7.

Finally, defining density matrices as $P_{\gamma\lambda} = \sum_{i=1}^{N} c_{\gamma i} c^*_{\lambda i}$, the electronic density reads as

$$\rho(\mathbf{r}) = \sum_{\lambda=1}^{M} \sum_{\gamma=1}^{M} P_{\gamma\lambda} \chi_\gamma(\mathbf{r}) \chi^*_\lambda(\mathbf{r}) \tag{1.73}$$

Except for the (long-range) hybrid functionals, the DFT-based methods scale asymptotically as $\mathcal{O}(N^3)$, resulting in a significant improvement in computational cost compared to HF ($\mathcal{O}(N^4)$) and CCSD ($\mathcal{O}(N^6)$) calculations.

1.6 Environmental Effects

Throughout this thesis, we investigated the processes of absorption and ionization in systems of varying extents or degrees of complexity, specifically molecules and condensed phase systems. Despite the progress in computing, which has transformed the landscape of theoretical chemistry from a field that used to require weeks to produce results stored on paper or disks to one that can perform calculations on supercomputers in a matter of hours or days [149, 150], the fundamental challenge remains unchanged: computational complexity scales with the size of the system being studied [134, 151, 152].

While not all theoretical methods are computationally feasible, not all approximations can accurately represent a system under investigation. Therefore, developing and applying approximations to the different regions of a system are essential components of theoretical chemistry [153–159].

Environmental effects, such as solvent effects, intermolecular interactions, and electrostatic fields, have been shown to play a crucial role in the physical and chemical properties of f-elements in both solution and solid-state [160–165], as showcased in the works of Vallet et al. [46–48, 161, 166–172], among others [173–175]. Thus, part of the development of this thesis consisted in evaluating such effects in the X-ray observables of uranyl-containing systems.

1.6.1 Embedding methods

When addressing environmental effects, it is helpful to divide the molecular ensemble by its degrees of freedom – an active subsystem, which is the primary focus and often treated with a more sophisticated theory level than its environment.

In the case of electrostatic interactions, a simple approximation is to treat the environment implicitly, as is done in continuum methods such as the polarizable continuum method (PCM) [176] and the conductor-like screening model (COSMO) [177, 178]. The molecular structure of the environment is disregarded in these methods and is instead a continuum (characterized by a dielectric constant ϵ^{env}) in which the active system is confined within a cavity. These methods are commonly employed to investigate solvent effects, and here we refer to the works of Oher et al. [46–48] and Su et al. [179], were these methods were employed to model the valence-level spectroscopy of systems containing the uranyl moiety.

Hybrid approaches offer another alternative for treating environmental problems. Fragment-embedding models, such as the quantum mechanics/molecular mechanics (QM/MM) method [153, 180], employ an electrostatic [181–183] or polarizable embedding [152, 184] approach to represent the environment as a molecular force field (MM) acting on the active system. The works of Infante et al. [185, 186], Liu et al. [187] and Odoh et al. [188] showcase the applications of such models within the context of actinide chemistry.

As highlighted by Vallet et al. [161] and Lan et al. [189], the embedding approaches above outlined can provide valuable insights into the chemistry of lanthanides and actinides in solution. This is particularly important in the context of nuclear fuel reprocessing, as significant amounts of radioactive waste can be released into the environment, posing a potential hazard to human health and the ecosystem [190–194].

Therefore, the development of efficient extraction methods is of great importance to mitigate these potential hazards, and theoretical predictions may help in such investigations. In a recent experimental-theoretical study, Oher et al. [47] employed the conductor-like polarizable continuum model (CPCM) to evaluate changes in the luminescence properties of uranyl nitrate ($UO_2(NO_3)_2$) complexes in different solvents. TD-DFT results in this study were consistent with time-resolved laser-induced fluorescence spectroscopy (TRLFS) experiments.

In the study presented in Sections 4 and 6, we investigated the spectroscopic observables of the uranyl ion in a $Cs_2UO_2Cl_4$ crystal lattice. This investigation is of great interest, given the numerous applications of actinides in material science [195, 196], nanotechnology [17, 197], and geochemistry [192, 198]. Moreover, as highlighted by Rothe et al. [199] and Scheinost et al. [200], X-ray spectroscopies such as X-ray absorption (XAS) and photoelectron (XPS) spectroscopies have been extensively employed for various purposes in actinide science for over a century, including the evaluation of actinide speciation as further discussed by Maher et al. [192].

Despite the strengths of *ab initio* methods, their computational scaling considerably limits their ability to treat even a single unit cell, resulting in the extensive use of semi-empirical methods for investigating such materials [13, 201–204]. To overcome these constraints and employ high-level *ab initio* methods in our calculations, we have chosen to use a potential-embedding model, also known as the quantum embedding approach (QM/QM) in the literature.

In QM/QM approaches, the active system's wave function or electronic density is embedded in the wave function (WFT-in-WFT) or electronic density of the environment (WFT-in-DFT). Alternatively, the electronic density of the active system can be treated as being embedded in the electronic density of the environment (DFT-in-DFT).

Frozen Density Embedding

The FDE approach has its origins in subsystem DFT theory developed by Cortona [205] and in the frozen density embedding theory developed by Wesolowski and Warshel [206, 207]. Various alternative approaches such as partition density functional theory [208] and potential-functional embedding theory [209] have also been proposed in the literature. The following discussion is based on the work of De Santis et al. [210, 211].

In the FDE approach, the total electronic density of the system reads as the sum of the active subsystem density (denoted ρ_I) and the environment or remaining subsystem density (denoted as ρ_{II} for simplicity), $\rho_{total}(\mathbf{r}) = \rho_I(\mathbf{r}) + \rho_{II}(\mathbf{r})$. The decomposition of the total energy functional reads as:

$$E_{tot}[\rho_I, \rho_{II}] = E_I[\rho_I] + E_{II}[\rho_{II}] + E_{int}[\rho_I, \rho_{II}] \tag{1.74}$$

In the expression above, the total energy functional is decomposed into subsystem energies ($E_i[\rho_i]$; i = I, II) and interaction energy ($E_{int}[\rho_I, \rho_{II}]$), the latter reading as

$$\begin{aligned} E_{int}[\rho_I, \rho_{II}] = \int \rho_I(\mathbf{r}) v_{nuc}^{II}(\mathbf{r})\, d\mathbf{r} + \int \rho_{II}(\mathbf{r}) v_{nuc}^{I}(\mathbf{r})\, d\mathbf{r} + E_{nuc}^{I,II} \\ \iint \frac{\rho_I(\mathbf{r})\rho_{II}(\mathbf{r}')}{|\mathbf{r}-\mathbf{r}'|} d\mathbf{r}\, d\mathbf{r}' + E_{xc}^{nadd}[\rho_I, \rho_{II}] + T_s^{nadd}[\rho_I, \rho_{II}] \end{aligned} \tag{1.75}$$

where $v_{nuc}^{i}(\mathbf{r})$ denotes the nuclear potential associated with the atoms in the i-th subsystem, $E_{xc}^{nadd}[\rho]$ and $T_s^{nadd}[\rho]$ are respectively the non-additive exchange-correlation and kinetic energy.

If all subsystems are at the Kohn-Sham DFT level, the individual subsystem energies $E_i[\rho_i]$ are obtained as discussed in Section 1.5. For procedures that use WFT-based methods, we recommend referring to the work of Gomes et al. [167]. By minimizing the total energy with respect to $\rho_I(\mathbf{r})$ for a fixed (or frozen) $\rho_{II}(\mathbf{r})$, the optimal set of active system spin-orbitals $\left\{\psi_i^I(\mathbf{r})\right\}$ can be obtained. This is accomplished by solving the set of Kohn-Sham-like equations given by:

$$\left(-\frac{\nabla^2}{2} + v_{eff}^{KS}[\rho_I](\mathbf{r}) + v_{emb}^{I}[\rho_I, \rho_{II}](\mathbf{r})\right)\psi_i^I(\mathbf{r}) = \varepsilon_i^I \psi_i^I(\mathbf{r}) \tag{1.76}$$

Therefore, in the ground state, the different subsystems are coupled to each other through the so-called embedding potential $v_{emb}^{I}[\rho_I, \rho_2]$, which reads as:

$$v^{I}_{emb}[\rho_I,\rho_{II}](\mathbf{r}) = \frac{\delta E_{int}[\rho_I,\rho_{II}]}{\delta\rho_I} = v^{II}_{nuc}(\mathbf{r})+ \\ \int \frac{\rho_{II}(\mathbf{r}')d\mathbf{r}'}{|\mathbf{r}-\mathbf{r}'|} + \frac{\delta E^{nadd}_{xc}[\rho_I,\rho_{II}]}{\delta\rho_I} + \frac{\delta T^{nadd}_{s}[\rho_I,\rho_{II}]}{\delta\rho_I} \quad (1.77)$$

Finally, after minimizing $E_{int}[\rho_I,\rho_2]$, the $v_{emb}(\mathbf{r})$ is included as an additional one-electron operator to the Fock matrix in the calculations that follow. An additional step in this treatment involves optimizing densities via the so-called freeze-and-thaw procedure [212], in which the roles of ρ_I and ρ_{II} are exchanged when solving Equation 1.76.

As discussed by De Santis et al. [210], the FDE method provides an effective and viable approach to incorporating environmental effects into high-level calculations. Such an approximated method is especially advantageous when using a DFT variant in the FDE method since DFT methods have a favorable computational scaling compared to higher-level methods, as discussed in the previous sections. Furthermore, the quality of such an embedding model is evident in its plethora of applications and comparisons to more approximate quantum embedding approaches discussed earlier in this section, as further demonstrated by Jacob et al. [213] and in the previous references.

In this work, we employed the FDE scheme, originally developed by Jacob et al. [212] in the Amsterdam Density Functional (ADF) [214] software, using the scripting framework of `PyADF` [215] to export the obtained embedding potential into `DIRAC` calculations.

To conclude this section, the effectiveness of the FDE framework for studying the $Cs_2UO_2Cl_4$ crystal has been previously demonstrated by Gomes et al. [167]. By systematically comparing the performance of various structural models and different WFT-in-DFT and DFT-in-DFT approaches to represent the crystalline environment, achieved valence-level excitation energies close to experimental values. Building upon this, the work presented in Sections 5 (DFT-in-DFT) and 5 (CVS-EOM-CCSD-in-DFT) represents a significant extension of this application to core-excited and ionized states, thereby contributing to the advancement of the field.

1.7 Approximate functionals

As extensively discussed in Section 1.5, there is currently no exact expression for the exchange-correlation energy functional (E_{xc}), and achieving chemical accuracy in (Perdew's) Jacob's ladder [139, 216, 217] remains a theoretical ideal. Therefore, we use density functional approximations (DFAs) in simulations.

We can classify DFAs into two main classes: local and non-local. It is also common to express exchange and correlation contributions as two independent terms:

$$E_{xc}[\rho] = E_x[\rho] + E_c[\rho] \tag{1.78}$$

In this section, we provide a brief overview of the classes of exchange-correlation functionals employed in this thesis. To maintain conciseness, the parametrization of these functionals, which may rely on empirical fitting to datasets of physicochemical properties such as atomic energies, barrier heights, and thermochemistry [139, 217], will not be discussed. We encourage readers to consult the original references cited throughout the text for further information. Additionally, this section does not cover the topics of exchange-correlation holes and adiabatic-connection formalism [136, 218–220]. However, we note that most DFAs rely on this formalism, and we refer readers to the references provided for more information on these topics.

This thesis primarily utilized the long-range-corrected exchange-correlation functional CAM-B3LYP originally proposed by Yanai et al. [221], which belongs to the class of range-separated hybrid functionals. CAM-B3LYP has been demonstrated in numerous studies to exhibit reliable results in computing spectroscopic observables of actinides, including absorption energies at both valence [46, 48, 222–224] and core levels [225, 226], and also and emission energies [46, 48].

In our FDE calculations, the non-additive kinetic energy terms in Equation 1.75 are described using the reparametrization of the Perdew-Wang functional [227] done by Lembarki and Chermette [228] (PW91k), while the Perdew-Burke-Ernzerhof (PBE) exchange-correlation functional [229] is used for subsystem energies in our FDE simulations. Both of these functionals belong to the class of functionals within the gradient-corrected approximation (GGA) and have been extensively employed in FDE applications, from biomolecules in solution [230] to actinides in the solid phase [167], such as the crystalline host environment investigated in this work.

Before delving into the specific classes of functionals employed in this work, let us first review the simplest ones.

Local Density Approximation

The simplest type of DFAs is called the local density approximation (LDA), first introduced by Kohn and Sham for the aforementioned uniform electron gas (UEG). This approximation assumes that the exchange-correlation energy depends only on the density at a given point, as expressed in the equation:

$$E_{xc}^{LDA}[\rho] = \int \rho(\mathbf{r})\epsilon_{xc}^{UEG}[\rho]d\mathbf{r} \;;\; \epsilon_{xc}^{UEG}[\rho] = \epsilon_{x}^{UEG}[\rho] + \epsilon_{c}^{UEG}[\rho] \tag{1.79}$$

where $\epsilon_{xc}^{UEG}[\rho]$ denotes the exchange-correlation energy density function per particle for the UEG. The exchange contribution is analytical and reads:

$$\epsilon_{x}^{UEG}[\rho] = C_x\, \rho^{1/3}(\mathbf{r}) = -\frac{3}{4}\left(\frac{3}{\pi}\right)^{1/3} \rho^{1/3}(\mathbf{r}) \tag{1.80}$$

When bypassing the correlation contribution from Equation 1.80, the resulting energy functional is the so-called Slater exchange functional. On the other hand, the correlation contribution in Equation 1.80 does not have an analytical expression. Therefore, for a given set of densities, this value is obtained using numerical methods, such as Monte Carlo simulations [231], and then fitted to a parametrized function of $\rho(\mathbf{r})$.

By using this local density approximation (LDA) functional, one is approximating the exchange-correlation energy $E_{xc}[\rho]$ of an interacting system of electrons to that of a uniform electron gas of the same density. Such an approximation deplets the majority, to not say not all, of the real system correlation.

Another important point to note in Equation 1.80 is the absence of any mention of spin. This issue is addressed within the local spin density approximation

(LSDA), first proposed by [232] [232], whose general form for the exchange-correlation functional reads as:

$$E_{xc}^{LSDA}[\rho] = \int \rho(\mathbf{r})\epsilon_{xc}\left(\rho_\alpha, \rho_\beta\right) d\mathbf{r} \tag{1.81}$$

As examples of DFAs within the LSDA, we can consider parametrizations proposed by Vosko et al. [233] (VWN models) and Perdew and Wang [234] (PW92).

Generalized Gradient Approximation

The inclusion of the first derivative of the density, $\nabla\rho(\mathbf{r})$, in the exchange-correlation functional $E_{xc}[\rho]$ constitutes a class of semi-local functionals within the so-called generalized gradient approximation (GGA) proposed by Perdew et al. [218]. Such an approximation improves upon the LSDA by considering the immediate vicinity of the calculated density, making these functionals semi-local. The approximate exchange-correlation functional within the GGA is given by

$$E_{xc}^{GGA}[\rho] = \int \rho(\mathbf{r})\epsilon_{xc}\left(\rho_\alpha, \rho_\beta, \nabla\rho_\alpha, \nabla\rho_\beta\right) d\mathbf{r}$$

(1.82)

GGA functionals are constructed differently from LDA functionals due to the lack of an exact model for fitting $\epsilon_c[\rho]$ within the GGA, in contrast to the UEG model used in the LSDA. Therefore, other strategies are commonly employed to develop these kinds of functionals. Furthermore, Mardirossian and Head-Gordon [139] demonstrated that GGA functionals outperform LSDA functionals in calculating thermodynamic properties.

The Meta-Generalized Gradient Approximation (meta-GGA), proposed by Tao et al. [235], takes a step further by introducing higher order derivatives, such as the Laplacian of the density ($\nabla^2\rho(\mathbf{r})$) or the non-interacting kinetic energy density ($\tau(\mathbf{r})$) in $E_{xc}[\rho]$. Consequently, meta-GGA functionals can take on one of the following forms:

$$E_{xc}^{meta-GGA}[\rho] = \int \rho(\mathbf{r})\epsilon_{xc}\left(\rho_\alpha, \rho_\beta, \nabla\rho_\alpha, \nabla\rho_\beta, \nabla^2\rho_\alpha, \nabla^2\rho_\beta\right) d\mathbf{r} \tag{1.83}$$

$$E_{xc}^{meta-GGA}[\rho] = \int \rho(\mathbf{r})\epsilon_{xc}\left(\rho_\alpha, \rho_\beta, \nabla\rho_\alpha, \nabla\rho_\beta, \tau_\alpha, \tau_\beta\right) d\mathbf{r} \tag{1.84}$$

where the former equation includes the Laplacian of the density and the latter includes the non-interacting kinetic energy density, yielding:

$$\tau(\mathbf{r}) = \sum_i \left|\nabla\phi_i(\mathbf{r})\right|^2 \tag{1.85}$$

The non-interacting kinetic energy density has a relationship with the electronic density given by:

$$\tau(\mathbf{r}) = \frac{\nabla^2\rho(\mathbf{r})}{2} - \sum_i \psi_i^*(\mathbf{r})\nabla^2\psi_i(\mathbf{r}) \tag{1.86}$$

Examples of these functionals are the strongly constrained and appropriately normed (SCAN) [236] and the Tao-Perdew-Staroverov-Scuseria (TPSS) [235] functionals, which have been shown to provide improved results over GGA and LDSA functionals in various applications, as appointed by Mardirossian and Head-Gordon [139].

Single-determinant Hybrid Approximation

As previously mentioned in Section 1.2, one of the strong points of Hartree-Fock's theory comes from the exact cancellation of the self-repulsion (J_{ii}) and exchange (K_{ii}) terms, as seen in Equation 1.16. However, this lack of self-repulsion beyond the single-electron case can lead to the *over-localization* of orbitals/electron density, resulting in higher energies than the exact solution obtained with methods such as CCSD(T) or full-CI [66, 67]. This effect also impacts other properties, such as the values of dipole moment and barrier heights in reactions [139, 237, 238].

In contrast, in the case of DFT, it can be observed from the expression for the Hartree energy functional (Equation 1.61) that this term includes spurious self-repulsion. As this is a non-local term, the functionals previously mentioned don't correct this contribution, leading to an *over-delocalization* of orbitals/electron density in all DFT methods, affecting, among other things, numerous issues related to systems where fractional charges appear, as discussed in literature several authors [139, 239–244].

One shall then convey that one way to compensate for this self-interaction error in DFT would be by introducing a certain amount of HF exchange in $E_{xc}[\rho]$, by the construction of a *hybrid functional*. A general form for a hybrid exchange-correlation reads:

$$E_{xc} = -\frac{c}{2}\sum_{ij} K_{ij} + (1-c)E_x[\rho] + E_c[\rho] \tag{1.87}$$

where c is a parameter that will balance the contribution of HF exchange to a given exchange energy functional contribution, thus avoiding double counting of exchange.

Undoubtedly, the most popular functional in this class is the one proposed by Becke [245], which uses three parameters and is known as the B3LYP functional. This functional achieves a balance between the HF exchange and $E_x[\rho]$ from the VWN LSDA functional and the Becke 88 GGA functional [246]. The correlation terms are a balance between the VWN functional and the LYP GGA functional [247], yielding:

$$E_{xc} = aE_x^{HF} + (1-a)E_x^{VWN}[\rho] + b\Delta E_x^{B88}[\rho] + (1-c)E_x^{VWN}[\rho] + cE_c^{LYP}[\rho] \tag{1.88}$$

where the parameters are given as $a = 0.20, b = 0.72$ and $c = 0.81$.

One way to further improve hybrid functionals is to introduce a distance-dependent HF exchange [248, 249], in opposition to its fixed value in Equation 1.87. Range-separated functionals, such as the CAM-B3LYP functional, include such a correction whose HF exchange reads:

$$K_{ij}^{'} = \int \psi_i^*(\mathbf{x}_1)\,\psi_j^*(\mathbf{x}_2)\,\frac{c+(1-c)\,erf\,(\omega|\mathbf{r}_1-\mathbf{r}_2|)}{|\mathbf{r}_1-\mathbf{r}_2|}\,\psi_j(\mathbf{x}_1)\,\psi_i(\mathbf{x}_2)\,d\mathbf{x}_1 d\mathbf{x}_2 \quad (1.89)$$

where the interelectron repulsion operator ($1/|\mathbf{r}_1-\mathbf{r}_2|$) is replaced to balance short- and long-distance exchanges, i.e., resulting in the name Coulomb-attenuated method B3LYP (CAM-B3LYP). Therefore, a global expression for these functionals is

$$E_{xc}[\rho] = -\frac{1}{2}\sum_{ij} K_{ij}^{'} + E_x^{'}[\rho] + E_c[\rho] \quad (1.90)$$

A step forward in DFT simulations is to use double hybrid functionals, which combine a hybrid functional with correlation contributions from methods such as MP2 correlation energy [250, 251]. Although we did not utilize these functionals in this work, we encourage the reader to refer to the previous references for further information, as double hybrids lie in a higher rung in (Perdew's) Jacob's ladder for DFAs.

To finish, when selecting a functional for a given problem, it is essential to trade off the required accuracy for the problem addressed while keeping the computational cost in mind. The here employed CAM-B3LYP functional demonstrated a significant improvement in the computation of valence-level excitation energies of the bare uranyl ion compared to its standard version, as demonstrated by Réal et al. [168]. Tecmer et al. [222] also reported good agreement with experimental data for $UO_2Cl_4^{2-}$ using the Coulomb-attenuated functional.

In this chapter, we aimed to present a representative part of the theoretical framework used to obtain ground and core-ionized states. We have discussed the balance between accuracy and computational cost, as well as the suitability of approximations, at each theory level presented. In doing so, we have demonstrated how these theoretical methods translate the language of quantum mechanics into the chemical world.

As extensively discussed in the literature, wave function methods provide a systematic framework for recovering electronic correlation, while DFT methods and their DFAs often struggle to do so, and conclusions are often based on the results of benchmark calculations involving several functionals. However, a systematic cancelation of errors can lead to a biased interpretation of a functional's suitability for a given problem. This does not make DFT a worse theory, but its extensive use reflects the absence of infinite resources to attain the *gold standard* across complex systems. Therefore, it is the responsibility of the computational chemist to comprehend the underlying theory and carefully evaluate any possible constraints.

Bibliography of the current chapter

(13) Kvashnina, K. O.; De Groot, F. M. Invisible structures in the X-ray absorption spectra of actinides. *Journal of Electron Spectroscopy and Related Phenomena* **2014**, *194*, 88–93.

(17) Pan, Z.; Bártová, B.; LaGrange, T.; Butorin, S. M.; Hyatt, N. C.; Stennett, M. C.; Kvashnina, K. O.; Bernier-Latmani, R. Nanoscale mechanism of UO2 formation through uranium reduction by magnetite. *Nature communications* **2020**, *11*, 4001.

(46) Oher, H.; Réal, F.; Vercouter, T.; Vallet, V. Investigation of the Luminescence of [UO2X4] 2–(X= Cl, Br) Complexes in the Organic Phase Using Time-Resolved Laser-Induced Fluorescence Spectroscopy and Quantum Chemical Simulations. *Inorganic Chemistry* **2020**, *59*, 5896–5906.

(47) Oher, H.; Ferru, G.; Couston, L.; Berthon, L.; Guillaumont, D.; Réal, F.; Vercouter, T.; Vallet, V. Influence of the First Coordination of Uranyl on Its Luminescence Properties: A Study of Uranyl Binitrate with N, N-Dialkyl Amide DEHiBA and Water. *Inorganic Chemistry* **2021**, *61*, 890–901.

(48) Oher, H.; Vercouter, T.; Réal, F.; Shang, C.; Reiller, P. E.; Vallet, V. Influence of Alkaline Earth Metal Ions on Structures and Luminescent Properties of Na m M n UO2 (CO3) 3 (4–m–2 n)–(M= Mg, Ca; m, n= 0–2): Time-Resolved Fluorescence Spectroscopy and Ab Initio Studies. *Inorganic Chemistry* **2020**, *59*, 15036–15049.

(54) Schrödinger, E. An undulatory theory of the mechanics of atoms and molecules. *Physical review* **1926**, *28*, 1049.

(55) Mackey, G. W. Quantum mechanics and Hilbert space. *The American Mathematical Monthly* **1957**, *64*, 45–57.

(56) Carroll, S. M. In *Quantum mechanics and fundamentality: naturalizing quantum theory between scientific realism and ontological indeterminacy*; Springer: 2022, pp 211–224.

(57) Hanson, N. R. Copenhagen interpretation of quantum theory. *American Journal of Physics* **1959**, *27*, 1–15.

(58) Stapp, H. P. The copenhagen interpretation. *American journal of physics* **1972**, *40*, 1098–1116.

(59) Howard, D. Who invented the "Copenhagen Interpretation"? A study in mythology. *Philosophy of Science* **2004**, *71*, 669–682.

(60) Faye, J. Copenhagen interpretation of quantum mechanics. **2002**.

(61) Born, M. Quantenmechanik der stoßvorgänge. *Zeitschrift für physik* **1926**, *38*, 803–827.

(62) Von Neumann, J., *Mathematische grundlagen der quantenmechanik*; Springer-Verlag: 2013; Vol. 38.

(63) Gleason, A. M. Measures on the closed subspaces of a Hilbert space. *The Logico-Algebraic Approach to Quantum Mechanics: Volume I: Historical Evolution* **1975**, 123–133.

(64) Masanes, L.; Galley, T. D.; Müller, M. P. The measurement postulates of quantum mechanics are operationally redundant. *Nature communications* **2019**, *10*, 1361.

(65) Vaidman, L. Derivations of the Born rule. *Quantum, probability, logic: The work and influence of itamar pitowsky* **2020**, 567–584.

(66) Helgaker, T.; Jorgensen, P.; Olsen, J., *Molecular electronic-structure theory*; John Wiley & Sons: 2013.

(67) Jensen, F., *Introduction to computational chemistry*; John wiley & sons: 2017.

(68) Yarkony, D. R. Diabolical conical intersections. *Reviews of Modern Physics* **1996**, *68*, 985.

(69) Domcke, W.; Köppel, H.; Cederbaum, L. Spectroscopic effects of conical intersections of molecular potential energy surfaces. *Molecular Physics* **1981**, *43*, 851–875.

(70) Jasper, A. W.; Zhu, C.; Nangia, S.; Truhlar, D. G. Introductory lecture: Nonadiabatic effects in chemical dynamics. *Faraday Discussions* **2004**, *127*, 1–22.

(71) Matsika, S.; Krause, P. Nonadiabatic events and conical intersections. *Annual review of physical chemistry* **2011**, *62*, 621–643.

(72) Domcke, W.; Yarkony, D. R.; Köppel, H., *Conical intersections: theory, computation and experiment*; World Scientific: 2011; Vol. 17.

(73) Schuurman, M. S.; Stolow, A. Dynamics at conical intersections. *Annual review of physical chemistry* **2018**, *69*, 427–450.

(74) Domcke, W.; Yarkony, D.; Köppel, H., *Conical intersections: electronic structure, dynamics & spectroscopy*; World Scientific: 2004; Vol. 15.

(75) Domcke, W.; Yarkony, D. R. Role of conical intersections in molecular spectroscopy and photoinduced chemical dynamics. *Annual review of physical chemistry* **2012**, *63*, 325–352.

(76) Neville, S. P.; Averbukh, V.; Patchkovskii, S.; Ruberti, M.; Yun, R.; Chergui, M.; Stolow, A.; Schuurman, M. S. Beyond structure: ultrafast X-ray absorption spectroscopy as a probe of non-adiabatic wavepacket dynamics. *Faraday discussions* **2016**, *194*, 117–145.

(77) Neville, S. P.; Chergui, M.; Stolow, A.; Schuurman, M. S. Ultrafast x-ray spectroscopy of conical intersections. *Physical review letters* **2018**, *120*, 243001.

(78) Kjær, K. S.; Van Driel, T. B.; Harlang, T. C.; Kunnus, K.; Biasin, E.; Ledbetter, K.; Hartsock, R. W.; Reinhard, M. E.; Koroidov, S.; Li, L., et al. Finding intersections between electronic excited state potential energy surfaces with simultaneous ultrafast X-ray scattering and spectroscopy. *Chemical science* **2019**, *10*, 5749–5760.

(79) Heitler, W.; London, F. Wechselwirkung neutraler Atome und homöopolare Bindung nach der Quantenmechanik. *Zeitschrift für Physik* **1927**, *44*, 455–472.

(80) Pauling, L. The nature of the chemical bond. Application of results obtained from the quantum mechanics and from a theory of paramagnetic susceptibility to the structure of molecules. *Journal of the American Chemical Society* **1931**, *53*, 1367–1400.

(81) Slater, J. C. Directed valence in polyatomic molecules. *Physical Review* **1931**, *37*, 481.

(82) Dunning Jr, T. H.; Xu, L. T.; Takeshita, T. Y.; Lindquist, B. A. Insights into the electronic structure of molecules from generalized valence bond theory. *The Journal of Physical Chemistry A* **2016**, *120*, 1763–1778.

(83) Dunning Jr, T. H.; Gordon, M. S.; Xantheas, S. S. The nature of the chemical bond, 2023.

(84) Shaik, S.; Danovich, D.; Hiberty, P. C. On the nature of the chemical bond in valence bond theory. *The Journal of Chemical Physics* **2022**, *157*, 090901.

(85) Hund, F. Zur deutung der molekelspektren. iv. *Zeitschrift für Physik* **1928**, *51*, 759–795.

(86) Mulliken, R. S. Bonding Power of Electrons and Theory of Valence. *Chemical Reviews* **1931**, *9*, 347–388.

(87) Roothaan, C. C. J. New developments in molecular orbital theory. *Reviews of modern physics* **1951**, *23*, 69.

(88) Hall, G. The molecular orbital theory of chemical valency VIII. A method of calculating ionization potentials. *Proceedings of the Royal Society of London. Series A. Mathematical and Physical Sciences* **1951**, *205*, 541–552.

(89) Hartree, D. R. In *Mathematical Proceedings of the Cambridge Philosophical Society*, 1928; Vol. 24, pp 111–132.

(90) Gerlach, W.; Stern, O. Der experimentelle nachweis der richtungsquantelung im magnetfeld. *Zeitschrift für Physik* **1922**, *9*, 349–352.

(91) Pauli, W. Über den Zusammenhang des Abschlusses der Elektronengruppen im Atom mit der Komplexstruktur der Spektren. *Einführ. Orig* **1925**, *229*, 765–783.

(92) Fermi, E. Sulla quantizzazione del gas perfetto monoatomico. *Rendiconti Lincei* **1926**, *145*.

(93) Dirac, P. A. M. On the theory of quantum mechanics. *Proceedings of the Royal Society of London. Series A, Containing Papers of a Mathematical and Physical Character* **1926**, *112*, 661–677.

(94) Fock, V. Näherungsmethode zur Lösung des quantenmechanischen Mehrkörperproblems. *Zeitschrift für Physik* **1930**, *61*, 126–148.

(95) Fock, V. „Selfconsistent field "mit Austausch für Natrium. *Zeitschrift für Physik* **1930**, *62*, 795–805.

(96) Slater, J. C. Note on Hartree's method. *Physical Review* **1930**, *35*, 210.

(97) Slater, J. C. A simplification of the Hartree-Fock method. *Physical review* **1951**, *81*, 385.

(98) Sakurai, J. J.; Commins, E. D. Modern quantum mechanics, revised edition, 1995.

(99) Van Lenthe, E.; Baerends, E. J. Optimized Slater-type basis sets for the elements 1–118. *Journal of computational chemistry* **2003**, *24*, 1142–1156.

(100) Dunning Jr, T. H.; Hay, P. J. In *Methods of electronic structure theory*; Springer: 1977, pp 1–27.

(101) Dyall, K. G. Core correlating basis functions for elements 31–118. *Theoretical Chemistry Accounts* **2012**, *131*, 1–11.

(102) Löwdin, P.-O. Correlation Problem in Many-Electron Quantum Mechanics I. Review of Different Approaches and Discussion of Some Current Ideas. *Advances in chemical physics* **1958**, 207–322.

(103) Hollett, J. W.; Gill, P. M. The two faces of static correlation. *The Journal of Chemical Physics* **2011**, *134*, 114111.

(104) Cizek, J.; Paldus, J. Coupled cluster approach. *Physica Scripta* **1980**, *21*, 251.

(105) Monkhorst, H. J. Calculation of properties with the coupled-cluster method. *International Journal of Quantum Chemistry* **1977**, *12*, 421–432.

(106) Bartlett, R. J.; Musiał, M. Coupled-cluster theory in quantum chemistry. *Reviews of Modern Physics* **2007**, *79*, 291.

(107) Crawford, T. D.; Schaefer III, H. F. An introduction to coupled cluster theory for computational chemists. *Reviews in computational chemistry* **2007**, *14*, 33–136.

(108) Liu, J.; Cheng, L. Relativistic coupled-cluster and equation-of-motion coupled-cluster methods. *Wiley Interdisciplinary Reviews: Computational Molecular Science* **2021**, *11*, e1536.

(109) Stanton, J. F.; Bartlett, R. J. The equation of motion coupled-cluster method. A systematic biorthogonal approach to molecular excitation energies, transition probabilities, and excited state properties. *The Journal of chemical physics* **1993**, *98*, 7029–7039.

(110) Comeau, D. C.; Bartlett, R. J. The equation-of-motion coupled-cluster method. Applications to open-and closed-shell reference states. *Chemical Physics Letters* **1993**, *207*, 414–423.

(111) Nooijen, M.; Bartlett, R. J. Equation of motion coupled cluster method for electron attachment. *The Journal of chemical physics* **1995**, *102*, 3629–3647.

(112) Kucharski, S. A.; Włoch, M.; Musiał, M.; Bartlett, R. J. Coupled-cluster theory for excited electronic states: The full equation-of-motion coupled-cluster single, double, and triple excitation method. *The Journal of Chemical Physics* **2001**, *115*, 8263–8266.

(113) Krylov, A. I. Equation-of-motion coupled-cluster methods for open-shell and electronically excited species: The hitchhiker's guide to Fock space. *Annu. Rev. Phys. Chem.* **2008**, *59*, 433–462.

(114) Bartlett, R. J. Coupled-cluster theory and its equation-of-motion extensions. *Wiley Interdisciplinary Reviews: Computational Molecular Science* **2012**, *2*, 126–138.

(115) Coester, F. Bound states of a many-particle system. *Nuclear Physics* **1958**, *7*, 421–424.

(116) Čıžek, J.; Paldus, J. Correlation problems in atomic and molecular systems III. Rederivation of the coupled-pair many-electron theory using the traditional quantum chemical methodst. *International Journal of Quantum Chemistry* **1971**, *5*, 359–379.

(117) Čıžek, J. On the correlation problem in atomic and molecular systems. Calculation of wavefunction components in Ursell-type expansion using quantum-field theoretical methods. *The Journal of Chemical Physics* **1966**, *45*, 4256–4266.

(118) Čıžek, J. On the use of the cluster expansion and the technique of diagrams in calculations of correlation effects in atoms and molecules. *Advances in chemical physics* **1969**, 35–89.

(119) Nesbet, R. Configuration interaction in orbital theories. *Proceedings of the Royal Society of London. Series A. Mathematical and Physical Sciences* **1955**, *230*, 312–321.

(120) Møller, C.; Plesset, M. S. Note on an approximation treatment for many-electron systems. *Physical review* **1934**, *46*, 618.

(121) DAVIDSOrq, E. Theiterative calculation ofafew ofthe lowest eigenvalues and corresponding eigenvectors oflarge real-symmetric matrices. *J. Comput. Phys* **1975**, *17*, 87–94.

(122) Cederbaum, L. S.; Domcke, W.; Schirmer, J. Many-body theory of core holes. *Physical Review A* **1980**, *22*, 206.

(123) Coriani, S.; Koch, H. Communication: X-ray absorption spectra and core-ionization potentials within a core-valence separated coupled cluster framework. *The Journal of Chemical Physics* **2015**, *143*, 181103.

(124) Fransson, T.; Coriani, S.; Christiansen, O.; Norman, P. Carbon X-ray absorption spectra of fluoroethenes and acetone: A study at the coupled cluster, density functional, and static-exchange levels of theory. *The Journal of Chemical Physics* **2013**, *138*, 124311.

(125) Norman, P.; Dreuw, A. Simulating X-ray spectroscopies and calculating core-excited states of molecules. *Chemical reviews* **2018**, *118*, 7208–7248.

(126) Vidal, M. L.; Feng, X.; Epifanovsky, E.; Krylov, A. I.; Coriani, S. New and efficient equation-of-motion coupled-cluster framework for core-excited and core-ionized states. *Journal of Chemical Theory and Computation* **2019**, *15*, 3117–3133.

(127) Nanda, K. D.; Vidal, M. L.; Faber, R.; Coriani, S.; Krylov, A. I. How to stay out of trouble in RIXS calculations within equation-of-motion coupled-cluster damped response theory? Safe hitchhiking in the excitation manifold by means of core–valence separation. *Physical Chemistry Chemical Physics* **2020**, *22*, 2629–2641.

(128) Halbert, L.; Vidal, M. L.; Shee, A.; Coriani, S.; Severo Pereira Gomes, A. Relativistic EOM-CCSD for Core-Excited and Core-Ionized State Energies Based on the Four-Component Dirac–Coulomb (- Gaunt) Hamiltonian. *Journal of Chemical Theory and Computation* **2021**, *17*, 3583–3598.

(129) Stener, M.; Fronzoni, G.; de Simone, M. d. Time dependent density functional theory of core electrons excitations. *Chemical physics letters* **2003**, *373*, 115–123.

(130) Lopata, K.; Van Kuiken, B. E.; Khalil, M.; Govind, N. Linear-response and real-time time-dependent density functional theory studies of core-level near-edge x-ray absorption. *Journal of chemical theory and computation* **2012**, *8*, 3284–3292.

(131) Besley, N. A.; Asmuruf, F. A. Time-dependent density functional theory calculations of the spectroscopy of core electrons. *Physical Chemistry Chemical Physics* **2010**, *12*, 12024–12039.

(132) Rezac, J.; Hobza, P. Describing noncovalent interactions beyond the common approximations: how accurate is the “gold standard,” CCSD (T) at the complete basis set limit? *Journal of chemical theory and computation* **2013**, *9*, 2151–2155.

(133) Bertels, L. W.; Lee, J.; Head-Gordon, M. Polishing the gold standard: The role of orbital choice in CCSD (T) vibrational frequency prediction. *Journal of chemical theory and computation* **2021**, *17*, 742–755.

(134) Pototschnig, J. V.; Papadopoulos, A.; Lyakh, D. I.; Repisky, M.; Halbert, L.; Severo Pereira Gomes, A.; Jensen, H. J. A.; Visscher, L. Implementation of relativistic coupled cluster theory for massively parallel GPU-accelerated computing architectures. *Journal of chemical theory and computation* **2021**, *17*, 5509–5529.

(135) Engel, E.; Dreizler, R. M. Density functional theory. *Theoretical and mathematical physics* **2011**, 11–56.

(136) Toulouse, J. Review of approximations for the exchange-correlation energy in density-functional theory. *arXiv preprint arXiv:2103.02645* **2021**.

(137) Sholl, D. S.; Steckel, J. A., *Density functional theory: a practical introduction*; John Wiley & Sons: 2022.

(138) Pribram-Jones, A.; Gross, D. A.; Burke, K. DFT: A theory full of holes? *Annual review of physical chemistry* **2015**, *66*, 283–304.

(139) Mardirossian, N.; Head-Gordon, M. Thirty years of density functional theory in computational chemistry: an overview and extensive assessment of 200 density functionals. *Molecular Physics* **2017**, *115*, 2315–2372.

(140) Teale, A. M.; Helgaker, T.; Savin, A.; Adamo, C.; Aradi, B.; Arbuznikov, A. V.; Ayers, P. W.; Baerends, E. J.; Barone, V.; Calaminici, P., et al. DFT exchange: sharing perspectives on the workhorse of quantum chemistry and materials science. *Physical chemistry chemical physics* **2022**, *24*, 28700–28781.

(141) Thomas, L. H. In *Mathematical proceedings of the Cambridge philosophical society*, 1927; Vol. 23, pp 542–548.

(142) Dirac, P. A. In *Mathematical proceedings of the Cambridge philosophical society*, 1930; Vol. 26, pp 376–385.

(143) Hohenberg, P.; Kohn, W. Inhomogeneous electron gas. *Physical review* **1964**, *136*, B864.

(144) Kohn, W.; Sham, L. J. Self-consistent equations including exchange and correlation effects. *Physical review* **1965**, *140*, A1133.

(145) Levy, M. Universal variational functionals of electron densities, first-order density matrices, and natural spin-orbitals and solution of the v-representability problem. *Proceedings of the National Academy of Sciences* **1979**, *76*, 6062–6065.

(146) Levy, M. Electron densities in search of Hamiltonians. *Physical Review A* **1982**, *26*, 1200.

(147) Lieb, E. H. Density functionals for Coulomb systems. *Inequalities: Selecta of Elliott H. Lieb* **2002**, 269–303.

(148) Seidl, A.; Görling, A.; Vogl, P.; Majewski, J. A.; Levy, M. Generalized Kohn-Sham schemes and the band-gap problem. *Physical Review B* **1996**, *53*, 3764.

(149) Gavroglu, K.; Simões, A., *Neither physics nor chemistry: A history of quantum chemistry*; MIT Press: 2011.

(150) Hoffmann, R.; Malrieu, J.-P. Simulation vs. understanding: a tension, in quantum chemistry and beyond. Part A. Stage setting. *Angewandte Chemie International Edition* **2020**, *59*, 12590–12610.

(151) Ochsenfeld, C.; Kussmann, J.; Lambrecht, D. S. Linear-scaling methods in quantum chemistry. *Reviews in computational chemistry* **2007**, *23*, 1.

(152) Olsen, J. M.; Aidas, K.; Kongsted, J. Excited states in solution through polarizable embedding. *Journal of Chemical Theory and Computation* **2010**, *6*, 3721–3734.

(153) Lin, H.; Truhlar, D. G. QM/MM: what have we learned, where are we, and where do we go from here? *Theoretical Chemistry Accounts* **2007**, *117*, 185–199.

(154) Mennucci, B. Polarizable continuum model. *Wiley Interdisciplinary Reviews: Computational Molecular Science* **2012**, *2*, 386–404.

(155) Tomasi, J.; Mennucci, B.; Cammi, R. Quantum mechanical continuum solvation models. *Chemical reviews* **2005**, *105*, 2999–3094.

(156) Gomes, A. S. P.; Jacob, C. R. Quantum-chemical embedding methods for treating local electronic excitations in complex chemical systems. *Annual Reports Section" C"(Physical Chemistry)* **2012**, *108*, 222–277.

(157) Sun, Q.; Chan, G. K.-L. Quantum embedding theories. *Accounts of chemical research* **2016**, *49*, 2705–2712.

(158) Jones, L. O.; Mosquera, M. A.; Schatz, G. C.; Ratner, M. A. Embedding methods for quantum chemistry: Applications from materials to life sciences. *Journal of the American Chemical Society* **2020**, *142*, 3281–3295.

(159) Ma, H.; Sheng, N.; Govoni, M.; Galli, G. Quantum embedding theory for strongly correlated states in materials. *Journal of Chemical Theory and Computation* **2021**, *17*, 2116–2125.

(160) Szabó, Z.; Toraishi, T.; Vallet, V.; Grenthe, I. Solution coordination chemistry of actinides: Thermodynamics, structure and reaction mechanisms. *Coordination Chemistry Reviews* **2006**, *250*, 784–815.

(161) Vallet, V.; Macak, P.; Wahlgren, U.; Grenthe, I. Actinide chemistry in solution, quantum chemical methods and models. *Theoretical Chemistry Accounts* **2006**, *115*, 145–160.

(162) Morss, L. R.; Edelstein, N. M.; Fuger, J.; Katz, J., *The Chemistry of the Actinide and Transactinide Elements (Volumes 1-5)*; Springer: 2006.

(163) Knope, K. E.; Soderholm, L. Solution and solid-state structural chemistry of actinide hydrates and their hydrolysis and condensation products. *Chemical Reviews* **2013**, *113*, 944–994.

(164) Vukovic, S.; Hay, B. P.; Bryantsev, V. S. Predicting stability constants for uranyl complexes using density functional theory. *Inorganic chemistry* **2015**, *54*, 3995–4001.

(165) Dolg, M., *Computational methods in lanthanide and actinide chemistry*; John Wiley & Sons: 2015.

(166) Vallet, V.; Wahlgren, U.; Schimmelpfennig, B.; Szabó, Z.; Grenthe, I. The mechanism for water exchange in [UO2 (H2O) 5] 2+ and [UO2 (oxalate) 2 (H2O)] 2-, as studied by quantum chemical methods. *Journal of the American Chemical Society* **2001**, *123*, 11999–12008.

(167) Gomes, A. S. P.; Jacob, C. R.; Réal, F.; Visscher, L.; Vallet, V. Towards systematically improvable models for actinides in condensed phase: the electronic spectrum of uranyl in Cs 2 UO 2 Cl 4 as a test case. *Physical Chemistry Chemical Physics* **2013**, *15*, 15153–15162.

(168) Réal, F.; Vallet, V.; Marian, C.; Wahlgren, U. Theoretical investigation of the energies and geometries of photoexcited uranyl (VI) ion: A comparison between wave-function theory and density functional theory. *The Journal of chemical physics* **2007**, *127*, 214302.

(169) Vallet, V.; Privalov, T.; Wahlgren, U.; Grenthe, I. The mechanism of water exchange in AmO2 (H2O) 52+ and in the isoelectronic UO2 (H2O) 5+ and NpO2 (H2O) 52+ complexes as studied by quantum chemical methods. *Journal of the American Chemical Society* **2004**, *126*, 7766–7767.

(170) Réal, F.; Trumm, M.; Vallet, V.; Schimmelpfennig, B.; Masella, M.; Flament, J.-P. Quantum chemical and molecular dynamics study of the coordination of Th (IV) in aqueous solvent. *The Journal of Physical Chemistry B* **2010**, *114*, 15913–15924.

(171) Réal, F.; Trumm, M.; Schimmelpfennig, B.; Masella, M.; Vallet, V. Further insights in the ability of classical nonadditive potentials to model actinide ion–water interactions. *Journal of Computational Chemistry* **2013**, *34*, 707–719.

(172) Marsac, R.; Réal, F.; Banik, N. L.; Pédrot, M.; Pourret, O.; Vallet, V. Aqueous chemistry of Ce (IV): estimations using actinide analogues. *Dalton Transactions* **2017**, *46*, 13553–13561.

(173) Wang, D.; van Gunsteren, W. F.; Chai, Z. Recent advances in computational actinoid chemistry. *Chemical Society Reviews* **2012**, *41*, 5836–5865.

(174) Ikeda-Ohno, A.; Hennig, C.; Rossberg, A.; Funke, H.; Scheinost, A. C.; Bernhard, G.; Yaita, T. Electrochemical and complexation behavior of neptunium in aqueous perchlorate and nitrate solutions. *Inorganic chemistry* **2008**, *47*, 8294–8305.

(175) Minasian, S. G.; Krinsky, J. L.; Arnold, J. Evaluating f-element bonding from structure and thermodynamics. *Chemistry–A European Journal* **2011**, *17*, 12234–12245.

(176) Cossi, M.; Barone, V.; Cammi, R.; Tomasi, J. Ab initio study of solvated molecules: a new implementation of the polarizable continuum model. *Chemical Physics Letters* **1996**, *255*, 327–335.

(177) Klamt, A. Conductor-like screening model for real solvents: a new approach to the quantitative calculation of solvation phenomena. *The Journal of Physical Chemistry* **1995**, *99*, 2224–2235.

(178) Pye, C. C.; Ziegler, T. An implementation of the conductor-like screening model of solvation within the Amsterdam density functional package. *Theoretical Chemistry Accounts* **1999**, *101*, 396–408.

(179) Su, J.; Zhang, K.; Schwarz, W. E.; Li, J. Uranyl-glycine-water complexes in solution: Comprehensive computational modeling of coordination geometries, stabilization energies, and luminescence properties. *Inorganic Chemistry* **2011**, *50*, 2082–2093.

(180) Field, M. J.; Bash, P. A.; Karplus, M. A combined quantum mechanical and molecular mechanical potential for molecular dynamics simulations. *Journal of computational chemistry* **1990**, *11*, 700–733.

(181) Warshel, A.; Levitt, M. Theoretical studies of enzymic reactions: dielectric, electrostatic and steric stabilization of the carbonium ion in the reaction of lysozyme. *Journal of molecular biology* **1976**, *103*, 227–249.

(182) Wang, Y.; Dolg, M. Pseudopotential study of the ground and excited states of Yb2. *Theoretical Chemistry Accounts* **1998**, *100*, 124–133.

(183) Kirsch, T.; Olsen, J. M. H.; Bolnykh, V.; Meloni, S.; Ippoliti, E.; Rothlisberger, U.; Cascella, M.; Gauss, J. Wavefunction-based electrostatic-embedding QM/MM using CFOUR through MiMiC. *Journal of Chemical Theory and Computation* **2021**, *18*, 13–24.

(184) Stillinger, F. H.; David, C. W. Polarization model for water and its ionic dissociation products. *The Journal of Chemical Physics* **1978**, *69*, 1473–1484.

(185) Infante, I.; Van Stralen, B.; Visscher, L. A QM/MM Study on the Aqueous Solvation of the Tetrahydroxouranylate [UO2 (OH) 4] 2- Complex ion. *Journal of computational chemistry* **2006**, *27*, 1156–1162.

(186) Infante, I.; Visscher, L. QM/MM study of aqueous solvation of the uranyl fluoride [UO2F] complex. *Journal of computational chemistry* **2004**, *25*, 386–392.

(187) Liu, J.-B.; Chen, G. P.; Huang, W.; Clark, D. L.; Schwarz, W. E.; Li, J. Bonding trends across the series of tricarbonato-actinyl anions [(AnO 2)(CO 3) 3] 4-(An= U–Cm): the plutonium turn. *Dalton Transactions* **2017**, *46*, 2542–2550.

(188) Odoh, S. O.; Walker, S. M.; Meier, M.; Stetefeld, J.; Schreckenbach, G. QM and QM/MM Studies of Uranyl Fluorides in the Gas and Aqueous Phases and in the Hydrophobic Cavities of Tetrabrachion. *Inorganic Chemistry* **2011**, *50*, 3141–3152.

(189) Lan, J.-H.; Shi, W.-Q.; Yuan, L.-Y.; Li, J.; Zhao, Y.-L.; Chai, Z.-F. Recent advances in computational modeling and simulations on the An (III)/Ln (III) separation process. *Coordination Chemistry Reviews* **2012**, *256*, 1406–1417.

(190) Silva, R.; Nitsche, H. Actinide environmental chemistry. *Radiochimca Acta* **1995**, *70*, 377–396.

(191) Choppin, G. R.; Jensen, M. P. Actinides in solution: complexation and kinetics. *The chemistry of the actinide and transactinide elements* **2006**, 2524–2621.

(192) Maher, K.; Bargar, J. R.; Brown Jr, G. E. Environmental speciation of actinides. *Inorganic chemistry* **2013**, *52*, 3510–3532.

(193) Alam, M. S.; Cheng, T. Uranium release from sediment to groundwater: influence of water chemistry and insights into release mechanisms. *Journal of contaminant hydrology* **2014**, *164*, 72–87.

(194) Vengosh, A.; Coyte, R. M.; Podgorski, J.; Johnson, T. M. A critical review on the occurrence and distribution of the uranium-and thorium-decay nuclides and their effect on the quality of groundwater. *Science of the Total Environment* **2022**, *808*, 151914.

(195) Söderlind, P.; Kotliar, G.; Haule, K.; Oppeneer, P. M.; Guillaumont, D. Computational modeling of actinide materials and complexes. *MRS bulletin* **2010**, *35*, 883–888.

(196) Caciuffo, R.; Lander, G. H. X-ray synchrotron radiation studies of actinide materials. *Journal of Synchrotron Radiation* **2021**, *28*, 1692–1708.

(197) Shi, W.-Q.; Yuan, L.-Y.; Li, Z.-J.; Lan, J.-H.; Zhao, Y.-L.; Chai, Z.-F. Nanomaterials and nanotechnologies in nuclear energy chemistry. *Radiochimica Acta* **2012**, *100*, 727–736.

(198) Geckeis, H.; Rabung, T. Actinide geochemistry: From the molecular level to the real system. *Journal of contaminant hydrology* **2008**, *102*, 187–195.

(199) Rothe, J.; Altmaier, M.; Dagan, R.; Dardenne, K.; Fellhauer, D.; Gaona, X.; González-Robles Corrales, E.; Herm, M.; Kvashnina, K. O.; Metz, V., et al. Fifteen years of radionuclide research at the KIT synchrotron source in the context of the nuclear waste disposal safety case. *Geosciences* **2019**, *9*, 91.

(200) Scheinost, A. C.; Claussner, J.; Exner, J.; Feig, M.; Findeisen, S.; Hennig, C.; Kvashnina, K. O.; Naudet, D.; Prieur, D.; Rossberg, A., et al. ROBL-II at ESRF: a synchrotron toolbox for actinide research. *Journal of Synchrotron Radiation* **2021**, *28*, 333–349.

(201) Fillaux, C.; Den Auwer, C.; Guillaumont, D.; Shuh, D. K.; Tyliszczak, T. Investigation of actinide compounds by coupling X-ray absorption spectroscopy and quantum chemistry. *Journal of alloys and compounds* **2007**, *444*, 443–446.

(202) Tobin, J.; Sokaras, D. Application of FEFF analyses to actinide 5f systems. *Journal of Vacuum Science & Technology A: Vacuum, Surfaces, and Films* **2020**, *38*, 036001.

(203) Tobin, J.; Ramanantoanina, H.; Daul, C.; Roussel, P.; Yu, S.-W.; Nowak, S.; Alonso-Mori, R.; Kroll, T.; Nordlund, D.; Weng, T.-C., et al. Unoccupied electronic structure of actinide dioxides. *Physical Review B* **2022**, *105*, 125129.

(204) Butorin, S. M. 3d-4f resonant inelastic X-ray scattering of actinide dioxides: Crystal-field multiplet description. *Inorganic Chemistry* **2020**, *59*, 16251–16264.

(205) Cortona, P. Self-consistently determined properties of solids without band-structure calculations. *Physical Review B* **1991**, *44*, 8454.

(206) Wesolowski, T. A.; Warshel, A. Frozen density functional approach for ab initio calculations of solvated molecules. *The Journal of Physical Chemistry* **1993**, *97*, 8050–8053.

(207) Wesolowski, T. A.; Shedge, S.; Zhou, X. Frozen-density embedding strategy for multilevel simulations of electronic structure. *Chemical reviews* **2015**, *115*, 5891–5928.

(208) Elliott, P.; Cohen, M. H.; Wasserman, A.; Burke, K. Density functional partition theory with fractional occupations. *Journal of chemical theory and computation* **2009**, *5*, 827–833.

(209) Huang, C.; Carter, E. A. Potential-functional embedding theory for molecules and materials. *The Journal of chemical physics* **2011**, *135*, 194104.

(210) De Santis, M.; Vallet, V.; Gomes, A. S. P. Environment effects on X-ray absorption spectra with quantum embedded real-time Time-dependent density functional theory approaches. *Frontiers in Chemistry* **2022**, *10*.

(211) De Santis, M.; Sorbelli, D.; Vallet, V.; Gomes, A. S. P.; Storchi, L.; Belpassi, L. Frozen-Density Embedding for Including Environmental Effects in the Dirac-Kohn–Sham Theory: An Implementation Based on Density Fitting and Prototyping Techniques. *Journal of Chemical Theory and Computation* **2022**, *18*, 5992–6009.

(212) Jacob, C. R.; Neugebauer, J.; Visscher, L. A flexible implementation of frozen-density embedding for use in multilevel simulations. *Journal of computational chemistry* **2008**, *29*, 1011–1018.

(213) Jacob, C. R.; Neugebauer, J.; Jensen, L.; Visscher, L. Comparison of frozen-density embedding and discrete reaction field solvent models for molecular properties. *Physical Chemistry Chemical Physics* **2006**, *8*, 2349–2359.

(214) Te Velde, G. t.; Bickelhaupt, F. M.; Baerends, E. J.; Fonseca Guerra, C.; van Gisbergen, S. J.; Snijders, J. G.; Ziegler, T. Chemistry with ADF. *Journal of Computational Chemistry* **2001**, *22*, 931–967.

(215) Jacob, C. R.; Beyhan, S. M.; Bulo, R. E.; Gomes, A. S. P.; Götz, A. W.; Kiewisch, K.; Sikkema, J.; Visscher, L. PyADF—A scripting framework for multiscale quantum chemistry. *Journal of computational chemistry* **2011**, *32*, 2328–2338.

(216) Perdew, J. P.; Schmidt, K. In *AIP Conference Proceedings*, 2001; Vol. 577, pp 1–20.

(217) Su, N. Q.; Xu, X. Development of new density functional approximations. *Annual Review of Physical Chemistry* **2017**, *68*, 155–182.

(218) Perdew, J. P.; Burke, K.; Wang, Y. Generalized gradient approximation for the exchange-correlation hole of a many-electron system. *Physical review B* **1996**, *54*, 16533.

(219) Levy, M. Density-functional exchange correlation through coordinate scaling in adiabatic connection and correlation hole. *Physical Review A* **1991**, *43*, 4637.

(220) Yang, W. Generalized adiabatic connection in density functional theory. *The Journal of chemical physics* **1998**, *109*, 10107–10110.

(221) Yanai, T.; Nakajima, T.; Ishikawa, Y.; Hirao, K. A new computational scheme for the Dirac–Hartree–Fock method employing an efficient integral algorithm. *The Journal of Chemical Physics* **2001**, *114*, 6526–6538.

(222) Tecmer, P.; Bast, R.; Ruud, K.; Visscher, L. Charge-Transfer Excitations in Uranyl Tetrachloride ([UO2Cl4] 2–): How Reliable are Electronic Spectra from Relativistic Time-Dependent Density Functional Theory? *The Journal of Physical Chemistry A* **2012**, *116*, 7397–7404.

(223) Tecmer, P.; Gomes, A. S. P.; Ekström, U.; Visscher, L. Electronic spectroscopy of UO 2 2+, NUO+ and NUN: an evaluation of time-dependent density functional theory for actinides. *Physical Chemistry Chemical Physics* **2011**, *13*, 6249–6259.

(224) Tecmer, P.; Govind, N.; Kowalski, K.; De Jong, W. A.; Visscher, L. Reliable modeling of the electronic spectra of realistic uranium complexes. *The Journal of Chemical Physics* **2013**, *139*, 034301.

(225) Konecny, L.; Vicha, J.; Komorovsky, S.; Ruud, K.; Repisky, M. Accurate X-ray absorption spectra near L-and M-edges from relativistic four-component damped response time-dependent density functional theory. *Inorganic chemistry* **2021**, *61*, 830–846.

(226) Konecny, L.; Komorovsky, S.; Vicha, J.; Ruud, K.; Repisky, M. Exact two-component TDDFT with simple two-electron picture-change corrections: X-ray absorption spectra near L-and M-edges of four-component quality at two-component cost. *The Journal of Physical Chemistry A* **2023**, *127*, 1360–1376.

(227) Burke, K.; Perdew, J. P.; Wang, Y. Derivation of a generalized gradient approximation: The PW91 density functional. *Electronic Density Functional Theory: recent progress and new directions* **1998**, 81–111.

(228) Lembarki, A.; Chermette, H. Obtaining a gradient-corrected kinetic-energy functional from the Perdew-Wang exchange functional. *Physical Review A* **1994**, *50*, 5328.

(229) Ernzerhof, M.; Scuseria, G. E. Assessment of the Perdew–Burke–Ernzerhof exchange-correlation functional. *The Journal of chemical physics* **1999**, *110*, 5029–5036.

(230) Jacob, C. R.; Visscher, L. A subsystem density-functional theory approach for the quantum chemical treatment of proteins. *The Journal of chemical physics* **2008**, *128*, 04B612.

(231) Ceperley, D. M.; Alder, B. J. Ground state of the electron gas by a stochastic method. *Physical review letters* **1980**, *45*, 566.

(232) Gunnarsson, O.; Lundqvist, B. I. Exchange and correlation in atoms, molecules, and solids by the spin-density-functional formalism. *Physical Review B* **1976**, *13*, 4274.

(233) Vosko, S. H.; Wilk, L.; Nusair, M. Accurate spin-dependent electron liquid correlation energies for local spin density calculations: a critical analysis. *Canadian Journal of physics* **1980**, *58*, 1200–1211.

(234) Perdew, J. P.; Wang, Y. Accurate and simple analytic representation of the electron-gas correlation energy. *Physical review B* **1992**, *45*, 13244.

(235) Tao, J.; Perdew, J. P.; Staroverov, V. N.; Scuseria, G. E. Climbing the density functional ladder: Nonempirical meta–generalized gradient approximation designed for molecules and solids. *Physical review letters* **2003**, *91*, 146401.

(236) Sun, J.; Ruzsinszky, A.; Perdew, J. P. Strongly constrained and appropriately normed semilocal density functional. *Physical review letters* **2015**, *115*, 036402.

(237) Mori-Sánchez, P.; Cohen, A. J.; Yang, W. Many-electron self-interaction error in approximate density functionals. *The Journal of chemical physics* **2006**, *125*, 201102.

(238) Li, C.; Yang, W. On the piecewise convex or concave nature of ground state energy as a function of fractional number of electrons for approximate density functionals. *The Journal of Chemical Physics* **2017**, *146*, 074107.

(239) Zhang, Y.; Yang, W. A challenge for density functionals: Self-interaction error increases for systems with a noninteger number of electrons. *The Journal of chemical physics* **1998**, *109*, 2604–2608.

(240) Gräfenstein, J.; Kraka, E.; Cremer, D. The impact of the self-interaction error on the density functional theory description of dissociating radical cations: Ionic and covalent dissociation limits. *The Journal of chemical physics* **2004**, *120*, 524–539.

(241) Ruzsinszky, A.; Perdew, J. P.; Csonka, G. I.; Vydrov, O. A.; Scuseria, G. E. Spurious fractional charge on dissociated atoms: Pervasive and resilient self-interaction error of common density functionals. *The Journal of chemical physics* **2006**, *125*, 194112.

(242) Vydrov, O. A.; Scuseria, G. E.; Perdew, J. P. Tests of functionals for systems with fractional electron number. *The Journal of chemical physics* **2007**, *126*, 154109.

(243) Cohen, A. J.; Mori-Sánchez, P.; Yang, W. Insights into current limitations of density functional theory. *Science* **2008**, *321*, 792–794.

(244) Cohen, A. J.; Mori-Sánchez, P.; Yang, W. Challenges for density functional theory. *Chemical reviews* **2012**, *112*, 289–320.

(245) Becke, A. D. Density-functional thermochemistry. III. The role of exact exchange. *The Journal of chemical physics* **1993**, *98*, 5648–5652.

(246) Becke, A. D. Density-functional exchange-energy approximation with correct asymptotic behavior. *Physical review A* **1988**, *38*, 3098.

(247) Lee, C.; Yang, W.; Parr, R. G. Development of the Colle-Salvetti correlation-energy formula into a functional of the electron density. *Physical review B* **1988**, *37*, 785.

(248) Iikura, H.; Tsuneda, T.; Yanai, T.; Hirao, K. A long-range correction scheme for generalized-gradient-approximation exchange functionals. *The Journal of Chemical Physics* **2001**, *115*, 3540–3544.

(249) Tsuneda, T.; Hirao, K. Long-range correction for density functional theory. *Wiley Interdisciplinary Reviews: Computational Molecular Science* **2014**, *4*, 375–390.

(250) Grimme, S. Semiempirical hybrid density functional with perturbative second-order correlation. *The Journal of chemical physics* **2006**, *124*, 034108.

(251) Goerigk, L.; Grimme, S. Double-hybrid density functionals. *Wiley Interdisciplinary Reviews: Computational Molecular Science* **2014**, *4*, 576–600.

Chapter 2

Relativistic Quantum Chemistry

"... in what way the electron spin has to be taken into account in the present theory is yet unknown."

— Erwin Schrödinger in *"An undulatory theory of the mechanics of atoms and molecules."*, 1926.

The formalism presented in the preceding chapter does not account for the possibility of electrons in the vicinity of nuclei having high velocities that could give rise to relativistic effects.

Relativistic effects are present throughout the periodic table [252–254], but their contribution is generally small for elements with low atomic numbers, making a non-relativistic framework commonly suitable for the determination of observables. However, for heavy elements, relativistic effects play a significant role in determining their properties [254–256]. As illustrated by Pyykko [252, 257], the relevance of these effects across the periodic table can be qualitatively seen by considering the velocity of a $1s$ electron within the Bohr model:

$$v_{1s} = c\alpha Z \tag{2.1}$$

where α denotes the fine structure constant (0.0073).

Even in such a crude approximation, relativistic effects are of great extent in systems like the ones investigated here, for instance in the case of uranium ($Z = 92$), the value for v_{1s} is 91.99 times greater than the one for hydrogen.

In the relativistic regime, core orbitals (such as s and p) contract, while the outermost valence ones (such as d and f) become more diffuse, resulting in the so-called "scalar relativistic effects" [256, 258, 259]. Another class of relativistic effects arises from magnetic interactions, i.e., the mechanism of spin-orbit coupling, which lifts the degeneracies of certain energy levels (e.g. p orbitals into $p_{1/2}$ and $p_{3/2}$ ones) [254, 258, 260]. However, as the reader may have noticed, the previous framework added spin to the Schrödinger equation in an *ad hoc* manner.

In this chapter, we introduce the relativistic theory of the electron. For further information on the implications of relativistic effects on physicochemical properties, we recommend consulting the works of Pyykkö [252–255, 257, 261] and Autschbach [256, 259]. For a primer introduction into the mathematical formalism of this subject and the usually adopted approximations in electronic structure theory, we suggest reading the works of Saue [260], Dyall [262] and Liu [263–267]. For a more in-depth exploration of the relativistic quantum chemistry realm, we highly recommend the textbooks of Dyall and Fægri Jr [268] and Reiher and Wolf [269].

In the following, for the sake of simplicity, we avoid any reference to coordinate and temporal coordinates and write $\psi(\mathbf{r};t)$ as ψ.

2.1 Dirac equation for a free-moving particle

When incorporating Einstein's theory of relativity into the quantum mechanical treatment of microscopic particles, one may seek an equation of motion that contains relativistic velocities and is invariant under Lorentz transformations.

The simplest scenario to consider is that of a free-moving particle, such as an electron, moving with relativistic velocities. Therefore, we can proceed by quantizing the energy-momentum relation for a free particle with rest mass m_e and momentum of magnitude p:

$$E = \sqrt{p^2c^2 + m_e^2c^4} \tag{2.2}$$

which, by employing the correspondence principle, yields the Klein-Gordon equation [270, 271],

$$-\hbar^2 \frac{\partial^2}{\partial t^2}\psi = \left(-\hbar^2 c^2 \nabla^2 + m_e^2 c^4\right)\psi \tag{2.3}$$

However, applying the complex conjugate of ψ to both sides of Equation 2.3 leads to non-positive definite Klein-Gordon density distribution values. As discussed in the textbook by Reiher and Wolf, this renders the equation unsuitable for investigating electrons and necessitates further treatment. Moreover, Feynman [272, 273] proposed a reformulation of the Klein-Gordon equation to make it suitable for investigating particles that follow Bose-Einstein statistics, such as neutral mesons.

In one of the most important works of modern science, Dirac [274] proposed that Equation 2.2 could be written as the following linear ansatz:

$$E = \alpha p c + \beta m_e c^2 \tag{2.4}$$

The corresponding equation of motion, the Dirac equation, reads

$$i\hbar \frac{\partial}{\partial t}\psi = \left(c\boldsymbol{\alpha} \cdot \hat{\boldsymbol{p}} + \beta m_e c^2\right)\psi \tag{2.5}$$

where α and β denote the so-called Dirac matrices:

$$\boldsymbol{\alpha} = \begin{pmatrix} 0 & \boldsymbol{\sigma} \\ \boldsymbol{\sigma} & 0 \end{pmatrix} ; \beta = \begin{pmatrix} \mathbb{1}_2 & 0 \\ 0 & -\mathbb{1}_2 \end{pmatrix} \tag{2.6}$$

As Dirac noted, α is a dynamical variable that describes the *internal motions of the electron*. Consequently, the theory naturally embeds spin, and there is no need for further attempts to include it. The components of this term read in terms of the Pauli spin matrices,

$$\sigma_x = \begin{pmatrix} 0 & 1 \\ 1 & 0 \end{pmatrix} ; \sigma_y = \begin{pmatrix} 0 & -i \\ i & 0 \end{pmatrix} ; \sigma_z = \begin{pmatrix} 1 & 0 \\ 0 & -1 \end{pmatrix} \tag{2.7}$$

The 4×4 Dirac matrices require that solutions of the Dirac equation have a consistent form. Therefore, the solutions to the Dirac equation can be described by 4-*spinors* or 4-*component* wave functions, yielding:

$$\psi = \begin{pmatrix} \psi_1 \\ \psi_2 \\ \psi_3 \\ \psi_4 \end{pmatrix} = \begin{pmatrix} \psi^L \\ \psi^S \end{pmatrix} \tag{2.8}$$

where we have used that the β matrix divides the solutions into two subsets: *large-* and *small-*components, related by

$$\psi^L = \left(\frac{c\boldsymbol{\sigma} \cdot \hat{\boldsymbol{p}}}{E - m_e c^2}\right)\psi^S \ ; \ \psi^S = \left(\frac{c\boldsymbol{\sigma} \cdot \hat{\boldsymbol{p}}}{E + m_e c^2}\right)\psi^L \tag{2.9}$$

Solving the set of four coupled equations gives us the following expression for energy:

$$E = \pm\sqrt{c^2 p^2 + m_e^2 c^4} \tag{2.10}$$

Notably, Dirac's theory predicts that electrons can occupy energy states that are either positive or negative and separated by $\pm 2mc^2$. While Dirac did not find this result particularly satisfying at first, he used it to develop his *hole theory* [275], which predicted the existence of the charge conjugate of an electron state, establishing the Dirac sea of negative continuum states. This particle, known as the *antielectron* or *positron*, was experimentally observed for the first time by Anderson [276] a few years later.

2.2 Dirac equation in the presence of external fields

We can apply the *principle of minimal electromagnetic coupling* [277] to consider a particle subject to external electromagnetic fields, such as those produced by stationary nuclei. This principle involves making the following minimal substitutions

$$p \rightarrow p - eA, \qquad E \rightarrow E - e\phi, \tag{2.11}$$

where e is the fundamental charge, A is the potential vector, and ϕ is the potential scalar. The resulting equation of motion is:

$$i\hbar\frac{\partial}{\partial t}\psi = \left(c\boldsymbol{\alpha}\cdot\hat{\boldsymbol{\pi}} + \beta m_e c^2 - e\phi\right)\psi, \tag{2.12}$$

where the mechanical-momentum operator is given by $\hat{\boldsymbol{\pi}} \equiv \hat{\boldsymbol{p}} + e\boldsymbol{A}$.

In multi-electron atoms, electrons are subjected to scalar and vector potentials from other electrons, generating the so-called *spin-orbit interaction*, recast into theory via the two-electron operator $\hat{g}(i,j)$. As discussed by Saue [260], in the non-relativistic case, the full two-electron operator reduces to the electrostatic case and reads as a *charge-charge interaction* given by the instantaneous Coulomb term in Equation 1.4. On the other hand, 4-component calculations that truncate the two-electron operator at this term yield the *Dirac-Coulomb Hamiltonian*:

$$\hat{h}^{DC} = \hat{h}^{Dirac}(i) + \hat{g}^{Coulomb}(i,j) = c\boldsymbol{\alpha}\cdot\hat{\boldsymbol{\pi}} + \beta m_e c^2 - e\phi + \frac{1}{r_{ij}} \tag{2.13}$$

It should be noted that in this equation, we are only including the *spin-same orbit interaction* (SSO), which arises from the interaction between electrons and nuclei. Furthermore, in Section 6, we refer to this Hamiltonian as the ^4DC Hamiltonian.

Electrodynamics must come into play for a more consistent treatment of the electron-electron interaction in the relativistic case, and the use of the Breit operator becomes more appropriate [260, 267], yielding:

$$\hat{g}^{Breit}(i,j) = \hat{g}^{Gaunt}(i,j) + \hat{g}^{Gauge}(i,j) = -\frac{c\boldsymbol{\alpha}_i\cdot c\boldsymbol{\alpha}_j}{2c^2 r_{ij}} - \frac{\left(c\boldsymbol{\alpha}_i\cdot\mathbf{r}_{ij}\right)\left(c\boldsymbol{\alpha}_j\cdot\mathbf{r}_{ij}\right)}{2c^2 r_{ij}^3} \tag{2.14}$$

where the first term, the so-called Gaunt term, computes current-current interactions and thus is responsible for the spin-other-orbit interaction (SOO) [260]. When included in 4-component simulations, it generates the *Dirac-Coulomb-Gaunt Hamiltonian* (^4DCG). Furthermore, the second term in Equation 2.14 is a scalar gauge term. While we did not include it in our simulations, a thorough discussion is provided in the previous references.

2.3 Electronic structure calculations

In the context of electronic structure theory, the work of Kim [278] is widely acknowledged as the first attempt to propose a relativistic version of the self-consistent-field Hartree-Fock method discussed in Chapter 1.2. Since then, several formulations of the Dirac-Hartree-Fock method (DHF) have been proposed in the literature [221, 279–282]. Likewise, various relativistic formulations for the Kohn-Sham method presented in Chapter 1.5, also known as the Dirac-Kohn-Sham method (DKS), were proposed over the years [281, 283, 284].

This thesis primarily utilized `DIRAC`, a relativistic *ab initio* quantum chemistry program, which employs a double group symmetry contraction scheme and quaternion algebra in the framework proposed by Saue and Jensen [281]. In the interest of concision, we refer the reader to the original work for a detailed discussion of this formalism. Furthermore, we tackled the electronic correlation problem using the relativistic coupled-cluster framework developed by Shee et al. [285] and extended to the computation of core-level properties by Halbert et al. [128].

2.3.1 2-component Hamiltonians

While the theory above is an elegant treatment of quantum mechanics, performing simulations with 4-component Hamiltonians and wave functions is computationally expensive and resource-intensive. Therefore, one usually resorts to 2-component approximations, such as those provided by the Zeroth Order regular approximation (ZORA) by van Lenthe et al. [286], the method proposed by Hess, Douglas and Kroll [287, 288], and the eXact 2-component (X2C) framework [289, 290] employed in this work.

Based on the early work by Foldy and Wouthuysen [291], in the X2C framework the positive and negative solutions of the Dirac equation are decoupled by finding a matrix whose unitary transformation yields:

$$U^{\dagger}\begin{bmatrix} h_{LL} & h_{LS} \\ h_{SL} & h_{SS} \end{bmatrix} U = \begin{bmatrix} \tilde{h}_{++} & 0 \\ 0 & \tilde{h}_{--} \end{bmatrix} \tag{2.15}$$

As discussed in the literature and highlighted by Knecht et al. [290], several strategies, including the *Atomic Mean-Field approximation* (amfX2C) [292], can be employed to achieve such decoupling. In this approach, the Coulomb interaction is computed non-relativistically using atomic corrections, and the 4-component decoupling is performed before the self-consistent field iterations. An alternative approach is to perform the decoupling based on block-diagonalizing the 4-component Fock matrix after the 4-component SCF process has converged, which results in the so-called *molecular mean-field approximation* (mmfX2C) [293].

2.3.2 Quantum electrodynamic corrections

The inclusion of quantum electrodynamics (QED) effects is widely acknowledged in the literature as a requirement for highly accurate simulations of ionization and affinity energies across the whole periodic table [253, 254, 294–299]. These contributions reads as vacuum polarization (VP) and self-energy (SE). Figure 2.1 depicts these contributions for an electron.

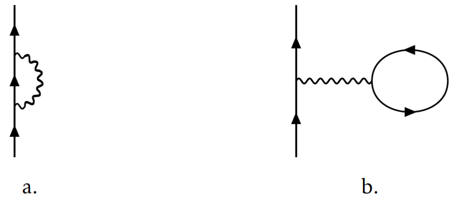

Figure 2.1: Feynman diagram for the (a) self-energy of an electron and (b) vacuum polarization around an electron.

In particular, SE denotes the observed mass change resulting from the interaction between a particle, such as an electron, and its electromagnetic field, as famously described by Feynman [272] as *"the action of an electron on itself"*. Conversely, VP is the difference in the observed charge that rises from the creation and annihilation of virtual electron-positron pairs around a given charge.

Like relativistic effects, such contributions become increasingly significant as we move across the periodic table [253, 254], which translates into the interest in investigating such effects in early actinides [300, 301] and super-heavy elements [254, 300, 302–304]. However, like relativistic effects, computing QED contributions can be computationally expensive, and thus alternatives such as (non-)relativistic pseudopotentials [182, 301–303, 305] and effective QED potentials [306, 307] have been reported in the literature.

Section 6 presents a systematic evaluation of the Hamiltonians introduced in this chapter for simulating the core-ionization energies of the uranyl ion. To account for QED effects in our investigations, we incorporated atomic corrections for individual atomic orbital energies reported by Kozioł and Aucar [308] using the multi-configurational DHF method [309]. To the best of our knowledge, this work represents the first investigation of core-ionization energies of actinides using such Hamiltonians and recovering correlation effects using a high-level theory, such as the CVS-EOM-CC framework.

In conclusion, this chapter presented an advanced theory of atoms and molecules based on Dirac's equation. This theory is grounded in a robust mathematical formalism, and here we only presented a small portion. Despite the well-established significance of relativistic effects on properties such as bond lengths and ionization potentials, they are often overlooked or treated within the framework of perturbation theory in conventional approaches. However, it is important to recognize the considerable efforts made to apply Dirac's theory to the chemical world. Rather than being seen as an exotic treatment, these efforts should be viewed as an endeavor to utilize the most complete theory of the electron available.

Bibliography of the current chapter

(128) Halbert, L.; Vidal, M. L.; Shee, A.; Coriani, S.; Severo Pereira Gomes, A. Relativistic EOM-CCSD for Core-Excited and Core-Ionized State Energies Based on the Four-Component Dirac–Coulomb (- Gaunt) Hamiltonian. *Journal of Chemical Theory and Computation* **2021**, *17*, 3583–3598.

(182) Wang, Y.; Dolg, M. Pseudopotential study of the ground and excited states of Yb2. *Theoretical Chemistry Accounts* **1998**, *100*, 124–133.

(221) Yanai, T.; Nakajima, T.; Ishikawa, Y.; Hirao, K. A new computational scheme for the Dirac–Hartree–Fock method employing an efficient integral algorithm. *The Journal of Chemical Physics* **2001**, *114*, 6526–6538.

(252) Pyykko, P.; Desclaux, J. P. Relativity and the periodic system of elements. *Accounts of Chemical Research* **1979**, *12*, 276–281.

(253) Pyykko, P. The physics behind chemistry and the periodic table. *Chemical reviews* **2012**, *112*, 371–384.

(254) Schwerdtfeger, P.; Smits, O. R.; Pyykkö, P. The periodic table and the physics that drives it. *Nature reviews chemistry* **2020**, *4*, 359–380.

(255) Pyykkö, P. Theoretical chemistry of gold. *Angewandte Chemie International Edition* **2004**, *43*, 4412–4456.

(256) Autschbach, J. Perspective: relativistic effects. *The Journal of chemical physics* **2012**, *136*, 150902.

(257) Pyykko, P. Relativistic effects in structural chemistry. *Chemical Reviews* **1988**, *88*, 563–594.

(258) Visscher, L.; van Lenthe, E. On the distinction between scalar and spin–orbit relativistic effects. *Chemical physics letters* **1999**, *306*, 357–365.

(259) Autschbach, J.; Siekierski, S.; Seth, M.; Schwerdtfeger, P.; Schwarz, W. Dependence of relativistic effects on electronic configuration in the neutral atoms of d-and f-block elements. *Journal of computational chemistry* **2002**, *23*, 804–813.

(260) Saue, T. Relativistic Hamiltonians for chemistry: A primer. *ChemPhysChem* **2011**, *12*, 3077–3094.

(261) Pyykkö, P. Relativistic effects in chemistry: more common than you thought. *Annual review of physical chemistry* **2012**, *63*, 45–64.

(262) Dyall, K. G. A systematic sequence of relativistic approximations. *Journal of computational chemistry* **2002**, *23*, 786–793.

(263) Liu, W. Ideas of relativistic quantum chemistry. *Molecular Physics* **2010**, *108*, 1679–1706.

(264) Liu, W. Perspectives of relativistic quantum chemistry: the negative energy cat smiles. *Physical Chemistry Chemical Physics* **2012**, *14*, 35–48.

(265) Liu, W. Advances in relativistic molecular quantum mechanics. *Physics Reports* **2014**, *537*, 59–89.

(266) Liu, W. Perspective: relativistic hamiltonians. *International Journal of Quantum Chemistry* **2014**, *114*, 983–986.

(267) Liu, W. Essentials of relativistic quantum chemistry. *The Journal of chemical physics* **2020**, *152*, 180901.

(268) Dyall, K. G.; Fægri Jr, K., *Introduction to relativistic quantum chemistry*; Oxford University Press: 2007.

(269) Reiher, M.; Wolf, A., *Relativistic quantum chemistry: the fundamental theory of molecular science*; John Wiley & Sons: 2014.

(270) Klein, O. Quantentheorie und fünfdimensionale Relativitätstheorie. *Zeitschrift für Physik* **1926**, *37*, 895–906.

(271) Gordon, W. Der comptoneffekt nach der schrödingerschen theorie. *Zeitschrift für Physik* **1926**, *40*, 117–133.

(272) Feynman, R. P. Space-time approach to quantum electrodynamics. *Physical Review* **1949**, *76*, 769.

(273) Feynman, R. P. Space-time approach to non-relativistic quantum mechanics. *Reviews of modern physics* **1948**, *20*, 367.

(274) Dirac, P. A. M. The quantum theory of the electron. *Proceedings of the Royal Society of London. Series A, Containing Papers of a Mathematical and Physical Character* **1928**, *117*, 610–624.

(275) Dirac, P. A. M. A theory of electrons and protons. *Proceedings of the Royal Society of London. Series A, Containing papers of a mathematical and physical character* **1930**, *126*, 360–365.

(276) Anderson, C. D. The positive electron. *Physical Review* **1933**, *43*, 491.

(277) Lévy-Leblond, J.-M. Minimal electromagnetic coupling as a consequence of Lorentz invariance. *Annals of Physics* **1970**, *57*, 481–495.

(278) Kim, Y.-K. Relativistic self-consistent-field theory for closed-shell atoms. *Physical Review* **1967**, *154*, 17.

(279) Goldman, S. Variational Dirac-Hartree-Fock method: Results for the He, Be, C, and Ne isoelectronic sequences. *Physical Review A* **1988**, *37*, 16.

(280) Sun, S.; Stetina, T. F.; Zhang, T.; Hu, H.; Valeev, E. F.; Sun, Q.; Li, X. Efficient Four-Component Dirac–Coulomb–Gaunt Hartree–Fock in the Pauli Spinor Representation. *Journal of Chemical Theory and Computation* **2021**, *17*, 3388–3402.

(281) Saue, T.; Jensen, H. A. Quaternion symmetry in relativistic molecular calculations: The Dirac–Hartree–Fock method. *The Journal of chemical physics* **1999**, *111*, 6211–6222.

(282) Visscher, L. Approximate molecular relativistic Dirac-Coulomb calculations using a simple Coulombic correction. *Theoretical Chemistry Accounts* **1997**, *98*, 68–70.

(283) Belpassi, L.; Storchi, L.; Quiney, H. M.; Tarantelli, F. Recent advances and perspectives in four-component Dirac–Kohn–Sham calculations. *Physical Chemistry Chemical Physics* **2011**, *13*, 12368–12394.

(284) Nakajima, T.; Suzumura, T.; Hirao, K. A new relativistic scheme in Dirac–Kohn–Sham theory. *Chemical physics letters* **1999**, *304*, 271–277.

(285) Shee, A.; Saue, T.; Visscher, L.; Severo Pereira Gomes, A. Equation-of-motion coupled-cluster theory based on the 4-component Dirac–Coulomb (–Gaunt) Hamiltonian. Energies for single electron detachment, attachment, and electronically excited states. *The Journal of chemical physics* **2018**, *149*, 174113.

(286) Lenthe, E. v.; Baerends, E.-J.; Snijders, J. G. Relativistic regular two-component Hamiltonians. *The Journal of chemical physics* **1993**, *99*, 4597–4610.

(287) Hess, B. A. Relativistic electronic-structure calculations employing a two-component no-pair formalism with external-field projection operators. *Physical Review A* **1986**, *33*, 3742.

(288) Douglas, M.; Kroll, N. M. Quantum electrodynamical corrections to the fine structure of helium. *Annals of Physics* **1974**, *82*, 89–155.

(289) Liu, W.; Peng, D. Exact two-component Hamiltonians revisited. *The Journal of chemical physics* **2009**, *131*, 031104.

(290) Knecht, S.; Repisky, M.; Jensen, H. J. A.; Saue, T. Exact two-component Hamiltonians for relativistic quantum chemistry: Two-electron picture-change corrections made simple. *The Journal of Chemical Physics* **2022**, *157*, 114106.

(291) Foldy, L. L.; Wouthuysen, S. A. On the Dirac theory of spin 1/2 particles and its non-relativistic limit. *Physical Review* **1950**, *78*, 29.

(292) Liu, J.; Cheng, L. An atomic mean-field spin-orbit approach within exact two-component theory for a non-perturbative treatment of spin-orbit coupling. *The Journal of Chemical Physics* **2018**, *148*, 144108.

(293) Sikkema, J.; Visscher, L.; Saue, T.; Iliaš, M. The molecular mean-field approach for correlated relativistic calculations. *The Journal of chemical physics* **2009**, *131*, 124116.

(294) Chung, K. T. Ionization potential of the lithiumlike 1 s 2 2s states from lithium to neon. *Physical Review A* **1991**, *44*, 5421.

(295) Chung, K. T.; Zhu, X.-W.; Wang, Z.-W. Ionization potential for ground states of berylliumlike systems. *Physical Review A* **1993**, *47*, 1740.

(296) King, F. W. Progress on high precision calculations for the ground state of atomic lithium. *Journal of Molecular Structure: THEOCHEM* **1997**, *400*, 7–56.

(297) Indelicato, P.; Boucard, S.; Lindroth, E. Relativistic and many-body effects in K, L, and M shell ionization energy for elements with and the determination of the 1s Lamb shift for heavy elements. *The European Physical Journal D-Atomic, Molecular, Optical and Plasma Physics* **1998**, *3*, 29–41.

(298) Thierfelder, C.; Schwerdtfeger, P. Quantum electrodynamic corrections for the valence shell in heavy many-electron atoms. *Physical Review A* **2010**, *82*, 062503.

(299) Pašteka, L.; Eliav, E.; Borschevsky, A.; Kaldor, U.; Schwerdtfeger, P. Relativistic coupled cluster calculations with variational quantum electrodynamics resolve the discrepancy between experiment and theory concerning the electron affinity and ionization potential of gold. *Physical review letters* **2017**, *118*, 023002.

(300) Dolg, M.; Cao, X. Relativistic pseudopotentials: their development and scope of applications. *Chemical reviews* **2012**, *112*, 403–480.

(301) Petrov, A.; Mosyagin, N.; Titov, A.; Tupitsyn, I. Accounting for the Breit interaction in relativistic effective core potential calculations of actinides. *Journal of Physics B: Atomic, Molecular and Optical Physics* **2004**, *37*, 4621.

(302) Hangele, T.; Dolg, M.; Schwerdtfeger, P. Relativistic energy-consistent pseudopotentials for superheavy elements 119 and 120 including quantum electrodynamic effects. *The Journal of chemical physics* **2013**, *138*, 174113.

(303) Hangele, T.; Dolg, M.; Hanrath, M.; Cao, X.; Schwerdtfeger, P. Accurate relativistic energy-consistent pseudopotentials for the superheavy elements 111 to 118 including quantum electrodynamic effects. *The Journal of chemical physics* **2012**, *136*, 214105.

(304) Schwerdtfeger, P.; Pašteka, L. F.; Punnett, A.; Bowman, P. O. Relativistic and quantum electrodynamic effects in superheavy elements. *Nuclear Physics A* **2015**, *944*, 551–577.

(305) Häussermann, U.; Dolg, M.; Stoll, H.; Preuss, H.; Schwerdtfeger, P.; Pitzer, R. Accuracy of energy-adjusted quasirelativistic ab initio pseudopotentials: all-electron and pseudopotential benchmark calculations for Hg, HgH and their cations. *Molecular Physics* **1993**, *78*, 1211–1224.

(306) Sunaga, A.; Salman, M.; Saue, T. 4-component relativistic Hamiltonian with effective QED potentials for molecular calculations. *The Journal of Chemical Physics* **2022**, *157*, 164101.

(307) Sunaga, A.; Saue, T. Towards highly accurate calculations of parity violation in chiral molecules: relativistic coupled-cluster theory including QED-effects. *Molecular Physics* **2021**, *119*, e1974592.

(308) Kozioł, K.; Aucar, G. A. QED effects on individual atomic orbital energies. *The Journal of Chemical Physics* **2018**, *148*, 134101.

(309) Grant, I.; McKenzie, B.; Norrington, P.; Mayers, D.; Pyper, N. Atomic multiconfigurational Dirac-Fock package. *Comput. Phys. Commun.;(Netherlands)* **1980**, *21*.

Chapter 3

Molecular Response Theory

"One had to cram all this stuff into one's mind for the examinations, whether one liked it or not. This coercion had such a deterring effect on me that, after I had passed the final examination, I found the consideration of any scientific problems distasteful to me for an entire year."

— Albert Einstein

The previous chapters of this thesis have focused exclusively on determining ground states. However, since this thesis investigates light-matter interaction in the X-ray range, a general framework for computing excited states is needed.

One can achieve this extension through response theory, in which one-photon processes are studied by computing the first-order response function, also known as the electric-dipole polarizability. In the upcoming chapter, we provide an overview of this theoretical framework. Firstly, in Section 3.1, we present the exact formulation of this framework and how to incorporate relaxation effects into theory in Section 3.1.1. Then, we finish this chapter by briefly introducing approximate response theory in the context of density functional theory (Section 3.2).

For a more detailed discussion of this captivating subject, we recommend referring to the works of Helgaker et al. [310] and Norman and Dreuw [125]. The following discussion is based on Chapters 5 and 7 in the textbook by Norman et al. [31].

3.1 Exact-State Response Theory

A molecular system may undergo electronic transitions in the presence of an external field. When such fields are significantly weaker than internal fields of the molecule and have a short interaction time with a system under investigation [125], the following partitioned Hamiltonian can be used:

$$\hat{H}(t) = \hat{H}_0 + \hat{V}(t), \tag{3.1}$$

where $\hat{H}_0$ is the unperturbed Hamiltonian, and $\hat{V}(t)$ is the time-dependent perturbation operator, such as an oscillating electric field:

$$\hat{V}(t) = \sum_{\omega} \hat{V}_{\alpha}^{\omega} F_{\alpha}^{\omega} e^{-i\omega t}, \tag{3.2}$$

with F_{α}^{ω} denoting the field amplitude along the α-axis.

Within the electric-dipole approximation, the electric dipole coupling with an external field like the one given in the above expression produces the features observed in an electronic spectrum. Perturbations on a system can be theoretically tracked by following the contribution of non-zero order terms on the field expansion of the time-dependent polarization:

$$\begin{split}\mu_{\alpha}(t) = \mu_{\alpha}^{0} + \sum_{\omega} \alpha_{\alpha\beta}(-\omega;\omega) F_{\beta}^{\omega} e^{-i\omega t} \\ + \sum_{\omega_1 \omega_2} \beta_{\alpha\beta\gamma}(-\omega_\sigma;\omega_1,\omega_2) F_{\beta}^{\omega_1} F_{\gamma}^{\omega_2} e^{-i\omega_\sigma t} + \cdots\end{split} \tag{3.3}$$

where μ_{α}^{0} denotes the permanent electric-dipole moment, $\alpha_{\alpha\beta}(\omega;\omega)$ is the polarizability tensor, and $\beta_{\alpha\beta\gamma}(\omega_\sigma;\omega_1\omega_2)$ is the first-order contribution to non-linear processes, where $\omega_\sigma = \omega_1 + \omega_2$.

Measurements of certain observables allow for the investigation of a system's response to external perturbations. On the theoretical side, the postulates of quantum mechanics come into play, and several considerations must be made [66].

The simplest case to consider is that of a static field, where the exponential in Equation 3.2 is disregarded. By invoking the Hellmann-Feynman theorem [311, 312], molecular properties can be identified as the field derivatives in the Taylor series expansion of the energy :

$$E = E_0 + F_\alpha \frac{\partial E}{\partial F_\alpha}\bigg|_{F_\alpha = 0} + \frac{1}{2} F_\alpha F_\beta \frac{\partial E}{\partial F_\alpha \partial F_\beta}\bigg|_{F_\alpha = F_\beta = 0} + \cdots \tag{3.4}$$

where the limit of zero field strength is assumed.

In the time-dependent case, we identify molecular properties through a Taylor expansion of the expectation value for a given perturbation operator. Perturbation theory can thus be employed to determine different orders of the perturbed wave function, i.e.,

$$|\psi(t)\rangle = |\psi^{(0)}(t)\rangle + |\psi^{(1)}(t)\rangle + |\psi^{(2)}(t)\rangle \cdots \tag{3.5}$$

However, determining such a perturbed wave function is not as straightforward as it may seem. The algebraic work is extensive and involves choosing an equation of motion to obtain time-dependent amplitudes within a given wave-function parametrization. Commonly, reference-state parametrizations are constructed from a projection or rotation ansatz, as explored by Norman et al. [31]. In the former case, the desired time-dependent amplitudes can be easily obtained through the time-dependent Schrödinger equation, while the latter case utilizes the Ehrenfest theorem [313], which provides an alternative (but equivalent) formulation of Equation 1.1. In this case, the time evolution of the expectation value is given by:

$$\frac{\partial}{\partial t}\langle \psi(t)|\hat{\Omega}|\psi(t)\rangle = \frac{1}{i\hbar}\langle \psi(t)|[\hat{\Omega}, \hat{H}_0 + \hat{V}]|\psi(t)\rangle \tag{3.6}$$

We will not delve further into how to obtain amplitudes using these techniques. However, regardless of the reference-state parametrization, a complete set of wave functions yields an *exact theory*. In practice, one refrains to a subspace of the N-electron Hilbert space, consisting of a *approximate* treatment of the problem.

After determining the different orders of the perturbed wave function, the expectation value reads:

$$\langle\psi(t)|\hat{\Omega}|\psi(t)\rangle = \langle\psi^{(0)}|\hat{\Omega}|\psi^{(0)}\rangle + \langle\psi^{(1)}|\hat{\Omega}|\psi^{(0)}\rangle + \langle\psi^{(0)}|\hat{\Omega}|\psi^{(1)}\rangle + \cdots \tag{3.7}$$

The formula proposed by Kubo [314] provides a general expression for such a series expansion. Applying the perturbation operator defined in Equation 3.2 to the Kubo formula yields:

$$\begin{aligned}\langle\psi(t)|\hat{\Omega}|\psi(t)\rangle = \langle 0|\hat{\Omega}|0\rangle &+ \sum_{\omega_1}\langle\langle\hat{\Omega};\hat{V}_\beta^{\omega_1}\rangle\rangle F_\beta^{\omega_1} e^{-i\omega_1 t} \\ &+ \sum_{\omega_1\omega_2}\langle\langle\hat{\Omega};\hat{V}_\beta^{\omega_1},\hat{V}_\gamma^{\omega_2}\rangle\rangle F_\beta^{\omega_1} F_\gamma^{\omega_2} e^{-i(\omega_1+\omega_2)t} + \cdots\end{aligned} \tag{3.8}$$

Similar to Equation 3.3, in the above expression $\langle 0|\hat{\Omega}|0\rangle$ is a first-order property associated with the ground state wave function (or reference state), for instance, the permanent electric-dipole moment (μ_0). The following terms denote other molecular properties obtained by solving higher-order equations. In the following, we introduce the property used in this work to evaluate the absorption spectra of actinides.

The second-order term in Equation 3.8 contains the so-called linear response function $\langle\langle\hat{\Omega};\hat{V}_\beta^{\omega_1}\rangle\rangle$, also called *first-order polarization propagator* in the context of electric properties. In exact state theory, the spectral representation of the linear response function yields the following sum-over-states:

$$\langle\langle\hat{\Omega};\hat{V}_\beta^{\omega}\rangle\rangle = \frac{1}{\hbar}\sum_n\left[\frac{\langle 0|\hat{\Omega}|n\rangle\langle n|\hat{V}_\beta^{\omega}|0\rangle}{\omega_{0n}-\omega} + \frac{\langle 0|\hat{V}_\beta^{\omega}|n\rangle\langle n|\hat{\Omega}|0\rangle}{\omega_{0n}+\omega}\right] \tag{3.9}$$

where ω_{0n} is the transition energy between states $|0\rangle$ and $|n\rangle$. It is worth noting that this expression is suitable for investigating one-photon processes such as absorption and emission, as it contains a single perturbation frequency. Furthermore, the linear-response function exhibits a singularity at transition frequencies and is therefore said to be resonant-divergent.

Extracting the poles of Equation 3.9 yields transition energies, and computing its residues yields transition moments – proportional to intensities in a spectrum. Once such values are known, the absorption cross-section reads:

$$\sigma(\omega) = \frac{4\pi\omega}{3c} \sum_{i=x,y,z} \left|\alpha_i^{Im}(-\omega;\omega)\right|^2 \tag{3.10}$$

3.1.1 Damped-Response Theory

In addressing the presence of singularities in response functions, Norman et al. [315] introduced a damped formulation of response theory. This approach effectively handles the issue by incorporating the process of spontaneous relaxation through the formalism of density matrices.

When using density matrices, the equation of motion to be solved is the so-called Liouville equation [316]. The phenomenological introduction of a damping term (γ_{mn}) yields:

$$\frac{\partial}{\partial t}\rho_{mn} = \frac{1}{i\hbar}\left[\hat{H},\hat{\rho}\right]_{mn} - \gamma_{mn}\left(\rho_{mn} - \rho_{mn}^{eq}\right) \tag{3.11}$$

where ρ_{mn} denotes the density matrix of a given configuration (s) and $\hat{\rho}$ denotes the density operator,

$$\hat{\rho} = \sum_s p(s)|\psi(t)\rangle\langle\psi(t)| = \sum_s p(s)c_m^s c_n^{s*} \tag{3.12}$$

in which c_i's are the expansion coefficients for a linear expansion of a wave function.

This formulation of response theory assumes a statistical ensemble of system configurations and their respective probabilities $p(s)$. The relaxation parameters (γ_{mn}) in Equation 3.11 account for the decay rate of a given configuration towards the system's equilibrium value, ρ_{mn}^{eq}, i.e., the ground state.

Similar to Equation 3.5, a perturbative treatment of the density matrix is made:

$$\rho_{mn}(t) = \rho_{mn}^{(0)} + \rho_{mn}^{(1)} + \rho_{mn}^{(2)} + \cdots \tag{3.13}$$

and the spectral representation of the linear response function within this formalism reads:

$$\langle\langle\hat{\Omega}; \hat{V}_{\beta}^{\omega_1}\rangle\rangle = \frac{1}{\hbar}\sum_{n}\left[\frac{\langle 0|\hat{\Omega}|n\rangle\langle n|\hat{V}_{\beta}^{\omega}|0\rangle}{\omega_{0n} - \omega - i\gamma} + \frac{\langle 0|\hat{V}_{\beta}^{\omega}|n\rangle\langle n|\hat{\Omega}|0\rangle}{\omega_{0n} + \omega + i\gamma}\right] \tag{3.14}$$

and the polarizability tensor is a resonant-convergent complex quantity.

Furthermore, if high-resolution data is available is possible to relate damping parameters to spectral widths, as $\tau_{mn} = 1/\gamma_{mn}$. In practice, only one damping parameter is used in simulations, $\gamma_{n0} = \gamma$.

3.2 Time-Dependent Functional Theory

As discussed in the first chapter of this thesis, approximate methods are employed to build multi-electronic systems wave-function, and the basis set expansion is not exact. Therefore, we used approximate state theory to investigate molecular properties in this thesis.

Within an approximate formalism, the steps to obtain response functions are similar to those indicated in the previous section. However, more ingredients are needed to yield the linear response function, and for the sake of brevity, we refer the reader to Chapter 7 in the textbook Norman et al. [31] for a more detailed discussion. We also refer the reader to the work of Casida [317] for a more detailed discussion on the extension of Hohenberg-Kohm theorems for the time-dependent case, which basis is the work of Gross et al. [318].

Using the set of occupied $\left\{\psi_i, \psi_j, \cdots\right\}$ and virtual $\{\psi_a, \psi_b, \cdots\}$ orbitals from a KS reference, the equation describing the linear response of a system to an external field is the so-called the Casida equation [317], a non-Hermitian generalized eigenvalue problem, which reads as:

$$\begin{pmatrix} A & B \\ B^* & A^* \end{pmatrix}\begin{pmatrix} X \\ Y \end{pmatrix} = \omega_k \begin{pmatrix} 1 & 0 \\ 0 & -1 \end{pmatrix}\begin{pmatrix} X \\ Y \end{pmatrix} \tag{3.15}$$

where the set of X and Y eigenvectors and their respective eigenvalues ω_k (the excitation energies) can be obtained through orbital rotations. A and B matrices are given by:

$$A_{ia,jb} = (\epsilon_a - \epsilon_i)\delta_{ij}\delta_{ab} + \langle ij|ab\rangle + \langle ij|f_{xc}|ab\rangle \tag{3.16}$$

$$B_{ia,jb} = \langle ib|aj\rangle + \langle ib|f_{xc}|aj\rangle \tag{3.17}$$

where ϵ_p denotes the energy of orbital p, and the two-electron integrals reads as:

$$\langle ij|ab\rangle = \int\int \psi_i^*(\mathbf{x}_1)\psi_j^*(\mathbf{x}_2)\left(\frac{1}{\mathbf{r}_{12}}\right)\psi_a(\mathbf{x}_1)\psi_b(\mathbf{x}_2)d\mathbf{x}_2 d\mathbf{x}_1 \tag{3.18}$$

$$\langle ij|f_{xc}|ab\rangle = \int\int \psi_i^*(\mathbf{x}_1)\psi_j^*(\mathbf{x}_2)\left(\frac{\partial^2 E_{xc}}{\partial\rho(\mathbf{x}_1)\partial\rho(\mathbf{x}_2)}\right)\psi_a(\mathbf{x}_1)\psi_b(\mathbf{x}_2)d\mathbf{x}_2 d\mathbf{x}_1 \tag{3.19}$$

where the terms in which f_{xc} appears denote exchange-correlation kernels. Similar to the exchange-correlation functionals discussed in Section 1.5, the exact expression for f_{xc} remains elusive.

For closed-shell systems, a commonly used approximation is one where the B matrix is neglected, simplifying the problem to diagonalize the following Hermitian matrix:

$$AX = \omega X \tag{3.20}$$

Consisting of the Tamm-Dancoff approximation (TDA) [319, 320]. The literature extensively discusses the validity of this approximation, and interested readers can refer to previous references for a more comprehensive discussion.

To finish this chapter, we also refer to the works of Norman et al. [31, 125, 315, 321] for a more comprehensive discussion regarding the inclusion of relaxation effects in the case of approximate theory. The implementation employed in 4-component damped-response simulations in this work is based on the work by Villaume et al. [322].

Bibliography of the current chapter

(31) Norman, P.; Ruud, K.; Saue, T., *Principles and practices of molecular properties: Theory, modeling, and simulations*; John Wiley & Sons: 2018.

(66) Helgaker, T.; Jorgensen, P.; Olsen, J., *Molecular electronic-structure theory*; John Wiley & Sons: 2013.

(125) Norman, P.; Dreuw, A. Simulating X-ray spectroscopies and calculating core-excited states of molecules. *Chemical reviews* **2018**, *118*, 7208–7248.

(310) Helgaker, T.; Coriani, S.; Jørgensen, P.; Kristensen, K.; Olsen, J.; Ruud, K. Recent advances in wave function-based methods of molecular-property calculations. *Chemical reviews* **2012**, *112*, 543–631.

(311) Hellmann, H. et al. Einfuhrung in die Quantenchemie. **1937**.

(312) Feynman, R. P. Forces in molecules. *Physical review* **1939**, *56*, 340.

(313) Ehrenfest, P. Bemerkung über die angenäherte Gültigkeit der klassischen Mechanik innerhalb der Quantenmechanik. *Zeitschrift für physik* **1927**, *45*, 455–457.

(314) Kubo, R. Statistical-mechanical theory of irreversible processes. I. General theory and simple applications to magnetic and conduction problems. *Journal of the Physical Society of Japan* **1957**, *12*, 570–586.

(315) Norman, P.; Bishop, D. M.; Jensen, H. J. A.; Oddershede, J. Nonlinear response theory with relaxation: The first-order hyperpolarizability. *The Journal of chemical physics* **2005**, *123*, 194103.

(316) Boyd, R. W. Nonlinear optics Academic press. *San Diego* **1992**, *155*.

(317) Casida, M. E. In *Recent Advances In Density Functional Methods: (Part I)*; World Scientific: 1995, pp 155–192.

(318) Gross, E. K.; Ullrich, C.; Gossmann, U., *Density functional theory of time-dependent systems*; Springer: 1995.

(319) Dancoff, S. Non-adiabatic meson theory of nuclear forces. *Physical Review* **1950**, *78*, 382.

(320) Tamm, I.; Tamm, I. Relativistic interaction of elementary particles. *Selected Papers* **1991**, 157–174.

(321) Norman, P. A perspective on nonresonant and resonant electronic response theory for time-dependent molecular properties. *Physical chemistry chemical physics* **2011**, *13*, 20519–20535.

(322) Villaume, S.; Saue, T.; Norman, P. Linear complex polarization propagator in a four-component Kohn–Sham framework. *The Journal of chemical physics* **2010**, *133*, 064105.

Part II

Core Excitations and Ionizations in Uranyl Complexes

Chapter 4

Core excitations of uranyl in $Cs_2UO_2Cl_4$

"And I am freaking out in the middle of the street, with the complete conviction of someone who's never had anything actually really bad happen to them. But I am committed, now, to the feeling. I don't know how it started, don't know how to stop it. Suddenly, I'm dancing to imaginary music."

— Choreomania, Florence & the Machine

This chapter is dedicated to exploring the application of the damped-response theory, which was introduced in Chapter 3.1.1, to further elucidate the method's capabilities in studying the electronic excited states of uranyl-containing compounds. Part of the material presented in this chapter has been published [323].

Before presenting the manuscript, we will now discuss two important aspects: the polarization dependence that can be investigated in XAS experiments and the characterization of excited states utilizing natural transition orbitals (NTOs).

Polarization dependence in core-excited states

Beyond determining the excited states by means of the calculation of the complex polarizability tensor, one can also employ damped-response theory to provide insights into angle-resolved experiments. In the following, we summarize the aspects of angular dependence in X-ray absorption spectra. A more comprehensive exploration of this subject can be found in the textbooks of Stöhr [324] and Willmott [1].

The directional character of molecular orbitals, determined by their spatial orientation within a specific molecular geometry, can be effectively utilized to study the polarization-dependence in the photoabsorption process, also taking advantage of the linear polarization feature of synchrotron radiation.

For instance, as elaborated in the textbook by Stöhr [324], using the expression for the absorption cross section in Equation 6 it can be shown that the transition intensity ($I_{i\to f}$) of 1s → σ^* and 1s → π^* resonances in diatomic molecules (such as N_2 and CO) exhibits angular dependence in the dipole matrix element, given by:

$$I_{1s\to\sigma^*} \propto |\mathbf{e}\cdot\mathbf{e_z}|^2 \propto \cos^2(\theta^{'}) \tag{4.1}$$

$$I_{1s\to\pi^*} \propto |\mathbf{e}\cdot\mathbf{e_x}|^2 + \left|\mathbf{e}\cdot\mathbf{e_y}\right|^2 \\ \propto \sin^2(\theta^{'})\cos^2(\phi^{'}) + \sin^2(\theta^{'})\sin^2(\phi^{'}) \propto \sin^2(\theta^{'}) \tag{4.2}$$

where **e** represents the orientation of the unit electric field vector using spherical angles $\theta^{'}$ and $\phi^{'}$, while $\mathbf{e}_i$ signifies the components of the unit vectors in a specific coordinate system, such as the one employed for describing a molecule.

Therefore, resonances associated with final states exhibiting σ and π symmetries display a strong and opposite polarization dependence, making them suitable for studying the angular dependence in the photoabsorption process. This can be achieved by varying the direction of the incoming X-rays or by rotating a sample. Transitions to orbitals with σ symmetry are more intense when the incoming electromagnetic radiation is parallel to the internuclear axis (i.e., at grazing incidence), whereas π transitions are more intense when the light incidence is perpendicular to this axis [3].

In the case of the dicesium uranyl tetrachloride crystal ($Cs_2UO_2Cl_4$, depicted in Figure 4.2), a prototype system in actinide chemistry [325–328], different absorption edges allow transitions to orbitals with specific symmetries localized in the uranyl unit, such as π_u^*, σ_u^*, and π_g^*, as well as non-bonding orbitals like $5f\phi_u$ and $6d\pi_g$ in the UO_2^{2+} unit. Consequently, a significant degree of polarization dependence in the spectral features is expected when probing these transitions. Indeed, this feature was investigated by Denning et al. [326] in the early 2000s for XANES spectra at the O K-edge and in the last decade by Vitova et al. [328] for the uranium M_4- and L_3-edges using the HERFD technique. Figure 4.2 also shows a schematization of such experiments, as reported by Denning et al. [326]. For further details, we refer the readers to the original works [326–328].

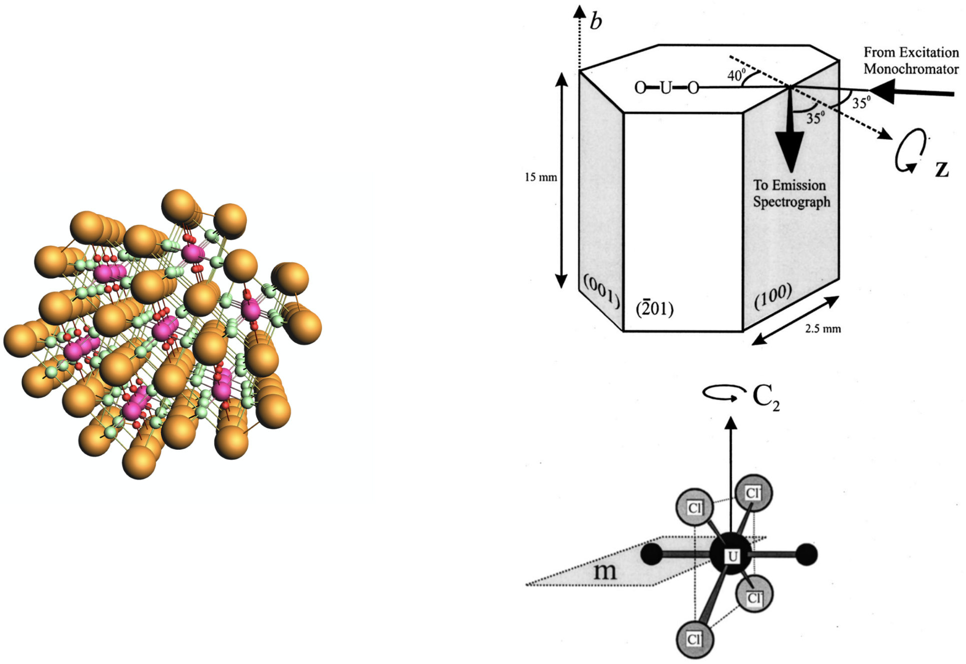

Figure 4.2: Right: Dicesium uranyl tetrachloride crystal ($Cs_2UO_2Cl_4$). Left: Depiction of the crystal habit of $Cs_2UO_2Cl_4$ showing the molecular axes and sample configuration. The diagram shows the incident X-ray beam originating from the excitation monochromator and the emitted X-rays directed toward the analyzing spectrograph. Angular dependence in the X-ray absorption spectra can be acquired by sample rotation around the C_2 crystal axis. Adapted from Denning et al. [326]. Figure used with permission from Denning et al. Copyright 2002 AIP Publishing.

Theoretical simulations can investigate such phenomena using the damped-response approach presented in Chapter 3.1.1. This protocol involves decomposing the spectral representation of the resonant-convergent linear-response function, given by:

$$\alpha_{\alpha\beta}(-\omega;\omega) = -\frac{1}{\hbar}\sum_{n>0}\left[\frac{\langle 0|\hat{\mu}_\alpha|n\rangle\left\langle n|\hat{\mu}_\beta|0\right\rangle}{\omega_{0n}-\omega-i\gamma}+\frac{\left\langle 0|\hat{\mu}_\beta|n\right\rangle\langle n|\hat{\mu}_\alpha|0\rangle}{\omega_{0n}+\omega+i\gamma}\right] \tag{4.3}$$

where $\hat{\mu}_i$ represents a component of the electric-dipole operator along a specific direction, ω_{0n} corresponds to the frequency associated with a transition between the ground state ($|0\rangle$) and an excited state ($|n\rangle$), ω represents the frequency of the perturbing field, and γ denotes the damping factor.

For a randomly oriented molecular sample, the damped response absorption cross section can be expressed as the isotropic average of the complex component of the polarizability:

$$\sigma(\omega) = \frac{\omega}{\varepsilon_0 c} Im\left[\frac{1}{3}(\alpha_{xx}(\omega)+\alpha_{yy}(\omega)+\alpha_{zz}(\omega))\right] \tag{4.4}$$

where ε_0 represents the vacuum permittivity and c the speed of light.

Therefore, within this approach, the polarization dependence of a system is determined by the partial components of the total absorption cross section across the range of calculated frequencies, denoted as $\sigma_{ii}(\omega)$. Our results show the success of the adopted methodology.

Caracterization of core-excited states

Following the work of Krylov[33], Plasser et al.[329], we consider excited states as electron-hole pairs, representing the virtual and occupied orbitals, respectively.

Characterizing excited states can be a challenging task, particularly when considering the use of a Slater determinant from an HF-SCF calculation to describe excited states within the TDA (see Equation 3.20). In this scenario, the wavefunction of each targeted state (ψ^I_{CIS}) can be represented as a linear combination of singly excited Slater determinants:

$$\psi^I_{CIS} = \sum_{\mu\nu} C^\nu_\mu \phi^\nu_\mu \tag{4.5}$$

Therefore, for each excited state (I), there is a set of excitation amplitudes ($C^I_{\mu\nu}$) that each electron-hole pair – with orbital indices μ and ν – contributes to the excited state wavefunction. Often, there are numerous contributions, and in some cases, there is no dominant configuration among the excitation amplitudes, making a straightforward interpretation of the excited state challenging.

To address this issue, the one-particle transition density matrix (1PTDM) can be employed. For a transition between states ψ_i and ψ_j, this quantity is defined as [33]:

$$\gamma^{ij}_{\mu\nu} = \langle \psi_i | \hat{a}^\dagger_\mu \hat{a}_\nu | \psi_j \rangle \tag{4.6}$$

where $\hat{a}^\dagger_\mu$ and $\hat{a}_\nu$ are creation and annihilation operators for molecular orbitals φ_μ and φ_ν, respectivelly.

First introduced by Batista and Martin [330], natural transition orbitals (NTOs) provide a compact orbital representation for 1PTDM. In this framework, γ is obtained through a singular value decomposition (SVD):

$$\gamma = \mathbf{V}\Sigma\mathbf{U}^T \tag{4.7}$$

where Σ is a diagonal matrix of singular values (σ_t) for each transition. **V** and **U** are matrices that allow us to construct two new sets of orbitals: the hole (ψ^h_t) and particle (ψ^e_t) NTOs for a given transition:

$$\begin{aligned}\psi^h_t(\mathbf{r}) &= \sum_q U_{qt}\phi_t(\mathbf{r}) \\ \psi^e_t(\mathbf{r}) &= \sum_q V_{qt}\phi_t(\mathbf{r})\end{aligned}$$

What makes this approach considerably more appealing than simply considering the set of $C^I_{\mu\nu}$ is that, in contrast to the numerous $C^I_{\mu\nu}$ values, only a few σ_t values are non-vanishing. Furthermore, these are of particular interest as they deviate from the ground-state canonical orbital picture and provide insights into excited states at a one-electron representation level. These characteristics are further discussed in the references mentioned earlier.

Another compelling aspect of this approach is the direct connection between transition densities and observables, unlike wave-function amplitudes. By utilizing the transition matrix for the electron (particle) and hole coordinates, x_e and x_h, respectively:

$$\rho(x_e, x_h) = \sum_t \sigma_t \phi_t^e(x_e) \phi_t^h(x_h) \tag{4.8}$$

one can construct the transition dipole moment by doing:

$$\langle \psi_i | \hat{\mu} | \psi_j \rangle = Tr\left[\gamma^{ij} \mu\right]$$

(4.9)

Natural Transition Orbitals (NTOs) have been extensively applied in various areas of quantum chemistry. They have proven useful in quantifying charge transfer in push-pull systems and assigning states in transition metal complexes, among other applications [329]. To the best of our knowledge, this work represents the first application of such an approach to studying the (core) excitation process in actinides.

4.1 Manuscript

Abstract

X-ray spectroscopies, by their high selectivity and sensitivity to the chemical environment around the atoms, probed, provide significant insight into the electronic structure of molecules and materials. Interpreting experimental results requires reliable theoretical models, accounting for environment, relativistic, electron correlation, and orbital relaxation effects in a balanced manner.

In this work, we present a protocol for the simulation of core excited spectra with damped response time-dependent density functional theory based on the Dirac-Coulomb Hamiltonian (4c-DR-TD-DFT), in which environmental effects are accounted for through the frozen density embedding (FDE) method. We showcase this approach for the uranium M_4-, L_3-edge and oxygen K-edge of uranyl tetrachloride ($UO_2Cl_4^{2-}$) unit as found in a host $Cs_2UO_2Cl_4$ crystal.

We have found that the 4c-DR-TD-DFT simulations yield excitation spectra that very closely match the experiment for the uranium M_4- and oxygen K-edges, with good agreement for the broad experimental spectra for the L_3-edge. By decomposing the complex polarizability in terms of its components we have been able to correlate our results with angle-resolved spectra.

We have observed that for all edges, but in particular the uranium M_4-edge, an embedded model in which the chloride ligands are replaced by an embedding potential, reproduces rather well the spectral profile obtained for $UO_2Cl_4^{2-}$. Our results underscore the importance of the equatorial ligands to simulating core spectra at both uranium and oxygen edges.

4.1.1 Introduction

Actinides are relevant to modern societies, first and foremost due to their central role in the nuclear industry [331–335], and the potentially harmful effects that can occur with their release in the biosphere in the case of industrial accidents [336–339]. In more recent years, the peculiar properties of materials containing actinides have also spurred interest from both a fundamental perspective as well as for industrial applications in catalysis [340–342], materials [341, 343–346] and nanotechnology [347–350].

As these properties stem from subtle differences in the electronic structure of different compounds [5, 327, 351, 352], a key objective in actinide science is to characterize their electronic structure under different conditions. To this end, spectroscopies involving core electrons [324, 353–356] are particularly interesting since they are very sensitive to changes in oxidation state and on the local chemical environment of the actinides [20, 40, 357–359].

In recent years, with the development of high-energy fourth-generation synchrotron radiation facilities around the world and the availability of X-ray Free Electron Lasers (XFELs) [354, 356, 360], one has witnessed the development and applications of High-Energy Resolution X-ray Spectroscopy (HERXS) to actinides [196, 199, 200, 361–363].

The set of HERXS techniques includes spectroscopies such as High-Energy Resolution Fluorescence Detected X-ray Absorption Near Edge Structure (HERFD-XANES), High-Energy Resolution Auger Detection (HERAD-XANES), High-Energy X-ray Scattering (HEXS) and Extended X-ray Absorption Fine Structure (EXAFS) [40, 196, 340, 363–365]. For actinides, a particularly appealing feature of HERXS measurements is their larger penetration depth, which allows for smaller samples[1, 196, 200, 355, 361, 362], this way minimizing the need for extensive radiation exposure protection measures. These experiments also offer increased sensitivity in probing processes that involve transitions to and from *d* and *f* orbitals, with the latter playing a pivotal role in actinide bonding [21, 328, 366–369].

Therefore, these experimental developments, and the inherent complexities of interpreting the data generated, have stimulated the use of accurate molecular electronic structure methods as a means to interpret, predict and suggest new measurements in the X-ray range [125, 126, 370–373]. While it has long been established that in this regime theoretical approaches must properly account for electron correlation[371, 372, 374–377] and orbital relaxation[373, 378–381] in order to yield reliable results, the importance of relativistic effects [260, 267–269, 382], indispensable for heavy elements, is now also recognized for elements as light as those in the second row of the periodic table.

Since most measurements of core spectra are done for molecules in the gas phase, it may become necessary to include environmental effects in the calculations. This can be done efficiently and accurately with embedding approaches [156, 158, 383, 384], whereby a sufficiently accurate fully quantum mechanical (QM) description is applied to the region of interest and a significant portion of the system is represented via quantum (QM/QM) or classically-derived (QM/MM) effective operators, without any *a priori* assumptions on the nature of the region of interest or the environment–which makes them potentially more flexible than other proven approaches based on e.g. explicit and continuum (implicit) solvation models [46, 47, 385, 386] and ligand field theory [387–389].

Among actinides, a particularly important class of complexes contains the uranyl ($UO_2^{n+}, n = 1, 2$) moiety, which is ubiquitous in the solution and solid-state chemistry of uranium. It is known to show very strong U-O triple bonds [327] and generally presents a linear O-U-O geometry, with other ligands coordinating with uranium in the equatorial plane, via less strong interactions. The core spectroscopy of uranyl coordination complexes has been investigated with several theoretical methods, ranging from complete and restricted active space self-consistent field [369, 390–394], crystal ligand-field multiplet theory and its variations [20, 203, 365, 389, 395–397], density functional theory in its different flavors [225, 328, 365, 374, 398–400], self-consistent real-space multiple scattering [364, 365], static exchange approximation [374] and perturbation theory [374].

For molecular-based approaches, relativistic correlated many-body ones are among the most accurate approaches that can be used [128, 392–394], but their relatively high computational cost makes it difficult to employ for the experimentally relevant systems in the condensed phase. In the case of absorption spectroscopy, it has been found that with a suitable choice of density functional approximation (DFA) – notably the CAM-B3LYP functional [401] – density functional theory (DFT) can provide reliable excitation energies of actinides in the ultraviolet-visible region [46–48, 167, 168, 222], with a recent, very comprehensive work by Konecny et al. [225] employing the four component Damped Response Time-Dependent Density Functional Theory (4c-DR-TD-DFT) formalism, indicating that the same holds for core excited states of uranium complexes.

One aspect that, in our view, was not sufficiently addressed in the work by Konecny and co-workers, is the extent to which the environment can play a role in the spectral features. While Konecny et al. [225] provided a comparison between theory and experiment for the uranium M_4-edge of uranium nitrate oxide ($UO_2(NO_3)_2$), there are other systems such as the $Cs_2UO_2Cl_4$ crystal, for which there are HERFD-XANES spectra for the uranium M_4-edge as well as XANES spectra for the uranium L_3-edge [328], and oxygen K-edge [326], which could provide more comprehensive comparisons to experiment.

The present work, therefore, aims to employ embedding approaches and the 4c-DR-TD-DFT formalism to investigate the effect of the chloride ligands bound to the equatorial plane of uranyl in the $Cs_2UO_2Cl_4$ crystal, on the oxygen K-edge and uranium M_4- and L_3-edges excited states, with a detailed comparison to experimental results available in the literature for this system. We start by presenting the computational details from our calculations, followed by our results for the simulated X-ray absorption spectra. Finally, we present our conclusions and some future perspectives.

4.1.2 Computational details

DR-TD-DFT and the corresponding 4c-DR-TD-DFT-in-DFT calculations were performed in DIRAC22 [402] version of the `DIRAC` electronic structure code [403]. We employed Dyall's all-electron basis sets of double and triple-zeta quality [404, 405] for uranium and Dunning's cc-pVTZ basis set [325] for all other atoms. These basis sets were left uncontracted. We have employed a Gaussian nuclear model in all calculations [406].

For all DFT calculations with `DIRAC`, we have employed the Dirac-Coulomb (^{4}DC) Hamiltonian and the long-range corrected CAM-B3LYP[401] functional.

In all of our calculations, the structures employed were based on the experimental crystal structure of $Cs_2UO_2Cl_4$ reported by Watkin et al. [407], whose U-O and U-Cl bond lengths are 1.774 Å and 2.673 Å respectively. For the embedding calculations, we employed the same structural models and subsystem partitioning as outlined by Gomes et al. [167]. All calculations on the bare uranyl and uranyl tetrachloride were carried out in D_{∞_h} and D_{2h} symmetry, respectively, while for embedded uranyl simulations the crystalline site symmetry (C_{2h}) was used.

The embedding potentials employed here were obtained from freeze-thaw calculations employing the scalar-relativistic ZORA Hamiltonian [408], TZ2P basis sets, the PW91k kinetic energy [409], the PBE exchange-correlation functional [229] for the non-additive terms and subsystem energies. These calculations were carried out via the `PyADF` scripting framework [215] and the embedding potentials were subsequently imported into the `DIRAC` calculations.

For the 4c-DR-TD-DFT calculations we selected a frequency range that covered the energy ranges bracketing the main features in the oxygen K-edge (around 510–540 eV) and the uranium M_4- and L_3-edges (around 3680–3710 eV and 17070–17100 eV, respectively). Given the expected shift in these simulations, the first frequency for each interval was obtained through TD-DFT simulations using the restricted-energy window scheme (REW-TD-DFT) [410] implementation on `DIRAC`.

In addition to the calculations with `DIRAC`, for the uranyl tetrachloride dianion species we have carried out standard (without embedding) TD-DFT calculations with the X2C Hamiltonian (including spin-orbit coupling, 2c-TD-DFT), triple-zeta basis functions with two polarization functions (TZ2P) [99], and the CAM-B3LYP functional with the Amsterdam Density Functional (ADF) software package [214]. As 4c-DR-TD-DFT calculations including spin-orbit coupling are not currently supported by ADF, we employed 2c-REW-TD-DFT calculations to target the core excited states of interest and employed the Tamm-Dancoff approximation (TDA) [411], as it yielded spectra of the same quality as standard TD-DFT calculations at a lower computational cost. A comparison of TD-DFT and TDA can be found in Figures A.1 and A.2 in the supplementary information.

Due to a lack of equivalent functionality in `DIRAC`, from the ADF 2c-REW-TD-DFT calculations we obtained natural transition orbitals (NTOs) [412], which we used to provide a qualitative analysis of the changes to the electronic structure involved in the core excitations of uranyl tetrachloride.

For simplicity, in the following, we shall refer to our 4c-DR-TD-CAM-B3LYP calculations as 4c-DR, and to our 2c-REW-TD-DFT and 2c-REW-TD-DFT-TDA CAM-B3LYP calculations as 2c-TD and 2c-TDA, respectively.

4.1.3 Results and discussion

In the following section, we present the theoretical absorption spectra at the oxygen K-edge and uranium M_4- and L_3-edges of the uranyl tetrachloride dianion ($UO_2Cl_4^{2-}$), a model in which the chloride ions bound to the equatorial plane of the uranyl ion (UO_2^{2+}) are represented by an FDE embedding potential (UO_2^{2+} @

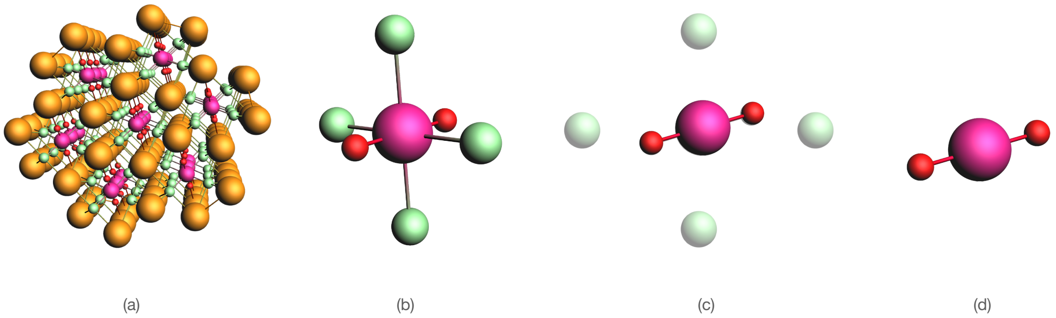

Figure 4.3: Reference system for this study: (a) Dicesium uranyl(VI) tetrachloride crystal ($Cs_2UO_2Cl_4$). Models here investigated: (b) uranyl(VI) tetrachloride dianion, $UO_2Cl_4^{2-}$ (c) uranyl(VI) ion in the FDE embedding potential of four chloride atoms, UO_2^{2+} @ Cl_4^{4-} and (d) bare uranyl(VI) ion, UO_2^{2+} (cesium: orange; uranium: pink; oxygen: red; chlorine: green). See Gomes et al. [167] for further details on the structural models.

Cl_4^{4-}), and the uranyl ion without any chloride ligands (respectively structures **b**, **c** and **d** in Figure 4.3).

Before discussing the relative performance of these different models, we focus on a comparison between our results for $UO_2Cl_4^{2-}$ and the available experimental spectra recorded for the $Cs_2UO_2Cl_4$ crystal. Our results will be interpreted on the basis of the dominant NTOs for each peak, depicted in Figure 4.4, whereas the simulated spectra are depicted in Figure 4.5.

From the NTO analysis we see that the dominant contributions involve low-lying virtual orbitals centered around the uranyl moiety, and as discussed below the associated excited states will be rather well described. That said, one should be careful if highly diffuse orbitals such as Rydberg orbitals [413, 414] are found to be involved in the transitions since apart from the general difficulty of describing such orbitals with standard Gaussian basis sets [415], not all density functional approximations can describe long-range interactions as accurately as CAM-B3LYP [222].

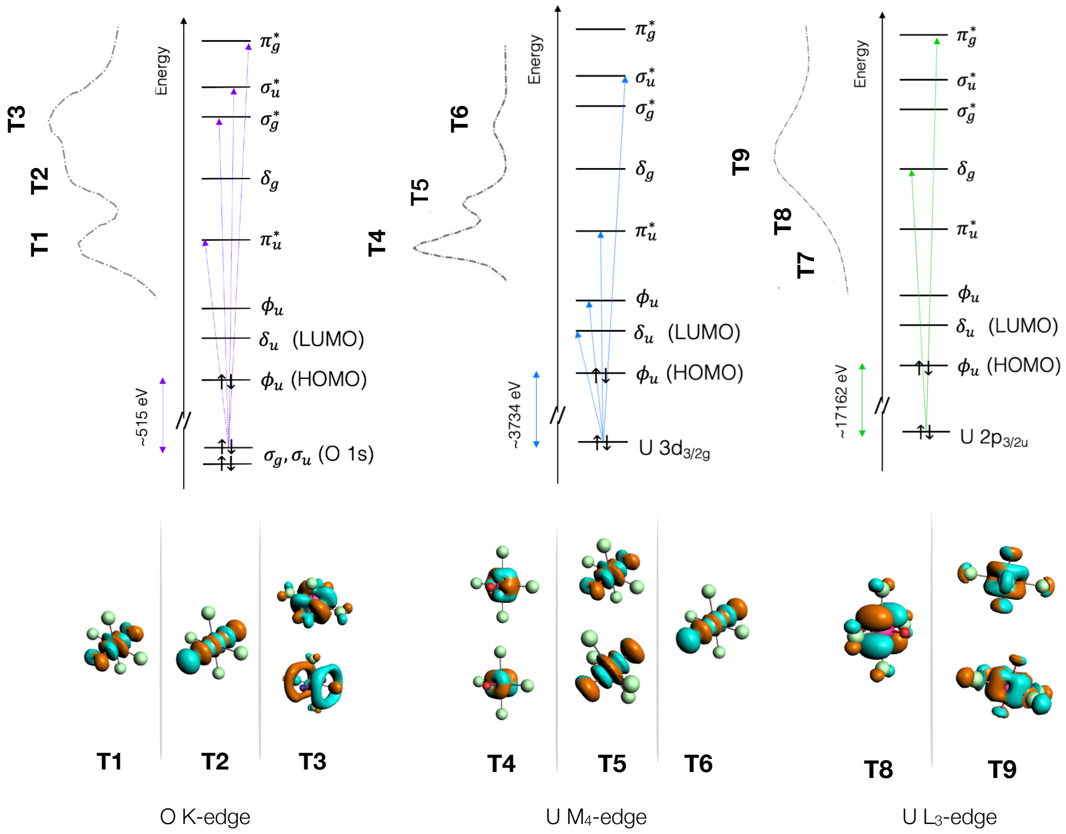

Figure 4.4: Top: Qualitative MO diagram for the relevant orbitals of uranyl being accessed in this work. Bottom: Dominant 2c-TD natural transition orbitals (NTOs) for the peaks pertaining to the oxygen K-edge, and uranium M_4- and L_3-edges. Plots have employed 0.03 as the isosurface value. See the text for the nature of the transitions (labeled **T1**–**T9**). We do not display NTOs for **T7** as the associated transition does not have intensity within the dipole approximation and is therefore not discussed. Digitalized spectra for the O K-edge was used with permission from Denning et al. Copyright 2002 AIP Publishing. Copyright 2015 American Chemical Society applies to the uranium edges.

Features in the X-ray absorption spectra

The absorption spectrum of the $Cs_2UO_2Cl_4$ crystal has been utilized in multiple studies as a tool to examine the electric properties of the uranyl(VI) ion in diverse environments, including one- and two-photon absorption at visible light [325, 416]. The X-ray Absorption Near Edge Structure (XANES) spectrum at the oxygen K-edge of $Cs_2UO_2Cl_4$ was first reported by Denning et al. [326] in the early 2000s, and the High Energy Resolution Fluorescence Detection (HERFD) spectra at the uranium M_4- and L_3-edges of $Cs_2UO_2Cl_4$ was reported by Vitova et al. [328] in the past decade.

As previously reported by Denning et al. [326], the O K-edge absorption spectrum (Figure 4.5 **a**) exhibits three prominent features identified as (**T1**) a low-intensity pre-edge feature at 531.4 eV corresponding to an O 1s $\rightarrow \pi_u^*$ transition, followed by (**T2**) an intermediate-intensity pre-edge feature around 534.1 eV, arising from an O 1s $\rightarrow \sigma_u^*$ transition, and (**T3**) the white-line feature at 536.5 eV, where an O 1s $\rightarrow \pi_g^*$ transition is observed.

Using the HERFD mode for the evaluation of the U M_4-edge spectra it is possible to achieve experimental spectral widths below the natural core-hole lifetime broadening of approximately 4 eV. As a result, the high-resolution U M_4-edge spectra in $Cs_2UO_2Cl_4$ exhibit three well-defined features (Figure 4.5 **b**), which have been reported in previous studies [40, 328]: (**T4**) a U $3d_{3/2g} \rightarrow 5f\delta_u$ and U $3d_{3/2g} \rightarrow 5f\phi_u$ excitation observed at 3726.4 eV, (**T5**) a U $3d_{3/2g} \rightarrow 5f\pi_u^*$ resonance at 3728.6 eV, and a satellite peak (**T6**) U $3d_{3/2g} \rightarrow 5f\sigma_u^*$ at 3732.3 eV.

Interpreting the spectra at the U L_3-edge (Figure 4.5 **c**) remains challenging due to the significant core-hole lifetime width spanned in this absorption edge, which extends between 7.4 – 8.4 eV [417, 418]. This results in a significant portion of the spectral content being obscured.

The first transition in this spectra is a $2p_{3/2u} \rightarrow 5f$ quadrupolar transition (**T7**) at 17168.8 eV, which is absent in our simulations. This is due to our use of the dipole approximation so that by symmetry the associated transition does not carry any intensity. Beyond that, the experimental white line is observed at 17175.2 eV, and our simulations predict that this feature it is mainly composed of (**T8, T9**) two $2p_{3/2u} \rightarrow (6d\delta_g, 6d\pi_g)$ contributions, with a separation of 3.5 eV.

Theoretical vs experimental peak positions

All of our calculated transition energies shown in Table 4.1 were considered for the analysis. We observe these are shifted in a very systematic manner to higher energies with respect to the experiment, with these differences of energy becoming increasingly pronounced at higher absorption edges. For instance, at the O K-edge, the energy shift values for the 2c-TDA and 4c-DR simulations are respectively 13.3 eV and 13.8 eV, whereas, for the U L_3-edge, these values are 95.2 eV and 86.3 eV. Therefore, in order to compare the theoretical and experimental results, we have aligned these based on specific transitions, identified by orange vertical lines in Figure 4.5.

	O K-edge		
	T1	T2	T3
	O 1s $\rightarrow \pi^*_u$	O 1s $\rightarrow \sigma^*_u$	O 1s $\rightarrow \pi^*_g$
2c-TDA	518.6 (-12.8)	521.4 (-12.7)	523.2 (-13.3)
4c-DR	518.5 (-12.9)	521.4 (-12.7)	522.7 (-13.8)
Exp. [326]	531.4	534.1	536.5
	U M_4-edge		
	T4	T5	T6
	U $3d_{3/2g} \rightarrow 5f\delta_u$	U $3d_{3/2g} \rightarrow \pi^*_u$	U $3d_{3/2g} \rightarrow 5f\sigma^*_u$
2c-TDA	3686.6 (-40.8)	3688.4 (-40.2)	3692.5 (-39.8)
4c-DR	3689.5 (-36.9)	3691.4 (-37.2)	3695.3 (-37.0)
Exp. [328]	3726.4	3728.6	3732.3
	U L_3-edge		
	T7	T8	T9
	U $2p_{3/2u} \rightarrow 5f$	U $2p_{3/2u} \rightarrow 6d\delta_g$	U $2p_{3/2u} \rightarrow 6d\pi_g$
2c-TDA	-	17076.5 (-95.2)	17080.0 (-95.2)
4c-DR	-	17085.4 (-86.3)	17088.9 (-86.3)
Exp. [328]	17168.8	17171.7	17175.2

Table 4.1: Transition energies (in eV) calculated using 2c-TDA and 4c-DR compared to experimental values for the O K-edge, U M_4-edge, and U L_3-edge. Shifts with respect to the experiment (in eV) are shown in parenthesis.

The increasing discrepancy between experimental and theoretical peak positions (and hence the increase in the value of the shift to be applied to theoretical results) for deeper cores is related to the difficulty of TD-DFT to properly account for the orbital relaxation that should accompany the creation of a core hole–which will be increasingly important as the core orbitals under consideration become closer to the nucleus.

The magnitude of orbital relaxation effects for the deeper core in heavy elements is clearly illustrated for ionization energies, obtained for small actinide species [374] with state-specific correlated methods (ΔMP2) or for heavy halogenated species [128, 419, 420] employing equation of motion coupled-cluster approaches (CVS-EOM-IP-CCSD), with the results by Halbert et al. [128] and Knecht et al. [420] illustrating that (small) differences between 2- and 4-component Hamiltonians as seen here may arise, depending on which 2-component approach is used. More recently, orbital relaxation has also been investigated for excitation energies at the U M_4-edge of the bare uranyl using multiconfigurational approaches [390, 392, 393].

In the latter case, Polly et al. [392] evaluated the performance of various active spaces in SO-RASSCF and SO-RASPT2 simulations. Their results to excitation energies at the U M_4-edge were found to overestimate experimental values by 12.9 eV and 17.4 eV at RASSCF and RASPT2 theory levels, respectively. This corresponds to about half of the overestimation found for our 4c-DR and 2c-TDA results (37.2 eV and 39.8 eV, respectively).

The relatively modest changes upon including dynamical electron correlation (about 5 eV) are consistent with the findings of South et al. [374] on the contribution from electron correlation (at MP2 level) to the binding energies in uranyl, as most of the core hole relaxation is coming from the orbital optimization enabled by the RASSCF approach. It is nevertheless interesting to note that the RASSCF calculations are closer to the experiment than RASPT2, suggesting a possible cancellation of errors when comparing the bare uranyl to the experimental system. We will return to this point when discussing the performance of embedding.

As final remarks, we note that the damping factors employed for determining the 4c-DR absorption spectra shown in Figure 4.5 are not arbitrary but were selected to best reflect the profile observed in the experimental data for the $Cs_2UO_2Cl_4$ crystal, after exploring different values for each edge. For the oxygen K-edge, the value is somewhat larger ($\gamma = 1.0$ eV) than for the uranium M_4- and

L_3-edges ($\gamma = 0.5$ eV), but nevertheless our results show that with these choices the key features of both conventional and high-resolution spectra can be clearly identified.

Furthermore, the broadening profile presented in Figure 4.5 was chosen to better fit the experimental data: for the O K-edge and U L_3-edge spectra, we employed a Voigt profile, and Gaussian function for the U M_4-edge. In the supplementary information, Figure A.3 presents the effect of the damping factors, and Figures A.4, **??**, and A.6 the effect of the broadening profiles on the simulated spectra.

Polarization dependence of calculated intensities

Synchrotron-based experiments can also handle dichroism in the X-ray regime. Linear dichroism is studied using angle-resolved and polarization-dependent X-ray absorption spectroscopy [326, 328, 421], while magnetic circular dichroism has been extensively studied through X-ray magnetic circular dichroism (XMCD) [422, 423].

By utilizing the damped-response theory, linear dichroism can be explored through the analysis of the components of the complex polarizability tensor ($\alpha_{xx}(\omega)$, $\alpha_{yy}(\omega)$, $\alpha_{zz}(\omega)$). As we shall see in the following, the breakdown into individual components–or here, due to the symmetry of the system into parallel (σ_{zz}) and perpendicular ($\sigma_{xx+yy} = \sigma_{xx} + \sigma_{yy}$) components with respect to the uranyl bond axis–is helpful to understand the origin of the asymmetries observed experimentally.

In Figure 4.5 we show the parallel and perpendicular contributions to the total absorption cross-section ($\sigma_{xx+yy+zz} = \sigma_{zz} + \sigma_{xx+yy}$) for the edges under investigation, alongside the experimental polarization-dependent spectra [326, 328], in which the angle indicated is the one between the incident light beam and the O-U-O axis in the $Cs_2UO_2Cl_4$ crystal.

Effects of polarization dependence are particularly prominent in the experimental spectra at the O K-edge by Denning et al. [326] and U L_3-edge by Vitova et al. [328] (Figure 4.5 **a** and 4.5 **c** respectively), which were recorded at greater incidence angles than the ones for the U M_4-edge. For clarity, here we will

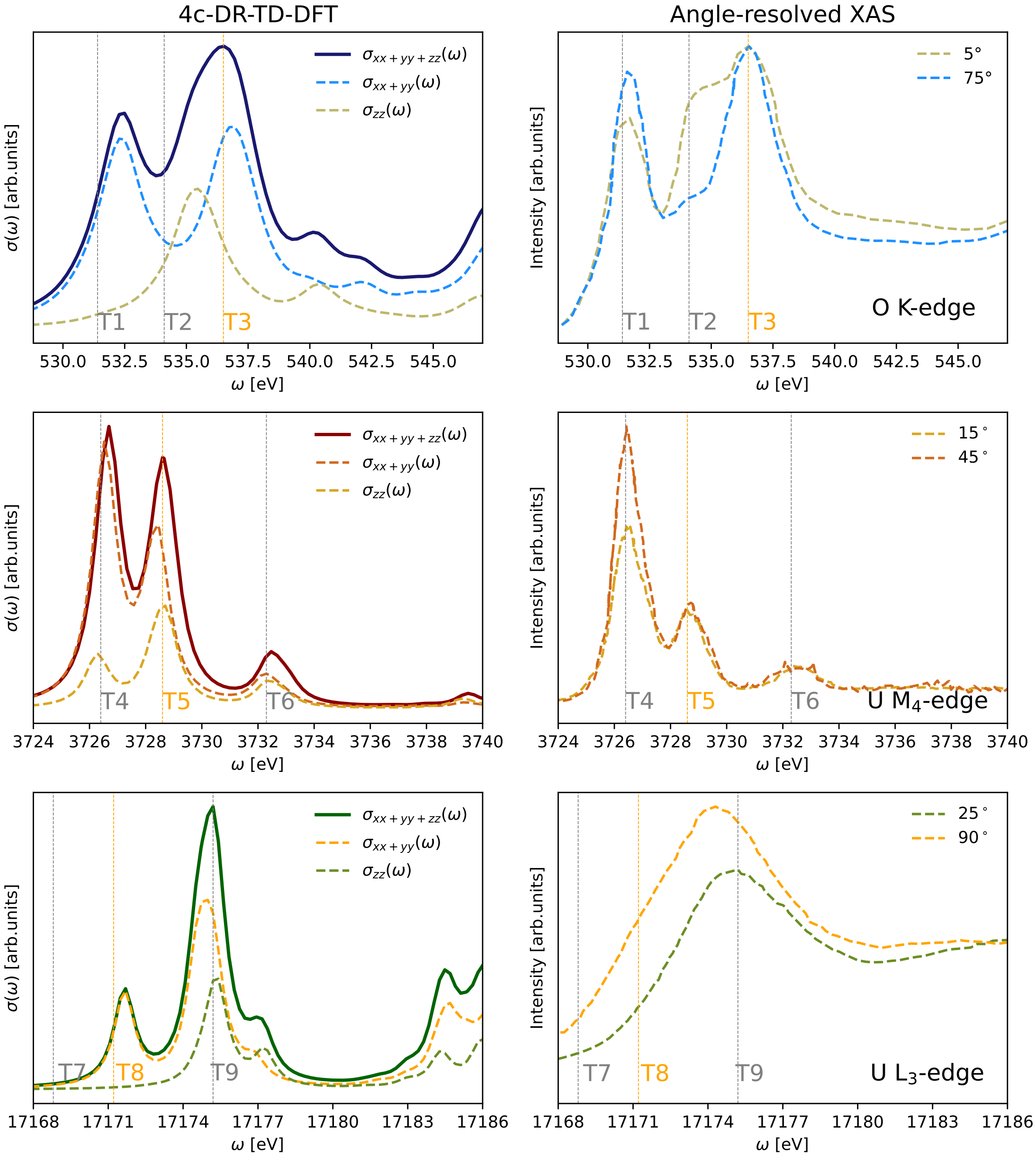

Figure 4.5: Left: Partial (dashed) and total (solid) contributions to total oscillator strengths in the 4c-DR XAS spectra at (a) oxygen K-edge and uranium (b) M_4- and (c) U L_3-edges of $UO_2Cl_4{}^{2-}$. Right: Experimental data ($Cs_2UO_2Cl_4$) at the O K-edge (digitized from Denning et al. [326]) and U M_4-, L_3-edges (digitized from Vitova et al. [328]). Digitalized spectra for the O K-edge were used with permission from Denning et al. Copyright 2002 AIP Publishing. Copyright 2015 American Chemical Society applies to the uranium edges. Spectra from this work reprinted with permission from Misael and Gomes. Copyright 2023 American Chemical Society. The angle indicated in the figures corresponds to the angle between the incident light beam and the O-U-O axis, respectively.

compare our results to the experiments under grazing and nearly perpendicular light incidence conditions.

For the O K-edge, our analysis finds that transitions **T1** and **T3** are dominated by perpendicularly polarized components with respect to the O-U-O axis, whereas **T2** was found to exhibit parallel polarization, in agreement with experiment. For the L_3-edge, we observe that **T8** is completely dominated by perpendicularly polarized components. For **T9**, the spectrum shows non-negligible contributions from the parallel component, which we consider to be consistent with the observation by Vitova et al. [328] that angle dependence shifts the U L_3-edge absorption edge to the right when incoming light is parallel to the O-U-O axis.

Finally, for the U M_4-edge (Figure 4.5 **b**), a strong angular dependence in the white line (**T4**) is observed, and as for the other edges, the perpendicular components are the major contributors to the intensity. For **T5** we see that the parallel component contributes proportionally more to the total signal, and this trend is accentuated for **T6**, for which we see nearly equal contributions from both components to the total intensity.

A closer look on the role of the equatorial ligands

Having established that 4c-DR and 2c-TDA can faithfully describe the spectra for the edges under consideration, we can turn to a comparison of the different structural models described in Figure 4.3 ($UO_2Cl_4^{2-}$, the bare uranyl ion and the uranyl ion embedded onto the equatorial chloride ligands) in order to gain further understanding on the role of the equatorial ligands.

As mentioned above, the core spectra of bare uranyl ion have been investigated by Polly et al. [392], but also by Sergentu et al. [390]. The embedded uranyl model (UO_2^{2+} @ Cl_4^{4-}), on the other hand, has only been previously investigated for valence excited states [167] and shown to yield a rather good description of the low-lying states of $UO_2Cl_4^{2-}$ in $Cs_2UO_2Cl_4$.

Given the high sensitivity of core excited states to the description of the environment around the absorbing sites, it remains to be seen to which extent the embedded model can faithfully reproduce the reference ($UO_2Cl_4^{2-}$) calculations.

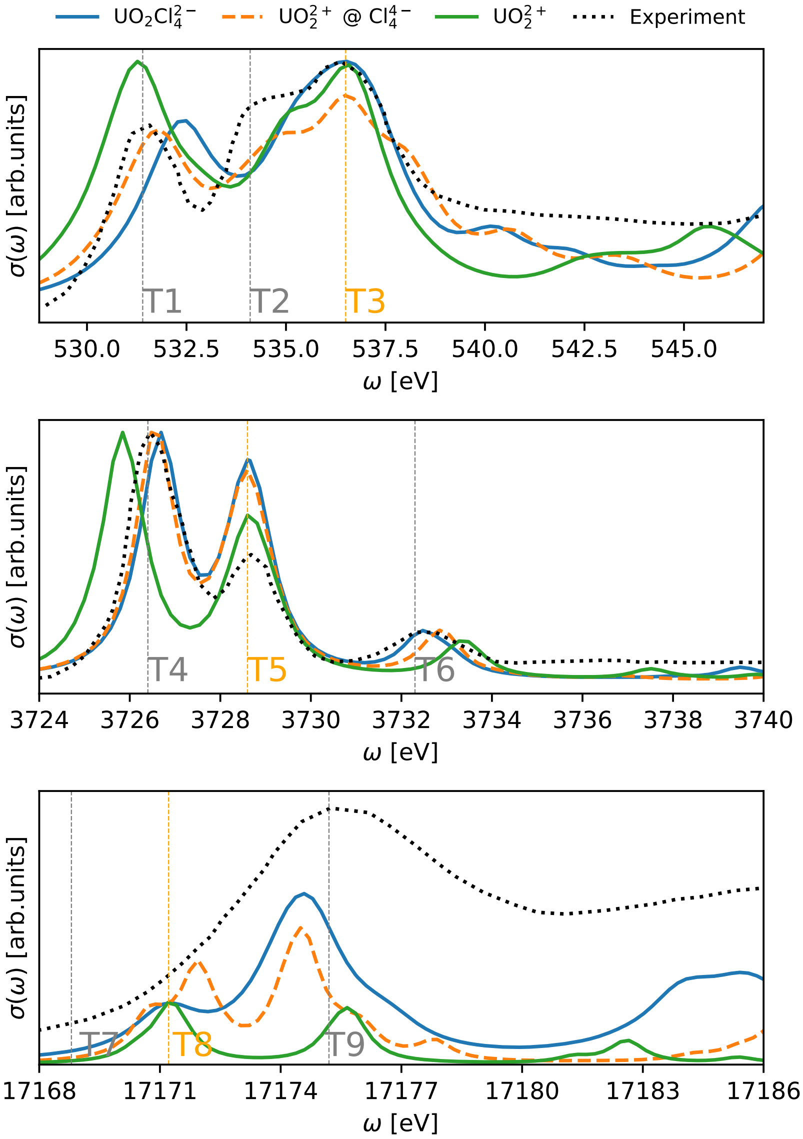

Figure 4.6: From top to bottom: Comparison of the 4c-DR XAS spectra at the oxygen K-edge, uranium M_4 and L_3-edges of UO_2^{2+}, UO_2^{2+} @ Cl_4^{4-} and $UO_2Cl_4^{2-}$. Experimental data at the O K-edge in $Cs_2UO_2Cl_4$ was digitized from Denning et al. [326], and for the U M_4- and L_3-edges from Vitova et al. [328], respectively. Digitalized spectra for the O K-edge was used with permission from Denning et al. Copyright 2002 AIP Publishing. Copyright 2015 American Chemical Society applies to the uranium edges. Spectra from this work reprinted with permission from Misael and Gomes. Copyright 2023 American Chemical Society.

In this respect, an interesting feature to track is the relative positions of the different peak maxima as well as their relative intensities, and how these compare to the experimental ones.

At the O K-edge (Figure 4.6, top), there are rather small differences between the energy shifts (less than 1 eV) with respect to the experiment among the three simulations. This is in line with a systematic error in the calculations due to the shortcomings in describing relaxation due to the creation of the core hole, mentioned in the previous section.

For the intensities, on the other hand, we observe for **T1** that the bare uranyl model shows a significant overestimation. Intensities for the reference and embedded models on the other hand are very similar to one another, though the maximum for the embedded model is slightly shifted to lower energies. For **T2** and **T3**, the different models show an overall good agreement with each other, and a finer comparison is more difficult than for **T1** in view of the overlapping contributions from different transitions to the final spectrum. We note however that for the bare and embedded uranyl the feature corresponding to the parallel component (**T2**, see Figure 4.5 **a**) appears slightly more shifted to the lower energies than for uranyl tetrachloride, resulting in the asymmetry in the region between **T2** and **T3**. We note that experimentally the intensity of absorption between **T2** and **T3** is rather sensitive to the polarization[326] (see Figure 4.5 **a**).

The simulations at the U M_4-edge spectra (Figure 4.6, middle) show an even better agreement between the embedding calculations and the reference ones than for the O K-edge, with both simulations reproducing the experiment rather well for all peaks. However, if the splitting between **T4** and **T5** is very well reproduced, we see that for the embedding calculation **T6** there is a slight shift in peak maximum to higher energies compared both to experiment and to the reference model while the latter two show again very good agreement. For the bare uranyl, on the other hand, we see a fairly significant overestimation of both **T4**-**T5** and **T5**-**T6** peak shifts compared to the reference model.

The ability of a theoretical model to accurately characterize peak splittings is of importance for the U M_4-edge since the solid-state community commonly attributes variations in peak splitting between the main feature and the satellite $5f_{\sigma^*}$ in actinyl spectra to changes in overlap-driven covalency from variations in

Method	System	peak positions			differences		
		T4	**T5**	**T6**	**T5-T4**	**T6-T4**	**T6-T5**
4c-DR	UO_2^{2+}	3689.0	3691.8	3696.5	2.8	7.5	4.7
RASSCF [390]	UO_2^{2+}	3750.1	3752.4	3758.0	2.3	7.9	5.6
RASSCF[a] [392]	UO_2^{2+}	3748.0	3750.1	3755.7	2.1	7.7	5.6
RASSCF[b] [392]	UO_2^{2+}	3750.6	3753.1	3759.4	2.5	8.8	6.3
RASPT2[b] [392]	UO_2^{2+}	3746.1	3748.8	3755.1	2.7	9.0	6.3
4c-DR	UO_2^{2+} @ Cl_4^{4-}	3690.1	3692.0	3696.2	1.9	6.1	4.2
4c-DR	$UO_2Cl_4^{2-}$	3689.5	3691.4	3695.3	1.9	5.8	3.9
FDMNES [424]	$Cs_2UO_2Cl_4$	3726.9	3729.3	3732.9	2.4	6.0	3.6
HERFD [328]	$Cs_2UO_2Cl_4$	3726.4	3728.6	3732.3	2.2	5.9	3.7

Active space: [a] 3d (σ_u,π_u)/5f, [b] 3d/5f

Table 4.2: U M_4-edge peak positions and differences (in eV) from theoretical molecular (4c-DR, RASPT2, and RASSCF) and finite-difference (FDMNES) calculations, and experiment (HERFD).

the An-O bond length, as suggested in the works of Kvashnina and Butorin [40], and Vitova and collaborators [21, 328]. This is somewhat at odds with the analysis based on *ab initio* simulations, such as that by Sergentu et al. [390] and also Polly et al. [392], which claim that there is not a clear correlation between those and the observed splitting in this spectrum. The natural localized molecular orbitals (NLMOs) analysis by Sergentu et al. [390] found a significant decrease in the σ covalency in the excited states of the actinyl absorption spectra at the M_4-edge of PuO_2^{2+}, NpO_2^{2+}, and UO_2^{2+}, in a trend that opposes the one observed in their ground states. Therefore, they were able to highlight the limitations of the previous interpretations of these spectra, by showing that the orbitals of the ground state should not be used as the sole guide in interpreting these actinyl spectra.

In Table 4.2, we present the peak positions and splitting of the U M_4-edge spectra obtained from experiments by Vitova et al. [328] and predicted by molecular *ab-initio* calculations (Sergentu et al. [390], Polly et al. [392] and this work) as well as *ab-initio* finite-difference calculations by Amidani et al. [424] using the FDMNES code [425, 426].

As previously discussed, the shortcomings of 4c-DR calculations in including relaxation result in excitation energies that are too low compared to experiment or RASSCF/RASPT2. The peak splitting values, on the other hand, indicate that despite better accounting for orbital relaxation, RASSCF and RASPT2 calculations do not compare more favorably to the experiment than 4c-DR calculations relying on the TDDFT/CAM-B3LYP, and changing the size of the active space changes peak positions by a few eV but peak splittings by a few tenths of eV. Relaxation aside, the comparable performance of CAM-B3LYP with respect to RASSCF/RASPT2 is in line with previous benchmark studies [427, 428], and has been explained in terms of its good ability to minimize self-interaction errors that plague other functionals, so that excitation energies can be reliably obtained with it, including for charge-transfer excitations [222, 429].

Taken as a whole we attribute the overestimation of peak splittings shown for all of these calculations to the lack of equatorial ligands since when these are included (embedding or supermolecular 4c-DR calculations) we achieve very good agreement with the experiment, especially for the **T6-T4** and **T6-T5** splittings. It is interesting to note that the RASPT2 approach, which one could expect to improve upon RASSCF, ends up further overestimating peak splittings. This could be due to a poor balance between orbital relaxation and the amount of dynamic correlation recovered with second-order perturbation theory, possibly coupled with the lack of equatorial ligands in the calculations.

Coming back to the **T6-T4** and **T6-T5** splittings, we observe slight differences between the embedding and supermolecule calculations, which would suggest that orbital interactions are somewhat more important for **T6** than for **T4** or **T5**, since for the **T5-T4** splitting for both models is essentially the same, whereas it increases slightly for **T6-T5**.

In the embedding calculation, apart from the symmetry breaking with respect to linear symmetry that allows for some mixing of the ϕ, δ spinors [430], the chloride ligands are included only through the embedding potential, which represents an effective interaction. As a result, by construction, the electrostatic interaction component of the embedding potential remains the dominant contribution. Therefore, the differences between the two models can be traced back to the lack of such interaction in the bare uranyl case.

The importance of electrostatic interactions, and the sensitivity of the actinyl electronic structure to these, have been addressed in more detail in our previous investigations of actinyl chlorides. First, for the valence states of uranyl [167], we have also considered a simple model with negative point charges placed in the positions of the chlorides and found that the valence excited states were in better agreement with uranyl tetrachloride than the bare uranyl, though this point-charge embedding model still showed poorer performance than the FDE (UO_2^{2+} @ Cl_4^{4-}) model. Second, in the investigation of f–f transitions in $NpO_2Cl_4^{2-}$ [430], we considered an embedding model equivalent to the one used here (NpO_2^{2+} @ Cl_4^{4-}), as well as a variant in which the density of the chlorides was not relaxed in the presence of the neptunyl ion, and a point-charge embedding model. We have shown the embedded model without relaxation of the chloride ligands' density yielded results that were comparable to the point charge one and did not reproduce the spectra of neptunyl chloride as well as NpO_2^{2+} @ Cl_4^{4-}.

From the above considerations and our current results, we argue that substantial contributions to the shifts in U M_4-edge peak position in table 4.2 can be attributed to electrostatic interactions with the equatorial ligands. It would be interesting to investigate to which extent that would hold for the core spectra of other actinyls, and that for ligands other than halides, but such a study is beyond the scope of this work. In the case of other actinyls, which may present a multi-reference ground-state, it will be in general necessary to replace the DFT treatment of the active subsystem by a wavefunction-based method, but as we have shown for neptunyl [430], that does not pose particular issues for the FDE calculations.

At the U L_3-edge (Figure 4.6) we have obtained the same results as South et al. [374] for the uranyl ion, which presents a second feature (**T9**) quite shifted to the right, therefore not being compatible with any spectra recorded at this absorption edge for uranium-containing species. The embedding calculation presents a broader and more intense **T8** feature, with the **T9** resembling rather well that of the reference model.

We note that here we have not considered more sophisticated models in which the crystal environment in $Cs_2UO_2Cl_4$ beyond the equatorial chloride ligands (structure **a** in Figure 4.3) are included in the embedding potential. This is due to the fact that in our previous investigation of valence excited states [167] we have compared the results for the embedded uranyl tetrachloride model employed here (UO_2^{2+} @ Cl_4^{4-}) with others in which the effect of the rest of the crystal was taken into account by embedding potentials. In these potentials we defined a frozen density region, consisting of the equatorial chlorides plus 20 uranyl tetrachloride and 90 cesium atoms surrounding the central uranyl unit; and beyond this quantum mechanical region, an array of point charges was used to simulate the long-range electrostatics in the crystal.

For a first model, in which all subsystem densities but that of the chloride equatorial ligands were kept frozen, we observed for the 12 lowest valence excited states changes in excitation energies that differed at most by 0.015 eV (with discrepancies being on average of about 0.0075 eV, in absolute value) from the UO_2^{2+} @ Cl_4^{4-} model. Furthermore, when the density of the nearest cesium atoms was also relaxed, the excitation energies only changed by around 0.002-0.004 eV.

As discussed by Gomes et al. [167], the physical process behind these changes is that the effect of the crystal environment lowers the energies of both occupied and virtual orbitals by roughly the same amounts. In addition to that, the energies of occupied valence [167, 430, 431] and core levels [432] are shifted by essentially the same amount by the environment. With that, relative measures such as excitation energies turn out to be weakly affected by the environment.

Apart from the arguments above, we consider the suitability of our uranyl tetrachloride models to be further supported by the good agreement between all of our peak splittings for the uranyl tetrachloride models and those from Amidani et al. [424], obtained with the FDMNES method.

In the latter calculation, all atoms within a 6 Å radius around the absorbing uranium atom in the $Cs_2UO_2Cl_4$ crystal are taken into account, which is in between our models without and with accounting for the rest of the crystal. We note that the FDMNES calculations are also based on DFT, and account for scalar and spin-orbit relativistic effects, but differ qualitatively from ours in that they include the effect of core hole creation through a screening parameter. With that, their absolute peak positions are also in good agreement with the experiment, while ours require a shift in energy to be compared to the experiment.

For ionizations on the other hand long-range interactions with the environment will be important [167, 431, 432], and will require the use of more sophisticated structural models. We shall address the ionizations of uranyl in $Cs_2UO_2Cl_4$ in a separate publication.

4.1.4 Conclusions

We have carried out an evaluation of relativistic quantum chemistry approaches for the calculation of excitation energies at the oxygen K-edge and uranium M_4-, L_3-edges, for the $UO_2Cl_4^{2-}$ system which makes up the $Cs_2UO_2Cl_4$ crystal. Besides calculating on this system, we have also investigated the performance of two other structural models, the bare uranyl ion and the uranyl ion embedded (via the frozen density embedding method, FDE) in an environment made up of the chloride equatorial ligands.

For these excitation energies, the use of the Coulomb-attenuating functional CAM-B3LYP in four-component damped-response simulations produced results that are consistent with the features observed in both conventional XANES and HERFD experiments. Additionally, through the analysis of natural transition orbitals (NTOs) obtained from equivalent two-component time-dependent DFT calculations, we showed that the O K-edge spectra primarily provide insight into the low-lying antibonding states of π_u^*, σ_u^* and π_g^* symmetries centered in the uranyl unit. In contrast, the lowest energy orbitals accessed at the U M_4- and U L_3- absorption edges are the uranium 5fϕ_u/δ_u and 6dδ_g/π_g non-bonding orbitals. These observations are in line with previous investigations.

We have determined that the bare uranyl model shows significant changes in spectral profiles in comparison to structural models containing equatorial ligands, notably in terms of relative intensities but also to some extent with respect to relative peak positions. This is seen for the uranium edges, to which the equatorial ligands are attached, but also for the oxygen K-edge.

In the soft and tender X-ray regime (O K- and U M_4-edge, respectively), we have observed that our simulations for the embedded model yield both excitation energies and intensities in very good agreement with those obtained for the $UO_2Cl_4^{2-}$ ion, though in the hard X-ray regime (U L_3-edge) this approximate model still performs well but deviates more significantly from the results obtained for the anion.

In conclusion, our study has provided valuable insights into the impact of equatorial ligands on the X-ray absorption spectra of the uranyl ion. Our findings emphasize the limitations of relying solely on a structural model consisting of either the bare uranyl ion or the ground state structure of the uranyl site, as these models do not accurately account for the influence of the equatorial ligands on peak positions.

Furthermore, our work demonstrates the potential of using accurate embedded models, such as those that can be constructed with frozen density embedding, to semi-quantitatively simulate actinyl core spectra. FDE-based embedding models have already been employed with multireference wavefunction-based treatment for the active subsystem, to treat systems that are challenging for DFT or other single-reference methods, though not yet for core spectra of actinides employing accurate ab initio relativistic quantum chemistry methods.

Bibliography of the current chapter

(1) Willmott, P., *An introduction to synchrotron radiation: techniques and applications*; John Wiley & Sons: 2019.

(3) Stöhr, J., *NEXAFS spectroscopy*; Springer Science & Business Media: 2013; Vol. 25.

(5) Lv, B.; Qian, T.; Ding, H. Angle-resolved photoemission spectroscopy and its application to topological materials. *Nature Reviews Physics* **2019**, *1*, 609–626.

(20) Vitova, T.; Kvashnina, K.; Nocton, G.; Sukharina, G.; Denecke, M.; Butorin, S.; Mazzanti, M.; Caciuffo, R.; Soldatov, A.; Behrends, T., et al. High energy resolution x-ray absorption spectroscopy study of uranium in varying valence states. *Physical Review B* **2010**, *82*, 235118.

(21) Vitova, T.; Pidchenko, I.; Fellhauer, D.; Bagus, P. S.; Joly, Y.; Pruessmann, T.; Bahl, S.; Gonzalez-Robles, E.; Rothe, J.; Altmaier, M., et al. The role of the 5 f valence orbitals of early actinides in chemical bonding. *Nature communications* **2017**, *8*, 16053.

(33) Krylov, A. I. From orbitals to observables and back. *The Journal of Chemical Physics* **2020**, *153*, 080901.

(40) Kvashnina, K. O.; Butorin, S. M. High-energy resolution X-ray spectroscopy at actinide M 4, 5 and ligand K edges: what we know, what we want to know, and what we can know. *Chemical Communications* **2022**, *58*, 327–342.

(46) Oher, H.; Réal, F.; Vercouter, T.; Vallet, V. Investigation of the Luminescence of [UO2X4] 2–(X= Cl, Br) Complexes in the Organic Phase Using Time-Resolved Laser-Induced Fluorescence Spectroscopy and Quantum Chemical Simulations. *Inorganic Chemistry* **2020**, *59*, 5896–5906.

(47) Oher, H.; Ferru, G.; Couston, L.; Berthon, L.; Guillaumont, D.; Réal, F.; Vercouter, T.; Vallet, V. Influence of the First Coordination of Uranyl on Its Luminescence Properties: A Study of Uranyl Binitrate with N, N-Dialkyl Amide DEHiBA and Water. *Inorganic Chemistry* **2021**, *61*, 890–901.

(48) Oher, H.; Vercouter, T.; Réal, F.; Shang, C.; Reiller, P. E.; Vallet, V. Influence of Alkaline Earth Metal Ions on Structures and Luminescent Properties of Na m M n UO2 (CO3) 3 (4–m–2 n)–(M= Mg, Ca; m, n= 0–2): Time-Resolved Fluorescence Spectroscopy and Ab Initio Studies. *Inorganic Chemistry* **2020**, *59*, 15036–15049.

(99) Van Lenthe, E.; Baerends, E. J. Optimized Slater-type basis sets for the elements 1–118. *Journal of computational chemistry* **2003**, *24*, 1142–1156.

(125) Norman, P.; Dreuw, A. Simulating X-ray spectroscopies and calculating core-excited states of molecules. *Chemical reviews* **2018**, *118*, 7208–7248.

(126) Vidal, M. L.; Feng, X.; Epifanovsky, E.; Krylov, A. I.; Coriani, S. New and efficient equation-of-motion coupled-cluster framework for core-excited and core-ionized states. *Journal of Chemical Theory and Computation* **2019**, *15*, 3117–3133.

(128) Halbert, L.; Vidal, M. L.; Shee, A.; Coriani, S.; Severo Pereira Gomes, A. Relativistic EOM-CCSD for Core-Excited and Core-Ionized State Energies Based on the Four-Component Dirac–Coulomb (- Gaunt) Hamiltonian. *Journal of Chemical Theory and Computation* **2021**, *17*, 3583–3598.

(156) Gomes, A. S. P.; Jacob, C. R. Quantum-chemical embedding methods for treating local electronic excitations in complex chemical systems. *Annual Reports Section" C"(Physical Chemistry)* **2012**, *108*, 222–277.

(158) Jones, L. O.; Mosquera, M. A.; Schatz, G. C.; Ratner, M. A. Embedding methods for quantum chemistry: Applications from materials to life sciences. *Journal of the American Chemical Society* **2020**, *142*, 3281–3295.

(167) Gomes, A. S. P.; Jacob, C. R.; Réal, F.; Visscher, L.; Vallet, V. Towards systematically improvable models for actinides in condensed phase: the electronic spectrum of uranyl in Cs 2 UO 2 Cl 4 as a test case. *Physical Chemistry Chemical Physics* **2013**, *15*, 15153–15162.

(168) Réal, F.; Vallet, V.; Marian, C.; Wahlgren, U. Theoretical investigation of the energies and geometries of photoexcited uranyl (VI) ion: A comparison between wave-function theory and density functional theory. *The Journal of chemical physics* **2007**, *127*, 214302.

(196) Caciuffo, R.; Lander, G. H. X-ray synchrotron radiation studies of actinide materials. *Journal of Synchrotron Radiation* **2021**, *28*, 1692–1708.

(199) Rothe, J.; Altmaier, M.; Dagan, R.; Dardenne, K.; Fellhauer, D.; Gaona, X.; González-Robles Corrales, E.; Herm, M.; Kvashnina, K. O.; Metz, V., et al. Fifteen years of radionuclide research at the KIT synchrotron source in the context of the nuclear waste disposal safety case. *Geosciences* **2019**, *9*, 91.

(200) Scheinost, A. C.; Claussner, J.; Exner, J.; Feig, M.; Findeisen, S.; Hennig, C.; Kvashnina, K. O.; Naudet, D.; Prieur, D.; Rossberg, A., et al. ROBL-II at ESRF: a synchrotron toolbox for actinide research. *Journal of Synchrotron Radiation* **2021**, *28*, 333–349.

(203) Tobin, J.; Ramanantoanina, H.; Daul, C.; Roussel, P.; Yu, S.-W.; Nowak, S.; Alonso-Mori, R.; Kroll, T.; Nordlund, D.; Weng, T.-C., et al. Unoccupied electronic structure of actinide dioxides. *Physical Review B* **2022**, *105*, 125129.

(214) Te Velde, G. t.; Bickelhaupt, F. M.; Baerends, E. J.; Fonseca Guerra, C.; van Gisbergen, S. J.; Snijders, J. G.; Ziegler, T. Chemistry with ADF. *Journal of Computational Chemistry* **2001**, *22*, 931–967.

(215) Jacob, C. R.; Beyhan, S. M.; Bulo, R. E.; Gomes, A. S. P.; Götz, A. W.; Kiewisch, K.; Sikkema, J.; Visscher, L. PyADF—A scripting framework for multiscale quantum chemistry. *Journal of computational chemistry* **2011**, *32*, 2328–2338.

(222) Tecmer, P.; Bast, R.; Ruud, K.; Visscher, L. Charge-Transfer Excitations in Uranyl Tetrachloride ([UO2Cl4] 2–): How Reliable are Electronic Spectra from Relativistic Time-Dependent Density Functional Theory? *The Journal of Physical Chemistry A* **2012**, *116*, 7397–7404.

(225) Konecny, L.; Vicha, J.; Komorovsky, S.; Ruud, K.; Repisky, M. Accurate X-ray absorption spectra near L-and M-edges from relativistic four-component damped response time-dependent density functional theory. *Inorganic chemistry* **2021**, *61*, 830–846.

(229) Ernzerhof, M.; Scuseria, G. E. Assessment of the Perdew–Burke–Ernzerhof exchange-correlation functional. *The Journal of chemical physics* **1999**, *110*, 5029–5036.

(260) Saue, T. Relativistic Hamiltonians for chemistry: A primer. *ChemPhysChem* **2011**, *12*, 3077–3094.

(267) Liu, W. Essentials of relativistic quantum chemistry. *The Journal of chemical physics* **2020**, *152*, 180901.

(268) Dyall, K. G.; Fægri Jr, K., *Introduction to relativistic quantum chemistry*; Oxford University Press: 2007.

(269) Reiher, M.; Wolf, A., *Relativistic quantum chemistry: the fundamental theory of molecular science*; John Wiley & Sons: 2014.

(323) Misael, W.; Gomes, A. Core Excitations of Uranyl in Cs2UO2Cl4 from Relativistic Embedded Damped Response Time-Dependent Density Functional Theory Calculations. *Inorganic Chemistry* **2023**, *62*, 11589–11601.

(324) Stöhr, J., *NEXAFS spectroscopy*; Springer Science & Business Media: 1992; Vol. 25.

(325) Denning, R.; Snellgrove, T.; Woodwark, D. The electronic structure of the uranyl ion: Part I. The electronic spectrum of Cs2UO2Cl4. *Molecular Physics* **1976**, *32*, 419–442.

(326) Denning, R.; Green, J.; Hutchings, T.; Dallera, C.; Tagliaferri, A.; Giarda, K.; Brookes, N.; Braicovich, L. Covalency in the uranyl ion: A polarized x-ray spectroscopic study. *The Journal of Chemical Physics* **2002**, *117*, 8008–8020.

(327) Denning, R. G. Electronic structure and bonding in actinyl ions and their analogs. *The Journal of Physical Chemistry A* **2007**, *111*, 4125–4143.

(328) Vitova, T.; Green, J. C.; Denning, R. G.; Löble, M.; Kvashnina, K.; Kas, J. J.; Jorissen, K.; Rehr, J. J.; Malcherek, T.; Denecke, M. A. Polarization dependent high energy resolution X-ray absorption study of dicesium uranyl tetrachloride. *Inorganic chemistry* **2015**, *54*, 174–182.

(329) Plasser, F.; Wormit, M.; Dreuw, A. New tools for the systematic analysis and visualization of electronic excitations. I. Formalism. *The Journal of chemical physics* **2014**, *141*, 024106.

(330) Batista, E. R.; Martin, R. L. Natural transition orbitals. *Encyclopedia of Computational Chemistry* **2002**.

(331) Crossland, I., *Nuclear fuel cycle science and engineering*; Elsevier: 2012.

(332) Veliscek-Carolan, J. Separation of actinides from spent nuclear fuel: A review. *Journal of hazardous materials* **2016**, *318*, 266–281.

(333) Mathur, J.; Murali, M.; Nash, K. Actinide partitioning—a review. *Solvent extraction and ion exchange* **2001**, *19*, 357–390.

(334) Hu, Y.; Shen, Z.; Li, B.; Tan, X.; Han, B.; Ji, Z.; Wang, J.; Zhao, G.; Wang, X. State-of-the-art progress for the selective crystallization of actinides, synthesis of actinide compounds and their functionalization. *Journal of Hazardous Materials* **2022**, *426*, 127838.

(335) De Jesus, K.; Rodriguez, R.; Baek, D.; Fox, R.; Pashikanti, S.; Sharma, K. Extraction of lanthanides and actinides present in spent nuclear fuel and in electronic waste. *Journal of Molecular Liquids* **2021**, *336*, 116006.

(336) Denecke, M. A.; Bryan, N.; Kalmykov, S.; Morris, K.; Quinto, F. In *Experimental and theoretical approaches to actinide chemistry*; Wiley Online Books: 2018.

(337) Pavlyuk, A. O.; Kotlyarevskii, S. G.; Kan, R. I.; Volkova, A. G.; Yapaskurt, V. O.; Zakharova, E. V.; Shiryaev, A. A. Actinides and fission products in reactor graphite after loss-of-flow accident. *npj Materials Degradation* **2022**, *6*, 23.

(338) Van der Meeren, A.; Angulo, J. F.; Bohand, S.; Griffiths, N. M. A quick and simple in vitro assay to predict bioavailability of actinides following accidental exposure. *Toxicology in Vitro* **2019**, *58*, 142–149.

(339) Grambow, B.; Nitta, A.; Shibata, A.; Koma, Y.; Utsunomiya, S.; Takami, R.; Fueda, K.; Ohnuki, T.; Jegou, C.; Laffolley, H., et al. Ten years after the NPP accident at Fukushima: review on fuel debris behavior in contact with water. *Journal of Nuclear Science and Technology* **2022**, *59*, 1–24.

(340) Hu, K.-Q.; Huang, Z.-W.; Zhang, Z.-H.; Mei, L.; Qian, B.-B.; Yu, J.-P.; Chai, Z.-F.; Shi, W.-Q. Actinide-Based Porphyrinic MOF as a Dehydrogenation Catalyst. *Chemistry–A European Journal* **2018**, *24*, 16766–16769.

(341) Leduc, J.; Frank, M.; Jürgensen, L.; Graf, D.; Raauf, A.; Mathur, S. Chemistry of actinide centers in heterogeneous catalytic transformations of small molecules. *ACS Catalysis* **2019**, *9*, 4719–4741.

(342) Dennett, C. A.; Poudel, N.; Simmonds, P. J.; Tiwari, A.; Hurley, D. H.; Gofryk, K. Towards actinide heterostructure synthesis and science. *Nature Communications* **2022**, *13*, 2221.

(343) Abney, C. W.; Mayes, R. T.; Saito, T.; Dai, S. Materials for the recovery of uranium from seawater. *Chemical reviews* **2017**, *117*, 13935–14013.

(344) Parker, B.; Zhang, Z.; Rao, L.; Arnold, J. An overview and recent progress in the chemistry of uranium extraction from seawater. *Dalton Transactions* **2018**, *47*, 639–644.

(345) Ji, S.; Su, M.; Liao, C.; Ma, S.; Wang, Z.; Shih, K.; Chang, C.-K.; Lee, J.-F.; Chan, T.-S.; Li, Y. Synchrotron x-ray spectroscopy investigation of the Ca1- xLnxZrTi2- x (Al, Fe) xO7 zirconolite ceramics (Ln= La, Nd, Gd, Ho, Yb). *Journal of the American Ceramic Society* **2020**, *103*, 1463–1475.

(346) Vallejo, K. D.; Kabir, F.; Poudel, N.; Marianetti, C.; Hurley, D. H.; Simmonds, P.; Dennett, C. A.; Gofryk, K. Advances in actinide thin films: synthesis, properties, and future directions. *Reports on Progress in Physics* **2022**.

(347) Zhai, B.; Tian, Q.; Li, N.; Yan, M.; Henderson, M. J. SAXS study of the formation and structure of polynuclear thorium (IV) colloids and thorium dioxide nanoparticles. *Journal of Synchrotron Radiation* **2022**, *29*.

(348) Pallares, R. M.; Abergel, R. J. Transforming lanthanide and actinide chemistry with nanoparticles. *Nanoscale* **2020**, *12*, 1339–1348.

(349) Ion, R.-M.; Sorescu, A.-A.; Nuta, A. In *Handbook of Greener Synthesis of Nanomaterials and Compounds*; Elsevier: 2021, pp 355–388.

(350) Bonato, L.; Virot, M.; Dumas, T.; Mesbah, A.; Dalodière, E.; Blanco, O. D.; Wiss, T.; Le Goff, X.; Odorico, M.; Prieur, D., et al. Probing the local structure of nanoscale actinide oxides: a comparison between PuO 2 and ThO 2 nanoparticles rules out PuO 2+ x hypothesis. *Nanoscale Advances* **2020**, *2*, 214–224.

(351) Sedigh Rahimabadi, P.; Khodaei, M.; Koswattage, K. R. Review on applications of synchrotron-based X-ray techniques in materials characterization. *X-Ray Spectrometry* **2020**, *49*, 348–373.

(352) Wernet, P. Chemical interactions and dynamics with femtosecond X-ray spectroscopy and the role of X-ray free-electron lasers. *Philosophical Transactions of the Royal Society A* **2019**, *377*, 20170464.

(353) Golubev, N. V.; Vanıček, J.; Kuleff, A. I. Core-valence attosecond transient absorption spectroscopy of polyatomic molecules. *Physical Review Letters* **2021**, *127*, 123001.

(354) Van Bokhoven, J. A.; Lamberti, C., *X-ray absorption and X-ray emission spectroscopy: theory and applications*; John Wiley & Sons: 2016; Vol. 1.

(355) Iwasawa, Y.; Asakura, K.; Tada, M., *XAFS techniques for catalysts, nanomaterials, and surfaces*; Springer: 2017.

(356) Stöhr, J. What are X-rays, Anyway: A Modern View of the Nature of Light and its Implications for the Future of X-ray Science, 2019.

(357) Vitova, T.; Pidchenko, I.; Fellhauer, D.; Pruessmann, T.; Bahl, S.; Dardenne, K.; Yokosawa, T.; Schimmelpfennig, B.; Altmaier, M.; Denecke, M., et al. Exploring the electronic structure and speciation of aqueous and colloidal Pu with high energy resolution XANES and computations. *Chemical Communications* **2018**, *54*, 12824–12827.

(358) Zegke, M.; Zhang, X.; Pidchenko, I.; Hlina, J. A.; Lord, R. M.; Purkis, J.; Nichol, G. S.; Magnani, N.; Schreckenbach, G.; Vitova, T., et al. Differential uranyl (v) oxo-group bonding between the uranium and metal cations from groups 1, 2, 4, and 12; a high energy resolution X-ray absorption, computational, and synthetic study. *Chemical science* **2019**, *10*, 9740–9751.

(359) Popa, K.; Prieur, D.; Manara, D.; Naji, M.; Vigier, J.-F.; Martin, P. M.; Blanco, O. D.; Scheinost, A. C.; Prü*β*mann, T.; Vitova, T., et al. Further insights into the chemistry of the Bi–U–O system. *Dalton Transactions* **2016**, *45*, 7847–7855.

(360) Lindroth, E.; Calegari, F.; Young, L.; Harmand, M.; Dudovich, N.; Berrah, N.; Smirnova, O. Challenges and opportunities in attosecond and XFEL science. *Nature Reviews Physics* **2019**, *1*, 107–111.

(361) Zimina, A.; Dardenne, K.; Denecke, M. A.; Grunwaldt, J.; Huttel, E.; Lichtenberg, H.; Mangold, S.; Pruessmann, T.; Rothe, J.; Steininger, R., et al. In *Journal of Physics: Conference Series*, 2016; Vol. 712, p 012019.

(362) Shi, W.-Q.; Yuan, L.-Y.; Wang, C.-Z.; Wang, L.; Mei, L.; Xiao, C.-L.; Zhang, L.; Li, Z.-J.; Zhao, Y.-L.; Chai, Z.-F. Exploring actinide materials through synchrotron radiation techniques. *Synchrotron Radiation in Materials Science: Light Sources, Techniques, and Applications* **2018**, *2*, 389–509.

(363) Husar, R.; Dumas, T.; Schlegel, M. L.; Schlegel, D.; Guillaumont, D.; Solari, P.-L.; Moisy, P. X-ray absorption spectroscopy and actinide electrochemistry: a setup dedicated to radioactive samples applied to neptunium chemistry. *Journal of Synchrotron Radiation* **2022**, *29*.

(364) Vitova, T.; Denecke, M.; Göttlicher, J.; Jorissen, K.; Kas, J.; Kvashnina, K.; Prüßmann, T.; Rehr, J.; Rothe, J. In *Journal of Physics: Conference Series*, 2013; Vol. 430, p 012117.

(365) Kvashnina, K.; Kvashnin, Y.; Butorin, S. Role of resonant inelastic X-ray scattering in high-resolution core-level spectroscopy of actinide materials. *Journal of Electron Spectroscopy and Related Phenomena* **2014**, *194*, 27–36.

(366) Nocton, G.; Mazzanti, M. Coordination Chemistry of Actinides. *Lanthanides And Actinides, The: Synthesis, Reactivity, Properties And Applications* **2021**, 149.

(367) McSkimming, A.; Su, J.; Cheisson, T.; Gau, M. R.; Carroll, P. J.; Batista, E. R.; Yang, P.; Schelter, E. J. Coordination chemistry of a strongly-donating hydroxylamine with early actinides: An investigation of redox properties and electronic structure. *Inorganic Chemistry* **2018**, *57*, 4387–4394.

(368) Gibson, J. K.; de Jong, W. A. Experimental and Theoretical Approaches to Actinide Chemistry. **2018**.

(369) Ganguly, G.; Sergentu, D.-C.; Autschbach, J. Ab Initio Analysis of Metal–Ligand Bonding in An (COT) 2 with An= Th, U in Their Ground-and Core-Excited States. *Chemistry–A European Journal* **2020**, *26*, 1776–1788.

(370) Besley, N. A. Modeling of the spectroscopy of core electrons with density functional theory. *Wiley Interdisciplinary Reviews: Computational Molecular Science* **2021**, *11*, e1527.

(371) Zheng, X.; Cheng, L. Performance of delta-coupled-cluster methods for calculations of core-ionization energies of first-row elements. *Journal of chemical theory and computation* **2019**, *15*, 4945–4955.

(372) Wenzel, J.; Holzer, A.; Wormit, M.; Dreuw, A. Analysis and comparison of CVS-ADC approaches up to third order for the calculation of core-excited states. *The Journal of Chemical Physics* **2015**, *142*, 214104.

(373) Sen, S.; Shee, A.; Mukherjee, D. Inclusion of orbital relaxation and correlation through the unitary group adapted open shell coupled cluster theory using non-relativistic and scalar relativistic Hamiltonians to study the core ionization potential of molecules containing light to medium-heavy elements. *The Journal of Chemical Physics* **2018**, *148*, 054107.

(374) South, C.; Shee, A.; Mukherjee, D.; Wilson, A. K.; Saue, T. 4-Component relativistic calculations of L 3 ionization and excitations for the isoelectronic species UO 2 2+, OUN+ and UN 2. *Physical Chemistry Chemical Physics* **2016**, *18*, 21010–21023.

(375) Park, J. W.; Al-Saadon, R.; MacLeod, M. K.; Shiozaki, T.; Vlaisavljevich, B. Multireference electron correlation methods: Journeys along potential energy surfaces. *Chemical Reviews* **2020**, *120*, 5878–5909.

(376) Lischka, H.; Nachtigallova, D.; Aquino, A. J.; Szalay, P. G.; Plasser, F.; Machado, F. B.; Barbatti, M. Multireference approaches for excited states of molecules. *Chemical reviews* **2018**, *118*, 7293–7361.

(377) Norman, P.; Ågren, H. Geometry optimization of core electron excited molecules. *Journal of Molecular Structure: THEOCHEM* **1997**, *401*, 107–115.

(378) Gulania, S.; Kjønstad, E. F.; Stanton, J. F.; Koch, H.; Krylov, A. I. Equation-of-motion coupled-cluster method with double electron-attaching operators: Theory, implementation, and benchmarks. *The Journal of Chemical Physics* **2021**, *154*, 114115.

(379) Vidal, M. L.; Pokhilko, P.; Krylov, A. I.; Coriani, S. Equation-of-motion coupled-cluster theory to model L-edge x-ray absorption and photoelectron spectra. *The journal of physical chemistry letters* **2020**, *11*, 8314–8321.

(380) Pavošević, F.; Rousseau, B. J.; Hammes-Schiffer, S. Multicomponent orbital-optimized perturbation theory methods: Approaching coupled cluster accuracy at lower cost. *The Journal of Physical Chemistry Letters* **2020**, *11*, 1578–1583.

(381) Krykunov, M.; Ziegler, T. Self-consistent formulation of constricted variational density functional theory with orbital relaxation. implementation and applications. *Journal of Chemical Theory and Computation* **2013**, *9*, 2761–2773.

(382) Pyykkö, P. In *Advances in quantum chemistry*; Elsevier: 1978; Vol. 11, pp 353–409.

(383) Thiel, W.; Hummer, G. Methods for computational chemistry. *Nature* **2013**, *504*, 96–97.

(384) Jacob, C. R.; Neugebauer, J. Subsystem density-functional theory. *Wiley Interdisciplinary Reviews: Computational Molecular Science* **2014**, *4*, 325–362.

(385) Di Remigio, R.; Bast, R.; Frediani, L.; Saue, T. Four-component relativistic calculations in solution with the polarizable continuum model of solvation: theory, implementation, and application to the group 16 dihydrides H2X (X= O, S, Se, Te, Po). *The Journal of Physical Chemistry A* **2014**, *119*, 5061–5077.

(386) Parmar, P.; Samuels, A.; Clark, A. E. Applications of polarizable continuum models to determine accurate solution-phase thermochemical values across a broad range of cation charge–the case of U (III–VI). *Journal of chemical theory and computation* **2015**, *11*, 55–63.

(387) Karbowiak, M.; Drozdzynski, J.; Murdoch, K.; Edelstein, N.; Hubert, S. Spectroscopic studies and crystal-field analysis of U3+ ions in RbY2Cl7 single crystals. *The Journal of chemical physics* **1997**, *106*, 3067–3077.

(388) Thouvenot, P.; Hubert, S.; Edelstein, N. Spectroscopic study and crystal-field analysis of Cm 3+ in the cubic-symmetry site of ThO 2. *Physical Review B* **1994**, *50*, 9715.

(389) Butorin, S. M.; Bauters, S.; Amidani, L.; Beck, A.; Weiss, S.; Vitova, T.; Tougait, O. X-ray spectroscopic study of chemical state in uranium carbides. *Journal of Synchrotron Radiation* **2022**, *29*.

(390) Sergentu, D.-C.; Duignan, T. J.; Autschbach, J. Ab initio study of covalency in the ground versus core-excited states and X-ray absorption spectra of actinide complexes. *The Journal of Physical Chemistry Letters* **2018**, *9*, 5583–5591.

(391) Ramanantoanina, H.; Kuri, G.; Martin, M.; Bertsch, J. Study of electronic structure in the L-edge spectroscopy of actinide materials: UO 2 as an example. *Physical Chemistry Chemical Physics* **2019**, *21*, 7789–7801.

(392) Polly, R.; Schacherl, B.; Rothe, J.; Vitova, T. Relativistic multiconfigurational Ab initio calculation of uranyl 3d4f resonant inelastic X-ray scattering. *Inorganic chemistry* **2021**, *60*, 18764–18776.

(393) Sergentu, D.-C.; Autschbach, J. X-ray absorption spectra of f-element complexes: insight from relativistic multiconfigurational wavefunction theory. *Dalton Transactions* **2022**.

(394) Sergentu, D.-C.; Autschbach, J. Covalency in actinide(IV) hexachlorides in relation to the chlorine K-edge X-ray absorption structure. *Chemical Science* **2022**, *13*, 3194–3207.

(395) Ilton, E. S.; Bagus, P. S. Ligand field effects on the multiplet structure of the U4f XPS of UO2. *Surface science* **2008**, *602*, 1114–1121.

(396) Ramanantoanina, H.; Kuri, G.; Daul, C.; Bertsch, J. Core electron excitations in U 4+: modelling of the nd 10 5f 2→ nd 9 5f 3 transitions with n= 3, 4 and 5 by ligand field tools and density functional theory. *Physical Chemistry Chemical Physics* **2016**, *18*, 19020–19031.

(397) Ramanantoanina, H. On the calculation of multiplet energies of three-open-shell 4f 13 5f n 6d 1 electron configuration by LFDFT: modeling the optical spectra of 4f core-electron excitation in actinide compounds. *Physical Chemistry Chemical Physics* **2017**, *19*, 32481–32491.

(398) Spencer, L. P. et al. Tetrahalide Complexes of the [U(NR)2]2+ Ion: Synthesis, Theory, and Chlorine K-Edge X-ray Absorption Spectroscopy. *Journal of the American Chemical Society* **2013**, *135*, 2279–2290.

(399) Pidchenko, I.; Kvashnina, K. O.; Yokosawa, T.; Finck, N.; Bahl, S.; Schild, D.; Polly, R.; Bohnert, E.; Rossberg, A.; Göttlicher, J., et al. Uranium redox transformations after U (VI) coprecipitation with magnetite nanoparticles. *Environmental science & technology* **2017**, *51*, 2217–2225.

(400) Minasian, S. G.; Keith, J. M.; Batista, E. R.; Boland, K. S.; Clark, D. L.; Conradson, S. D.; Kozimor, S. A.; Martin, R. L.; Schwarz, D. E.; Shuh, D. K., et al. Determining relative f and d orbital contributions to M–Cl covalency in MCl62–(M= Ti, Zr, Hf, U) and UOCl5–using Cl K-edge X-ray absorption spectroscopy and time-dependent density functional theory. *Journal of the American Chemical Society* **2012**, *134*, 5586–5597.

(401) Yanai, T.; Tew, D. P.; Handy, N. C. A new hybrid exchange–correlation functional using the Coulomb-attenuating method (CAM-B3LYP). *Chemical physics letters* **2004**, *393*, 51–57.

(402) DIRAC, a relativistic ab initio electronic structure program, Release DIRAC22 (2022), written by H. J. Aa. Jensen, R. Bast, A. S. P. Gomes, T. Saue and L. Visscher, with contributions from I. A. Aucar, V. Bakken, C. Chibueze, J. Creutzberg, K. G. Dyall, S. Dubillard, U. Ekström, E. Eliav, T. Enevoldsen, E. Faßhauer, T. Fleig, O. Fossgaard, L. Halbert, E. D. Hedegård, T. Helgaker, B. Helmich–Paris, J. Henriksson, M. van Horn, M. Iliaš, Ch. R. Jacob, S. Knecht, S. Komorovský, O. Kullie, J. K. Lærdahl, C. V. Larsen, Y. S. Lee, N. H. List, H. S. Nataraj, M. K. Nayak, P. Norman, G. Olejniczak, J. Olsen, J. M. H. Olsen, A. Papadopoulos, Y. C. Park, J. K. Ped-

ersen, M. Pernpointner, J. V. Pototschnig, R. di Remigio, M. Repisky, K. Ruud, P. Sałek, B. Schimmelpfennig, B. Senjean, A. Shee, J. Sikkema, A. Sunaga, A. J. Thorvaldsen, J. Thyssen, J. van Stralen, M. L. Vidal, S. Villaume, O. Visser, T. Winther, S. Yamamoto and X. Yuan (available at `http://dx.doi.org/10.5281/zenodo.6010450`, see also `http://www.diracprogram.org`).

(403) Saue, T.; Bast, R.; Gomes, A. S. P.; Jensen, H. J. A.; Visscher, L.; Aucar, I. A.; Di Remigio, R.; Dyall, K. G.; Eliav, E.; Fasshauer, E., et al. The DIRAC code for relativistic molecular calculations. *The Journal of chemical physics* **2020**, *152*, 204104.

(404) Dyall, K. G. Relativistic and nonrelativistic finite nucleus optimized triple-zeta basis sets for the 4 p, 5 p and 6 p elements. *Theoretical Chemistry Accounts* **2002**, *108*, 335–340.

(405) Dyall, K. G. Relativistic double-zeta, triple-zeta, and quadruple-zeta basis sets for the light elements H–Ar. *Theoretical Chemistry Accounts* **2016**, *135*, 128.

(406) Visscher, L.; Dyall, K. G. Dirac–Fock atomic electronic structure calculations using different nuclear charge distributions. *Atomic Data and Nuclear Data Tables* **1997**, *67*, 207–224.

(407) Watkin, D. J.; Denning, R. G.; Prout, K. Structure of dicaesium tetrachlorodioxouranium (VI). *Acta Crystallographica Section C: Crystal Structure Communications* **1991**, *47*, 2517–2519.

(408) Van Lenthe, E. v.; Snijders, J.; Baerends, E. The zero-order regular approximation for relativistic effects: The effect of spin–orbit coupling in closed shell molecules. *The Journal of chemical physics* **1996**, *105*, 6505–6516.

(409) Lembarki, A.; Chermette, H. Obtaining a gradient-corrected kinetic-energy functional from the Perdew-Wang exchange functional. *Physical Review A* **1994**, *50*, 5328–5331.

(410) Zhang, Y.; Biggs, J. D.; Healion, D.; Govind, N.; Mukamel, S. Core and valence excitations in resonant X-ray spectroscopy using restricted excitation window time-dependent density functional theory. *The Journal of chemical physics* **2012**, *137*, 194306.

(411) Hirata, S.; Head-Gordon, M. Time-dependent density functional theory within the Tamm–Dancoff approximation. *Chemical Physics Letters* **1999**, *314*, 291–299.

(412) Martin, R. L. Natural transition orbitals. *The Journal of chemical physics* **2003**, *118*, 4775–4777.

(413) Reisler, H.; Krylov, A. I. Interacting Rydberg and valence states in radicals and molecules: experimental and theoretical studies. *International Reviews in Physical Chemistry* **2009**, *28*, 267–308.

(414) Frati, F.; Hunault, M. O. J. Y.; de Groot, F. M. F. Oxygen K-edge X-ray Absorption Spectra. *Chemical Reviews* **2020**, *120*, 4056–4110.

(415) Kaufmann, K.; Baumeister, W.; Jungen, M. Universal Gaussian basis sets for an optimum representation of Rydberg and continuum wavefunctions. *Journal of Physics B: Atomic, Molecular and Optical Physics* **1989**, *22*, 2223–2240.

(416) Barker, T. J.; Denning, R. G.; Thorne, J. R. Applications of two-photon spectroscopy to inorganic compounds. 2. Spectrum and electronic structure of cesium uranyl nitrate, CsUO2 (NO3) 3. *Inorganic Chemistry* **1992**, *31*, 1344–1353.

(417) Campbell, J.; Papp, T. Widths of the atomic K–N7 levels. *Atomic Data and Nuclear Data Tables* **2001**, *77*, 1–56.

(418) Krause, M.; Oliver, J. Naturcal Wiciths of Atomic K and L. Levels, Kor X-Ray Lines and Several Kii. Auger Lines. *J. Phys. Chem. Ref. Data* **1979**, *8*.

(419) Southworth, S.; Dunford, R.; Ray, D.; Kanter, E.; Doumy, G.; March, A.; Ho, P.; Krässig, B.; Gao, Y.; Lehmann, C., et al. Observing pre-edge K-shell resonances in Kr, Xe, and XeF 2. *Physical Review A* **2019**, *100*, 022507.

(420) Knecht, S.; Repisky, M.; Jensen, H. J. A.; Saue, T. Exact two-component Hamiltonians for relativistic quantum chemistry: Two-electron picture-change corrections made simple. *The Journal of Chemical Physics* **2022**, *157*, 114106.

(421) Frati, F.; Hunault, M. O.; De Groot, F. M. Oxygen K-edge X-ray absorption spectra. *Chemical reviews* **2020**, *120*, 4056–4110.

(422) Ogasawara, H.; Kotani, A.; Thole, B. T. Calculation of magnetic x-ray dichroism in 4d and 5d absorption spectra of actinides. *Physical Review B* **1991**, *44*, 2169.

(423) Van der Laan, G.; Figueroa, A. I. X-ray magnetic circular dichroism—A versatile tool to study magnetism. *Coordination Chemistry Reviews* **2014**, *277*, 95–129.

(424) Amidani, L.; Retegan, M.; Volkova, A.; Popa, K.; Martin, P. M.; Kvashnina, K. O. Probing the Local Coordination of Hexavalent Uranium and the Splitting of 5f Orbitals Induced by Chemical Bonding. *Inorganic Chemistry* **2021**, *60*, 16286–16293.

(425) Bunău, O.; Ramos, A. Y.; Joly, Y. In *International Tables for Crystallography*; International Union of Crystallography: 2021.

(426) Joly, Y.; Ramos, A. Y.; Bunău, O. In *International Tables for Crystallography*; International Union of Crystallography: 2022.

(427) Tecmer, P.; Gomes, A. S. P.; Ekström, U.; Visscher, L. Electronic spectroscopy of UO_2^{2+}, NUO^+ and NUN: an evaluation of time-dependent density functional theory for actinides. *Physical Chemistry Chemical Physics* **2011**, *13*, 6249.

(428) Tecmer, P.; Gomes, A. S. P.; Knecht, S.; Visscher, L. Communication: Relativistic Fock-space coupled cluster study of small building blocks of larger uranium complexes. *The Journal of Chemical Physics* **2014**, *141*, 041107.

(429) Oher, H.; Gomes, A. S. P.; Wilson, R. E.; Schnaars, D. D.; Vallet, V. How Does Bending the Uranyl Unit Influence Its Spectroscopy and Luminescence? *Inorganic Chemistry* **2023**.

(430) Gomes, A. S. P.; Jacob, C. R.; Visscher, L. Calculation of local excitations in large systems by embedding wave-function theory in density-functional theory. *Physical Chemistry Chemical Physics* **2008**, *10*, 5353, DOI: `10.1039/b805739g`.

(431) Bouchafra, Y.; Shee, A.; Réal, F.; Vallet, V.; Gomes, A. S. P. Predictive Simulations of Ionization Energies of Solvated Halide Ions with Relativistic Embedded Equation of Motion Coupled Cluster Theory. *Physical Review Letters* **2018**, *121*, DOI: `10.1103/physrevlett.121.266001`.

(432) Opoku, R. A.; Toubin, C.; Gomes, A. S. P. Simulating core electron binding energies of halogenated species adsorbed on ice surfaces and in solution via relativistic quantum embedding calculations. *Physical Chemistry Chemical Physics* **2022**, *24*, 14390–14407.

Chapter 5

The core-excited states of linear and bent uranyl complexes

"It's funny how the colors of the real world only seem really real when you watch them on a screen."

— Anthony Burgess, A Clockwork Orange

The material presented in this chapter contains parts of a manuscript in preparation [433].

5.1 Introduction

In the previous chapter, we assessed the role of equatorial ligands in the excited states of the uranyl ion, which exhibits a linear O_{yl}–U–O_{yl} bond angle in the $Cs_2UO_2Cl_4$ crystal. This was achieved by comparing the O K-, U M_4-, and L_3-edge XAS spectra of UO_2^{2+} and $UO_2Cl_4^{2-}$ using 4c-DR-TD-CAMB3LYP simulations. In this chapter, our specific focus will be on the U M_4-edge XAS spectra of different uranyl-containing species.

The U M_4 XAS spectra exhibit three main features, which we will refer to as **A**, **B**, and **C**, in contrast to **T4**, **T5**, and **T6**, as we have done in the previous chapter. Our 4-component damped response theory (4c-DR-TD) simulations of the U M_4 XAS for UO_2^{2+} and $UO_2Cl_4^{2-}$ revealed significant differences in the peak splittings, as presented in Table 4.2. The absolute differences in **B**-**A**, **C**-**A**, and **C**-**B** peak splittings were found to be 0.9, 0.8, and 1.7 eV, respectively. As shown in this same table, the values for the dianion moved closer to High Energy Resolution Fluorescence Detected (HERFD) data for the $Cs_2UO_2Cl_4$ crystal. To investigate whether these spectral differences arise from orbital interactions or have an electrostatic nature, we also performed 4c-DR-TD simulations in which we treated the four chloride ligands as an embedding potential.

The results of these simulations, which we consider to be the main finding of our previous work, deviate from the most accepted interpretation of the U M_4-edge XAS. According to this interpretation, the position of the satellite peak (transition **C**) is directly correlated to the An-O_{yl} bond length in the AnO_2^{2+} species. In other words, the shorter the An-O_{yl} bond length, the higher the energy of the **C** feature [21, 328]. However, by representing the chloride atoms as an embedding potential, we demonstrated the dominant role of electrostatic interactions in the studied case, as the peak splittings closely matched those obtained with the supermolecular calculation. For instance, the **B**-**C** difference showed only a 0.3 eV deviation from the supermolecular calculation, in contrast to the bare uranyl case, which had a difference of 1.7 eV. These results are also shown in Table 4.2.

Given these findings from our previous investigation, it was an obvious perspective to explore the uranyl ion in different structural parameters and ligand environments. The first step was to investigate another system with a linear structure, $[UO_2(NO_3)_2(H_2O)_2](H_2O)_4$. Additionally, we explored two species, $UO_2Cl_2(H_2O)_3$ and $UO_2Cl_2(phen)_2$, for which the U M_4 HERFD-XAS spectra have not been studied in the literature to date, theoretically nor experimentally. These systems also exhibit distinct U–O_{yl} structural parameters compared to the $Cs_2UO_2Cl_4$ system. Moreover, these systems feature a bent uranyl structure, introducing another interesting aspect for the analysis. Figure 5.1 illustrates these systems schematically.

The present work comprises a theoretical-experimental investigation of the U M_4 XAS spectra of these species. We conducted experimental investigations of the X-ray Absorption Near Edge Structure (XAFS) using the High Energy

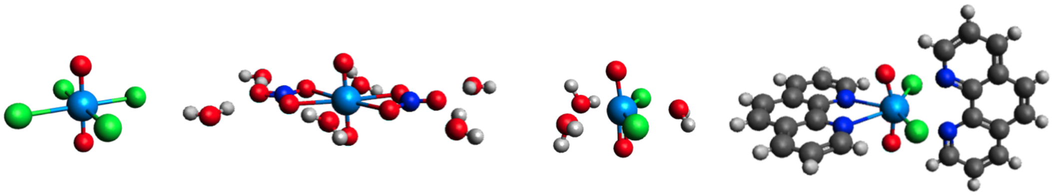

Figure 5.1: Systems investigated in this work. From left to the right: $UO_2Cl_4^{2-}$, $[UO_2(NO_3)_2(H_2O)_2](H_2O)_4$, $UO_2Cl_2(H_2O)_3$ and $UO_2Cl_2(phen)_2$.

Resolution Fluorescence Detected mode (HERFD-XANES). Additionally, Resonant Inelastic X-ray Scattering (RIXS) measurements were performed. The XAFS of these species was also subjected to theoretical investigations through 2-component time-dependent density functional theory simulations within the Tamm-Dancoff approximation (TDA).

The structure of this chapter is as follows. Firstly, we introduce the experimental setup and provide details on the acquired data for RIXS and HERFD measurements in Section 5.2. Subsequently, in Section 5.3, we outline the computational protocol employed in this study. In Section 5.4, we present the theoretical simulations and compare them with the experimental data and we provide an overview of the trends observed in our investigation. Finally, in Section 5.5 we present our conclusions and outline future perspectives for the research conducted in this study in Section 5.6.

5.2 Experiments

5.2.1 Experimental setup

Samples were prepared at the Helmholtz-Zentrum Dresden Rossendorf (HZDR) laboratory in Dresden, Germany. The measurements were conducted on a few milligrams of sample powder mixed with boron nitride and pressed into a pellet. To prevent the degradation of the samples, both transportation and measurements were carried out under cryogenic conditions.

All the HERFD-XANES spectra presented in this study were recorded at the Rossendorf Beamline (BM20) of the European Synchrotron Radiation Facility

(ESRF) in early October 2023. A comprehensive account of the fundamental characteristics associated with the extremely brilliant source storage ring of this synchrotron radiation facility (ESRF-EBS) has recently been described by Raimondi et al. [434]. Additionally, the optics and radiochemical safety system of this radionuclide beamline have been described in more detail by Scheinost et al. [200]. Further details about the HERFD-XANES experimental setup of the BM20 beamline can be found elsewhere [40, 200] and we summarize the key aspects of our measurements in the following.

The HERFD-XANES spectra were recorded by measuring the intensity of the $4f_{5/2} \rightarrow 3d_{3/2}$ fluorescence decay (3336.0 eV) as a function of the incident energy, i.e, by scanning the frequencies of the incoming photons while keeping the emission frequency fixed at the maximum of the U M_β fluorescence line. Photon energy was selected using the 220 reflection of a spherically bent five-crystal X-ray emission spectrometer aligned at a 75° Bragg angle. The sample, crystal analyzer, and photon detector were arranged in a Johann-type geometry, as depicted in Figure 5.2. The paths of the incident and emitted X-rays through the air were minimized to avoid intensity losses caused by soft X-ray absorption.

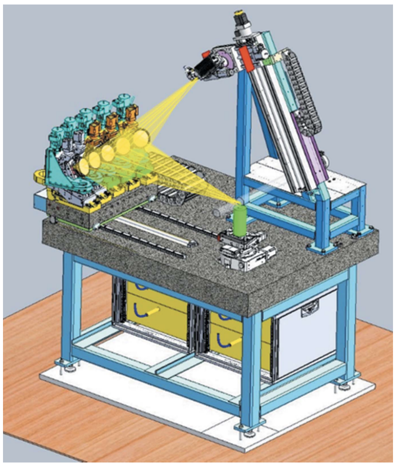

Figure 5.2: Schematic drawing of ROBL's five-crystal X-ray emission spectrometer. Extracted from Scheinost et al. [200]. Figure used with permission from IUCr Journals.

5.2.2 RIXS

As extensively discussed in the literature, the energy resolution of the recorded HERFD spectra strongly depends on the selected emission energy [9, 39, 40, 435]. As pointed out by Gel'mukhanov et al. [39] and Kvashnina and Butorin [40], improved energy resolution can be achieved by analyzing a RIXS map recorded prior to the HERFD experiment itself. In this analysis, one evaluates the intensity of non-resonant and resonant XES processes, which are associated with the energy resolution of the HERFD experiment.

The instrumentation used for the RIXS experiment performed here is the same as that described for the HERFD experiments in Section 5.2.1. However, the main difference between these experiments is that, while in HERFD one probes a single emission energy, in RIXS one records the intensity of scattering processes around the resonant X-ray emission of interest. In this work, the primary process investigated is the U $3d \rightarrow 5f$ transition (~ 3728 eV), and the fluorescence being probed in the HERFD experiment is from the $4f \rightarrow 3d$ transition (~ 3336 eV) [21, 40, 328, 436], as depicted on the left side of Figure 5.3 for uranyl.

As previously discussed in this thesis, the width of spectral features in a spectrum is determined by the core-hole lifetime of the process, although experimental resolution and other processes such as backscattering and dynamical processes can contribute to borrowing the photoabsorption cross section of interest [34, 39, 435–437]. Specifically, in the case of the $3d_{3/2} \rightarrow 5f$ transition, the core-hole lifetime broadening is approximately 3.2 eV [21, 40, 436]. Moreover, as further explored by Vitova et al. [21], the dominant contribution to the U M_4 HERFD spectra is the core-hole lifetime broadening from the $4f_{5/2} \rightarrow 3d_{3/2}$ decay (< 1 eV). This characteristic is why it is often stated that HERFD experiments effectively probe the absorption process with spectral narrowing below the natural core-hole lifetime, leading to improved resolution compared to the broad spectra obtained in total fluorescence yield (TFY) experiments.

The *3d4f* RIXS map recorded for the studied $UO_2Cl_2(H_2O)_3$ system is depicted in Figure 5.4a, in a plane of incident and emitted energies. This map clearly shows three regions of high intensity, which correspond to the expected peaks in the HERFD-XANES spectra at U M_4-edge, discussed in the following

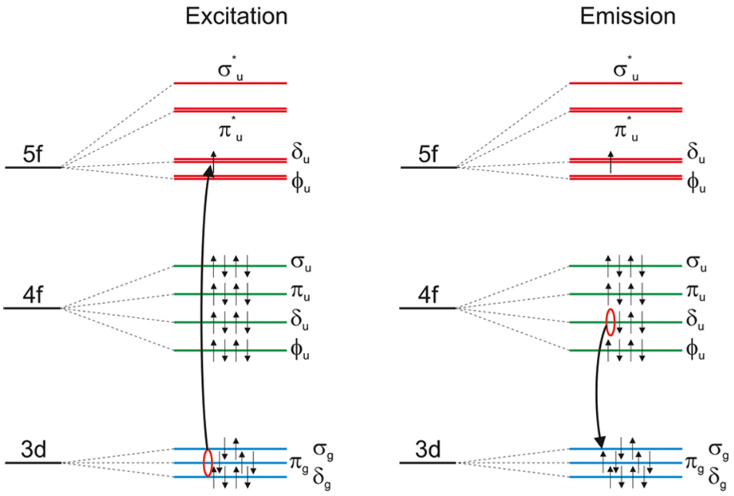

Figure 5.3: Excitation and emission schemes of the *3d4f* RIXS process in uranyl. Adapted from Polly et al. [392]. This article was published under a Creative Commons Attribution (CC-BY) license in Inorganic Chemistry, a journal from the American Chemical Society. This article is open-access and there was no further requirement to reproduce this figure.

section. From the first view of the spectra, no evident changes were observed in the core-to-core RIXS compared to previous spectra obtained for compounds containing uranium in the hexavalent oxidation state [21, 40, 392, 438]. Therefore, in this work, we performed experiments following the well-established procedure outlined by Kvashnina and Butorin [40], where the maximum of the normal XES process is employed in HERFD. These were performed with an energy resolution of 0.4 eV.

The subsequent discussion of this chapter solely focuses on comparing the HERFD experiments and theoretical data. For a more comprehensive understanding of RIXS theory, experiments, and analysis, we refer readers to the literature [9, 21, 34, 39, 40].

5.2.3 HERFD

In Figure 5.4b, we present the recorded U M_4-edge HERFD spectra, including the spectra reported by Vitova et al. [328] for $Cs_2UO_2Cl_4$. Although the U M_4

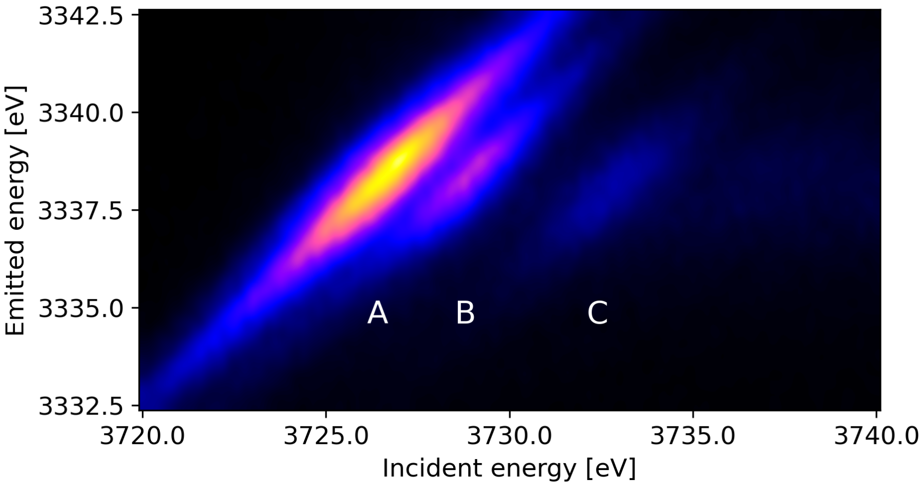

(a) RIXS

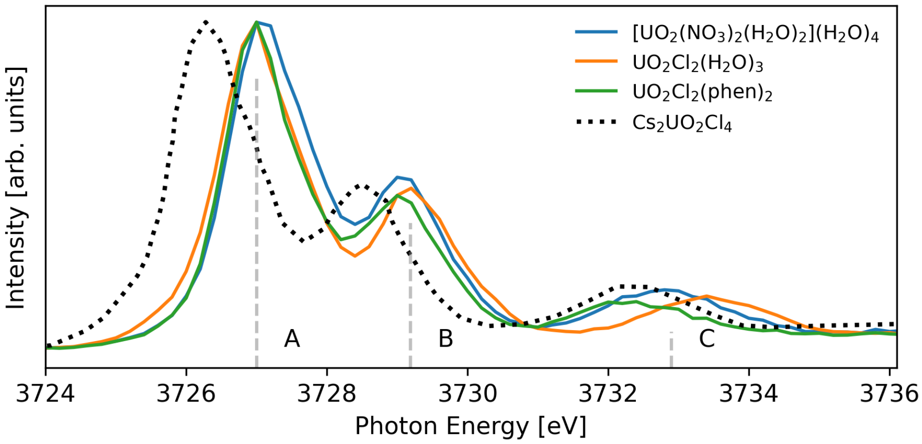

(b) HERFD

Figure 5.4: Top: Core-to-core RIXS spectra at the U M_4-edge of $UO_2Cl_2(H_2O)_3$. Bottom: U M_4-edge HERFD spectra of $[UO_2(NO_3)_2(H_2O)_2](H_2O)_4$, $UO_2Cl_2(H_2O)_3$ and $UO_2Cl_2(phen)_2$. Data for $Cs_2UO_2Cl_4$ as reported by Vitova et al. [328]. Copyright 2015 American Chemical Society. Labels are explained in the text.

HERFD spectra for $Cs_2UO_2Cl_4$ is shifted to the left by 0.6 eV with respect to our data, all of these spectra exhibit a similar profile characterized by three main features. The most intense feature in the spectra (white line) corresponds to U $3d_{3/2g} \rightarrow 5f\ \delta_u, \phi_u$ transitions (referred to as **A**). This feature is followed by a rapid decrease in intensity and the next feature in this spectra is that of the

$3d_{3/2g} \rightarrow 5f\ \pi_u^*$ transition (referred to as **B**). Finally, at the higher energy side, a peak of relatively low intensity is observed, corresponding to the U $3d_{3/2g} \rightarrow 5f$ σ_u^* satellite peak (referred to as **C**).

Overall, concerning our data, it is evident that the U M_4-edge HERFD spectra exhibit more noticeable variations in feature **C**. The subsequent sections of this chapter aim to thoroughly analyze these spectra through theoretical calculations. However, before proceeding with the analysis, it is important to discuss the computational methodologies employed in our simulations.

5.3 Computational modelling

5.3.1 Structures

As stated in the introduction, the main objective of this work is to evaluate the XANES spectra of systems containing either a linear or a bent uranyl moiety through molecular electronic structure calculations. Table 5.1 presents the structural parameters of each of the four systems studied in this work. The structure of $UO_2Cl_4^{2-}$ is based on the experimental crystal structure of $Cs_2UO_2Cl_4$ as reported by Watkin et al. [407]. For $[UO_2(NO_3)_2\ (H_2O)_2](H_2O)_4$ and its variants, we employed the crystal structure reported by Taylor and Mueller [439]. In the case of the $UO_2Cl_2(H_2O)_3$ system, we utilized the structure reported by Platts and Baker [440], which was obtained employing the BP86-D3 functional. For the $UO_2Cl_2(phen)_2$ compound, we utilized the recently published crystallographic structure by Oher et al. [441].

5.3.2 Methods

Core-excited states were described using Time-Dependent Functional Theory within the Tamn-Dancoff approximation (TDA) [411] and the long-range corrected CAM-B3LYP functional (2c-TDA-CAM-B3LYP) [221]. Slater-type basis sets [99] of triple zeta quality (TZP) were used for all atoms. These were left uncontracted in the calculations. Relativistic effects were included by employing the eXact two-component Hamiltonian (X2C), which we will refer to as 2c-TDA-

System	Bond distance (Å)		Bond angle (deg)
	U–O_{yl_1}	U–O_{yl_2}	O_{yl_1}–U–O_{yl_2}
$UO_2Cl_4^{2-(a)}$	1.774	1.774	180
$[UO_2(NO_3)_2\,(H_2O)_2](H_2O)_4^{(b)}$	1.771	1.750	179
$UO_2Cl_2(H_2O)_3^{(c)}$	1.793	1.789	173.3
$UO_2Cl_2(phen)_2^{(d)}$	1.781	1.776	161.7

Table 5.1: U–O bond lengths (Å) and O_{yl_1}–U–O_{yl_2} bond angle (deg) for the systems investigated in this work. U–O_{yl_1} refers to the longest bond length in the system, while U–O_{yl_2} represents the shortest. Structures taken from $^{(a)}$ Watkin et al. [407], $^{(b)}$Taylor and Mueller [439], $^{(c)}$Platts and Baker [440], $^{(d)}$Oher et al. [48].

CAMB3LYP. We employed a Gaussian nuclear model in all calculations. The electronic structure software Amsterdam Density Functional (ADF) [214] was utilized for these calculations.

U M_4-edge excitations were accessed by employing the restricted energy window (REW) projection scheme in the 2c-TDA-CAM-B3LYP simulations, specifically restricting excitations to those originating from the U $3d_{3/2}$ orbitals. Further details in this protocol are discussed in the following section. Similar to our previous XANES simulations (see Section 4.1.3 of the previous chapter), the orbital character of the investigated transitions was determined by analyzing their Natural Transition Orbitals (NTOs) [412] using ADFView. Furthermore, the spectral profiles were obtained by convolving the computed energies and oscillator strengths with a Gaussian function with a full width at half maximum of 1.2 eV.

5.3.3 Developing a protocol for non-symmetric systems

We have previously demonstrated one of the main advantages of using the 2c-TDA method in ADF compared to the 4c-DR-TD method in DIRAC: the ability to extract the NTOs associated with the calculated excited states. DIRAC does not have such a feature, which would limit our analysis to canonical orbitals. Thus, we consider this aspect a key contribution to our work. It allowed us to analyze excited states through a methodology that utilizes the transition density matrix to construct the excited state wave function, specifically particle and hole NTOs.

Regarding the comparison between 4- and 2-component simulations, we have demonstrated that there is no significant difference between these theoretical approaches when studying the excited states of the M_4-edge. For the $UO_2Cl_4^{2-}$ system, this difference was only 3.9 eV (see Table 4.1). Furthermore, we have demonstrated the consistency between the Tamm-Dancoff (TDA) and the random phase approximations (RPA) when simulating these excited states. Both methods exhibited identical spectral profiles for UO_2^{2+} (see Figure A.1). Thus, we have also leveraged the advantage of the lower computational cost associated with TDA simulations.

However, applying this level of theory to the systems investigated in this study was not straightforward. In the case of symmetric systems, such as those studied in the previous chapter (UO_2^{2+} and $UO_2Cl_4^{2-}$) only a limited number of roots are calculated since only certain transitions are allowed by symmetry. For instance, in the case of $UO_2Cl_4^{2-}$ at the 2c-TDA-CAMB3LYP/TZ2P level, only 33 roots are needed to cover a 7 eV range, with 7 of A_{2u} symmetry and 26 of E_u symmetry. However, when attempting to apply the same protocol to the UO_2Cl_2 subunit in a non-symmetric structure (such as $UO_2Cl_2(phen)_2$) using a double-zeta basis set, 63 roots were required. Even when constrained to a small basis set, such an increase in the number of roots to be determined for non-symmetric structures would make it impractical to investigate larger systems, such as the $UO_2Cl_2(phen)_2$ complex, within the scope of this thesis.

Consequently, the significant number of excited states needed to capture a representative region of the U M_4 XAS spectrum, including the three main peaks, posed a major challenge in our simulations. Therefore, it was essential to devise an approach that would allow us to complete these simulations feasibly within the timeframe of this thesis. In addition to the REW approach, which limits the active orbitals, two other useful approximations available in ADF were employed: reducing the number of virtual orbitals considered in the calculations and applying a cutoff for the calculated oscillator strengths. The effects of these approximations, as well as the role of the basis set, are discussed in the subsequent sections.

Restriction of virtual orbitals

Regarding this first approximation, we have included only those orbitals in the virtual space whose energy levels are lower than 10 E_h (approximately 272 eV). This is a reasonable choice, considering that the orbitals involved in the U M_4-edge XAS transitions do not typically have significantly higher energy levels than the first LUMOs (see for instance Figure 5.3).

Let's take the example of $[UO_2(NO_3)_2(H_2O)_2](H_2O)_4$, in which the LUMO is located at -2.7 eV. In the case of the transition at the higher energy side of the U M_4-edge XAS spectrum (3693.6 eV), a closer examination of the contributions from the particle NTO reveals that the highest energy orbital (LUMO+115) in this excited state contributes approximately 140 times less (0.0015) compared to the most significant contributing orbital (0.2373), which is the LUMO+11.

It is important to highlight that there is a clear physical justification for this approximation. In the considered experiments, such high-energy excitations ($\Delta E \approx 4000$ eV) are not observed. Additionally, these high-energy states represent unbound states, which are beyond the scope of the present study. We will revisit this strategy of restricting the virtual space when addressing core-ionized states in Chapter 6.

Oscillator strength cutoff

Another assessment conducted in this study focused on restricting the computed excited states to those with oscillator strengths above a certain threshold. This evaluation aimed to investigate the region corresponding to the least intense peak in the absorption spectrum at the U M_4-edge, specifically the third peak. The assessment was carried out for the UO_2Cl_2 subunit using the 2c-TDA-CAMB3LYP/DZ level.

As indicated in Table 5.2, within this region, the calculated oscillator strengths range from 1E-07 to 1E-04 in arbitrary units. Given that these values are relatively far apart, applying a cutoff of 1E-05 in arbitrary units would eliminate values that are comparatively smaller and potentially negligible in the context of the computed data. Moreover, it should be emphasized that all these values are significantly smaller than the main peak of the spectra, which exceeds 1E-02 in arbitrary units and, therefore, do not have a noticeable impact on the calculated spectra.

Transition Energy [eV]	Oscillator strength [arb.units]
3691.04	1.01E-07
3691.92	7.96E-05
3691.92	3.03E-07
3691.93	2.36E-05
3691.93	4.72E-06
3692.16	1.66E-05
3692.17	1.94E-07
3692.17	5.66E-05
3692.24	2.97E-06
3694.49	2.85E-05
3694.49	1.99E-05
3694.51	2.21E-04
3694.51	4.92E-04
3694.74	2.35E-06
3694.75	5.86E-05

Table 5.2: Oscillator strengths in the region of the third peak (**C**) at the U M_4-edge XAS for the UO_2Cl_2 subunit computed at the 2c-TDA-CAMB3LYP/DZ level.

Furthermore, these values have been shown to be similar to those obtained for $UO_2Cl_4^{2-}$ at the 2c-TDA-CAMB3LYP/TZ2P theory level. Considering these results and the fact that changing the basis set has only been shown to affect excitation energies (see the following section), another approach adopted in this work was to set a lower bound for the computation of oscillator strengths, limiting it to values above 1E-05 in arbitrary units. As discussed further below, this approximation did not have any noticeable impact on the spectroscopic profiles studied here.

Basis set assessment

A more common option is to reduce the size of the basis set. In the following analysis, we specifically focus on an intermediate case in our investigation: $UO_2(NO_3)_2(H_2O)_2$. This assessment is relevant because a change in the basis set can also impact the description of the ligands. We evaluated the XAS spectra at the U M_4-edge of $UO_2(NO_3)_2(H_2O)_2$ using DZ, TZP, and TZ2P basis sets. Additionally, we applied the previously discussed oscillator strength cutoff of 1E-05.

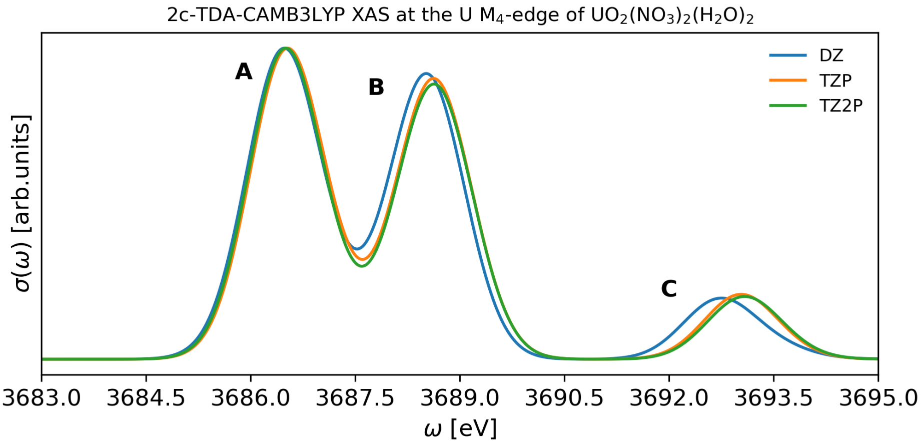

Figure 5.5: Comparison of 2c-TDA-CAMB3LYP XAS at the U M_4-edge of $UO_2(NO_3)_2(H_2O)_2$ for DZ, TZP, and TZ2P basis sets. The calculated oscillator strengths considered in the analysis were those that exceeded the threshold value of 1E-05 in arbitrary units. Only virtuals up to 10 E_h were included in the simulation. Labels are explained in the text.

The results are presented in Figure 5.5. Generally, all basis sets exhibit a similar first peak around 3686.5 eV. However, as we examine higher energies, more noticeable differences begin to appear. When comparing calculations at the triple-zeta level, modest changes are observed between transition **B** and **C**. A slight shift to the left is observed for the **C** transition when fewer polarization functions are used. Additionally, the TZP-level calculation shows slightly higher intensity for the second feature compared to the TZ2P-level calculation.

The spectral profile exhibits significant differences when transitioning to the less computationally expensive DZ case. Both features **B** and **C** are shifted to the left, with the shift in **C** being more noticeable, approximately 0.3 eV. Furthermore, the second feature has higher intensity compared to the other two cases. Considering the objective of exploring the sensitivity provided by the HERFD technique, the double-zeta case appears to be the least reliable for application.

In conclusion, the choice of basis set does have a significant impact. However, the other approximations used in this study have played a crucial role in achieving results within a reasonable timeframe. For example, despite employing the aforementioned approximations, the 2c-TDA-CAMB3LYP/TZP XAS simulation for U M_4 XAS of $UO_2Cl_2(phen)_2$ still required over 11 days to complete. Without these approximations, it would have been practically impossible to obtain the results within a reasonable timeframe.

We summarize our protocol as follows. All calculations were performed at the TDA-CAMB3LYP/TZP theory level. The REW projection scheme was applied, allowing only transitions from $3d_{3/2}$ orbitals to be computed. The calculated oscillator strengths considered were those exceeding the threshold value of 1E-05 in arbitrary units. The simulation included virtual orbitals up to 10 E_h. Within these restrictions, we found that typically 70 core-excited states were sufficient to cover the main features of the U M_4 XAS theoretical spectrum (3684 – 3696 eV) for all species here investigated.

5.4 Results

5.4.1 Linear uranyl structures

The $[UO_2(NO_3)_2(H_2O)_2](H_2O)_4$ system has been extensively explored in the literature, with its XANES at the U M_4-edge in the total electron yield (TEY) mode reported by Petiau et al. [442]. Furthermore, high-resolution data (HERFD-XANES) was reported by Butorin et al. [436]. On the theoretical side, Konecny et al. [225] has recently conducted a comprehensive assessment of various functionals and basis sets in simulating the $UO_2(NO_3)_2$ spectra within the damped-response theory framework. For the sake of brevity, we refer the reader to the original work for the details of their benchmark.

In the subsequent discussion, we will utilize the experimental data obtained during our beam time. We will also focus on a specific simulation by Konecny et al., which utilized a modified version of the PBE0 functional with 60% HF exchange instead of 25% (PBE0-60HF). In their simulations, uncontracted Dyall

(DZ) and augmented Dunning (aDZ) basis sets were employed for uranium and other atoms, respectively. Additionally, in our investigation, we have extended Konecny et al. study by including the first two spheres of water molecules in the system, $[UO_2(NO_3)_2(H_2O)_2](H_2O)_n(n=0,4)$, thereby assessing their role in determining the features in the U M_4 XAS spectra.

Figure 5.6 presents the experimental and theoretical spectra obtained in this investigation. In addition to the data for $[UO_2(NO_3)_2(H_2O)_2](H_2O)_n$ systems, we also include the spectra for another system in which the uranyl unit exhibits a linear structure. Specifically, we include the U M_4 XAS data for $Cs_2UO_2Cl_4$ as reported by Vitova et al. [328] and the data from our previous investigation on $UO_2Cl_4^{2-}$ (see Section 4.1.3 of the last chapter or manuscript [323] for further information). In these spectra, the theoretical data were shifted in relation to the main feature, being 3726.4 eV for $Cs_2UO_2Cl_4$ and 3727.0 eV for all the others species investigated here.

Table 5.3 presents the transition energies, shifts, and peak splittings for all species studied in this work. The table also includes Vitova et al. [328] HERFD and Amidani et al. [18] FDMNES data for the U M_4 HERFD of $Cs_2UO_2Cl_4$. Additionally, the results for the 4c-DR-TD-PBE-60HF/DZ+aDZ U M_4 XAS of $UO_2(NO_3)_2$ reported by Konecny et al. [225] are included. The shifts of our actual simulations relative to the experimental data are consistent among themselves, ranging from 39.7 to 40.9 eV for all transitions. As shown in Table 5.3, the values for the previously investigated $UO_2Cl_4^{2-}$ system also fall within this same range. Therefore, for the sake of brevity, we refer the reader to Section 4.1.3 for a more comprehensive discussion on the shift between theoretical and experimental transition energies.

The role of equatorial plane water ligands in the U M_4 XAS of uranyl nitrate: transition energies and peak splittings

Regarding the effect of the equatorial plane water molecules on the electronic structure of $UO_2(NO_3)_2$, an important factor to consider is the distance between the actinide center and the oxygen atom in the coordinating waters (referred to as U-O_{ow}). In the case of the first-coordination sphere, this distance is symmetric,

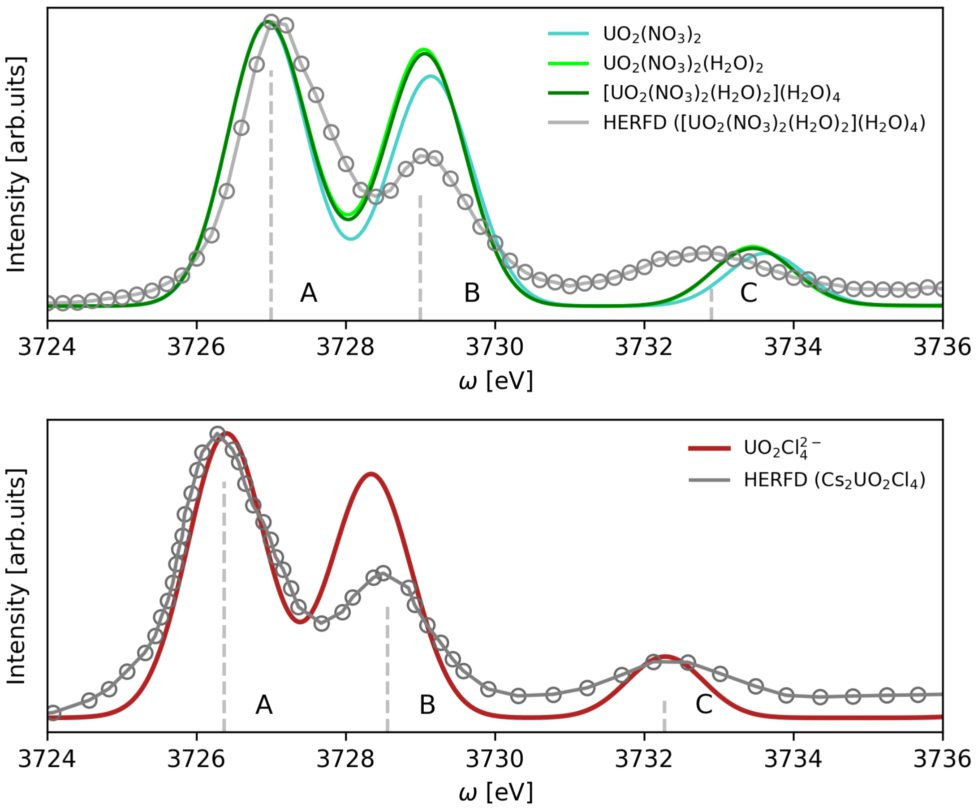

Figure 5.6: Top: Comparison of the 2c-TDA-CAMB3LYP/TZP XAS spectra at the U M_4-edge of $UO_2(NO_3)_2$, $[UO_2(NO_3)_2(H_2O)_2](H_2O)_n$ (n=0,4) to U M_4 HERFD of $[UO_2(NO_3)_2(H_2O)_2](H_2O)_4$. The calculated oscillator strengths were those exceeding the threshold value of 1E-05 in arbitrary units, and the cut-off of virtuals of 10 E_h was employed. Bottom: Comparison between 2c-TDA-CAMB3LYP/TZ2P XAS spectra of $UO_2Cl_4^{2-}$ as reported by Misael and Gomes [323] and the experimental data for $Cs_2UO_2Cl_4$ from Vitova et al. [328]. Copyright 2015 American Chemical Society. Spectra from this work was reprinted with permission from Misael and Gomes. Copyright 2023 American Chemical Society.

with a U-O_{ow_1} distance of 2.397 Å, while for the second one, the values are around 6 Å. By comparing the U-O_{ow_1} value with the U-Cl bond length in $UO_2Cl_4^{2-}$ (2.671 Å) and taking into account the significant role of electrostatic interactions observed in the U M_4 XAS spectra of $UO_2Cl_4^{2-}$, it is reasonable to expect that some extent of electrostatic interactions in the uranyl nitrate and its environment to be manifested in its spectra at least for the first-coordination

System	A	B	C	B-A	C-B	C-A
$UO_2Cl_4^{2-}$ (a)	3686.6 (-40.8)	3688.4 (-40.2)	3692.5 (-39.8)	1.9	3.9	5.8
$Cs_2UO_2Cl_4$ (b)	3726.9 (+0.5)	3728.6 (-0.7)	3732.9 (+0.6)	2.4	3.6	6.0
HERFD(c)	3726.4	3728.6	3732.3	2.2	3.7	5.9
$UO_2(NO_3)_2$ (d)	3727.9 (+0.9)	3730.4 (+1.4)	3736.6 (+3.8)	2.5	6.2	8.7
$UO_2(NO_3)_2$ †	3686.4 (-40.6)	3688.7 (-40.3)	3693.1 (-39.7)	2.3	4.4	6.8
$UO_2(NO_3)_2(H_2O)_2$	3686.5 (-40.5)	3689.0 (-40.0)	3693.0 (-39.8)	2.5	4.1	6.5
$[UO_2NO_3(H_2O)_2](H_2O)_4$	3686.5 (-40.5)	3689.0 (-40.0)	3693.0 (-39.8)	2.5	4.1	6.5
HERFD	3727.0	3729.0	3732.8	2.0	3.8	5.8
UO_2Cl_2 †	3686.5 (-40.5)	3688.8 (-40.4)	3692.6(-40.8)	2.3	3.7	6.1
$UO_2Cl_2(H_2O)_3$	3686.6 (-40.4)	3688.9 (-40.3)	3692.7 (-40.7)	2.3	3.8	6.1
HERFD	3727.0	3729.2	3733.4	2.2	4.2	6.4
UO_2Cl_2 †	3686.5 (-40.5)	3688.8 (-40.1)	3692.7 (-39.7)	2.2	4.0	6.2
$UO_2Cl_2(phen)_2$	3686.8 (-40.2)	3688.6 (-40.3)	3692.6 (-39.9)	1.8	4.0	5.8
HERFD	3727.0	3728.9	3732.4	1.9	3.5	5.4

Table 5.3: Comparison of the 2c-TDA-CAMB3LYP/TZP XAS spectra at the U M_4-edge of $UO_2(NO_3)_2$, $[UO_2(NO_3)_2(H_2O)_2](H_2O)_n$ (n=0,4), $UO_2Cl_2(H_2O)_3$ and $UO_2Cl_2(phen)_2$ with HERFD-XANES data. The calculated oscillator strengths were those exceeding the threshold value of 1E-05 in arbitrary units, and the cutoff of virtuals of 10 E_h was employed. (a) 2c-TDA-CAMB3LYP/TZ2P XAS spectra of $UO_2Cl_4^{2-}$ as reported by Misael and Gomes [323]. (b) Theoretical data for data for $Cs_2UO_2Cl_4$ from Amidani et al. [18]. (c) Experimental data for $Cs_2UO_2Cl_4$ from Vitova et al. [328]. (d) 4c-DR-TD-PBE-60HF/DZ+aDZ XAS spectra of $UO_2(NO_3)_2$ as reported by Konecny et al. [225]. † Simulations for the $UO_2(NO_3)_2$ or UO_2Cl_2 subunit using the same geometry as the complex structure in the following line.

sphere.

It is apparent from Figure 5.6 that the differences between the subunit case and the complexes are more significant than the differences among the complexes themselves. In terms of transition energies, the variations are relatively modest. As shown in Table 5.3, the complexes display transition energy differences below 0.1 eV in absolute value. However, the discrepancies can reach up to 0.3 eV when comparing the subunit and complexes. These differences are clearly evident in the peak splittings, which deviate from the experimental data by less than 0.7 eV in both cases.

With regard to peak splittings, it is worth noting that although the data from Konecny et al. slightly overestimates the feature **A** compared to the HERFD spectra (0.9 eV), it fails to accurately predict peak splittings, resulting in errors of up to 2.9 eV (**C**-**A**). This observation demonstrates that simply increasing the amount of exchange contribution in the DFT functional does not necessarily lead to overall improved results in the simulation of the U M_4 XAS.

To conclude, our actual results, combined with previous comparisons to methods that recover dynamical correlation (see Table 4.2), emphasize that accurately describing peak splittings in the U M_4 spectra primarily relies on properly accounting for long-range interactions, such as those from the uranyl ion with its equatorial ligands, rather than solely focusing on recovering electronic correlation in the uranyl unit (or the entire system). Furthermore, based on these findings, it can be concluded that the standard version of the CAMB3LYP functional provides a reliable framework for investigating the U M_4 XAS spectra. This has also been shown to be the case for valence-level excitations [167, 222, 443].

The role of equatorial plane water ligands in the U M_4 XAS of uranyl nitrate: intensities and characterization of its excited states

In addition to the variations in transition energies, Figure 5.6 also highlights differences in intensities between the complexes and the subunit case. Notably, these differences are particularly pronounced in feature **B**, which exhibits a lower intensity in the $UO_2(NO_3)_2$ subunit calculation. However, for transition **C**, the difference in intensity is negligible, while the main distinction from the other two cases remains the variation in transition energies. The complexes, on the other hand, display a generally similar spectral profile between themselves. Aligned with their resemblance on transition energies, it can be concluded that the first coordination sphere around the uranyl has a more significant role in determining the U M_4-edge XAS features than the second one.

The above mentioned changes in peak **B** can be understood within the most accepted interpretation of the U M_4 XAS spectra [40], which suggests that this feature provides information about the coordination environment surrounding the uranyl unit. When examining feature **C** using the current interpretation of the U M $_4$ XAS spectra [21], the situation becomes more complicated. As we observed in our previous investigation, relying solely on the U–O_{yl} bond length to interpret this spectrum, as it is commonly done in the literature [21], may not be the most appropriate approach for understanding these spectra. In our current case, the only difference between the considered structural models was the inclusion of the first two-coordination spheres in the calculations. As mentioned earlier, this minor modification proved sufficient to yield the aforementioned spectral differences, providing an initial indication of the significant role played by these ligands in shaping the features in the U M_4 XAS spectra.

In this context, NTOs can offer further insights into these spectra. As anticipated, feature **A** (see Figure 5.9 *b*, *c* and *d*) is predominantly localized within the uranyl unit, involving U $3d_{3/2}$ to U $5f\phi,\delta$ transitions. The same can be said for the feature **B** (see Figure 5.10 *b*, *c* and *d*). However, the situation differs for feature **C**, as depicted in the *b*, *c* and *d* components of Figure 5.11. While this feature primarily originates from transitions localized along the U–O_{yl} bond, the NTOs for $[UO_2(NO_3)_2(H_2O)_2](H_2O)_n$ also unveil a (small but) noteworthy charge transfer contribution from the uranyl unit to the nitrates, which is not seen in the subunit case.

Overall, these results underscore a small (but non-negligible) role of the first sphere water molecules in determining the features in the uranyl nitrate U M_4 XAS spectra. In other words, the presence of these additional equatorial ligands showed to provoke a decrease in the magnitude of the transition dipole moment of feature **B** and allows some extent of uranium-to-nitrates charge transfer excitations with the involvement of the nitrate π^* orbital (see feature **C**), which translates in a shift in transition energy in the σ^* feature.

5.4.2 Bent uranyl structures

While the majority of uranyl-containing complexes are known to exhibit a trans-oxo uranyl unit, i.e. a linear U–O_{yl} bond angle, the possibility of deviations from linearity and their implications on the electronic structure of this moiety have been subjects of debate in the literature, as discussed by Hayton [444]. Moreover, recent studies have reported synthetic routes for bent uranyl complexes, enabling their spectroscopic characterization [441, 445, 446].

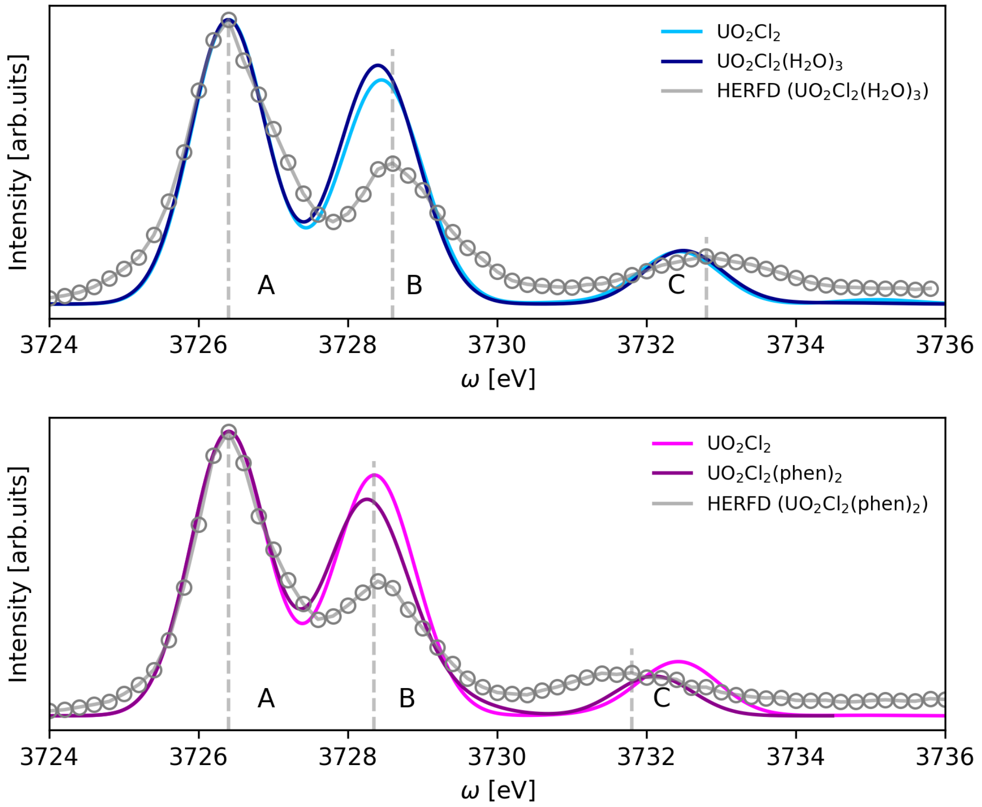

Figure 5.7: Comparison of the 2c-TDA-CAMB3LYP/TZP XAS spectra at the U M_4-edge of $UO_2Cl_2(H_2O)_3$ (top) and $UO_2Cl_2(phen)_2$ (bottom) to U M_4 HERFD. The calculated oscillator strengths were those exceeding the threshold value of 1E-05 in arbitrary units, and the cutoff of virtuals of 10 E_h was employed.

In this study, we have investigated two systems in which the uranyl moiety is bent, as shown in Table 5.1. The structure of the $UO_2Cl_2(H_2O)_3$ complex employed here [440] exhibits a deviation from linearity of 6.7 degrees and it has the longest U–O_{yl} bond length in this study. Additionally, we studied an even more bent system, $UO_2Cl_2(phen)_2$, whose structure [441] exhibits a deviation from linearity of 18.3 degrees. The results of our theoretical and experimental investigations on the U M_4 XAS of bent uranyl systems, including their respective subunits, are presented in Figure 5.7.

Although further discussion on the deviation between complex and UO_2Cl_2 subunit cases will follow, it is noteworthy that, as shown in Table 5.3, peak splittings for the UO_2Cl_2 subunit in different geometries exhibit very similar values for the **B-A** and **C-A** differences, with a deviation of 0.1 eV. However, for **C-B**, the difference is 0.3 eV. Additionally, these values deviate from the $UO_2Cl_4^{2-}$ simulation by 0.4 eV, underscoring the distinct role of the chloride equatorial ligands in determining the U M_4 XAS spectra peak splittings. Furthermore, as depicted in Table 5.3, there are only modest differences between the peak splittings for the nitrate and chloride HERFD data, all of which are smaller than 0.1 eV in absolute value. However, for both the $UO_2Cl_2(H_2O)_3$ and $UO_2Cl_2(phen)_2$ systems, more pronounced differences are observed in the **C-B** and **C-A** peak splittings, with values reaching up to 0.5 eV in both cases. In the following sections, we will discuss each of these cases in detail.

$\mathbf{UO_2Cl_2(H_2O)_3}$

As can be seen in Table 5.3 and Figure 5.7, regarding the $UO_2Cl_2(H_2O)_3$ complex, only subtle changes are observed in the U M_4 XAS spectra when compared to the subunit case. The differences in main features and peak splittings are up to 0.1 eV. Notably, the only observable difference in the spectral profile is found in feature **B**, where the subunit case exhibits a somewhat smaller intensity than in the full complex, as we also observed to a greater extent for the nitrates investigated in the previous section. In addition to these minor differences in the spectral profiles, we do not observe any charge transfer in any of the NTOs of the $UO_2Cl_2(H_2O)_3$ complex, as shown in Figures 5.9–5.11.

Based on these results, it can be concluded that the equatorial plane water ligands in the $UO_2Cl_2(H_2O)_3$ complex do not play a significant role in determining its U M_4 XAS spectra peak positions. The variations in the spectral profile are primarily attributed to electrostatic interactions between the chlorine ligands and the uranyl unit. These findings align with the study conducted by Vallet et al. [447], which systematically investigated the influence of ligand-induced effects on the U–O_{yl} bond in the uranyl unit using the quantum theory of atoms-in-molecule (QTAIM).

Concerning peak splittings, both simulations exhibit differences from the HERFD experiment of up to 0.4 eV for all cases. Additionally, when comparing

$UO_2Cl_2(H_2O)_3$ to the linear case (specifically $Cs_2UO_2Cl_4$), significant variations are observed in differences **B-A** (0.5 eV) and **C-A** (0.6 eV). This finding becomes considerably interesting when considering that, despite the larger U–O_{yl} bond length in $UO_2Cl_2(H_2O)_3$ by 0.019 and 0.015 Å compared to $Cs_2UO_2Cl_4$, the C-A difference deviates approximately 0.7 eV from the linear trend reported by Amidani et al., as depicted in Figure 5.8. Notably, a similar deviation in this trend is also observed for nitrates, where the differences in bond length with respect to $Cs_2UO_2Cl_4$ are more modest, 0.003 and 0.0024 Å.

Together, these results underscore the non-negligible role of the chlorides in determining the π^* and σ^* excited states in the U M_4 XAS spectra of UO_2Cl_2 containing systems. Furthermore, these results are in line with our previous claim about the pivotal role of the chloride ligands in determining the features of the U M_4 XAS spectra of $UO_2Cl_4^{2-}$.

UO_2Cl_2(phen)$_2$

When moving towards the most bent uranyl unit in this study, UO_2Cl_2(phen)$_2$, the role of the equatorial ligands in determining the spectral features in the U M_4 XAS spectra becomes even more evident. As shown in Table 5.3, the differences in transition energies are up to 0.3 eV, and the variations in peak splittings are up to 0.4 eV, making them the most significant among our series of uranyl compounds. The role of the phenanthroline ligand is also evident when comparing the computed transition energies to those from the HERFD data. The **C-A** difference shows a decrease of 0.4 eV from the subunit to the complex, though the splitting is overestimated by 0.4 eV with respect to the experimental data.

Overall, our theoretical data suggests a distinct role of the phenanthroline ligand in determining the U M_4 XAS features when compared to the other investigated complexes. As can be seen in Figure 5.7, the UO_2Cl_2 subunit case exhibits a less intense **B** feature compared to the full complex. Similar to the nitrate case, but to a larger extent, the NTOs for feature **C** also exhibit a clear metal-to-ligand charge transfer (MLCT) involving the π^* orbitals of the phenanthroline groups in the σ^* excitation. Such a contribution is also evident in the **A** feature of the U M_4 XAS spectra, which thus challenges the notion of these transitions being purely localized within the uranyl unit and emphasizes the utility of NTOs in our analysis.

These findings are reasonable, given that pyridine-based chelating ligands, such as phenantroline, are commonly employed to stabilize positively charged ions, through covalent interactions, as demonstrated by Garcıa-Ramos et al. [448] for cuprates, and Woods et al. [449] for the uranyl ion. Furthermore, the MLCT character in the excited states of these complexes has a rich and largely explored photochemistry, as reviewed by Bencini and Lippolis [448] and observed in the low-lying excited states of this complex by Oher et al. [441].

Furthermore, when combining these results with those for the $UO_2Cl_2(H_2O)_3$ complex, we can affirm that there is a clear balance between electrostatic (from chlorides and phenanthroline) and covalent interactions in the uranyl unit determining the features of the U M_4 XAS spectra of $UO_2Cl_2(phen)_2$.

5.5 Conclusions

To summarize, in this work we could demonstrate the pivotal role of the equatorial ligands of the uranyl unit in determining its core-excited states. Our systematic investigation, which consisted of evaluating the U M_4 XAS spectra of $[UO_2(NO_3)_2(H_2O)_2](H_2O)_n$ and the $UO_2Cl_2(H_2O)_3$ complexes and their subunits, underscored the capability of the equatorial plane water ligands in the first coordination shell to increase the magnitude of the transition dipole moment of these excited states, as well as their minor role in determining transition energy positions. Both of these variations were shown to be more pronounced for the nitrate complex than in the chloride case, underscoring the dominant contribution of the electrostatic interactions between the uranyl unit and the chlorides in determining the features in the U M_4 XAS spectra of the latter.

By employing NTOs, we could assess the extent to which charge transfer excitations determine the features in the U M_4 XAS spectra, allowing us to go beyond the notion that these transitions are solely localized in the uranyl unit. These states were found to be present to a lesser degree in $[UO_2(NO_3)_2(H_2O)_2](H_2O)_n$ systems and played a crucial role when interpreting the excited states of the

$UO_2Cl_2(phen)_2$ complex. With respect to the latter complex, supported by its HERFD spectra and NTOs, we observed a decrease in the transition dipole moment of feature π^* and a shift of the σ^* excited state towards lower energies when compared to its UO_2Cl_2 subunit case. These results indicate a balance between electrostatic and covalent interactions in determining the features of the U M_4 XAS spectra of the $UO_2Cl_2(phen)_2$ complex. Furthermore, by demonstrating considerable variations from a previously reported linear trend, we once again showed that the U–O_{yl} bond length does not necessarily determine the U M_4 XAS spectra, as it is usually attributed to.

In summary and conclusion, our results have emphasized that relying solely on the U–O_{yl} bond length is insufficient for a comprehensive understanding of both theoretical and experimental An M_4 XAS spectra. Both covalent and electrostatic interactions, as well as the extent to which charge transfer transitions occur must be taken into account.

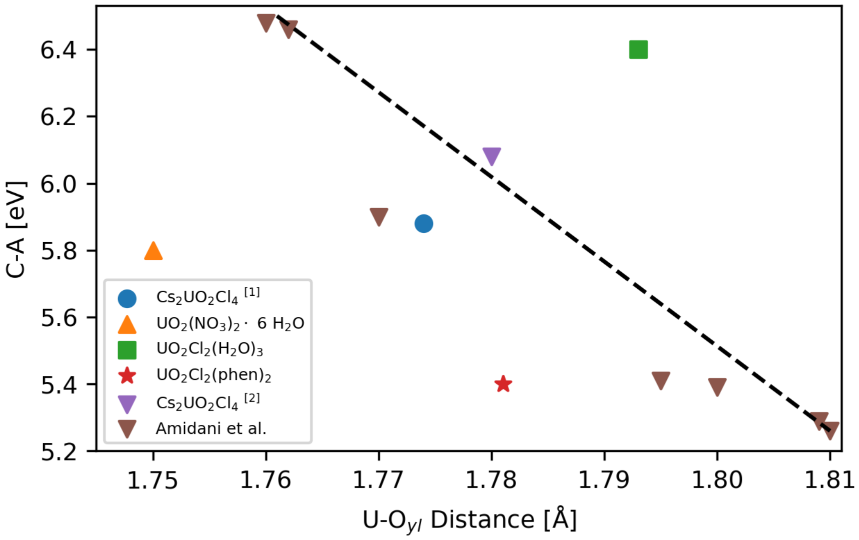

(a) HERFD

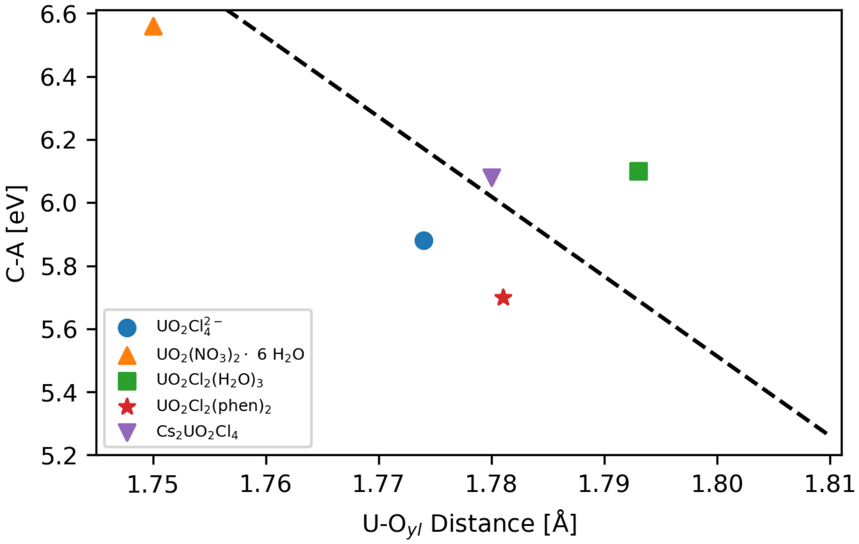

(b) Theory

Figure 5.8: Distance between peaks A and C of U M_4 XAS spectra versus the U–O_{yl} bond length from our study and those reported by Amidani et al. [18] (purple triangles). The dashed line is based on the linear fit reported by Amidani et al. To the systems that it concerns, the U–O_{yl} bond length depicted is the longest one in Table 5.1. With respect to the experimental data, we have represented the point referring to the C-A difference using the U-O_{yl} bond length equal to [1] 1.774 Å as employed in our study (blue circle) and [2] 1.780 Å as employed by Amidani et al. [18] (purple triangle) for $Cs_2UO_2Cl_4$.

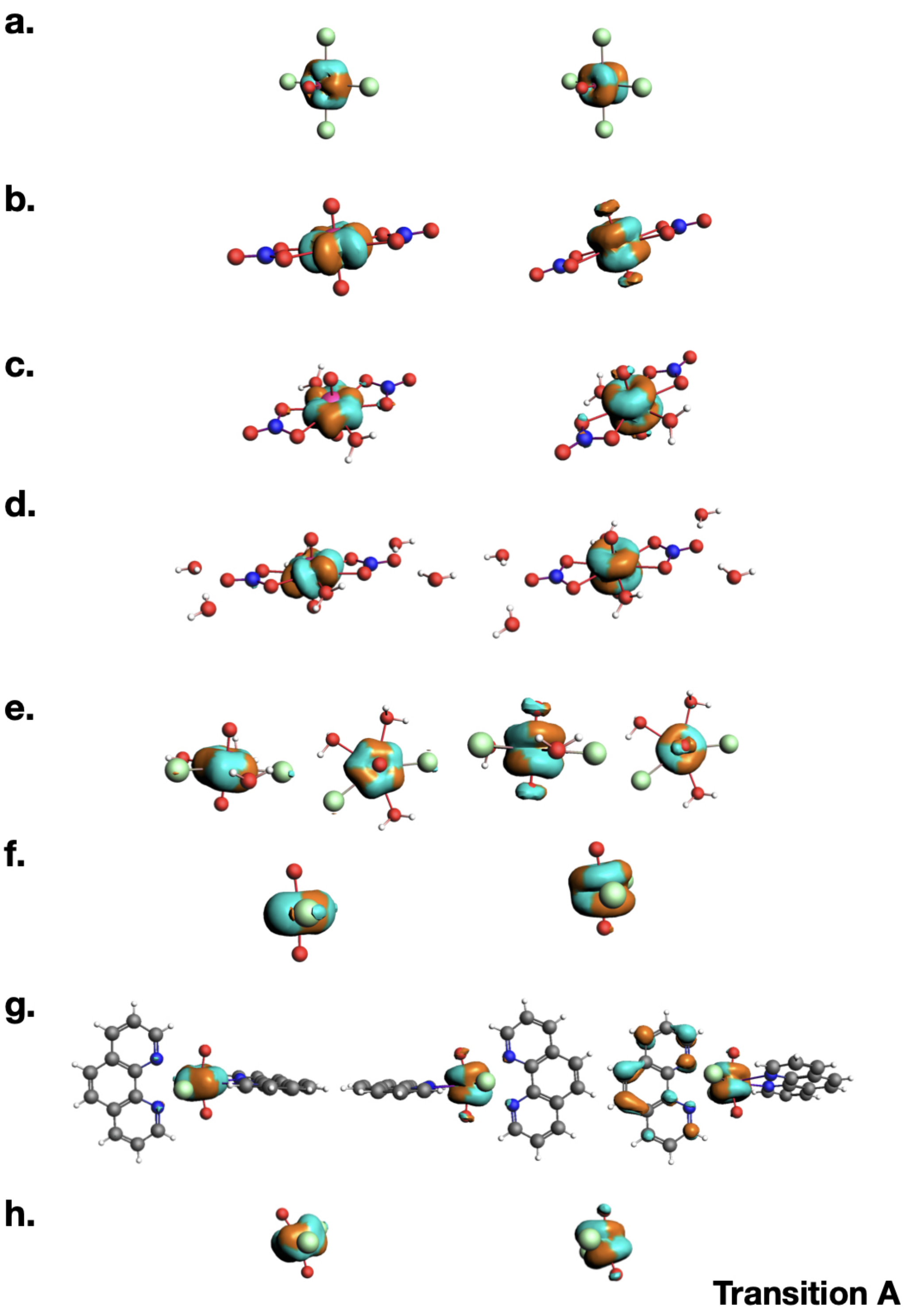

Figure 5.9: Dominant 2c-TD (particle) natural transition orbitals (NTOs) for the peaks pertaining to the U $3d_{5/2g} \rightarrow 5f\ \delta_u, \phi_u$ transition at uranium M_4-edge for (a) $UO_2Cl_4^{2-}$, (c) $UO_2(NO_3)_2(H_2O)_2$, (d) $[UO_2(NO_3)_2(H_2O)_2](H_2O)_4$, (e) $UO_2Cl_2(H_2O)_3$, (g) $UO_2Cl_2(phen)_2$. We also present the NTOs for their corresponding (b) $UO_2(NO_3)_2$ or (f, h) UO_2Cl_2 subunits. Plots have employed 0.03 as the isosurface value.

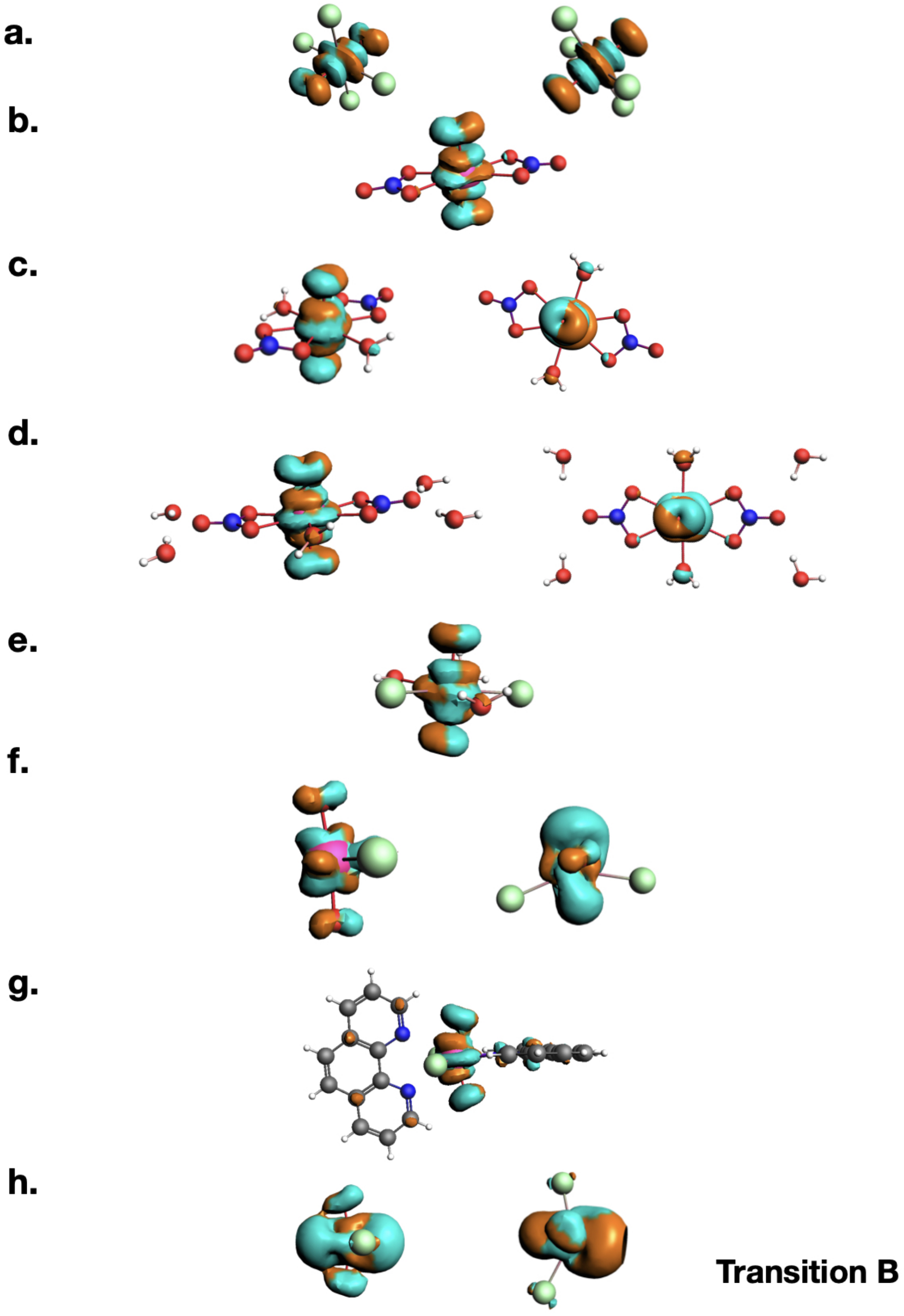

Figure 5.10: Dominant 2c-TD (particle) natural transition orbitals (NTOs) for the peaks pertaining to the U $3d_{5/2g} \rightarrow 5f\pi^*_u$ transition at uranium M_4-edge of (a) $UO_2Cl_4^{2-}$, (c) $UO_2(NO_3)_2(H_2O)_2$, (d) $[UO_2(NO_3)_2(H_2O)_2](H_2O)_4$, (e) $UO_2Cl_2(H_2O)_3$, (g) $UO_2Cl_2(phen)_2$. We also present the NTOs for their corresponding (b) $UO_2(NO_3)_2$ or (f, h) UO_2Cl_2 subunits. Plots have employed 0.03 as the isosurface value.

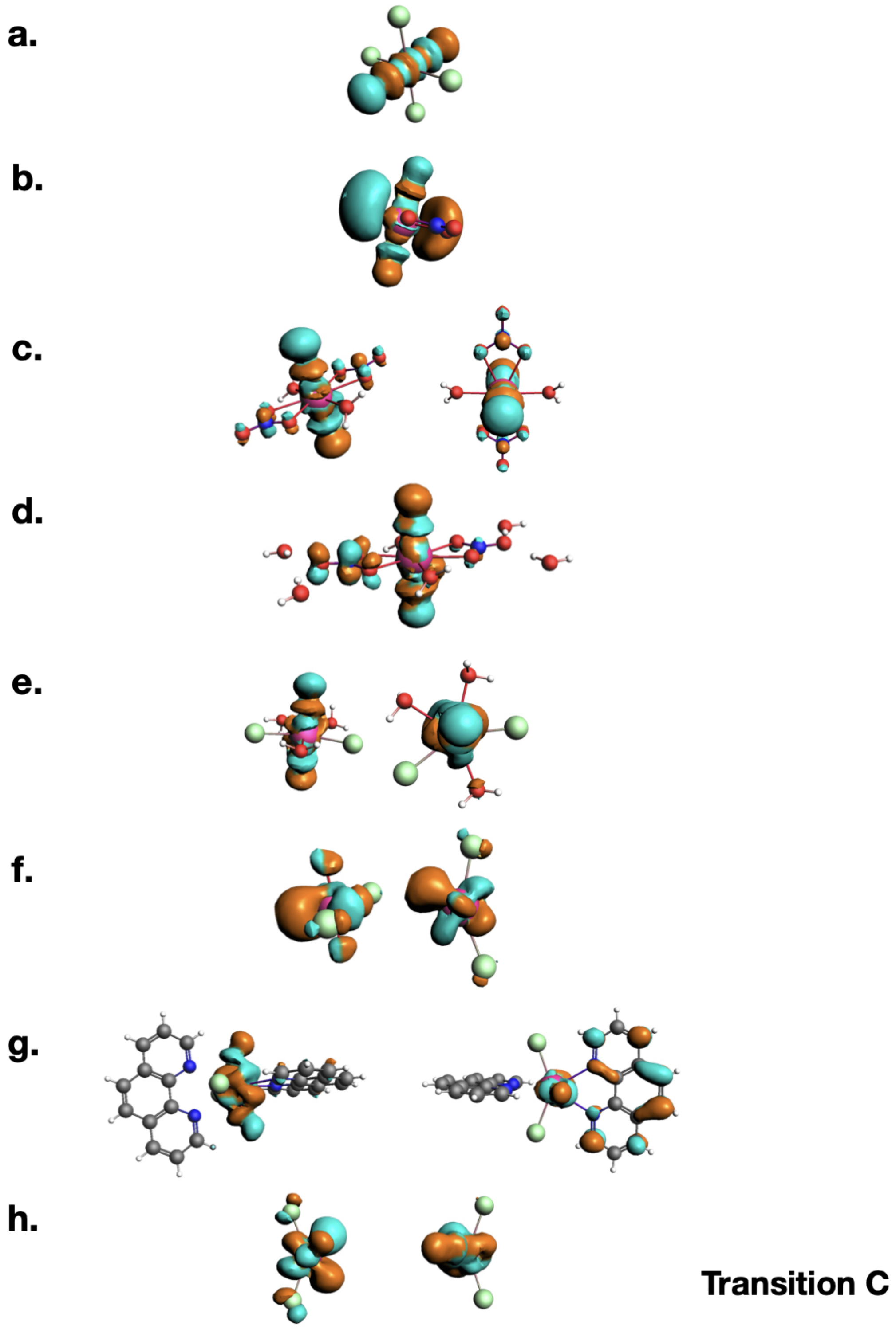

Figure 5.11: Dominant 2c-TD (particle) natural transition orbitals (NTOs) for the peaks pertaining to the U $3d_{5/2g} \rightarrow 5f\sigma_u^*$ transition at uranium M$_4$-edge of (a) $UO_2Cl_4^{2-}$, (c) $UO_2(NO_3)_2(H_2O)_2$, (d) $[UO_2(NO_3)_2(H_2O)_2](H_2O)_4$, (e) $UO_2Cl_2(H_2O)_3$, (g) $UO_2Cl_2(phen)_2$. We also present the NTOs for their corresponding (b) $UO_2(NO_3)_2$ or (f, h) UO_2Cl_2 subunits. Plots have employed 0.03 as the isosurface value.

5.6 Future perspectives

With respect to linear uranyl structures, as explored in the current chapter, by means of 2c-TDA simulations, we were able to provide a semi-quantitative U M_4 XAS spectra for the $Cs_2UO_2Cl_4$ system. This is not the case for the $[UO_2(NO_3)_2(H_2O)_2](H_2O)_4$ species, in which the **C** feature is considerably shifted to the right, even though we have investigated three different models. Therefore, one could investigate other structures of $[UO_2(NO_3)_2(H_2O)_2](H_2O)_n$ complexes. For instance, the role of the U–O_{yl} bond length could be reassessed by employing the same structure for $UO_2(NO_3)_2$ as the one reported by Konecny et al.[225]. Additionally, given the observed variation in transition energies and intensities observed in the U M_4 XAS spectra of the investigated nitrates, it would be worthwhile to explore whether the FDE framework would work well at describing the role of the first two spheres of water molecules in determining these excited states, as we have done for the $UO_2Cl_4^{2-}$ system in the previous chapter.

In a similar way, Figure 5.7 clearly demonstrates a significant deviation between the HERFD spectrum and the simulated spectra for the $UO_2Cl_2(H_2O)_3$ complex. Within the "An–O_{yl} bond length"-based interpretation of the U M_4 XAS, the most obvious hypothesis is that the system measured by HERFD exhibits a shorter U–O_{yl} bond compared to the one reported by Platts and Baker [440]. Another factor to consider is the possibility that the measurement was performed on a different conformer of the $UO_2Cl_2(H_2O)_n$ complex, which could exhibit a different extent of electrostatic interaction between the uranyl unit and its environment, as well as different U–O_{yl} bond lengths. These conformers were further highlighted in an investigation carried out by Yang et al. [451].

Therefore, similar to nitrates, the follow-up to this study should involve exploring alternative structural models of the $UO_2Cl_2(H_2O)_n$ complex, in addition to the ones investigated here. Regardless of whether the focus is on the U–O_{yl} bond length or the effects of the equatorial ligands, a starting point would be to perform simulations on the structures reported by Yang et al. [451] at the NEVPT2 level. Similarly, one could optimize these geometries, for instance, using the PBE0 functional with dispersion corrections, which has demonstrated good performance by matching the crystal structure of $UO_2Cl_2(phen)_2$ [441].

In this thesis, we have employed the formalism of response theory in a relativistic DFT framework to address the theoretical treatment of the core-excited states of AnO_2^{2+} species, specifically focusing on the excited states of the uranyl ion. Overall, this approach has demonstrated the ability to produce semi-quantitative results compared to experimental data. It is worth mentioning that wave function-based methods could also be utilized to tackle this problem, as demonstrated by Sergentu et al. [390, 393] and Polly et al. [392], who previously investigated the U, Np, Pu $M_{4,5}$ XAS using relativistic multiconfigurational methods. Moreover, as will be further explored in the final section of this thesis, coupled cluster methods (CC) also offer a powerful framework for investigating the core-excited states of molecules. In addition to the equation-of-motion (EOM-CC) framework employed here, other CC methods, such as its linear response formulation (LR-CC) can be applied to address these problems.

This way, conducting a comprehensive comparison between wave-function and density-based methods for computing core-excited states of AnO_2^{2+} species, similar to the work done by Réal et al.[443] on low-lying excitations, holds significance. Such a systematic study could effectively elucidate the role of dynamical and static correlation in determining the core-excited states of actinyls, which would be valuable when further dealing with open-shell systems.

Finally, our methodology has been shown to provide a more accurate description of peak splittings in the U M_4 XAS spectra compared to other *ab initio* molecular simulations that employ more correlated methods and other structural models. However, they exhibit a similar overestimation of the **B** transition. This challenge in accurately reproducing the relative intensity of this feature is not only observed in various uranyl species (as seen in the review by Kvashnina et al. [12]) but also in recent simulations of uranates, as reported by Amidani et al. [18] using multiplet calculations. Thus far, no theoretical level has provided a more accurate description of this feature. Therefore, this particular deviation remains unresolved in our current research. We hope that this particular aspect will serve as motivation for further investigations.

Bibliography of the current chapter

(9) Bauer, M. HERFD-XAS and valence-to-core-XES: new tools to push the limits in research with hard X-rays? *Physical Chemistry Chemical Physics* **2014**, *16*, 13827–13837.

(12) Kvashnina, K.; Butorin, S. M.; Martin, P.; Glatzel, P. Chemical state of complex uranium oxides. *Physical review letters* **2013**, *111*, 253002.

(18) Amidani, L.; Retegan, M.; Volkova, A.; Popa, K.; Martin, P. M.; Kvashnina, K. O. Probing the local coordination of hexavalent uranium and the splitting of 5f orbitals induced by chemical bonding. *Inorganic Chemistry* **2021**, *60*, 16286–16293.

(21) Vitova, T.; Pidchenko, I.; Fellhauer, D.; Bagus, P. S.; Joly, Y.; Pruessmann, T.; Bahl, S.; Gonzalez-Robles, E.; Rothe, J.; Altmaier, M., et al. The role of the 5 f valence orbitals of early actinides in chemical bonding. *Nature communications* **2017**, *8*, 16053.

(34) Gel'mukhanov, F.; Ågren, H. Resonant X-ray Raman scattering. *Physics Reports* **1999**, *312*, 87–330.

(39) Gel'mukhanov, F.; Odelius, M.; Polyutov, S. P.; Foehlisch, A.; Kimberg, V. Dynamics of resonant x-ray and Auger scattering. *Reviews of Modern Physics* **2021**, *93*, 035001.

(40) Kvashnina, K. O.; Butorin, S. M. High-energy resolution X-ray spectroscopy at actinide M 4, 5 and ligand K edges: what we know, what we want to know, and what we can know. *Chemical Communications* **2022**, *58*, 327–342.

(48) Oher, H.; Vercouter, T.; Réal, F.; Shang, C.; Reiller, P. E.; Vallet, V. Influence of Alkaline Earth Metal Ions on Structures and Luminescent Properties of Na m M n UO2 (CO3) 3 (4–m–2 n)–(M= Mg, Ca; m, n= 0–2): Time-Resolved Fluorescence Spectroscopy and Ab Initio Studies. *Inorganic Chemistry* **2020**, *59*, 15036–15049.

(99) Van Lenthe, E.; Baerends, E. J. Optimized Slater-type basis sets for the elements 1–118. *Journal of computational chemistry* **2003**, *24*, 1142–1156.

(167) Gomes, A. S. P.; Jacob, C. R.; Réal, F.; Visscher, L.; Vallet, V. Towards systematically improvable models for actinides in condensed phase: the electronic spectrum of uranyl in Cs 2 UO 2 Cl 4 as a test case. *Physical Chemistry Chemical Physics* **2013**, *15*, 15153–15162.

(200) Scheinost, A. C.; Claussner, J.; Exner, J.; Feig, M.; Findeisen, S.; Hennig, C.; Kvashnina, K. O.; Naudet, D.; Prieur, D.; Rossberg, A., et al. ROBL-II at ESRF: a synchrotron toolbox for actinide research. *Journal of Synchrotron Radiation* **2021**, *28*, 333–349.

(214) Te Velde, G. t.; Bickelhaupt, F. M.; Baerends, E. J.; Fonseca Guerra, C.; van Gisbergen, S. J.; Snijders, J. G.; Ziegler, T. Chemistry with ADF. *Journal of Computational Chemistry* **2001**, *22*, 931–967.

(221) Yanai, T.; Nakajima, T.; Ishikawa, Y.; Hirao, K. A new computational scheme for the Dirac–Hartree–Fock method employing an efficient integral algorithm. *The Journal of Chemical Physics* **2001**, *114*, 6526–6538.

(222) Tecmer, P.; Bast, R.; Ruud, K.; Visscher, L. Charge-Transfer Excitations in Uranyl Tetrachloride ([UO2Cl4] 2–): How Reliable are Electronic Spectra from Relativistic Time-Dependent Density Functional Theory? *The Journal of Physical Chemistry A* **2012**, *116*, 7397–7404.

(225) Konecny, L.; Vicha, J.; Komorovsky, S.; Ruud, K.; Repisky, M. Accurate X-ray absorption spectra near L-and M-edges from relativistic four-component damped response time-dependent density functional theory. *Inorganic chemistry* **2021**, *61*, 830–846.

(323) Misael, W.; Gomes, A. Core Excitations of Uranyl in Cs2UO2Cl4 from Relativistic Embedded Damped Response Time-Dependent Density Functional Theory Calculations. *Inorganic Chemistry* **2023**, *62*, 11589–11601.

(328) Vitova, T.; Green, J. C.; Denning, R. G.; Löble, M.; Kvashnina, K.; Kas, J. J.; Jorissen, K.; Rehr, J. J.; Malcherek, T.; Denecke, M. A. Polarization dependent high energy resolution X-ray absorption study of dicesium uranyl tetrachloride. *Inorganic chemistry* **2015**, *54*, 174–182.

(390) Sergentu, D.-C.; Duignan, T. J.; Autschbach, J. Ab initio study of covalency in the ground versus core-excited states and X-ray absorption spectra of actinide complexes. *The Journal of Physical Chemistry Letters* **2018**, *9*, 5583–5591.

(392) Polly, R.; Schacherl, B.; Rothe, J.; Vitova, T. Relativistic multiconfigurational Ab initio calculation of uranyl 3d4f resonant inelastic X-ray scattering. *Inorganic chemistry* **2021**, *60*, 18764–18776.

(393) Sergentu, D.-C.; Autschbach, J. X-ray absorption spectra of f-element complexes: insight from relativistic multiconfigurational wavefunction theory. *Dalton Transactions* **2022**.

(407) Watkin, D. J.; Denning, R. G.; Prout, K. Structure of dicaesium tetrachlorodioxouranium (VI). *Acta Crystallographica Section C: Crystal Structure Communications* **1991**, *47*, 2517–2519.

(411) Hirata, S.; Head-Gordon, M. Time-dependent density functional theory within the Tamm–Dancoff approximation. *Chemical Physics Letters* **1999**, *314*, 291–299.

(412) Martin, R. L. Natural transition orbitals. *The Journal of chemical physics* **2003**, *118*, 4775–4777.

(433) Misael, W. A.; Bazarkina, E. F.; Maerz, J.; Vallet, V.; Gomes, A. S. P.; Kvashnina, K. O. *In preparation* **2023**.

(434) Raimondi, P.; Benabderrahmane, C.; Berkvens, P.; Biasci, J. C.; Borowiec, P.; Bouteille, J.-F.; Brochard, T.; Brookes, N. B.; Carmignani, N.; Carver, L. R., et al. The Extremely Brilliant Source storage ring of the European Synchrotron Radiation Facility. *Communications Physics* **2023**, *6*, 82.

(435) Hämäläinen, K.; Siddons, D.; Hastings, J.; Berman, L. Elimination of the inner-shell lifetime broadening in x-ray-absorption spectroscopy. *Physical review letters* **1991**, *67*, 2850.

(436) Butorin, S. M.; Modin, A.; Vegelius, J. R.; Kvashnina, K. O.; Shuh, D. K. Probing chemical bonding in uranium dioxide by means of high-resolution X-ray absorption spectroscopy. *The Journal of Physical Chemistry C* **2016**, *120*, 29397–29404.

(437) De Groot, F. High-resolution X-ray emission and X-ray absorption spectroscopy. *Chemical Reviews* **2001**, *101*, 1779–1808.

(438) Butorin, S. M. Resonant inelastic X-ray scattering as a probe of optical scale excitations in strongly electron-correlated systems: quasi-localized view. *Journal of Electron Spectroscopy and Related Phenomena* **2000**, *110*, 213–233.

(439) Taylor, J.; Mueller, M. A neutron diffraction study of uranyl nitrate hexahydrate. *Acta Crystallographica* **1965**, *19*, 536–543.

(440) Platts, J. A.; Baker, R. J. Non-covalent interactions of uranyl complexes: a theoretical study. *Physical Chemistry Chemical Physics* **2018**, *20*, 15380–15388.

(441) Oher, H.; Gomes, A. S. P.; Wilson, R. E.; Schnaars, D. D.; Vallet, V. How Does Bending the Uranyl Unit Influence Its Spectroscopy and Luminescence? *Inorganic Chemistry* **2023**, *62*, 9273–9284.

(442) Petiau, J.; Calas, G.; Petitmaire, D.; Bianconi, A.; Benfatto, M.; Marcelli, A. Delocalized versus localized unoccupied 5f states and the uranium site structure in uranium oxides and glasses probed by x-ray-absorption near-edge structure. *Physical Review B* **1986**, *34*, 7350.

(443) Réal, F.; Gomes, A. S. P.; Visscher, L.; Vallet, V.; Eliav, E. Benchmarking electronic structure calculations on the bare UO22+ ion: How different are single and multireference electron correlation methods? *The Journal of Physical Chemistry A* **2009**, *113*, 12504–12511.

(444) Hayton, T. W. Understanding the origins of O yl–U–O yl bending in the uranyl (UO 2 2+) ion. *Dalton Transactions* **2018**, *47*, 1003–1009.

(445) Schöne, S.; Radoske, T.; März, J.; Stumpf, T.; Patzschke, M.; Ikeda-Ohno, A. [UO2Cl2 (phen) 2], a Simple Uranium (VI) Compound with a Significantly Bent Uranyl Unit (phen= 1, 10-phenanthroline). *Chemistry–A European Journal* **2017**, *23*, 13574–13578.

(446) Langer, E. M.; Kegler, P.; Kowalski, P. M.; Wang, S.; Alekseev, E. V. Achieving and Stabilizing Uranyl Bending via Physical Pressure. *Inorganic Chemistry* **2021**, *60*, 8419–8422.

(447) Vallet, V.; Wahlgren, U.; Grenthe, I. Probing the nature of chemical bonding in uranyl (VI) complexes with quantum chemical methods. *The Journal of Physical Chemistry A* **2012**, *116*, 12373–12380.

(448) Garcıa-Ramos, J. C.; Galindo-Murillo, R.; Tovar-Tovar, A.; Alonso-Saenz, A. L.; Gómez-Vidales, V.; Flores-Álamo, M.; Ortiz-Frade, L.; Cortes-Guzmán, F.; Moreno-Esparza, R.; Campero, A., et al. The π-Back-Bonding Modulation and Its Impact in the Electronic Properties of CuII Antineoplastic Compounds: An Experimental and Theoretical Study. *Chemistry–A European Journal* **2014**, *20*, 13730–13741.

(449) Woods, J. J.; Unnerstall, R.; Hasson, A.; Abou, D. S.; Radchenko, V.; Thorek, D. L.; Wilson, J. J. Stable chelation of the uranyl ion by acyclic hexadentate ligands: Potential applications for 230U targeted α-therapy. *Inorganic chemistry* **2022**, *61*, 3337–3350.

(450) Bencini, A.; Lippolis, V. 1, 10-Phenanthroline: A versatile building block for the construction of ligands for various purposes. *Coordination Chemistry Reviews* **2010**, *254*, 2096–2180.

(451) Yang, J.-J.; Zhao, Z.; Su, J. Theoretical Study of the Excited States and Luminescent Properties of (H2O) n UO2Cl2 (n= 1–3). *Inorganic Chemistry* **2023**, *62*, 1978–1987.

Chapter 6

Relativistic CVS-EOM-IP study of uranyl in $Cs_2UO_2Cl_4$

> *"Oh, the glory of it all was lost on me, 'til I saw how hard it'd be to reach you.*
> *And I would always be lightyears, lightyears away from you.*
> *Lightyears, lightyears away from you."*
>
> — Light Years, The National

The material presented in this chapter forms a manuscript in preparation [452].

Abstract

In this work, we investigate the core-level ionization energies of the bare uranyl ion (UO_2^{2+}) within a $Cs_2UO_2Cl_4$ crystalline environment. Our main focus is to evaluate the performance of 4- and 2-component Hamiltonians, assess truncation effects in the correlated molecular spinor basis, and examine the influence of dynamical correlation on the simulation of spectroscopic observables of actinyls. To achieve this, we employ a recent implementation of the core-valence-separated relativistic equation-of-motion coupled-cluster method (CVS-EOM-CC). Building upon our previous work [Inorg. Chem. 2023, 62, 29, 11589–11601], we also

compare the differences that arise in these properties when different structural models are employed. Specifically, we use the frozen density embedding method (FDE) to evaluate the effect of the chlorides in the closest vicinity of the uranyl unit on the investigated properties. By comparing the bare and embedded uranyl models, we observe significant changes in binding energies, highlighting the influence of equatorial ligands. These changes prove to be comparable to the results obtained for the uranyl tetrachloride dianion ($UO_2Cl_4^{2-}$) species, with differences smaller than 4 eV. Additionally, we compare our results with experimental data for the $Cs_2UO_2Cl_4$ crystal, which show deviations smaller than 7 eV in most cases.

6.1 Introduction

Photoemission spectroscopies, including ultraviolet and X-ray photoelectron spectroscopies (UPS and XPS) as well as angle-resolved photoemission spectroscopy (ARPES), are established spectroscopic techniques based on the photoelectric effect [26, 27]. These techniques serve as powerful tools for unraveling the electronic structure of materials [5, 453–458]. In particular, XPS experiments take advantage of the element-specificity and orbital-selective characteristics of X-ray spectroscopies, as the energy levels of core orbitals precisely fall within the X-ray range [125, 457].

Performing photoemission measurements in actinide-containing materials holds great significance due to their ability to provide valuable insights into chemical bonding, coordination chemistry, and oxidation states [1, 3]. Furthermore, comprehending these aspects is especially important given the risks posed by these species to human health and the environment. In fact, a considerable number of studies in the literature have highlighted the instrumental role that photoemission measurements play in studying the chemical environment of actinide materials and gaining an understanding of their complex speciation [11, 49–52, 459–464].

However, it is well-known that interpreting their photoemission spectra can be challenging due to factors such as the significant extent of electronic correlation, ligand field effects on the multiplet structure, satellite peaks, and vibronic coupling that show up in the recorded spectra [11, 368, 389, 395, 465–469]. When it comes to valence-level experiments, interpreting the spectra can be challenging due to significant peak overlap caused by the high density of states. This overlap makes it challenging to distinguish the partial cross sections from different excitations and decay processes, as they energetically coincide [50, 465, 466]. Nevertheless, as demonstrated by Kvashnina et al. [12, 389, 470] and Teterin et al. [50], X-ray experiments can serve as a complementary tool to provide valuable insights into the valence band of actinide-containing materials.

Considering all these aspects and the evolution of synchrotron radiation sources, there is considerable appeal in probing the electronic structure of actinide-containing materials by means of measurements in the X-ray range, as photoemission experiments can be performed with improved energy and spectral resolution. Furthermore, this underscores the importance of developing robust theoretical methods and protocols to investigate the ionized states of actinides and aid in understanding their interaction with X-ray photons.

In addition to electronic correlation, relativistic effects play a crucial role in determining the excited states of heavy (and superheavy) elements [46–48, 108, 167, 222, 223, 368, 471–475]. Our previous investigations have provided valuable insights into the roles of static and dynamic correlation in valence-level excited states of actinide-containing systems, such as AnO_2^{2+} (An = U, Np, Pu), recovered by relativistic wavefunction-based methods, including the relativistic intermediate Hamiltonian Fock-space coupled-cluster (IHFSCC) [167, 472, 473, 476] and linear-response coupled-cluster (LR-CC) methods [443, 473], as well as the complete active space second order perturbation theory (CASPT2) [168, 473, 474]. Additionally, van Besien et al. [477, 478] investigated the role of these contributions using CASPT2. The bare uranyl ion (UO_2^{2+}) has been shown by the previous studies to be well represented by a single reference determinant [443], opening the way for the use of single-reference coupled cluster approaches such as the equation of motion CC (EOM-CC) to investigate their spectra.

When investigating core-level spectroscopic observables, the remarkable agreement between CC simulations and experimental data becomes evident, often revealing differences of less than 1 eV in organic systems [123, 124, 126, 379, 479]. However, the computational complexity of these methods – with a formal scaling of $\mathcal{O}(n_o^2 n_v^4)$ for CCSD, where n_o and n_v respectively denote the number of occupied and virtual orbitals – imposes limitations on their application. These limitations restrict in practice their usage to highly symmetric systems with lighter elements and relatively small basis sets [134, 267, 480].

Therefore, the extension of these methods to accurately treat spectroscopic quantities in complex systems encompassing elements throughout the entire periodic table in a balanced manner is of great interest but remains a challenge to theory. Apart from recent advances in CC methods with reduced scaling, as reviewed by Crawford et al. [480], we note recent implementation efforts to enable large-scale relativistic CC implementations on next-generation architectures as reported by Pototschnig et al. [134]. To what concerns the evaluation of core-excited states by means of coupled-cluster methods, several efforts have been reported in the literature. Notably, the works of Coriani and Koch [123, 481, 482], Vidal et al. [126, 483], and Halbert et al. [128] have introduced effective techniques such as the asymmetric-Lanczos-chain and the core-valence separation (CVS) methods, which have demonstrated excellent performance in obtaining these excited states.

In the following sections, we present our findings on the oxygen 1s and various uranium core-level binding energies using the CVS-EOM-CC method. In Section 6.3.1, we investigate the impact of different Hamiltonians and spinors on simulating the core ionization energies of UO_2^{2+}. This complements the study conducted by Halbert et al. [128], with a specific focus on a heavier center.

In Section 6.3.2, we expand on the investigation carried out by South et al. [374] regarding the role of orbital correlation and relaxation in the ionization energies of uranium 2p electrons, extending it to include other core-level binding energies. Furthermore, in Section 6.3.3, we discuss the constraints within our protocol that may affect the extension of our investigation to more complex structural models.

In this regard, we complement the work of Gomes et al. [167] by evaluating different structural models for computing spectroscopic observables, specifically addressing core-level binding energies. We assess the UO_2^{2+} unit, as well as the computationally demanding $UO_2Cl_4^{2-}$ dianion. To address this challenge, we employ a model where the equatorial ligands are represented within the frozen density embedding (FDE) scheme [206, 207]. This strategy has proven highly successful in addressing core-level spectroscopic quantities, as recently demonstrated by Misael and Gomes [323] in their study of XANES in actinide-containing systems, using the same models examined in this work. Furthermore, this strategy has also been successfully applied to core-ionizations of halogenated species adsorbed on ice surfaces and in solution, as explored by Opoku et al. [484].

Finally, in Section 6.3.4, we compare our computed values with the photoemission measurements conducted by Teterin et al. [50] for the $Cs_2UO_2Cl_4$ crystal.

6.2 Computational details

CVS-EOM-IP-CCSD calculations and CVS-EOM-IP-CCSD-in-DFT calculations were performed in DIRAC22 version of the `DIRAC` electronic structure code [403]. We employed Dyall's all-electron basis sets of double and triple-zeta quality [404, 405] for uranium and Dunning's cc-pVTZ basis set [325] for all other atoms. These basis sets were left uncontracted. We have employed a gaussian nuclear model in all calculations [406].

For EOM-CC calculations, we have employed the X2Cmmf [293] Hamiltonian ($^2\mathrm{DC}^M$), in which the decoupling of the large and small components is done by block diagonalized the converged 4-component Fock matrix at the end of the SCF procedure. In benchmark calculations with EOM-IP-CCSD, we have also employed the X2Cmmf-Gaunt [293] Hamiltonian ($^2\mathrm{DCG}^M$), in which the Gaunt integrals are included in the construction of the (4-component) Fock matrix of the SCF step, but are not explicitly included in the transformation from atomic to molecular basis.

Also, as will be further discussed in more detail, for CVS-EOM-IP calculations we have explored various correlation spaces. Apart from the case of CVS-EOM-IP calculations on the bare uranyl ion, we replaced the contributions from $(SS|SS)$-type integrals by a simple Coulombic correction [282] for reasons of computational cost. Furthermore, we only employed double-zeta basis sets in calculations for the dianion. Bare and embedded uranyl calculations were performed using double- and triple-zeta basis sets. When applicable, QED+Breit values reported by Kozioł and Aucar [308] were added.

In all of our calculations, the structures employed were based on the experimental crystal structure of $Cs_2UO_2Cl_4$ reported by Watkin et al.[407], whose U-O and U-Cl bond lengths are 1.774 Å and 2.673 Å respectively. For the embedding calculations, we employed the same structural models and subsystem partitioning as outlined by Gomes et al.[167]. All calculations on the bare uranyl and uranyl tetrachloride were carried out in D_{∞_h} and D_{2h} symmetry, respectively, while for embedded uranyl simulations the crystalline site symmetry (C_{2h}) was used.

The embedding potentials employed here were obtained from freeze-thaw calculations employing the scalar-relativistic ZORA Hamiltonian [408], TZ2P basis sets, the PW91k kinetic energy functional [228], the PBE exchange-correlation functional [229] for the non-additive terms and subsystem energies. These calculations were carried out via the `PyADF` scripting framework [215] and the embedding potentials were subsequently imported into the `DIRAC` calculations.

6.3 Results and discussion

6.3.1 Comparing relativistic Hamiltonians

Decoupling the Dirac equation

Table 6.1 presents the results of our investigation, including the findings from ^{4}DC calculations and the variations observed when employing other Hamiltonians. Our results indicate that the discrepancies in binding energies between the reference ^{4}DC calculations and the computationally more efficient $^2DC^M$ calculations are generally negligible, with values of approximately 0.3 eV or less in absolute terms. However, for the uranium 1s binding energy, the differences reach approximately 2.4 eV in absolute value. The observed discrepancy in our results follows a trend observed by Halbert et al. [128] for halides, where it increases modestly with atomic number, being approximately 1.7 eV for At.

Our results contain a notable observation concerning the one-electron picture

Assignment		^{4}DC	Difference with respect to the ^{4}DC reference				
			^{4}DC (SS|SS)	^{2}DC^{M}	^{2}DC^{M} (SS|SS)	^{2}DCG^{M}	^{2}DCG^{M} (SS|SS)
U	1s	116432.54	-68.44	-2.42	-69.57	-525.14	-591.68
	2s	21905.11	-12.56	-0.14	-12.58	-64.17	-76.72
	$2p_{1/2}$	21095.75	-17.97	0.02	-17.83	-107.87	-125.57
	$2p_{3/2}$	17257.06	-5.86	-0.28	-6.08	-68.52	-74.27
		17256.97	-5.85	-0.28	-6.07	-68.51	-74.26
	3s	5609.00	-3.16	$< 3\times10^{-3}$	-3.14	-12.68	-15.80
	$3p_{1/2}$	5239.69	-4.10	0.02	-4.08	-21.44	-25.51
	$3p_{3/2}$	4348.50	-1.52	$< 3\times10^{-2}$	-1.54	-13.13	-14.64
		4347.97	-1.53	-0.03	-1.55	-13.13	-14.64
	$3d_{3/2}$	3765.71	-1.43	0.02	-1.40	-9.52	-10.92
		3765.45	-1.42	0.02	-1.39	-9.50	-10.90
	$3d_{5/2}$	3585.16	-0.21	-0.05	-0.26	-6.71	-6.92
		3584.86	-0.22	-0.06	-0.27	-6.70	-6.92
		3584.72	-0.22	-0.06	-0.27	-6.70	-6.91
	4s	1480.55	-0.83	0.01	-0.82	-2.93	-3.76
	$4p_{1/2}$	1313.23	-1.03	0.01	-1.03	-5.03	-6.06
	$4p_{3/2}$	1079.22	-0.37	$< 2\times10^{-3}$	-0.37	-2.79	-3.16
		1078.20	-0.37	$< 1\times10^{-4}$	-0.37	-2.78	-3.15
	$4d_{3/2}$	812.39	-0.30	$< 2\times10^{-3}$	-0.29	-1.59	-1.89
		811.47	-0.29	0.01	-0.29	-1.58	-1.87
	$4d_{5/2}$	768.84	-0.02	-0.01	-0.02	-0.92	-0.93
		768.06	-0.01	$< 2\times10^{-3}$	-0.01	-0.91	-0.92
		767.59	-0.01	$< 3\times10^{-3}$	-0.01	-0.90	-0.92
	$4f_{5/2}$	417.08	0.05	0.01	0.05	0.06	0.10
		416.36	0.04	$< 6\times10^{-4}$	0.05	0.06	0.10
		416.01	0.05	0.01	0.05	0.07	0.12
	$4f_{7/2}$	406.02	0.06	$< 5\times10^{-4}$	0.06	0.08	0.13
		405.39	0.05	0.01	0.05	0.07	0.12
		404.90	0.05	0.01	0.05	0.07	0.12
		404.70	0.05	0.01	0.05	0.07	0.12
O	1s	555.52	0.01	0.01	0.01	0.03	0.05
		555.52	0.01	0.01	0.01	0.03	0.05

Table 6.1: CVS-EOM-IP (^{4}DC) calculation results and ΔE differences (in eV) between the reference ^{4}DC values and various relativistic Hamiltonians for uranium and oxygen in UO_2^{2+}. Hamiltonians are discussed in the text. Uncontracted Dyall double-zeta basis sets [404, 405] are used for all atoms. It should be noted that different values for a given edge correspond to splitting caused by the reduction in symmetry in the molecular system compared to the isolated atoms.

change error (here denoted as PCE). Specifically, the PCE in the U 1s absolute binding energy corresponds to only 0.0021% of the calculated absolute binding energy. From this, we can conclude that the discrepancy arising from the PCE is not expected to be a significant source of error in the simulation of binding energies calculations for actinides and beyond (superheavy elements). However, it is important to note that this conclusion may not be generalized to other properties. In their paper, Repisky et al. acknowledges that although a significant portion of the PCE error can be recovered by employing their X2C approaches, they still observed qualitative discrepancies. For instance, they highlight their results for the contact density contribution of the Cn 1s shell in CnF_6, which experiences a shift of approximately 11% between the 2- and 4-component frameworks.

The role of small-type integrals

We also examined the significance of explicitly calculating two-electron integrals of (SS|SS)-type in the simulation simulating core-level spectroscopic properties of actinides, building upon the previous work of South et al. on uranium 2p binding energies [374]. The computation of these integrals is computationally demanding, and typically, the Coulombic correction method proposed by Visscher [282] is employed to alleviate the computational demands.

Based on our findings, also displayed in Table 6.1, it is evident that the inclusion of these integrals has a significant role when computing the innermost ionization energies of uranium. In addition, we also observe that the explicit inclusion of (SS|SS)-type integrals has a more pronounced effect on $p_{1/2}$ spinors compared to other spinors within the same shell. These findings align with the observations made by Halbert et al. for At.

Furthermore, our results indicate that these integrals generally increase the ionization energies above the $4f_{5/2}$ level, while for lower levels, the opposite trend is observed, with only modest variations. Finally, our calculated uranium $2p_{1/2}$ and $2p_{3/2}$ ionization energies, including (SS|SS)-type integrals, show quantitative agreement with the results reported by South et al., despite the differences in theory level (ΔHF/dyall.v3z).

Electron-electron interaction beyond the Coulomb term

Additionally, we explored the influence of current-current interactions on these spectroscopic observables, also shown in Table 6.1. Specifically, we included the Gaunt interaction in the two-electron operator, thereby taking into account the contributions from spin-other-orbit (SOO) interactions.

From our results, we observe that these interactions exhibit significantly larger magnitudes than those from (SS|SS)-type integrals. For instance, the uranium 1s ionization energy shows a contribution of 522.7 eV from the Gaunt interaction, whereas the (SS|SS)-type integrals contribute only 67.1 eV. Similarly, for the uranium 2s ionization energy, the Gaunt interaction contributes 68 eV, while the (SS|SS)-type integrals contribute 6 eV.

These results are consistent with the findings of South et al. regarding uranium 2p binding energies, as well as with the research conducted by Repisky et al. on the inner-core edges of (super)heavy elements. They underscore the relevance of considering the electron-electron repulsion beyond the zeroth order truncation, i.e., the Coulomb interaction.

6.3.2 Role of dynamical correlation and orbital relaxation

In single-reference CC-based methods, the ground state wave function is obtained from the exponential ansatz, $\Psi_{CC} \equiv e^{\hat{T}}|\Phi_0\rangle$, where dynamical correlation is systematically accounted for by truncating the cluster operator $\hat{T}$. Within the EOM-CC framework, orbital relaxation is incorporated through the excitation operator $\hat{R}$ [114, 310]. In this work, we have applied the EOM-CC method truncated at singles and doubles excitations (CCSD). Within the CVS approximation, core-excited states are easily obtained through the projection of unwanted contributions to the EOM trial vectors, as discussed in detail in the literature [126, 128].

Table 6.2 displays the contributions of orbital correlation and relaxation to the core-level ionization energies of UO_2^{2+} calculated using the CVS-EOM-IP method. These contributions were determined by subtracting the CVS-EOM-IP values from those obtained using Koopmans' theorem. Significant discrepancies are observed between the Koopmans' theorem and CVS-EOM-IP calculations, regardless of the Hamiltonian used. As expected, the influence of dynamical correlation and orbital relaxation becomes increasingly prominent for inner shells, ranging from 19 eV for the O 1s binding energy to over 100 eV for the U 1s binding energy. These findings are consistent with the investigation conducted by South et al. on 2p spinors using the ΔHF and ΔMP2 methods, where the former accounts for orbital relaxation and the latter also recovers orbital correlation.

The results demonstrate that the CVS-EOM-IP framework offers a promising alternative for exploring the effects of orbital correlation and relaxation in systems containing elements beyond the second row of the periodic table. Furthermore, this approach should provide a more reliable alternative for obtaining such excited states compared to methods that optimize the wave function of the ground and core-excited states, such as the ΔMP2 method. It has been shown by Ljubic [486] and Arias-Martinez et al. [487] that the ΔMP2 method often overestimates correlation energy and increases ionization energies, with additional convergence issues and an overall computational effort. Given that these limitations were observed for systems containing lighter elements, it is reasonable to anticipate their presence to plague the computation of excited states for heavier elements as well.

6.3.3 Evaluating approximate models

Before addressing the effect of chlorides in the immediate vicinity of the uranyl ion in the $Cs_2UO_2Cl_4$ crystal (structure **a** in Figure 6.1) and comparing our results to experimental data, we will briefly describe the constraints and the protocol we developed to explore various structural models in a computationally feasible manner.

To utilize our local cluster (Sakura), we have opted to conduct CVS-EOM-IP simulations in serial mode. This approach differs from our previous research on core-excited states of the uranyl unit, where we employed parallel-mode 4c-DR-TD-DFT calculations. To address the computational complexity and time constraints, we developed a protocol that leverages the lower computational cost of highly symmetric systems, such as the uranyl ion in its $D_{\infty h}$ symmetry (UO_2^{2+},

Assignment		^{4}DC	^{4}DC (SS|SS)	^{2}DC^M	^{2}DC^M (SS|SS)	^{2}DCG^M	^{2}DCG^M (SS|SS)
U	1s	102.96	104.18	105.37	105.31	105.09	104.96
	2s	66.68	66.72	66.81	66.74	66.90	67.20
	$2p_{1/2}$	70.31	70.32	70.28	70.18	70.15	70.16
	$2p_{3/2}$	65.58	65.53	65.67	65.75	65.61	65.64
	3s	38.98	38.87	38.98	38.86	38.87	39.00
	$3p_{1/2}$	41.48	41.50	41.46	41.48	41.43	41.42
	$3p_{3/2}$	38.37	38.39	38.39	38.41	38.44	38.45
	$3d_{3/2}$	41.15	41.21	41.13	41.18	41.13	41.18
	$3d_{5/2}$	41.09	41.03	41.14	41.08	41.08	41.20
	4s	20.97	20.98	20.96	20.98	20.90	20.92
	$4p_{1/2}$	21.75	21.70	21.75	21.69	21.62	21.56
	$4p_{3/2}$	20.08	20.04	20.08	20.05	20.01	19.97
	$4d_{3/2}$	19.92	19.95	19.92	19.94	19.88	19.90
	$4d_{5/2}$	19.70	19.71	19.70	19.71	19.79	19.80
	$4f_{5/2}$	19.53	19.58	19.53	19.57	19.56	19.51
	$4f_{7/2}$	19.45	19.35	19.45	19.36	19.42	19.47
O	1s	19.19	19.18	19.19	19.18	19.03	19.02

Table 6.2: Differences between the CVS-EOM-IP core ionization potentials and the corresponding Koopmans' values (in eV) are presented for UO_2^{2+} using the uncontracted Dyall double-zeta basis set for all atoms.

structure **c** in Figure 6.1), within the `DIRAC` program. As we delve into less symmetric models, the extent to which we can exploit this advantage diminishes.

In our previous works [167, 323], we have discussed the uranyl tetrachloride dianion ($UO_2Cl_4^{2-}$, structure **b** in Figure 6.1) as the simplest model for studying the influence of equatorial ligands on the spectroscopic properties of the uranyl ion. However, the $UO_2Cl_4^{2-}$ complex has a lower symmetry (D_{2h}) compared to the bare uranyl ion. Additionally, the introduction of additional ligands results in a substantial increase in the number of electrons (72 more than UO_2^{2+}). The computational demand required to correlate all spinors in such calculations becomes prohibitively expensive, making it impractical to tackle such a problem using the RELCCSD-EOM-CC implementation. This is due to the additional

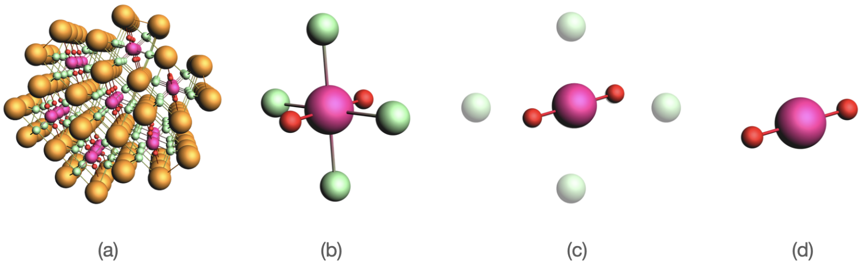

Figure 6.1: Reference systems for this study: (a) Dicesium uranyl(VI) tetrachloride crystal ($Cs_2UO_2Cl_4$). Models here investigated: (b) uranyl(VI) tetrachloride dianion, $UO_2Cl_4^{2-}$ (c) uranyl(VI) ion in the FDE embedding potential of four chloride atoms, UO_2^{2+} @ Cl_4^{4-} and (d) bare uranyl(VI) ion, UO_2^{2+} (cesium: orange; uranium: pink; oxygen: red; chloride: green).

computational steps required for integral transformations between atomic and molecular orbitals and respective sorting, as discussed by Liu and Cheng [108].

As previously observed for core excitations [323], electrostatic interactions, especially those between the uranyl unit and its equatorial ligands, play a pivotal role in determining the spectroscopic observables of actinide-containing systems. Hence, it is unfortunate that conducting a supermolecule investigation using robust *ab initio* simulations remains elusive. The significance of these interactions has been emphasized by various authors, including Amidani et al.[18].

To address this problem, viable solutions do exist. As we have previously explored, the FDE method has demonstrated its suitability for incorporating environmental effects and accurately computing spectroscopic observables at both valence [167] and core levels [323, 484]. By including the environment (e.g. equatorial ligands), *via* an embedding potential in the one-electron Fock matrix, this method showed to be a more cost-effective alternative to supermolecule calculations, which we expect to also provide a comprehensive representation of the influence of equatorial ligands on core-ionized states.

Here, it is necessary to mention another strategy for approximating such complex systems, specifically those that employ a cluster embedding scheme, as adopted by Bagus et al. [11, 395, 453]. In their work, they approximated the environment surrounding uranium oxide models (UO_n, where n=2,3) by employing point charges. By employing this approximation and utilizing the variational Dirac-Hartree-Fock method in conjunction with complete open shell CI (COSCI), Bagus et al. successfully replicated a substantial portion of the spectral features observed in the 4f XPS of U(VI) in their study. However, when it comes to addressing environmental effects, cluster embedding approaches are known to be more computationally demanding and less flexible compared to the FDE scheme. As emphasized by Gomes et al. [167] in the context of actinides, FDE stands out for its ability to explicitly treat smaller units while maintaining the overall quality of simulations.

Nonetheless, certain limitations persist when applying the CVS-EOM-CC-in-DFT flavor of the FDE method to the systems under investigation. In the case of the $Cs_2UO_2Cl_4$ crystal, where we examine the UO_2^{2+} ion in the presence of four chlorides (UO_2^{2+} @ Cl_4^{4-}, structure **c** in Figure 6.1) in its near neighborhood, we need to consider the symmetry breaking from $D_{\infty h}$ to its site symmetry C_{2h} in the crystaline environment. Although the total number of electrons remains the same as in the case of the bare uranyl ion, this symmetry breaking already results in a significant increase in computational time due to a fewer number of symmetry operations that can be applied during the integral sorting.

Role of the correlated virtual spinors space

In order to overcome the high computational demand of these simulations, we investigated the impact of utilizing various cutoffs for the correlated virtual spinors space. Table 6.3 presents the results of our investigation, where we utilized the less expensive ${}^2DC^M$ Hamiltonian and a double zeta basis set for the bare uranyl ion in its pristine $D_{\infty h}$ symmetry. These findings reveal significant variations, approximately 39 eV, in the binding energy of the uranium 1s orbital when transitioning from the full virtual space to a truncation that retains approximately 60% of the virtual space.

Additionally, noticeable deviations, reaching up to 10 eV for the uranium $2p_{3/2}$ binding energy, are observed. However, for lower energy levels, such truncations of the virtual space do not introduce significant errors, with deviations of approximately 1 eV or less when compared to calculations involving the full virtual space. Consequently, we have determined that it is feasible to accurately investigate uranium binding energies from the $4f_{3/2}$ level up to the 3s level by limiting our correlation space to spinors with energies ranging from -200 to 200 E_h. This approach encompasses approximately 61.4% of the available virtual orbitals when employing a double zeta basis set for the bare uranyl ion, and was the one applied in the subsequent investigation.

Assignment		^{2}DC^M	Percentage of correlated virtual orbitals				
			72.5	67.6	62.5	61.4	56.7
U	1s	116430.12	5.19	11.91	25.64	25.76	38.5
	2s	21904.97	0	-0.35	0.8	4.47	4.61
	$2p_{1/2}$	21095.77	0	-0.71	0.53	5.56	5.78
	$2p_{3/2}$	17256.74	-0.58	0.22	4.24	4.42	10.62
	3s	5609.00	-0.18	-0.14	0	0	0.98
	$3p_{1/2}$	5239.71	-0.26	-0.33	-0.05	0.07	1.42
	$3p_{3/2}$	4348.21	-0.21	-0.27	-0.08	-0.01	0.87
	$3d_{3/2}$	3765.60	-0.06	-0.34	-0.26	-0.38	0.9
	$3d_{5/2}$	3584.86	-0.05	-0.3	-0.41	-0.35	0.83
	4s	1480.56	-0.06	-0.05	-0.06	-0.06	-0.08
	$4p_{1/2}$	1313.24	-0.08	-0.12	-0.14	-0.15	-0.05
	$4p_{3/2}$	1078.71	-0.06	-0.09	-0.12	-0.11	-0.12
	$4d_{3/2}$	811.93	-0.02	-0.11	-0.16	-0.24	-0.26
	$4d_{5/2}$	768.16	-0.01	-0.1	-0.23	-0.23	-0.26
	$4f_{5/2}$	416.49	0.01	0.02	0.05	0.05	0.04
	$4f_{7/2}$	405.25	0.01	0.02	0.03	0.05	0.04
O	1s	555.52	0	0	-0.03	-0.03	-0.26

Table 6.3: Results from CVS-EOM-IP calculations for core ionization potentials (in eV) in UO_2^{2+} in which all orbitals are included in the correlation space, and the differences with this reference when employing different correlation spaces. All calculations were performed with the ^{2}DC^M Hamiltonian and using an uncontracted Dyall double-zeta basis set for all atoms.

The role of equatorial ligands tailored by Frozen Density Embedding simulations

Table 6.4 presents the ionization energy values obtained from CVS-EOM-IP calculations for the three models studied using double- and triple-zeta basis sets. At the double-zeta level, it is observed that the transition from the bare to the embedded uranyl results in significant changes in the binding energies, with a decrease of nearly 21.5 eV when moving from the bare to the embedded case.

When improving the basis set while keeping the correlation space unchanged, greater deviations are observed in the case of the bare uranyl system, reaching up to 1.4 eV, whereas the embedded case exhibits more modest variations, not exceeding 0.2 eV. This should serve as an initial indication of the role played by the equatorial ligands in determining these quantities. Moreover, when comparing the two models utilizing a triple-zeta basis set, the observed trends remain consistent with those at the double-zeta level, showing average differences of less than 0.1 eV.

In comparison to the supermolecule model (computed at the double zeta level), the differences between the embedded uranyl and this model are relatively small, ranging from 1.3 to 3.9 eV. However, the differences between the bare uranyl and the supermolecular calculations can be as large as 24.4 eV. This finding underscores the capability of the FDE method in providing an reliable description of such a complex system in a computationally efficient manner.

It is worth mentioning that we found that this strategy slightly overestimated the results for the valence-level excitations and ionizations in the supermolecule model by less than 2 eV, which exhibited good agreement with experimental observations. For XANES simulations, both models have demonstrated quantitative agreement in 4c-DR-TD simulations at the U M_4-edge. Moreover, both 4c-DR-TD and 4c-DR-TD-in-DFT simulations exhibited similar deviations from experiment (approximately 37 eV), which can be attributed to the poor description of orbital correlation within DFT methods.

Additionally, it is important to note that the binding energies of U 3d will not be further discussed in this thesis. As highlighted by Fujimori et al.[470], these energies fall outside the range detectable by most X-ray photoelectron spectroscopy (XPS) instruments, which typically operate within the energy range of 20-1500 eV [454]. Therefore, the values presented in this study should be considered as a purely qualitative estimate for U 3d binding energies.

Assignment		QED+Breit	4c-CVS-EOM-IP + QED + Breit				
			double-zeta			triple-zeta	
			UO_2^{2+}	UO_2^{2+} @ Cl_4^{4-}	$UO_2Cl_4^{2-}$	UO_2^{2+} @ Cl_4^{4-}	UO_2^{2+}
U	$3d_{3/2}$	8.34	3757.24	3736.97	3734.36	3736.80	3756.90
	$3d_{5/2}$	5.35	3579.57	3559.37	3556.76	3559.21	3579.31
	4s	5.37	1475.18	1455.24	1452.35	1455.13	1475.27
	$4p_{1/2}$	4.98	1308.26	1287.97	1285.11	1287.87	1308.02
	$4p_{3/2}$	2.72	1076.00	1055.75	1052.85	1055.63	1075.80
	$4d_{3/2}$	1.34	810.58	790.16	787.27	790.01	810.19
	$4d_{5/2}$	0.67	767.49	747.08	744.19	746.92	767.10
	$4f_{5/2}$	-	416.48	396.32	393.43	396.22	416.41
	$4f_{7/2}$	-	405.25	385.10	382.20	385.00	405.18
O	1s	-	555.52	534.29	533.00	534.24	555.41

Table 6.4: CVS-EOM-IP core ionization potentials (in eV) for the models (a) UO_2^{2+}, (b) UO_2^{2+} @ Cl_4^{4-}, and (c) $UO_2Cl_4^{2-}$ are reported using double- and triple-zeta basis sets for all atoms. All calculations were performed with the ^{4}DC Hamiltonian. When applicable, QED+Breit values reported by Kozioł and Aucar [308] were added.

6.3.4 Comparison to X-ray photoemission spectroscopy

Before proceeding, it is important to note that due to constraints in time and resources, the following study could not be extended to consider the entire crystalline environment of the $Cs_2UO_2Cl_4$ system. Therefore, the discussion that follows is limited to the available simulations and their relative positions to experimental data. However, it is planned to further extend this study in order to provide a more comprehensive analysis of the system.

The role of the crystalline environment on the production of chemical shifts in the binding energies of the uranyl ion becomes evident when comparing our results to experimental data. In Table 6.5, we present our CVS-EOM-IP results with those obtained by XPS, as reported by Teterin et al. [50], for various binding energies in the $Cs_2UO_2Cl_4$ crystal.

Our results, obtained using more elaborate models, demonstrate a trend towards better agreement with XPS data. For the bare uranyl ion, the calculated binding energies show relative positions ranging from 23 eV to 31 eV compared to the XPS data. In the case of the supermolecule calculation, all values, except for the U $4p_{3/2}$ binding energy which deviates by 8 eV, are higher than the XPS data by only 4.2 eV. As discussed in the previous section, the values obtained using the FDE scheme closely resemble those obtained for $UO_2Cl_4^{2-}$, being higher than the XPS data by 6.5 eV for most of the cases, and 10.8 eV higher than the value reported for the U $4p_{3/2}$ binding energy.

Here we would like to highlight several key points. Firstly, based on our benchmark of relativistic Hamiltonians, we anticipate that the calculated binding energies will show only modest variations when small-type integrals are explicitly computed. Specifically, at the double zeta level, these variations were found to be around 1.43 eV. Therefore, in addition to considering these integrals and making further advancements in electronic correlation and basis sets, it is expected, at the current stage of this work, that the rest of the crystalline environment – e.g. cesium atoms in the vicinity of the uranyl ion – to play a non-negligible role in determining the core-level binding energies here studied.

Based on the available data and the comparison with XPS values, it is anticipated that the U $4p_{3/2}$ binding energy, as reported in this study, will undergo a decrease of approximately 11 eV when the remaining crystalline environment is included in the simulations. Similarly, we expect a relatively modest impact on the binding energies of U $4f_{5/2}$, U $4f_{7/2}$, and O 1s, with an expected change of less than 3 eV compared to our current data. The subsequent work will adopt a similar approach to the one previously employed for analyzing low-lying binding energies [167]. Specifically, two additional models will be considered: one involving the inclusion of the cesium atoms, and another incorporating the rest of the crystalline environment.

In addition to that, our results provide further insights into the photoemission spectra reported by Teterin et al., exhibiting considerable agreement with their estimation for the spin-orbit doublet in the U 4d XPS. We calculated the value as 43.09 eV, which differs by only 0.59 eV from their estimated value. This discrepancy is likely attributable to the presence of shake-up structures and the Cs $3d_{3/2}$ features, which complicate the experimental attribution and are not accounted for in our protocol as well. In the case of U 4f doublet, our calculations demonstrate an even smaller deviation in the spin-orbit doublet, amounting to only 0.33 eV. The success of our methodology is also evident in the determination of the $4p_{3/2}$ binding energy, which also exhibits a complex structure and could not be experimentally determined. Based on our results, we expect the spin-orbit doublet for U 4p XPS to be around 232.3 eV. The results of our CVS-EOM-IP calculations alongside the experimental values reported by Teterin et al. are depicted in Figure 6.2.

Assignment	UO_2^{2+}	UO_2^{2+} @ Cl_4	UO_2Cl_4	$Cs_2UO_2Cl_4$ (XPS)
U $4p_{1/2}$	1308.02	1287.87	1285.11	-
U $4p_{3/2}$	1075.80	1055.63	1052.85	1044.90
Δ_{SO}	232.22	232.24	232.26	-
U $4d_{3/2}$	810.19	790.01	787.27	783.10
U $4d_{5/2}$	767.10	746.92	744.19	740.60
Δ_{SO}	43.09	43.09	43.08	42.50
U $4f_{5/2}$	416.41	396.22	393.43	393.00
U $4f_{7/2}$	405.18	385.00	382.20	382.10
Δ_{SO}	11.23	11.23	11.23	10.90
O 1s	555.41	534.24	533.00	531.60

Table 6.5: CVS-EOM-CCSD core ionization potentials and spin-orbit doublets (Δ_{SO}) in eV for models (a) UO_2^{2+}, (b) UO_2^{2+} @ Cl_4^{4-}, and (c) $UO_2Cl_4^{2-}$ using double- and triple-zeta basis sets for all atoms. The calculations were performed with the ^{4}DC Hamiltonian. When applicable, QED+Breit values reported by Kozioł and Aucar [308] were added. Experimental data from Teterin et al. [50].

6.4 Conclusions

In conclusion, we conducted an investigation of the core-level ionization energies of the uranyl ion in the $Cs_2UO_2Cl_4$ crystal. Notably, our study represents the first application of the CVS-EOM-CC method for actinides in the literature. Our study involved comparing different relativistic Hamiltonians, considering the influence of dynamical correlation and orbital relaxation, and accounting for basis set truncation effects in the computation of core-level binding energies. Through these efforts, we have obtained valuable insights into the core-level spectroscopic observables of the uranyl ion.

Building upon previous studies, we addressed the limitations associated with applying a 2-component Hamiltonian and adhering to the zeroth order truncation in electron-electron repulsion. With respect to the former, our simulations

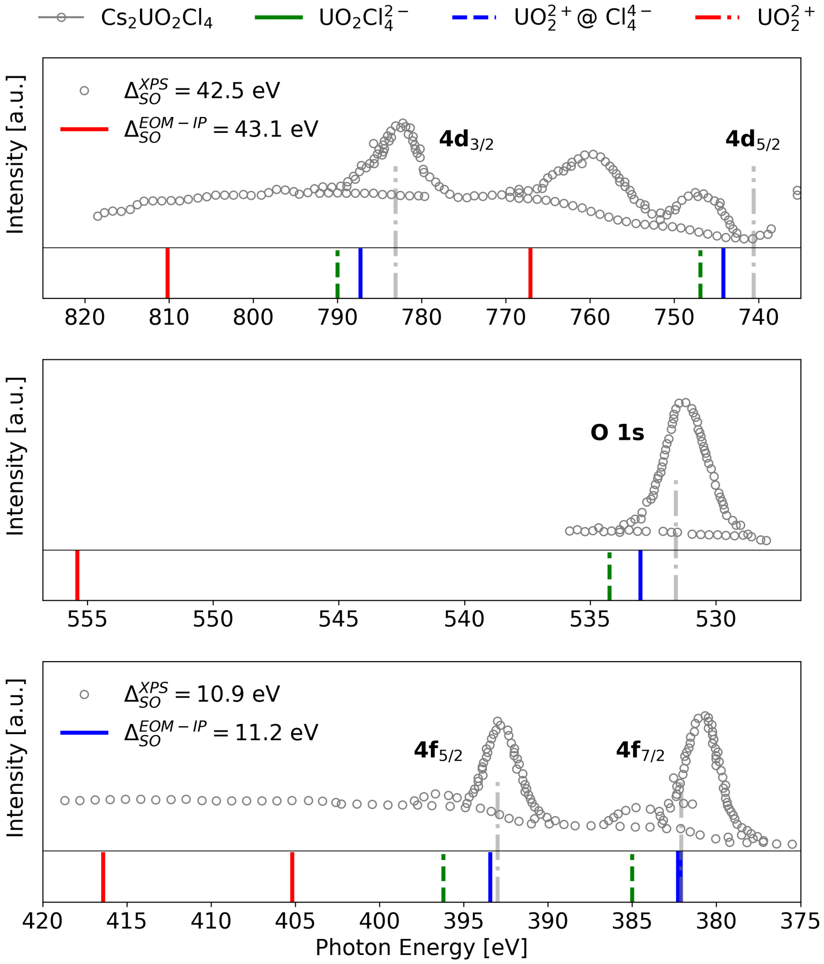

Figure 6.2: CVS-EOM-IP core ionization energies and spin-orbit doublets (Δ_{SO}) in eV for models (a) UO_2^{2+}, (b) UO_2^{2+} @ Cl_4^{4-}, and (c) $UO_2Cl_4^{2-}$ using double- and triple-zeta basis sets for all atoms. The calculations were performed with the ^{4}DC Hamiltonian. When applicable, QED+Breit values reported by Kozioł and Aucar [308] were added. Experimental data from Teterin et al. [50]. Figure used with permission from the Nuclear Technology & Radiation Protection journal.

that employed a 2-component Hamiltonian showed small variations with respect to those in which 4-component framework was used. By including the Gaunt interaction in our calculations we could provide additional insights into the influence of the spin-other-orbit interaction on the reduction of the 2p binding energies.

By incorporating electronic correlation in our simulations, we showed the liability of applying the CVS-EOM-CC framework to investigate systems that include atoms at the bottom of the periodic table. In our results the difference between CVS-EOM-IP and Koopmans' theorem didn't showed significative changes when applying different Hamiltonians. The alignment of this result with the observed small differences between 2- and 4-component calculations leads us to conclude that 2-component calculations can be employed without compromising the overall quality of simulations.

We also compared different structural models, including the bare uranyl ion (UO_2^{2+}), the uranyl ion in the embedding potential of four chlorides (UO_2^{2+} @ Cl_4^{4-}), and the uranyl tetrachloride dianion ($UO_2Cl_4^{2-}$). This comparison allowed us to analyze significant changes in binding energies attributed to the equatorial ligands in close vicinity to the uranyl ion. Furthermore, by comparing the embedded uranyl and supermolecular systems, we identified systematic differences with relatively small variations in binding energies, deviating by only 2.6 eV. By recovering non-negligible contributions across all the binding energies here investigated, these findings highlight the effectiveness of the FDE method in accurately recovering such electrostatic interactions.

With respect to experimental data, our methodology was particularly successful in determining the 4d and 4f spin-orbit doublets. Employing our protocol we were able to yield results that closely align with those reported in the literature for the $Cs_2UO_2Cl_4$ crystal. This outcome is noteworthy because the experimental determination of these doublets is challenging due to the obscuration caused by partial cross-section contributions arising from secondary processes such as satellite peaks and ligand excitations.

In line with our simulations of core-level absorption spectra using the 4c-DR-TD-DFT-in-DFT method, these findings provide further support for our claim that the embedded uranyl serves as a cost-effective model for the uranyl tetrachloride system. Moreover, they highlight the crucial role of electrostatic interactions with the equatorial ligands in determining the spectroscopic observables of the uranyl unit.

It is anticipated that our results to be improved in a subsequent investigation when we finally proceed to include cesium atoms and the rest of the crystalline environment of $Cs_2UO_2Cl_4$ in the calculations using the here employed FDE scheme. We expect that this will lower our actual binding energies up to 10 eV.

Given the broad range of applications of photoemission spectroscopies in studying actinides in condensed phases and the significant influence of their surrounding environment on determining chemical shifts, we foresee the need for further exploration of the current protocol in more complex systems. However, it is crucial to acknowledge that applying the CVS-EOM-CC method to larger systems, such as the $Cs_2UO_2Cl_4$ crystal, remains elusive. In light of this, we firmly believe that the CVS-EOM-CC-in-DFT method employed in this study represents the most promising framework for gaining valuable insights into the core-excited states of such complex systems through robust *ab-initio* molecular electronic structure calculations.

Bibliography of the current chapter

(1) Willmott, P., *An introduction to synchrotron radiation: techniques and applications*; John Wiley & Sons: 2019.

(3) Stöhr, J., *NEXAFS spectroscopy*; Springer Science & Business Media: 2013; Vol. 25.

(5) Lv, B.; Qian, T.; Ding, H. Angle-resolved photoemission spectroscopy and its application to topological materials. *Nature Reviews Physics* **2019**, *1*, 609–626.

(11) Ilton, E. S.; Bagus, P. S. XPS determination of uranium oxidation states. *Surface and Interface Analysis* **2011**, *43*, 1549–1560.

(12) Kvashnina, K.; Butorin, S. M.; Martin, P.; Glatzel, P. Chemical state of complex uranium oxides. *Physical review letters* **2013**, *111*, 253002.

(18) Amidani, L.; Retegan, M.; Volkova, A.; Popa, K.; Martin, P. M.; Kvashnina, K. O. Probing the local coordination of hexavalent uranium and the splitting of 5f orbitals induced by chemical bonding. *Inorganic Chemistry* **2021**, *60*, 16286–16293.

(26) Hertz, H. Ueber einen Einfluss des ultravioletten Lichtes auf die electrische Entladung. *Annalen der Physik* **1887**, *267*, 983–1000.

(27) Einstein, A. Indeed, it seems to me that the observations regarding" blackbody radiation," photoluminescence, production of cathode rays by ultraviolet. *Annalen der Physik* **1905**, *17*, 132–148.

(46) Oher, H.; Réal, F.; Vercouter, T.; Vallet, V. Investigation of the Luminescence of [UO2X4] 2–(X= Cl, Br) Complexes in the Organic Phase Using Time-Resolved Laser-Induced Fluorescence Spectroscopy and Quantum Chemical Simulations. *Inorganic Chemistry* **2020**, *59*, 5896–5906.

(47) Oher, H.; Ferru, G.; Couston, L.; Berthon, L.; Guillaumont, D.; Réal, F.; Vercouter, T.; Vallet, V. Influence of the First Coordination of Uranyl on Its Luminescence Properties: A Study of Uranyl Binitrate with N, N-Dialkyl Amide DEHiBA and Water. *Inorganic Chemistry* **2021**, *61*, 890–901.

(48) Oher, H.; Vercouter, T.; Réal, F.; Shang, C.; Reiller, P. E.; Vallet, V. Influence of Alkaline Earth Metal Ions on Structures and Luminescent Properties of Na m M n UO2 (CO3) 3 (4–m–2 n)–(M= Mg, Ca; m, n= 0–2): Time-Resolved Fluorescence Spectroscopy and Ab Initio Studies. *Inorganic Chemistry* **2020**, *59*, 15036–15049.

(49) Dau, P. D.; Su, J.; Liu, H.-T.; Huang, D.-L.; Li, J.; Wang, L.-S. Photoelectron spectroscopy and the electronic structure of the uranyl tetrachloride dianion: UO2Cl42-. *The Journal of Chemical Physics* **2012**, *137*, 064315.

(50) Teterin, Y. A.; Maslakov, K. I.; Ryzhkov, M. V.; Teterin, A. Y.; Ivanov, K. E.; Kalmykov, S. N.; Petrov, V. G.; Suglobov, D. N. Valence XPS structure and chemical bond in Cs2UO2Cl4. *Nuclear Technology and Radiation Protection* **2016**, *31*, 37–50.

(51) Maslakov, K. I.; Teterin, Y. A.; Ryzhkov, M. V.; Popel, A. J.; Teterin, A. Y.; Ivanov, K. E.; Kalmykov, S. N.; Petrov, V. G.; Farnan, I. The nature of the chemical bond in UO2. *International journal of quantum chemistry* **2019**, *119*, e26040.

(52) Evans, W. J.; Hanusa, T. P., *The Heaviest Metals: Science and Technology of the Actinides and Beyond*; John Wiley & Sons: 2019.

(108) Liu, J.; Cheng, L. Relativistic coupled-cluster and equation-of-motion coupled-cluster methods. *Wiley Interdisciplinary Reviews: Computational Molecular Science* **2021**, *11*, e1536.

(114) Bartlett, R. J. Coupled-cluster theory and its equation-of-motion extensions. *Wiley Interdisciplinary Reviews: Computational Molecular Science* **2012**, *2*, 126–138.

(123) Coriani, S.; Koch, H. Communication: X-ray absorption spectra and core-ionization potentials within a core-valence separated coupled cluster framework. *The Journal of Chemical Physics* **2015**, *143*, 181103.

(124) Fransson, T.; Coriani, S.; Christiansen, O.; Norman, P. Carbon X-ray absorption spectra of fluoroethenes and acetone: A study at the coupled cluster, density functional, and static-exchange levels of theory. *The Journal of Chemical Physics* **2013**, *138*, 124311.

(125) Norman, P.; Dreuw, A. Simulating X-ray spectroscopies and calculating core-excited states of molecules. *Chemical reviews* **2018**, *118*, 7208–7248.

(126) Vidal, M. L.; Feng, X.; Epifanovsky, E.; Krylov, A. I.; Coriani, S. New and efficient equation-of-motion coupled-cluster framework for core-excited and core-ionized states. *Journal of Chemical Theory and Computation* **2019**, *15*, 3117–3133.

(128) Halbert, L.; Vidal, M. L.; Shee, A.; Coriani, S.; Severo Pereira Gomes, A. Relativistic EOM-CCSD for Core-Excited and Core-Ionized State Energies Based on the Four-Component Dirac–Coulomb (- Gaunt) Hamiltonian. *Journal of Chemical Theory and Computation* **2021**, *17*, 3583–3598.

(134) Pototschnig, J. V.; Papadopoulos, A.; Lyakh, D. I.; Repisky, M.; Halbert, L.; Severo Pereira Gomes, A.; Jensen, H. J. A.; Visscher, L. Implementation of relativistic coupled cluster theory for massively parallel GPU-accelerated computing architectures. *Journal of chemical theory and computation* **2021**, *17*, 5509–5529.

(167) Gomes, A. S. P.; Jacob, C. R.; Réal, F.; Visscher, L.; Vallet, V. Towards systematically improvable models for actinides in condensed phase: the electronic spectrum of uranyl in Cs 2 UO 2 Cl 4 as a test case. *Physical Chemistry Chemical Physics* **2013**, *15*, 15153–15162.

(168) Réal, F.; Vallet, V.; Marian, C.; Wahlgren, U. Theoretical investigation of the energies and geometries of photoexcited uranyl (VI) ion: A comparison between wave-function theory and density functional theory. *The Journal of chemical physics* **2007**, *127*, 214302.

(206) Wesolowski, T. A.; Warshel, A. Frozen density functional approach for ab initio calculations of solvated molecules. *The Journal of Physical Chemistry* **1993**, *97*, 8050–8053.

(207) Wesolowski, T. A.; Shedge, S.; Zhou, X. Frozen-density embedding strategy for multilevel simulations of electronic structure. *Chemical reviews* **2015**, *115*, 5891–5928.

(215) Jacob, C. R.; Beyhan, S. M.; Bulo, R. E.; Gomes, A. S. P.; Götz, A. W.; Kiewisch, K.; Sikkema, J.; Visscher, L. PyADF—A scripting framework for multiscale quantum chemistry. *Journal of computational chemistry* **2011**, *32*, 2328–2338.

(222) Tecmer, P.; Bast, R.; Ruud, K.; Visscher, L. Charge-Transfer Excitations in Uranyl Tetrachloride ([UO2Cl4] 2–): How Reliable are Electronic Spectra from Relativistic Time-Dependent Density Functional Theory? *The Journal of Physical Chemistry A* **2012**, *116*, 7397–7404.

(223) Tecmer, P.; Gomes, A. S. P.; Ekström, U.; Visscher, L. Electronic spectroscopy of UO 2 2+, NUO+ and NUN: an evaluation of time-dependent density functional theory for actinides. *Physical Chemistry Chemical Physics* **2011**, *13*, 6249–6259.

(228) Lembarki, A.; Chermette, H. Obtaining a gradient-corrected kinetic-energy functional from the Perdew-Wang exchange functional. *Physical Review A* **1994**, *50*, 5328.

(229) Ernzerhof, M.; Scuseria, G. E. Assessment of the Perdew–Burke–Ernzerhof exchange-correlation functional. *The Journal of chemical physics* **1999**, *110*, 5029–5036.

(267) Liu, W. Essentials of relativistic quantum chemistry. *The Journal of chemical physics* **2020**, *152*, 180901.

(282) Visscher, L. Approximate molecular relativistic Dirac-Coulomb calculations using a simple Coulombic correction. *Theoretical Chemistry Accounts* **1997**, *98*, 68–70.

(293) Sikkema, J.; Visscher, L.; Saue, T.; Iliaš, M. The molecular mean-field approach for correlated relativistic calculations. *The Journal of chemical physics* **2009**, *131*, 124116.

(308) Kozioł, K.; Aucar, G. A. QED effects on individual atomic orbital energies. *The Journal of Chemical Physics* **2018**, *148*, 134101.

(310) Helgaker, T.; Coriani, S.; Jørgensen, P.; Kristensen, K.; Olsen, J.; Ruud, K. Recent advances in wave function-based methods of molecular-property calculations. *Chemical reviews* **2012**, *112*, 543–631.

(323) Misael, W.; Gomes, A. Core Excitations of Uranyl in Cs2UO2Cl4 from Relativistic Embedded Damped Response Time-Dependent Density Functional Theory Calculations. *Inorganic Chemistry* **2023**, *62*, 11589–11601.

(325) Denning, R.; Snellgrove, T.; Woodwark, D. The electronic structure of the uranyl ion: Part I. The electronic spectrum of Cs2UO2Cl4. *Molecular Physics* **1976**, *32*, 419–442.

(368) Gibson, J. K.; de Jong, W. A. Experimental and Theoretical Approaches to Actinide Chemistry. **2018**.

(374) South, C.; Shee, A.; Mukherjee, D.; Wilson, A. K.; Saue, T. 4-Component relativistic calculations of L 3 ionization and excitations for the isoelectronic species UO 2 2+, OUN+ and UN 2. *Physical Chemistry Chemical Physics* **2016**, *18*, 21010–21023.

(379) Vidal, M. L.; Pokhilko, P.; Krylov, A. I.; Coriani, S. Equation-of-motion coupled-cluster theory to model L-edge x-ray absorption and photoelectron spectra. *The journal of physical chemistry letters* **2020**, *11*, 8314–8321.

(389) Butorin, S. M.; Bauters, S.; Amidani, L.; Beck, A.; Weiss, S.; Vitova, T.; Tougait, O. X-ray spectroscopic study of chemical state in uranium carbides. *Journal of Synchrotron Radiation* **2022**, *29*.

(395) Ilton, E. S.; Bagus, P. S. Ligand field effects on the multiplet structure of the U4f XPS of UO2. *Surface science* **2008**, *602*, 1114–1121.

(403) Saue, T.; Bast, R.; Gomes, A. S. P.; Jensen, H. J. A.; Visscher, L.; Aucar, I. A.; Di Remigio, R.; Dyall, K. G.; Eliav, E.; Fasshauer, E., et al. The DIRAC code for relativistic molecular calculations. *The Journal of chemical physics* **2020**, *152*, 204104.

(404) Dyall, K. G. Relativistic and nonrelativistic finite nucleus optimized triple-zeta basis sets for the 4 p, 5 p and 6 p elements. *Theoretical Chemistry Accounts* **2002**, *108*, 335–340.

(405) Dyall, K. G. Relativistic double-zeta, triple-zeta, and quadruple-zeta basis sets for the light elements H–Ar. *Theoretical Chemistry Accounts* **2016**, *135*, 128.

(406) Visscher, L.; Dyall, K. G. Dirac–Fock atomic electronic structure calculations using different nuclear charge distributions. *Atomic Data and Nuclear Data Tables* **1997**, *67*, 207–224.

(407) Watkin, D. J.; Denning, R. G.; Prout, K. Structure of dicaesium tetrachlorodioxouranium (VI). *Acta Crystallographica Section C: Crystal Structure Communications* **1991**, *47*, 2517–2519.

(408) Van Lenthe, E. v.; Snijders, J.; Baerends, E. The zero-order regular approximation for relativistic effects: The effect of spin–orbit coupling in closed shell molecules. *The Journal of chemical physics* **1996**, *105*, 6505–6516.

(443) Réal, F.; Gomes, A. S. P.; Visscher, L.; Vallet, V.; Eliav, E. Benchmarking electronic structure calculations on the bare UO22+ ion: How different are single and multireference electron correlation methods? *The Journal of Physical Chemistry A* **2009**, *113*, 12504–12511.

(452) Misael, W.; Gomes, A. Relativistic equation-of-motion coupled-cluster study of uranyl in Cs2UO2Cl4. *In preparation* **2023**.

(453) Bagus, P. S.; Ilton, E. S.; Nelin, C. J. The interpretation of XPS spectra: Insights into materials properties. *Surface Science Reports* **2013**, *68*, 273–304.

(454) Hüfner, S., *Photoelectron spectroscopy: principles and applications*; Springer Science & Business Media: 2013.

(455) Sohn, B.; Kim, J. R.; Kim, C. H.; Lee, S.; Hahn, S.; Kim, Y.; Huh, S.; Kim, D.; Kim, Y.; Kyung, W., et al. Observation of metallic electronic structure in a single-atomic-layer oxide. *Nature Communications* **2021**, *12*, 6171.

(456) Mayer, D.; Lever, F.; Picconi, D.; Metje, J.; Alisauskas, S.; Calegari, F.; Düsterer, S.; Ehlert, C.; Feifel, R.; Niebuhr, M., et al. Following excited-state chemical shifts in molecular ultrafast x-ray photoelectron spectroscopy. *Nature communications* **2022**, *13*, 198.

(457) Al-Haddad, A.; Oberli, S.; González-Vázquez, J.; Bucher, M.; Doumy, G.; Ho, P.; Krzywinski, J.; Lane, T. J.; Lutman, A.; Marinelli, A., et al. Observation of site-selective chemical bond changes via ultrafast chemical shifts. *Nature Communications* **2022**, *13*, 7170.

(458) Whitten, J. E. Ultraviolet photoelectron spectroscopy: Practical aspects and best practices. *Applied Surface Science Advances* **2023**, *13*, 100384.

(459) Drot, R.; Simoni, E.; Alnot, M.; Ehrhardt, J. Structural environment of uranium (VI) and europium (III) species sorbed onto phosphate surfaces: XPS and optical spectroscopy studies. *Journal of colloid and interface science* **1998**, *205*, 410–416.

(460) El Jamal, G.; Gouder, T.; Eloirdi, R.; Jonsson, M. Monitoring the gradual change in oxidation state during surface oxidation or reduction of uranium oxides by photoemission spectroscopy of the 5f states. *Journal of Nuclear Materials* **2022**, *560*, 153504.

(461) Baker, R. J. Uranium minerals and their relevance to long term storage of nuclear fuels. *Coordination Chemistry Reviews* **2014**, *266*, 123–136.

(462) Perry, D. L. The tris (carbonato) dioxouranium (VI) ion: A structural model for uranium 4f7/2, 5/2 X-ray photoelectron spectra satellite structures for oxide and oxygen coordination cores. *Vacuum* **2015**, *114*, 162–165.

(463) Rout, S.; Ravi, P.; Kumar, A.; Tripathi, R. Spectroscopic investigation of uranium sorption on soil surface using X-ray photoelectron spectroscopy. *Journal of Radioanalytical and Nuclear Chemistry* **2017**, *313*, 565–570.

(464) Sun, Y.; Wu, M.; Zheng, L.; Wang, B.; Wang, Y. Uranium speciation in coal bottom ash investigated via x-ray absorption fine structure and x-ray photoelectron spectra. *Journal of Environmental Sciences* **2018**, *74*, 88–94.

(465) Kotani, A.; Ogasawara, H. Theory of core-level spectroscopy in actinide systems. *Physica B: Condensed Matter* **1993**, *186*, 16–20.

(466) Bagus, P. S.; Ilton, E. S. Theory for the XPS of Actinides. *Topics in Catalysis* **2013**, *56*, 1121–1128.

(467) Li, W.-L.; Su, J.; Jian, T.; Lopez, G. V.; Hu, H.-S.; Cao, G.-J.; Li, J.; Wang, L.-S. Strong electron correlation in UO2-: a photoelectron spectroscopy and relativistic quantum chemistry study. *The Journal of Chemical Physics* **2014**, *140*, 094306.

(468) Su, J.; Dau, P. D.; Liu, H.-T.; Huang, D.-L.; Wei, F.; Schwarz, W.; Li, J.; Wang, L.-S. Photoelectron spectroscopy and theoretical studies of gaseous uranium hexachlorides in different oxidation states: UCl6 q-(q= 0–2). *The Journal of Chemical Physics* **2015**, *142*, 134308.

(469) Li, Y.; Zou, J.; Xiong, X.-G.; Su, J.; Xie, H.; Fei, Z.; Tang, Z.; Liu, H. Probing Chemical Bonding and Electronic Structures in ThO–by Anion Photoelectron Imaging and Theoretical Calculations. *The Journal of Physical Chemistry A* **2017**, *121*, 2108–2113.

(470) Fujimori, S.-i.; Kobata, M.; Takeda, Y.; Okane, T.; Saitoh, Y.; Fujimori, A.; Yamagami, H.; Haga, Y.; Yamamoto, E.; Ōnuki, Y. Manifestation of electron correlation effect in 5 f states of uranium compounds revealed by 4 d–5 f resonant photoelectron spectroscopy. *Physical Review B* **2019**, *99*, 035109.

(471) Fleig, T. Invited review: Relativistic wave-function based electron correlation methods. *Chemical Physics* **2012**, *395*, 2–15.

(472) Infante, I.; Severo Pereira Gomes, A.; Visscher, L. On the performance of the intermediate Hamiltonian Fock-space coupled-cluster method on linear triatomic molecules: The electronic spectra of Np O 2+, Np O 2 2+, and Pu O 2 2+. *The Journal of chemical physics* **2006**, *125*, 074301.

(473) Gomes, A. S. P.; Réal, F.; Schimmelpfennig, B.; Wahlgren, U.; Vallet, V. Applied computational actinide chemistry. *Computational Methods in Lanthanide and Actinide Chemistry* **2015**, 269–298.

(474) Boguslawski, K.; Réal, F.; Tecmer, P.; Duperrouzel, C.; Gomes, A. S. P.; Legeza, Ö.; Ayers, P. W.; Vallet, V. On the multi-reference nature of plutonium oxides: PuO 2 2+, PuO 2, PuO 3 and PuO 2 (OH) 2. *Physical Chemistry Chemical Physics* **2017**, *19*, 4317–4329.

(475) Schreckenbach, G.; Shamov, G. A. Theoretical actinide molecular science. *Accounts of chemical research* **2010**, *43*, 19–29.

(476) Tecmer, P.; Severo Pereira Gomes, A.; Knecht, S.; Visscher, L. Communication: Relativistic Fock-space coupled cluster study of small building blocks of larger uranium complexes. *The Journal of Chemical Physics* **2014**, *141*, 041107.

(477) Van Besien, E.; Pierloot, K.; Görller-Walrand, C. Electronic spectra of uranyl chloride complexes in acetone: a CASSCF/CASPT2 investigation. *Physical Chemistry Chemical Physics* **2006**, *8*, 4311–4319.

(478) Pierloot, K.; van Besien, E. Electronic structure and spectrum of UO 2 2+ and UO 2 Cl 4 2-. *The Journal of chemical physics* **2005**, *123*, 204309.

(479) Schnack-Petersen, A. K.; Moitra, T.; Folkestad, S. D.; Coriani, S. New Implementation of an Equation-of-Motion Coupled-Cluster Damped-Response Framework with Illustrative Applications to Resonant Inelastic X-ray Scattering. *The Journal of Physical Chemistry A* **2023**, *127*, 1775–1793.

(480) Crawford, T. D.; Kumar, A.; Bazanté, A. P.; Di Remigio, R. Reduced-scaling coupled cluster response theory: Challenges and opportunities. *Wiley Interdisciplinary Reviews: Computational Molecular Science* **2019**, *9*, e1406.

(481) Coriani, S.; Fransson, T.; Christiansen, O.; Norman, P. Asymmetric-Lanczos-chain-driven implementation of electronic resonance convergent coupled-cluster linear response theory. *Journal of chemical theory and computation* **2012**, *8*, 1616–1628.

(482) Kauczor, J.; Norman, P.; Christiansen, O.; Coriani, S. Communication: A reduced-space algorithm for the solution of the complex linear response equations used in coupled cluster damped response theory. *The Journal of Chemical Physics* **2013**, *139*, 211102.

(483) Vidal, M. L.; Krylov, A. I.; Coriani, S. Dyson orbitals within the fc-CVS-EOM-CCSD framework: theory and application to X-ray photoelectron spectroscopy of ground and excited states. *Physical Chemistry Chemical Physics* **2020**, *22*, 2693–2703.

(484) Opoku, R. A.; Toubin, C.; Gomes, A. S. P. Simulating core electron binding energies of halogenated species adsorbed on ice surfaces and in solution via relativistic quantum embedding calculations. *Physical Chemistry Chemical Physics* **2022**, *24*, 14390–14407.

(485) Repisky, M.; Knecht, S.; Jensen, H. J. A.; Saue, T.; Konecny, L. Modern exact two-component Hamiltonians for relativistic quantum chemistry and physics: Two-electron picture-change corrections made simple. *Bulletin of the American Physical Society* **2023**.

(486) Ljubic, I. Reliability of density functional and perturbation theories for calculating core-ionization spectra of free radicals. *Journal of Chemical Theory and Computation* **2014**, *10*, 2333–2343.

(487) Arias-Martinez, J. E.; Cunha, L. A.; Oosterbaan, K. J.; Lee, J.; Head-Gordon, M. Accurate core excitation and ionization energies from a state-specific coupled-cluster singles and doubles approach. *Physical Chemistry Chemical Physics* **2022**, *24*, 20728–20741.

Conclusions

"On en rêve plus on y croit, on ira. Le meilleur est à venir, tu verras."

— On ira, Lujipeka feat. Cerrone

As a whole, during the course of this thesis, we have developed novel protocols based on relativistic quantum chemistry approaches to explore various aspects of the interaction of X-rays with actinides. Specifically, we have investigated the processes of absorption and ionization in uranyl-containing compounds using linear response time-dependent density functional theory (TD-DFT) and the equation-of-motion coupled-cluster method (EOM-CC), respectively. Additionally, we have accounted for environmental effects through the frozen density embedding (FDE) framework.

Regarding resonant processes, in Chapter 4, we evaluated the XAS spectra at the O K-edge and U M_4-, L_3-edges of a prototype system, $Cs_2UO_2Cl_4$. By employing the resonant convergent formalism of response theory (4c-DR-TD-CAMB3LYP), we addressed the polarization dependence observed in the absorption spectra at the O K- and U L_3-edges. Moreover, the examination of the absorption spectrum at the U M_4- edge added an interesting aspect to this study. Using the FDE method (4c-DR-TD-CAMB3LYP-in-DFT), we successfully demonstrated the influence of the equatorial ligands in determining the spectral features of the An M_4-edge XAS of AnO_2^{2+} species. We achieved transition energies and spectral profiles similar to those obtained from supermolecule calculations. Notably, our study revealed significant spectral changes when comparing three different structural models with the same U–O_{yl} bond length.

The only difference among these models was the presence or absence of the equatorial ligand, suggesting the significant role of electrostatic interactions in determining the U M_4 XAS features. These findings contradict the well-established interpretation of the An M_4 XAS spectra, which directly correlates its features to the bond length within the uranyl unit.

Therefore, in Chapter 5, we extended this study by investigating complexes with varying U–O_{yl} bond lengths and equatorial ligands. The results of this work underscore the non-negligible role of equatorial ligands in determining the features in the U M_4-edge XAS spectra. Our results highlighted the significant influence of the equatorial ligands on the position of the σ^* transition, especially evident in the $UO_2Cl_2(phen)_2$ complex, where peak splittings differed by up to 0.8 eV from the UO_2Cl_2 subunit case. In this system, as well as in the case of $[UO_2(NO_3)_2(H_2O)_2](H_2O)_4]$ (albeit to a lesser extent), the presence of metal-to-ligand charge transfer transitions directly affected the position of the feature on the high-energy side of the U M_4 XAS spectra. Additionally, our HERFD experiments and 2c-TDA simulations deviated from the previously reported linear trend. Consequently, we can conclude that while the An–O_{yl} bond lengths can be correlated with the position of the features in the An M_4 XAS spectra in some cases, the interpretation must also take into account the role of the equatorial ligands as well.

Chapter 6 focused on simulating core ionized states of actinide systems employing coupled-cluster theory. Our results demonstrated the pivotal role of relativistic effects, orbital correlation, and relaxation in determining the binding energies of the uranyl ion. Similar to Chapter 4, by employing the FDE scheme, we further emphasized the role of electrostatic interactions in determining the core-level spectroscopic observables of actinides. Our results demonstrated a significant reduction in core-level binding energies between the bare uranyl ion and the systems in which the equatorial ligands are implicitly or explicitly taken into account.

Throughout this work, the FDE method, a quantum embedding approach, has demonstrated its effectiveness in studying the inner-shell spectroscopy of actinides. By employing simpler structural models compared to alternative approaches like cluster embedding, this method effectively maintained the overall quality of simulations while reducing computational time. In other words, its application has been shown to produce results comparable or even identical to those obtained from supermolecule calculations. Considering the computational constraints associated with studying such complex systems using robust *ab initio* methods, we assert that the FDE framework is one of the most promising alternatives for further advancing these investigations.

Therefore, future studies can complement the work presented in Chapters 4 and 6 by including the embedding potential of the cesium atoms and the rest of the unit cell of the $Cs_2UO_2Cl_4$ crystal in the calculations. In addition to applying the FDE framework to the systems discussed in Chapter 5, it is possible to explore other structures reported in the literature and perform geometry optimizations to continue addressing the role of the equatorial ligands and geometric parameters of the uranyl ion in determining the features at the U M_4-edge XAS spectra.

Furthermore, future simulations should consider employing a theory level that better accounts for electronic correlation and the relaxation of the core hole, as demonstrated in the last chapter of this thesis. Over the period covered by this research project, a promising relativistic equation-of-motion coupled-cluster framework was under development in our research group. We strongly believe that once this code becomes available, it will enable significant advancements in investigating the core-excited states of heavy elements. However, these new implementations should consider a type of system not accessed in this thesis: those with open shells, which are known to represent a significant fraction of actinide-containing molecules, and requires the application of multi-reference methods.

Overall, through the methodologies and applications presented in this thesis, we hope to provide a new framework for addressing the physicochemical properties of actinide-containing systems, where X-ray spectroscopies are recognized as *state-of-the-art* techniques for accessing their spectroscopic observables, and the theory early developed by Paul Dirac remains the most complete theory of the electron.

Finally, in conclusion, it will be interesting to observe the further advancements in experimental and theoretical methods that will be used to unravel the *end* of the periodic table.

Scientific Contributions

Oral presentations

- Oral presentatation at the *GDR SciNÉE: Sciences Nucléaires pour l'Energie et l'Environnement*. **On-line**, January 2023.
- Oral presentation at the *School on UV and X-Ray Spectroscopies of Correlated-Electron Systems*. **École de Physique des Houches**, September 2022, Les Houches, France.
- Oral presentation at the *GDR NBODY: Problème Quantique à N Corps en Chimie et Physique 2022*. **Université Paul Sabatier**, January 2022, Toulouse, France.

Poster presentations

- Poster at the *13th European Conference on Computational and Theoretical Chemistry*. **Aristotle University of Thessaloniki**, August 2023, Thessaloniki, Greece.
- Poster at the *58th Symposium on Theoretical Chemistry*. **Universität Heidelberg**, September 2022, Heidelberg, Germany.
- Poster at the *5th International Workshop on Advanced Techniques in Actinide Spectroscopy*. **European Synchrotron Radiation Facility**, October 2022, Grenoble, France.

- Poster at the *Journées Théorie, Modélisation et Simulation 2021*. **Université de Rennes**, December 2021, Rennes, France.
- Poster at the *57th Symposium on Theoretical Chemistry*. **Universität Würzburg**, September 2021, Würzburg, Germany.
- Poster at the *CONEXS Conference 2021: Emerging Trends in X-Ray Spectroscopy*. **Diamond Light Source**, March 2021, Chilton, England.
- Poster at the *Journées Théorie, Modélisation et Simulation 2020*. **On-line**, December 2020.

Publications

- Core excitations of uranyl in $Cs_2UO_2Cl_4$ from relativistic embedded damped response time-dependent density functional theory. *Inorg. Chem. 2023, 62, 29, 11589–11601*.
- Relativistic equation-of-motion coupled-cluster calculations of core-ionization energies of uranyl in $Cs_2UO_2Cl_4$. *In preparation*, `https://arxiv.org/abs/2302.07223`.

Appendix A

Supplementary Information to Manuscript I

A.1 Comparison of 2- and 4-component calculations for uranyl tetrachloride

In Figure A.1, we compare 2-component XAS spectra obtained with TD-DFT with (2c-TDA) and without (2c-TD) invoking the Tamm-Dancoff approximation, and we see that there is no discernible difference.

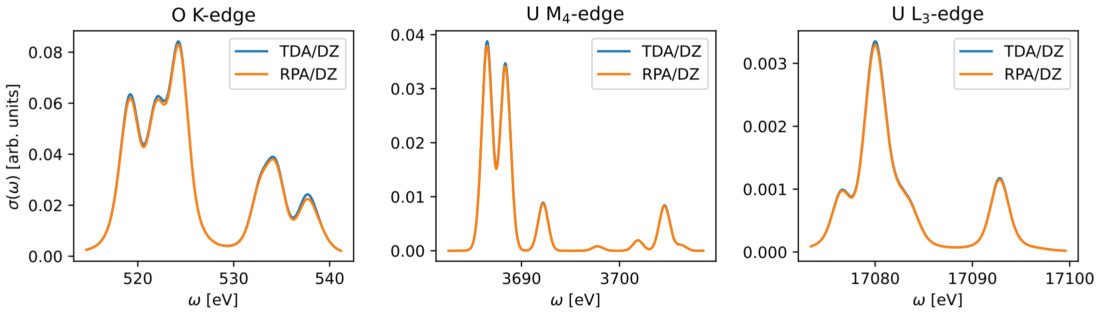

Figure A.1: Comparison of 2c-TDA and 2c-TD (RPA) XAS spectra at the edges here investigated using a double-zeta basis set, both with and without employing the Tamm-Dancoff approximation. Spectra from this work reprinted with permission from Misael and Gomes. Copyright 2023 American Chemical Society.

In figure A.2 we compare the simulated spectra for the O K-edge, U M_4- and L_3-edges obtained from 2- and 4-component calculations. It can be seen that overall there are non-negligible but overall small changes in peak positions due to the Hamiltonian (and possibly due to the use of Slater orbitals in ADF) for all edges, though the spectral changes are rather well reproduced–differences here come from the fact that in 2c-TDA one is limited on the number of roots solved for, and on how the stick spectrum obtained with 2c-TDA is subsequently broadened. Further details on the assessment of broadening can be found below.

Except for U L_3-edge case, where the experimental broadening is considerably large, the gamma factors were chosen to better fit the experimental spectra, as discussed in the manuscript text.

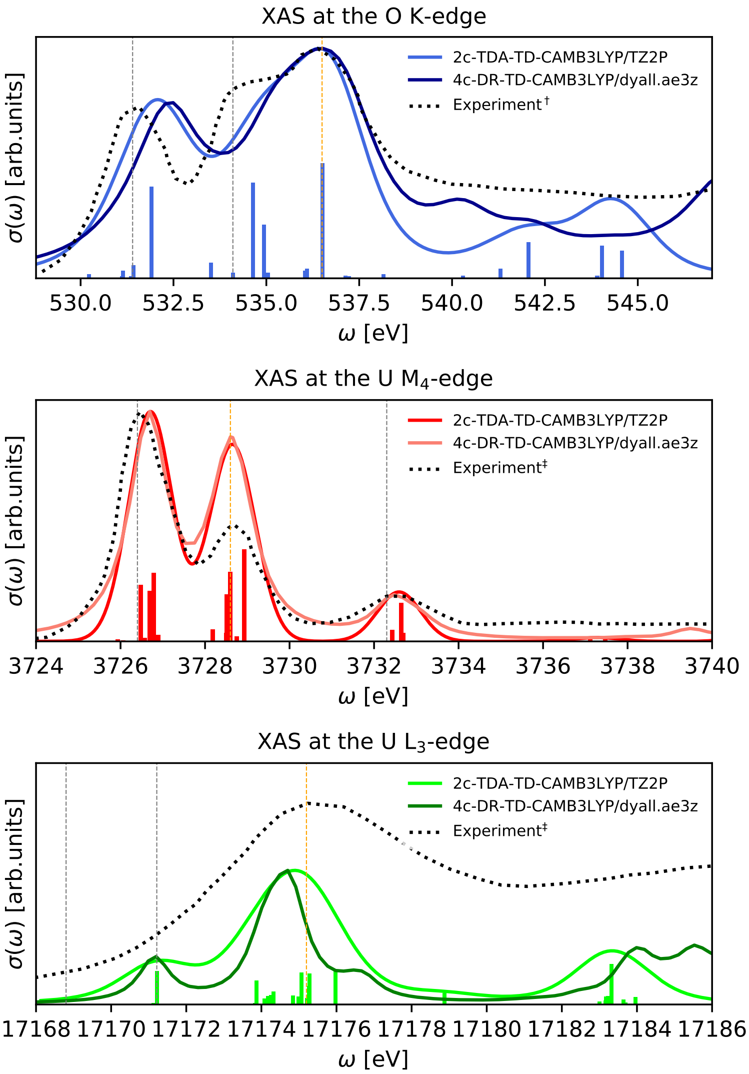

Figure A.2: From top to bottom: 4c-DR and 2c-TDA XAS spectra at the O K-edge, U M_4- and L_3-edges of $UO_2Cl_4^{2-}$. Experimental data at the O K-edge and U M_4 and L_3- edges of $Cs_2UO_2Cl_4$ digitized from †Denning et al.[326] and ‡Vitova et al. [328], respectively. Digitalized spectra for the O K-edge were used with permission from Denning et al. Copyright 2002 AIP Publishing. Copyright 2015 American Chemical Society applies to the uranium edges. Spectra from this work reprinted with permission from Misael and Gomes. Copyright 2023 American Chemical Society.

A.2 Damping parameter for DR-TD-DFT calculations

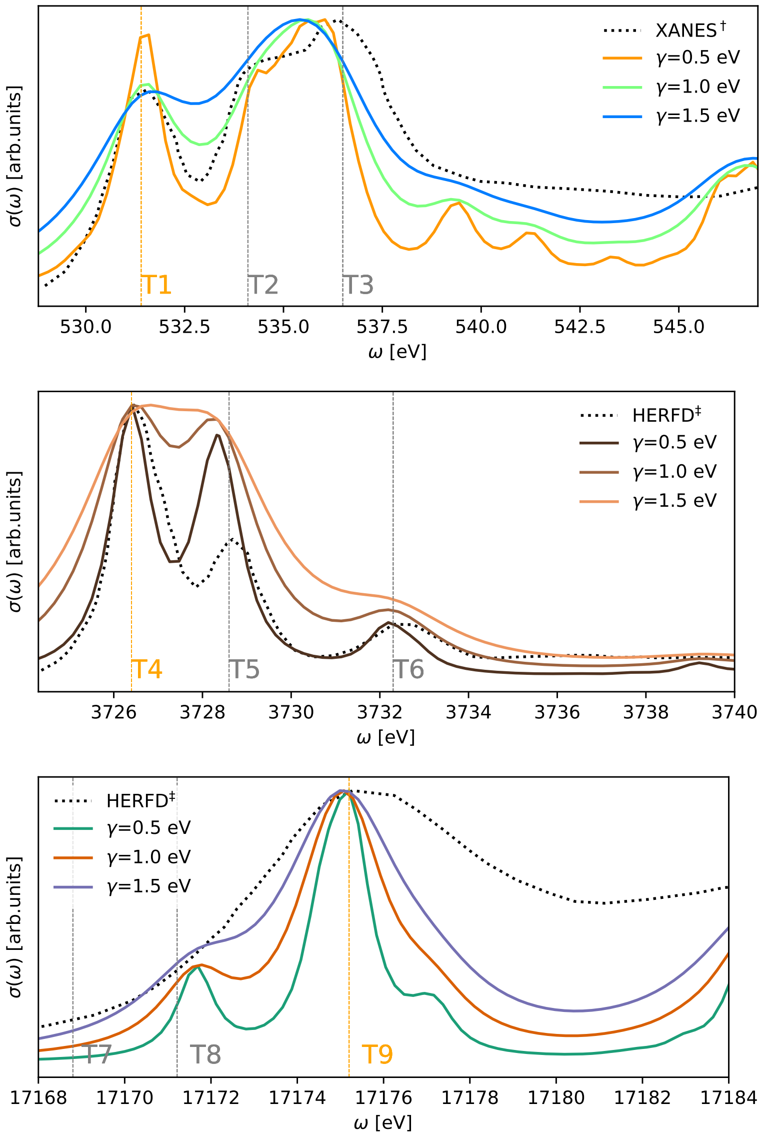

Figure A.3: Comparison of 4c-DR XAS spectra at the Oxygen K-edge, Uranium M_4- and L_3-edge for different damping factors. Shift (depicted as the orange straight line) with respect to the experimental data ($Cs_2UO_2Cl_4$) from Vitova et al. [328]. Digitalized spectra for the O K-edge were used with permission from Denning et al. Copyright 2002 AIP Publishing. Copyright 2015 American Chemical Society applies to the uranium edges. Spectra from this work reprinted with permission from Misael and Gomes. Copyright 2023 American Chemical Society.

A.3 Comparison of broadening functions

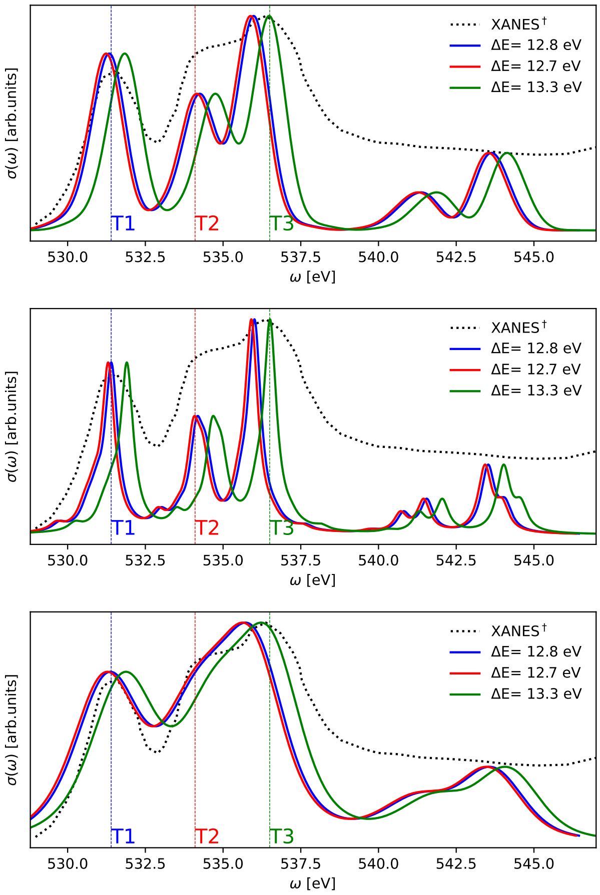

Figure A.4: Comparison of 2c-TDA XAS spectra at the oxygen K-edge for different broadening functions and shifts (depicted as the colored straight line) with respect to the experimental data ($Cs_2UO_2Cl_4$) from Denning et al. [326]. Digitalized spectra for the O K-edge were used with permission from Denning et al. Copyright 2002 AIP Publishing. Spectra from this work reprinted with permission from Misael and Gomes. Copyright 2023 American Chemical Society.

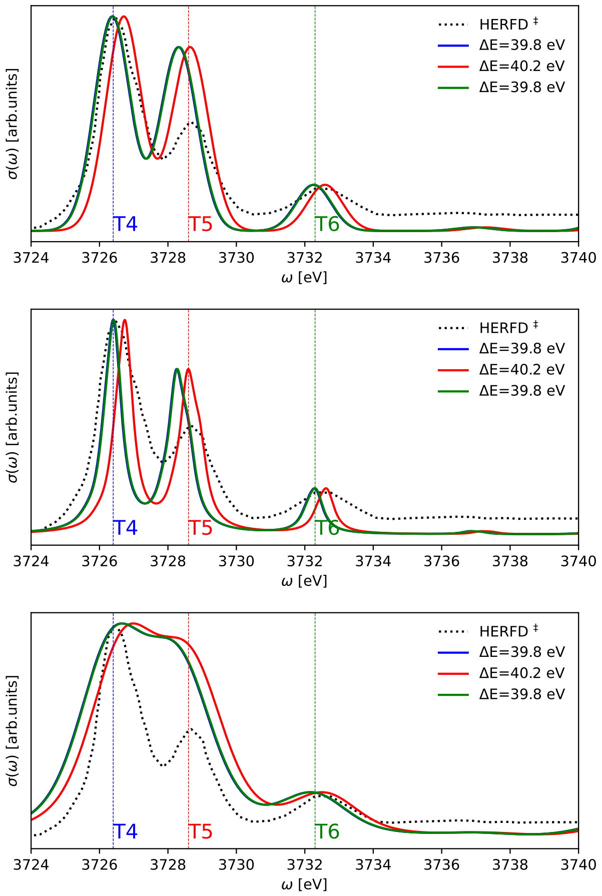

Figure A.5: Comparison of 2c-TDA XAS spectra at the uranium M_4-edge for different broadening functions with respect to the experimental data ($Cs_2UO_2Cl_4$) from Vitova et al. [328]. Shift to the main line in the experiment, depicted as the orange straight line. Copyright 2015 American Chemical Society applies to the uranium edges. Spectra from this work reprinted with permission from Misael and Gomes. Copyright 2023 American Chemical Society.

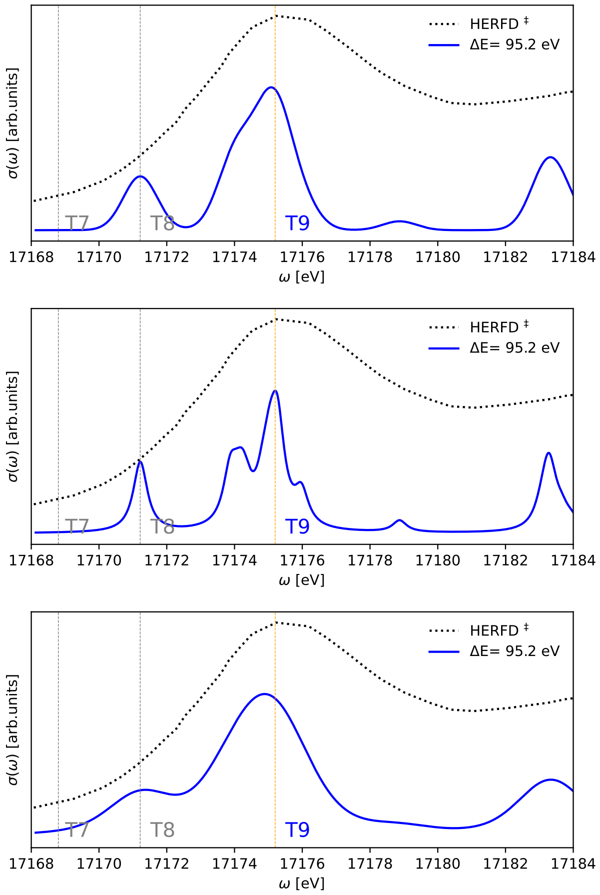

Figure A.6: Comparison of 2c-TDA XAS spectra at the uranium L_3-edge for different broadening functions with respect to the experimental data ($Cs_2UO_2Cl_4$) from Vitova et al. [328]. Shift to the main line in the experiment, depicted as the orange straight line. Copyright 2015 American Chemical Society applies to the uranium edges. Spectra from this work reprinted with permission from Misael and Gomes. Copyright 2023 American Chemical Society.

A.4 Comparison of 4-component calculations for the three models investigated

In the following table, we presented the shifts for all calculations performed in this work. In the manuscript text, we present the $UO_2Cl_4^{2-}$ results.

	O K-edge		
	UO_2^{2+}	UO_2^{2+} @ Cl_4^{4-}	$UO_2Cl_4^{2-}$
2c-TDA	-	-	13.5
4c-DR-TD (γ=1.0 eV)	13.0	13.6	13.8
	U M_4-edge		
2c-TDA	-	-	39.8
4c-DR-TD (γ=0.5 eV)	36.8	36.6	37.2
	U L_3-edge		
2c-TDA	-	-	95.2
4c-DR-TD (γ=0.5 eV)	89.9	84.5	86.3

Table A.1: Shifts from 2c-TDA-CAMB3LYP and 4-DR-TD-CAMB3LYP XAS spectra with respect to the experimental data ($Cs_2UO_2Cl_4$) from Denning, Vitova et al. [327, 328].

Bibliography of the current chapter

(326) Denning, R.; Green, J.; Hutchings, T.; Dallera, C.; Tagliaferri, A.; Giarda, K.; Brookes, N.; Braicovich, L. Covalency in the uranyl ion: A polarized x-ray spectroscopic study. *The Journal of Chemical Physics* **2002**, *117*, 8008–8020.

(327) Denning, R. G. Electronic structure and bonding in actinyl ions and their analogs. *The Journal of Physical Chemistry A* **2007**, *111*, 4125–4143.

(328) Vitova, T.; Green, J. C.; Denning, R. G.; Löble, M.; Kvashnina, K.; Kas, J. J.; Jorissen, K.; Rehr, J. J.; Malcherek, T.; Denecke, M. A. Polarization dependent high energy resolution X-ray absorption study of dicesium uranyl tetrachloride. *Inorganic chemistry* **2015**, *54*, 174–182.

List of Tables

List of Figures

SHEDDING X-RAYS ON MOLECULES THROUGH THE LENSES OF RELATIVISTIC ELECTRONIC STRUCTURE THEORY

Abstract

This thesis aims to investigate the electronic structure of actinides by means of *ab initio* relativistic quantum chemistry methods, with a specific emphasis on the spectroscopic observables of the uranyl moiety (UO_2^{2+}). Considering the pivotal role of this unit in the solid-state and solution chemistry of uranium, one of the most abundant and stable actinides on earth, as well as recent advancements in synchrotron radiation facilities, our investigation relies on evaluating the interaction of x-ray photons with the uranyl unit in varying degrees of complexity, ranging from molecules to crystalline solids.
First, we showcase how the resonant-convergent formulation of response theory can be employed to investigate the X-ray absorption fine structure (XAFS) of actinides. 4-component damped-response time-dependent density functional theory (4c-DR-TD-DFT) simulations for the uranyl tetrachloride dianion ($UO_2Cl_4^{2-}$) were found to be consistent with previous data for angle-resolved near edge x-ray absorption spectroscopy (NEXAFS) at the oxygen K-edge and high energy resolution fluorescence detected (HERFD) at the uranium M_4- and L_3-edges of the dicesium uranyl tetrachloride crystal ($Cs_2UO_2Cl_4$), a prototype system for actinide electronic structure investigations. We then will present the results of collaborative work with the Rossendorf Beamline at the European Synchrotron Radiation Facility (ESRF). 2-component TD-DFT simulations within the Tamm-Dancoff approximation (2c-TDA) and HERFD measurements of linear and bent uranyl systems highlight the role of charge transfer states in determining the spectral features at the uranium M_4-edge. The role of orbital correlation and relaxation in the core-ionization energies of heavy elements was investigated using the recently developed core-valence-separation equation-of-motion coupled-cluster method (CVS-EOM-CC). We also evaluated the performance of various 4- and 2-component Hamiltonians for calculating these properties. The results of this investigation demonstrate qualitative agreement with previously reported X-ray photoemission spectroscopy (XPS) data for $Cs_2UO_2Cl_4$ in the soft x-ray range (0.1 – 1 keV) and highlight the importance of computing two-electron interaction beyond the zeroth order truncation, i.e., the Coulomb term, when working at the tender (1 keV – 5 keV) and hard x-ray (5 keV – 200 keV) ranges. We also evaluated the performance of quantum-chemical embedding methods to account for environmental effects. Specifically, we employed the frozen density embedding (FDE) method, which allowed us to gain valuable insights into how the equatorial ligands of the uranyl ion influence its spectroscopic properties. Notably, this method successfully addressed the role of such interactions in binding energies in the soft x-ray range and in the peak splittings observed in the emission spectra at the U M_4-edge. The latter is particularly significant as it has been instrumental in addressing a long-standing problem in actinide science: the role of 5*f* orbitals in actinyl bonding.
In summary, this thesis presents fundamental research work that aims to push the boundaries of *ab initio* quantum chemical methods when addressing spectroscopic observables towards the bottom of the periodic table, and the findings of this work capture how these approaches can provide further insights into state-of-the-art experiments.

Keywords: x-ray spectroscopy, electronic structure theory, actinides

Laboratoire PhLAM
Laboratoire PhLAM – CNRS UMR 8523 – Université de Lille – Bâtiment P5 –
59655 Villeneuve d'Ascq – France

L’interaction des rayons X avec des molécules à travers le prisme de la théorie de la structure électronique relativiste

Résumé

Cette thèse vise à étudier la structure électronique des actinides au moyen de méthodes de chimie quantique relativiste *ab initio*, avec une emphase particulière sur les observables spectroscopiques de l’unité uranyle (UO_2^{2+}). Considérant le rôle central de cette unité en chimie des solides et en milieux aqueux et organique, ainsi que les avancées récentes dans les installations de rayonnement synchrotron, notre étude repose sur l’évaluation de l’interaction des photons de rayons X avec l’unité uranyle dans des degrés de complexité variés, allant des molécules aux solides cristallins.

Tout d’abord, nous mettons en avant comment la formulation résonante-convergente de la théorie de la réponse peut être utilisée pour étudier la structure fine d’absorption des rayons-X (XAFS) des actinides. Les simulations de la théorie de la fonctionnelle de la densité dépendante du temps avec réponse amortie en 4 composantes (4c-DR-TD-DFT) pour le dianion tétrachlorure de diuranyl ($UO_2Cl_4^{2-}$) se sont avérées cohérentes avec les données antérieures de méthodes spectroscopiques avec résolution angulaire, à savoir celles d’absorption des rayons X près du seuil (NEXAFS) au seuil K de l’oxygène et de détection de fluorescence à haute résolution énergétique (HERFD) aux seuils M_4 et L_3 de l’uranium du cristal de tétrachlorure de diuranyl de dicesium ($Cs_2UO_2Cl_4$), un système prototype pour les études de structure électronique des actinides. En plus, nous présenterons les résultats d’un travail collaboratif avec la ligne de lumière Rossendorf de l’Installation Européenne de Rayonnement Synchrotron (ESRF). Les simulations TD-DFT dans l’approximation de Tamm-Dancoff à 2 composantes (2c-TDA) et HERFD des différents complexes d’uranyle mettent en évidence le rôle des états de transfert de charge dans la détermination des caractéristiques spectrales au niveau du seuil M_4 de l’uranium. Le rôle de la corrélation et de la relaxation des orbitales dans les énergies d’ionisation de cœur des éléments lourds a été étudié en utilisant la méthode des équations de mouvement de cluster couplé avec la séparation cœur-valence (CVS-EOM-CC) récemment développée. Nous avons également évalué les performances de différents Hamiltoniens à 4- et 2- composantes pour le calcul de ces propriétés. Les résultats de cette étude soulignent l’importance du calcul des intégrales à deux électrons au-delà de la troncature d’ordre zéro, c’est-à-dire du terme de Coulomb, lorsqu’on travaille dans les gammes de rayons X tendres (1 – 5 keV) et durs (5 – 200 keV). Par ailleurs, nous avons également évalué les performances des méthodes de chimie quantique pour tenir compte des effets environnementaux. Plus précisément, nous avons utilisé la méthode d’intégration de densité figée (FDE) qui nous a permis d’acquérir des connaissances précieuses sur la manière dont les ligands équatoriaux de l’ion uranyle influencent ses propriétés spectroscopiques. Notamment, cette méthode a réussi à aborder le rôle des interactions électrostatiques dans les énergies de liaison dans la gamme des rayons X mous et dans les dédoublements de pics observés dans les spectres d’émission au niveau du seuil M_4 de l’uranium. Ce dernier est particulièrement significatif car il contribue de manière déterminante à aborder un problème de longue date dans la science des actinides : le rôle des orbitales 5*f* dans la liaison actinyle.

En résumé, cette thèse présente un travail de recherche fondamentale qui vise à repousser les limites des méthodes quantiques *ab initio* dans l’étude des observables spectroscopiques pour les éléments situés en bas du tableau périodique. Les résultats de cette étude illustrent comment ces approches peuvent apporter de nouvelles compréhensions sur les expériences de pointe.

Mots clés : spectroscopie des rayons x, théorie de la structure électronique, actinides